Een vergelijkende studie van mechanische en elektrische variabele transmissies

A Comparative Study of Mechanical and Electrical Variable Transmissions

Florian Verbelen

Promotoren: prof. dr. ing. K. Stockman, prof. dr. ir. P. Sergeant
Proefschrift ingediend tot het behalen van de graad van
Doctor in de industriële wetenschappen: elektromechanica

UNIVERSITEIT
GENT

Vakgroep Elektrische Energie, Metalen, Mechanische Constructies en Systemen
Voorzitter: prof. dr. ir. L. Dupré
Faculteit Ingenieurswetenschappen en Architectuur
Academiejaar 2019 - 2020

ISBN 978-94-6355-287-5
NUR 959
Wettelijk depot: D/2019/10.500/95

A Comparative Study of Mechanical and Electrical Variable Transmissions

Florian Verbelen

Dissertation submitted to obtain the academic degree of
Doctor of Electromechanical Engineering Technology

Supervisors:
Prof. dr. ing. Kurt Stockman
Prof. dr. ir. Peter Sergeant
Department of Electrical Energy, Metals, Mechanical Constructions and Systems (EEMMeCS)
Faculty of Engineering and Architecture
Ghent University
Tech Lane Ghent Science Park 131
B-9052 Zwijnaarde, Belgium
http://www.ugent.be/ea/eemmecs/en

Members of the examining board:

Prof. dr. ir. Gert De Cooman (chairman)	Ghent University
Prof. dr. ir. Mia Loccufier (secretary)	Ghent University
Prof. dr. ir. Peter Sergeant (supervisor)	Ghent University
Prof. dr. ing. Kurt Stockman (supervisor)	Ghent University
Prof. dr. ir. Sebastian Verhelst	Ghent University
Prof. dr. ir. Wim De Waele	Ghent University
dr. ir. Hendrik Vansompel	Ghent University
Prof. dr. ir. Walter Lhomme	Université de Lille
Prof. dr. ir. Omar Hegazy	Vrije Universiteit Brussel

The research of Florian verbelen was carried out for the EMTechno project (project ID: IWT150513) supported by VLAIO and Flanders Make, the strategic research center for the manufacturing industry

FACULTY OF ENGINEERING AND ARCHITECTURE

GHENT UNIVERSITY

Preface

Dit doctoraat heeft me veel bijgebracht zowel op technisch als persoonlijk vlak. De weg richting het behalen van dit doctoraat verliep niet altijd even vlot. Het is dan ook maar logisch dat ik de mensen die hiertoe hebben bijgedragen, bedank.

Eerst en vooral wil ik de mensen bedanken die mijn doctoraatsonderzoek mogelijk gemaakt hebben. Zonder mijn promotoren, prof. dr. ing. Kurt Stockman en prof. dr. ir. Peter Sergeant, zou er geen doctoraat geweest zijn. Ik heb de voorbije 4 jaar altijd beroep op hen kunnen doen, ook wanneer het onderzoek wat minder vlotte. Ook bedankt voor al die uren aan review werk van papers, rapporten en dit proefschrift. Bedankt voor de kans die ik gekregen heb.

Naast mijn promotoren zou ik ook graag prof. dr. ing. Stijn Derammelaere willen bedanken die me de kans gaf om als wetenschappelijk medewerker te starten. Dit bleek een prima springplank om 2 jaar later mijn doctoraat aan te vangen.

Tijdens een doctoraat kan je uiteraard niet al je hersenspinsels bespreken met je promotoren. Een groot deel van mijn EVT gerelateerde kennis heb ik rechtstreeks of onrechtstreek van dr. ir. Joachim Druant. Bedankt om, ondanks de stortvloed aan vragen, altijd zeer uitgebreid en met veel geduld te antwoorden. Verder wil ik ook graag dr. ir. Hendrik Vansompel vermelden. Zonder u zou de EVT opstelling niet werken. Uw schijnbaar onbeperkte kennis omtrent elektrische machines, dSPACE, STARTER en CAN heeft mij ongelofelijk veel bijgebracht.

Vervolgens zou ik graag de juryleden willen bedanken voor het nalezen van dit proefschrift. Dit vergt behoorlijk wat tijd en ik wil dan ook mijn appreciatie uitdrukken voor dit werk.

Dan kom ik nu toe aan mijn collega's. Zowel in Kortrijk als in Gent heb ik in een ontspannen sfeer kunnen werken aan mijn onderzoek. Ik ben jullie dan ook dankbaar en hoop nog vele jaren met jullie te kunnen samenwerken.

Mijn ouders wil ik bedanken voor de steun die ik altijd ervaren heb en de kans die ik gekregen heb om te studeren. Mijn schoonouders voor de vele praktische

hulp tijdens de afgelopen 4 jaar. Veel dank gaat ook uit naar mijn vrienden. Bedankt voor de uitputtende squashwedstrijdjes, gezellige etentjes, weekendjes weg, quiz/café bezoekjes,...

Tot slot wil ik mijn 4 grootste supporters bedanken: mijn vrouw, Finn, Fleur en Lily. Bedankt Lies om me te motiveren, chocomousse of taartjes te brengen, huishoudelijke taakjes over te nemen, kortom om er te zijn voor mij. Mijn kinderen wil ik bedanken voor de vele keren dat ze me verplicht hebben te ontspannen. Je zegt namelijk geen nee tegen een 5 jarige die Duplotorens tot aan het plafon willen bouwen ... Ze hielpen me relativeren en verder te kijken dan het tijdelijke probleem waarop ik mijn hoofd zat te breken. Doctoreren met opgroeiende kinderen, het is een opgave, maar ik zou het zo opnieuw doen.

Kortrijk, oktober 2019

Florian Verbelen

Contents

Summary

In drive trains, a gearbox is used to match the required torque and speed of the load with the operating range of the source. This source could be anything, from an electrical machine to an Internal Combustion Engine (ICE). In most of the industrial applications, the gearbox is used to increase the speed towards the source. Therefore, the torque that has to be delivered by the source is smaller, resulting in a smaller sized electrical machine (or other source). Classical vehicles with a manual transmission go one step further as the driver can select multiple gear ratios (in a vehicle with automatic transmission, shifting is done by a controller). At standstill, a small gear ratio is chosen resulting in a low speed of the wheels but with a high starting torque. During acceleration, a higher gear is selected to reduce the required speed of the ICE. This is important as at high engine speed, the ICE is operated at a lower efficiency. Shifting gears is thus done, among other things, to reduce the fuel consumption.

The problem with the manual transmission is that it only contains a fixed number of gear ratios. Although it could be interesting to use a gear between first and second, the transmission obviously does not allow that. To solve this, the variable transmission has been developed, also known as a Continuously Variable Transmission (CVT). A variable transmission is basically a gearbox of which the speed ratio can be varied continuously between 2 finite values. Consequently, any gear ratio between the limits can be selected. Therefore, the ICE can be operated on its optimal operating line, which results, in theory, in a lower fuel consumption compared to the manual transmission.

Besides adding a variable transmission, another possibility to reduce the fuel consumption is to change the topology of the drive train. An example of such an enhanced drive train is a Hybrid Electrical Vehicle (HEV). In these HEVs, the ICE and the wheels are decoupled. Therefore, the operating point of the ICE can be chosen independently of the wheels and that significantly reduces the fuel consumption. A well-known HEV drive train is the Toyota Hybrid System (THS). This drive train consists of a planetary gear that is used as power split device. The planetary gear is able to distribute the power to 2 electrical machines. As a result, one extra degree of freedom is obtained. That explains why the ICE can be operated

independently of the requested power of the wheels. Despite the many advantages, the planetary gear introduces losses due to friction and valuable space is taken by the 2 electrical machines.

An alternative for the classical HEV is a transmission based on an Electrical Variable Transmission (EVT). An EVT is basically a combination of two electrical machines and consists of 2 rotors and 1 stator. The permanent magnet EVT that is considered in this PhD has 2 electrical ports and 2 mechanical ports. Alternative topologies of the EVT, such as an induction based version, have not been considered due to its small power density. In case of a vehicle, the ICE could be connected to the inner rotor (shaft 1) and the wheels to the outer rotor (shaft 2). Both shafts are connected via the electrical ports by a common DC-bus. A battery can be connected to this DC-bus making it possible to store energy while braking.

There are thus several concepts that all aim to reduce the fuel consumption of a car. So far, a detailed comparison of these technologies has not been made. Consequently, it is not clear which technology offers the best solution for the given set of constraints. Therefore, in this PhD an extensive comparison is presented between EVT and CVT on component level and system level. The system level has been split in an analysis on a CVT based vehicle and on a drive train of a HEV.

To be able to compare the considered variable transmissions, models have been developed to estimate the efficiency for given operating points both in static as dynamic situations (for example during ratio variation). The model of the toroidal CVT consists of a contact model and a mechanical model. In the contact model, the traction coefficient between the elements is determined, based on which the transferred torque is calculated. This torque is than used in the mechanical model to determine the speed based on the applied torque. The component control of the toroidal CVT is related to a specific clamping force that defines the slip in the component and thus also the traction. The toroidal CVT relies thus on traction to transmit the torque. Traction means that a certain amount of slip between the driving elements is required. It is important that the slip does not become too high as this causes wear and results in high losses. Defining adequate control is thus essential. For a toroidal CVT, this clamping force can be controlled in an active way (by using a hydraulic cylinder) and a passive way (by using a loading cam). Due to its simplicity and stable operation, the loading cam is used as actuation system. Besides the slip, the speed ratio needs to be controlled as well. Therefore, an entirely new method has been developed focusing on the maximum torque of the CVT. During that analysis a clear link between the loading cam and the obtained dynamics is derived. Hence, a stiffer design of the loading cam will improve the dynamic response of the CVT. However, this comes at a cost of a reduction in efficiency. To calculate that efficiency, losses in the contact, loading cam and thrust bearings are taken into account.

The model of the belt CVT consists of a contact model, a mechanical model and a variator model. The contact model and mechanical model have the same purpose as with the toroidal CVT. The goal of the variator model is to calculate the clamping forces that are necessary to hold the belt in position. Hence, the ratio of both clamping forces is related to the obtained speed ratio. The belt CVT is, just like the toroidal CVT, a traction device. This means that slip needs to be controlled. To do so, hydraulic cylinders are used to apply a specific clamping force. The controller itself is derived based on the slip dynamics of the variable transmission. For the speed ratio control, a standard PI controller is used. To calculate the efficiency, losses in the contact, belt, bearings and hydraulic system are taken into account.

Several models of the EVT have been derived: a static model, a hybrid model and a dynamic model. Each model consists of a series of look-up tables that contain data based on a FE model. The theory behind this model has been derived in the PhD of Joachim Druant. For the convenience of the reader, a summary has been added in this thesis. The static model ignores dynamics of motion and current dynamics, i.e. speed and current variations can happen instantaneous. In the hybrid model, the current dynamics are still ignored. However, speed variations are now linked to the applied torque and inertia of the rotors. Finally, in the dynamic model, current dynamics are included as well. As discussed in this PhD, the dynamic model is only needed when highly dynamic phenomena are investigated. For example studying the impact of the pulsating torque of an ICE on the EVT has to be done with the dynamic model. If high speed variations occur for quasi static torque variations, the dynamic model should be used and for applications with a low dynamic content, both in torque and speed, the static model can be used. An example of such an application is a vehicle. Moreover, as the focus of this PhD is on automotive applications, the static model will be used.

Now the component models and their control are finished, the variable transmissions can be compared. To have a fair comparison, the maximum output torque is considered equal for all devices. The belt CVT is considered as reference. To match the output torque, design rules have been developed for the toroidal CVT (based on an expression for the maximum torque used in the optimal ratio variation) and for the EVT (based on scaling laws). Applying scaling laws to an EVT has never been done before. It enables a fast redesign of the EVT, based on an axial and radial scaling factor, in terms of minutes. Based on an FE model, this would take weeks. The size of the EVT and toroidal CVT are thus changed to match the output torque of the belt CVT. Moreover, the EVT is used in CVT mode. This means that no power is exchanged with the battery. The comparison of the efficiency of the components shows that the belt CVT performs best although the differences are limited. In terms of operating range, the maximum torque is of course the same but the speed ratio range of the EVT is much wider compared to

both CVTs.

Comparing the variable transmissions in a CVT based vehicle (no possibility to store energy) proves that the EVT based vehicle performs best, i.e. lowest fuel consumption. This shows that the slightly lower efficiency of the EVT in CVT mode compared to the traditional CVTs has no significant impact on the fuel consumption. Much more important is how the ICE can be used as explained at the beginning of this summary. Due to the wider speed ratio range of the EVT, the ICE can be controlled more optimally, especially for low wheel speeds. That explains why the EVT based vehicle has the lowest fuel consumption.

Finally, an EVT based HEV is compared with the THS based HEV (with battery to store energy). To compare both, the impact of the Energy Management Strategy (EMS) has to be excluded. The goal of this EMS is to find the optimal power flow through the drive train in order to minimize the fuel consumption. Rule based methodologies are not a good option for such a comparison as they can, unintentionally, bias the results. To be certain that the EMS is as optimal for the EVT as for the THS, dynamic programming has to be used. Dynamic programming basically solves the drive train for all possible power flows and consequently, the best solution is found for both drive trains. Comparing the results shows that the electrical losses in the THS are slightly higher than in the EVT. Furthermore, the EVT only needs a single gearbox to transfer power to the wheels, while the THS is equipped with 2 gears, one for the power split and one for the wheels. Therefore, the losses and thus fuel consumption of the THS are higher. The comparison shows that an EVT based drive train can reduce the fuel consumption up to 13% compared to a THS. It is important to mention that the models used to determine the losses of the EVT are validated on an actual prototype. With the THS, the overall efficiency estimations are realistic, but the models are not validated. It is thus to be expected that the differences in reality can be even bigger, in favor of the EVT.

Samenvatting

In aandrijftreinen wordt een tandwieloverbrenging gebruikt om het vereiste koppel en snelheid van de last af te stemmen op het werkingsgebied van de bron. Deze bron kan variëren van een elektrische machine tot een verbrandingsmotor. In het grootste deel van de industriële toepassingen, wordt een tandwieloverbrenging gebruikt om de snelheid naar de bron te verhogen. Daardoor zal het koppel dat door de bron moet worden geleverd kleiner zijn, wat resulteert in een kleinere elektrische machine (of een andere bron). Klassieke voertuigen met een manuele transmissie gaan nog een stap verder omdat de bestuurder meerdere verhoudingen kan selecteren. Bij stilstand wordt een kleine overbrengingsverhouding gekozen resulterend in een lage snelheid van de wielen maar een hoog startkoppel. Tijdens acceleratie wordt een hogere versnelling geselecteerd om de vereiste snelheid van de verbrandingsmotor te reduceren. Dit is belangrijk omdat bij een hoog toerental de verbrandingsmotor in een werkingspunt wordt gebruikt met lagere efficiëntie. Schakelen wordt dus onder andere gedaan om het brandstofverbruik te verminderen.

Het probleem met de manuele transmissie is dat er maar een beperkt aantal versnellingen zijn waaruit gekozen kan worden. Hoewel het interessant kan zijn om een versnelling te gebruiken tussen eerste en tweede, staat de transmissie dat natuurlijk niet toe. Om dit op te lossen is de variabele transmissie ontwikkeld, ook wel een Continu Variable Transmissie (CVT) genoemd. Een variabele transmissie is een versnellingsbak waarvan de overbrengingsverhouding continu kan worden gevarieerd tussen 2 eindige waarden. Bijgevolg kan elke overbrengingsverhouding tussen de limieten worden geselecteerd. Daardoor kan de verbrandingsmotor op zijn optimale operationele lijn worden gebruikt, wat in theorie resulteert in een lager brandstofverbruik in vergelijking met de manuele transmissie.

Een andere mogelijkheid om het verbruik te optimaliseren, naast het toevoegen van een variabele transmissie, is om de topologie van de aandrijftrein aan te passen. Een voorbeeld van zo'n aangepaste topologie is een Hybride Elektrisch Voertuig (HEV). In deze HEV's zijn de verbrandingsmotor en de wielen ontkoppeld. Daardoor kunnen de werkingspunten van de verbrandingsmotor onafhankelijk gekozen worden van de werkingspunten van de wielen en dat vermindert het brandstof verbruik aanzienlijk. Een voorbeeld van een HEV is het Toyota Hybrid System (THS). Deze aandrijflijn bestaat uit een planetair tandwiel dat het vermogen kan verdelen over 2 elektrische machines. Als gevolg wordt één vrijheidsgraad verkregen en dat verklaard waarom de verbrandingsmotor onafhankelijk van het gevraagde vermogen van de wielen kan worden gebruikt. Ondanks de vele voordelen introduceert het planetaire tandwiel verlies als gevolg van wrijving en bovendien wordt waardevolle ruimte ingenomen door de 2 elektrische machines.

Een alternatief voor de klassieke HEV is een transmissie op basis van een Elektrische Variabele Transmissie (EVT). Een EVT is in feite een combinatie van twee elektrische machines die bestaat uit 2 rotoren en 1 stator. De permanent magneet EVT die in dit proefschrift is bestudeerd bevat 2 elektrische poorten en 2 mechanische poorten. Alternatieve topologieën zoals een inductie gebaseerde EVT zijn niet opgenomen in de vergelijking door de te lage vermogensdichtheid. In het geval van een voertuig kan de verbrandingsmotor worden aangesloten op de binnenste rotor (as 1) en de wielen op de buitenste rotor (as 2). Beide assen zijn verbonden via de elektrische poorten door een gemeenschappelijke DC-bus. Op deze DC-bus kan een batterij aangesloten worden wat het mogelijk maakt om energie op te slaan tijdens het remmen.

Er zijn dus verschillende concepten die er allemaal op gericht zijn om het brandstofverbruik van een wagen te verminderen. Tot dus ver is er geen gedetailleerde vergelijking van deze technologieën gemaakt. Bijgevolg is het niet duidelijk welke technologie de beste oplossing biedt voor de gegeven set van randvoorwaarden. Daarom wordt in dit proefschrift een uitgebreide vergelijking voorgesteld tussen EVT en CVT, op componentniveau en systeemniveau. Het systeemniveau is daarna nog opgesplitst in een analyse op een CVT gebaseerd voertuig en een volwaardige HEV.

Om de variabele transmissies te kunnen vergelijken, zijn modellen ontwikkeld die de efficiëntie kunnen berekenen voor gegeven werkingspunten, zowel tijdens statische als dynamische situaties (bijvoorbeeld tijdens variërende overbrengsverhouding). Het model van de toroïdale CVT bestaat uit een contactmodel en een mechanisch model. In het contactmodel wordt de tractiecoëfficiënt tussen de elementen bepaald, op basis waarvan het overgedragen koppel wordt berekend. Dit koppel wordt dan gebruikt in het mechanische model om de snelheid te bepalen op basis van het aangelegde koppel. De controle op componentniveau van de toroïdale CVT is gerelateerd aan een specifieke klemkracht die de slip definieert tussen de onderlinge componenten en dus ook de tractie. Slip is noodzakelijk, anders is er geen tractie en dus geen koppeloverdracht. De slip mag echter niet te groot worden omdat dit leidt tot slijtage en hoge verliezen. Een adequate controller is dus van groot belang. Voor een toroïdale CVT kan deze klemkracht worden bekomen door gebruik te maken van een actieve controle (op basis van een hydraulische cilinder) of door een passieve controle (op basis van een nokkenkoppeling). Vanwege zijn eenvoud en stabiele werking is de nokkenkoppeling gekozen als actuator voor de klemkracht. Naast de slip moet ook de overbrengingsverhouding worden gecontroleerd. Daarvoor is een geheel nieuwe methode ontwikkeld die zich richt op het maximumkoppel van de CVT. Bovendien is een duidelijke link tussen de gebruikte nokkenkoppeling en de verkregen dynamiek aangetoond. Een stijver ontwerp van de nokkenkoppeling zorgt namelijk voor betere dynamische eigenschappen. Dit gaat echter ten koste van de efficiëntie. Om die efficiëntie te berekenen, worden de verliezen in de contacten, nokkenkoppeling en lagers in rekening gebracht.

Het model van de duwband CVT bestaat uit een contactmodel, een mechanisch model en een variatormodel. Het contactmodel en het mechanische model hebben hetzelfde doel als bij de toroïdale CVT. Het doel van het variatormodel is het berekenen van de klemkrachten die nodig zijn om de duwband op zijn plaats te houden. De verhouding van beide klemkrachten is immers gerelateerd aan de verkregen overbrengingsverhouding. De duwband CVT is, zoals de toroidale CVT, een tractie-apparaat. Dit betekent dat de slip moet worden gecontroleerd. Om dit te doen, worden hydraulische cilinders gebruikt om een specifieke klemkracht uit te oefenen. De controller zelf is afgeleid op basis van de slipdynamiek van de variator. Voor de regeling van de overbrengingsverhouding wordt een standaard PI-regelaar gebruikt. Om de efficiëntie te berekenen, worden verliezen in het contact, riem, lagers en hydraulisch systeem in rekening gebracht.

Er zijn verschillende modellen voor de EVT afgeleid: een statisch model, een hybride model en een dynamisch model. Elk model bestaat uit een reeks tabellen met gegevens die data bevatten bekomen via een eindige-elementen methode. De theorie hierachter is afgeleid in het proefschrift van Joachim Druant (2018). Voor het gemak van de lezer is een samenvatting toegevoegd in dit proefschrift. Het statisch model verwaarloosd de mechanische en elektrische dynamiek, d.w.z dat snelheid en stroom wenswaarden ogenblikkelijk bereikt worden. In het hybride model wordt wel rekening gehouden met de dynamiek van de roterende onderdelen. De snelheid wordt nu bepaald aan de hand van het aangelegde koppel en de inertie van de rotoren. Tot slot wordt in het dynamisch model ook rekening gehouden met stroom dynamiek. Zoals besproken in dit proefschrift kan het dynamisch model gebruikt worden voor het analyseren van hoog dynamische fenomenen. Het bestuderen van de impact van de koppelpulsen afkomstig van de verbrandingsmotor op de EVT, moet bijvoorbeeld met het dynamisch model gebeuren. Wanneer enkel een vrij hoge dynamiek in snelheid vereist is kan het hybride model gebruikt worden. Indien zowel koppel als snelheidsvariaties beperkt zijn, gaat de voorkeur uit naar het statisch model. Een voorbeeld van een dergelijke applicatie is een voertuig. Omdat de focus in dit proefschrift op voertuigtoepassing ligt is het statische model gebruikt.

Zodra de componentmodellen en hun controle functioneel zijn, kunnen ze worden vergeleken. Voor een eerlijke vergelijking wordt het maximale belastingskoppel als gelijk beschouwd voor alle apparaten. De duwband CVT wordt als referentie beschouwd. Om het belastingskoppel van de verschillende technologieën op elkaar af te stemmen, zijn ontwerpregels ontwikkeld voor de toroïdale CVT (op basis van een uitdrukking voor het maximum koppel) en voor de EVT (gebaseerd op schalingswetten). Schalingswetten toepassen op een EVT is nog nooit eerder gedaan. Het maakt het mogelijk om een EVT opnieuw te ontwerpen, gebaseerd op een axiale en radiale schaalfactor, in een tijdspanne van minuten. Gebaseerd op een eindige-elementen methode zou dit weken duren. De grootte van de EVT en toroïdale CVT wordt dus aangepast zodat hun maximale belastingskoppel overeen komt met dat van de duwband CVT. Bovendien wordt de EVT gebruikt in de CVT-modus. Dit betekent dat er geen vermogen wordt uitgewisseld met de batterij. De vergelijking van de efficiëntie van de componenten laat zien dat de duwband CVT de hoogste efficiëntie bereikt, hoewel de verschillen beperkt zijn. In termen van werkingsgebied is het maximale koppel natuurlijk hetzelfde, maar de spreiding van de overbrengingsverhouding van de EVT is veel groter vergeleken met beide CVT's.

De vergelijking op systeemniveau waarbij een CVT gebaseerd voertuig beschouwd is (geen mogelijkheid tot energie opslag), toont aan dat het voertuig op basis van de EVT het best presteert, d.w.z. het laagste brandstofverbruik. Dit laat zien dat de enigszins lagere efficiëntie van de EVT in CVT-modus in vergelijking met de traditionele CVT's, geen significante invloed heeft op het brandstofverbruik. Veel belangrijker is hoe de verbrandingsmotor kan worden gebruikt zoals uitgelegd aan het begin van deze samenvatting. Vanwege het bredere bereik waarin de overbrengingsverhouding kan worden gevarieerd, kan de verbrandingsmotor optimaler worden gebruikt, vooral bij hele lage snelheden. Dat verklaart waarom het EVT gebaseerde voertuig het laagste brandstofverbruik heeft.

Tot slot is een op EVT gebaseerde HEV vergeleken met de THS gebaseerde HEV (met de mogelijkheid tot energie opslag). Om beide te vergelijken, moet de impact van de Energie Management Strategie (EMS) worden uitgesloten. Het doel van de EMS is om de vermogensverdeling te vinden die ervoor zorgt dat het brandstofverbruik tot een minimum beperkt wordt. Regelgebaseerde methodologieën voor de EMS zijn geen goede optie voor een dergelijke vergelijking omdat ze, onbedoeld, de resultaten kunnen beïnvloeden. Om er zeker van te zijn dat de EMS even optimaal is voor de EVT als THS, moet "Dynamic Programming" (DP) worden gebruikt. DP berekent voor iedere mogelijke verdeling van de vermogens het brandstofverbruik en selecteert daarna de beste oplossing voor beide aandrijflijnen. Uit de vergelijking van de resultaten blijkt dat de elektrische verliezen van de THS groter zijn dan die van de EVT. Bovendien heeft de EVT heeft maar één tandwielkast nodig (transportvermogen naar de wielen), terwijl de THS is uitgerust met 2 tandwielkasten (één voor de splitsing van de vermogens en één voor de wielen). Daarom zijn de verliezen en dus het brandstofverbruik van de THS hoger. De vergelijking laat zien dat het brandstofverbruik van een HEV met EVT 13% lager kan liggen in vergelijking met een THS. Belangrijk om te vermelden is dat de modellen die worden gebruikt om de verliezen van de EVT te bepalen zijn gevalideerd op een daadwerkelijk prototype. Voor de THS is een schatting van de efficiëntie gemaakt, maar de modellen zijn niet gevalideerd. Het valt dus te verwachten dat de verschillen in de werkelijkheid nog groter kunnen zijn, in het voordeel van de EVT.

List of Abbreviations

ICE	Internal Combustion Engine
CVT	Continuously Variable Transmission
EVT	Electrical Variable Transmission
HEV	Hybrid Electrical Vehicle
THS	Toyota Hybrid System
FE	Finite Element
EMS	Energy Management System
DP	Dynamic Programming
PM	Permanent Magnet
CMM	Carbone Mangialardi Mantriota
MEC	Magnetic Equivalent Circuit
PWM	Pulse Width Modulation
LUT	Look-up Table
NEDC	New European Driving Cycle
WLTC	Worldwide Harmonized Light Vehicles Test Cycle
PMSM	Permanent Magnet Synchronous Machine
OP	Operating Point
SoC	State of Charge
DOF	Degree Of Freedom
AF	Absolute Fault
RF	Relative Fault

Chapter 1

Introduction

In this first chapter, the work performed in the scope of this PhD is introduced. In section 1.1 the problem statement is presented. The reader is introduced in the world of the variable transmission and the motivation for this research is presented. Following on this introduction, the research goals are summed up in section 1.2. Section 1.3 gives an outline of this work. Finally, in section 1.4 a list with the published scientific publications made in scope of this PhD is incorporated.

1.1 Problem statement

Manufacturers of advanced drive trains for the automotive industry encounter an ever growing pressure to reduce fuel consumption and emissions, as a result of increasingly stringent regulation. As a result, they are forced to innovate in order to find new solutions that can assist in reaching the climate goals. Possible solutions are related to an alternative drive train structure or the introduction of an emerging component (variable transmission, improved Internal Combustion Engine (ICE), innovative fuel, fuel cell, ...). Innovative fuels, fuel cells or improvements in the design of the ICE are considered out of scope for this thesis. The focus of this work is thus on the topology of the drive train and more importantly on the use of variable transmissions automotive applications.

Reducing the fuel consumption based on alternative drive train configurations can be characterized in 3 groups: Hybrid Electrical Vehicles (HEV), pure Electrical Vehicles (EV) and Continuously Variable Transmission (CVT) based Vehicles (CVTV, later on discussed). The main advantage of the EVs is that the ICE is removed and as a result, no harmful greenhouse gases are emitted (ignoring greenhouse gasses related to the production of the battery and electricity). The main disadvantages, as commonly known, are the limited range, the precious time that is lost to charge the batteries and the cost [1,2]. A lot of research has been done so far to better estimate the remaining range [3], battery charging [4, 5] or to even swap the batteries [6, 7]. Even though a lot of effort has been put into the development of EVs, their market share world-wide is still fairly limited.

HEVs offer a solution, to a certain extend, to the listed problems. As there is an ICE in the vehicle, the range is significantly extended and the battery pack can be reduced. Furthermore, charging of the battery is done while driving, so no time is lost. The side-effect is of course that there is exhaust of green house gasses (in case of fossil-fueled ICE). However, HEVs tend to be more efficient than classical vehicles due to the power split capabilities of the drive train. These power split transmissions have a long history in the agricultural industry [8, 9] (mechanical power split combined with hydraulic motor/pump) of which the main principles have been adopted by the automotive industry [10]. The device that is used, in all kinds of industries, to enable the power split is the mechanical planetary gearset (the magnetic equivalent could be an alternative [11, 12]). By using this planetary gearset, it is possible to operate the ICE independently from the wheels [13, 14]. As a consequence, the ICE can be operated at its most efficient operating point, which increases the drive train efficiency and thus reduces fuel consumption. Furthermore, the electrical machines used in a HEV allow to store a part of the braking energy in the battery [15].

Despite the many advantages of HEVs, the power split concept based on a planetary gearset has some drawbacks related to the mechanical gears that are used.

Mechanical gears come with friction and thus wear and heat dissipation. Heat needs to be evacuated. Consequently, there is a need for a coolant (typically oil) that needs to be sealed off from the environment. Finally, the concept incorporates the use of 2 electrical machines, which take valuable space.

The main gain of a HEV compared to a classical vehicle is thus the reduction in fuel consumption due to a better selection of the operating points of the ICE. In a classical car, the driver selects the operating points of the ICE by shifting the gear. The better the driver tunes the gear shift with the speed of the ICE, the lower the fuel consumption will be. For example, at high speed a high gear is chosen, which corresponds with a high gear ratio. By shifting, the speed of the ICE can be somewhat controlled and that optimizes the fuel consumption. The problem with this method is that there are only a limited number of gears from which the driver can choose. In many cases, one can choose out of 5 or 6 gears (and one for driving backwards). Shifting in between two gears is not possible, nevertheless it could be interesting. The component, capable of doing this, is called the variable transmission.

A variable transmission is a torque converter that has the capability to vary the speed ratio between input and output shaft in a continuous way between two finite values. Variable transmissions can be classified in 3 main groups: hydraulic, mechanic and electromagnetic devices.

Hydrostatic transmissions are often used in off-road applications where large peak torques are required at low speeds. High power density is the main advantage of this technology. The efficiency of the system is in the order of 50% to a maximum of 70% depending on the operating point [16]. The efficiency is rather low in comparison with mechanical and electromagnetic alternatives. Therefore, this transmission is not considered in this thesis.

The mechanical devices, also referred to as CVTs, are used in vehicles to vary the speed ratio of the drive train (earlier denoted as CVTV) in order to reduce the fuel consumption [17, 18]. Besides the automotive industry, these transmissions are also used in wind power systems to regulate the speed ratio in order to maintain a relatively constant generator speed which increases the efficiency of the drive train [19–21].

In literature, many types of CVT are examined of which the belt CVT and the toroidal CVT are most frequently used. The belt CVT consists of 2 pulleys that are composed of a fixed half and a movable half (sheave), see Fig. 1.1 (b). By adapting the position of the movable sheaves, the belt runs on another radius and as a result the speed ratio is altered. The belt CVT was the first CVT that was made commercially available. Therefore, a lot of research has already been done on dynamics [22,23], power losses in the belt [24] and control strategies [25].

The main advantages of the belt CVT are ease of implementation while the main drawbacks are the limited torque capacity and low efficiency. The low efficiency is mainly related to steady state losses in the hydraulic actuation system and due to suboptimal control. Hence, there is a trade-off between losses and stable operation.

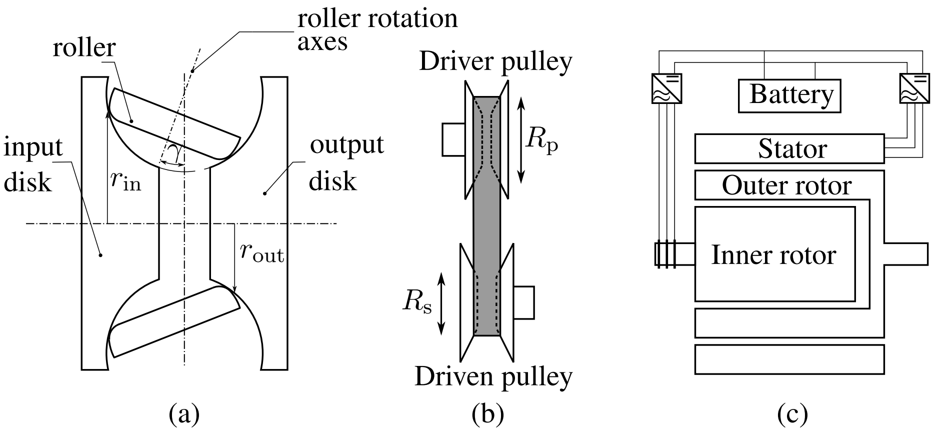

Figure 1.1: Principle scheme of the considered variable transmissions: (a) toroidal CVT, (b) belt CVT, (c) EVT.

In the toroidal CVT, power is transmitted from the input disc to the output disc through a system of rollers (Fig. 1.1 (a)). From the geometrical speed ratio, defined as $\tau = \frac{r_{\text{out}}}{r_{\text{in}}}$, it can be seen that by varying the contact points of the rollers given by the distances r_{in} and r_{out} respectively, the speed ratio can be varied in a continuous way. Indeed, these contact points can be changed smoothly by manipulating the tilting angle γ of the rollers. To avoid a moving contact between two metal components and the corresponding wear, a traction fluid is used. The main advantage of the toroidal CVT is the high torque capacity while the main drawback is the complexity of the system.

The drawbacks of the belt CVT open up a window of opportunities for the toroidal CVT. Kluger described in [26] a number of transmissions and concluded that the toroidal CVT has an overall efficiency which is 5.4% higher than the belt CVT. Imanishi published in [27] on the progress in torque capacity for CVTs. The reported limit for the toroidal CVT is around 400 Nm while the maximum torque capacity for a belt CVT is approximately 250 Nm. These findings are supported by Simons in [28] (belt CVT 250 Nm) and Shinojima in [29] (toroidal CVT 390 Nm). A solution for the rather low torque capacity of the belt CVT is provided in [30, 31] where a two stage chain CVT is presented. The maximum torque of that prototype is 500 Nm and could be scaled up towards 2000 Nm which makes it capable of driving SUVs and truck applications. Moreover, an improved design of the hydraulics that allows higher clamping forces to be used or optimized control can also significantly increase the torque capacity and efficiency as will be shown in chapter 3.

While much research has been done on CVTs, nowadays the electromagnetic alternative receives more and more attention. The Electrical Variable Transmission (EVT) also known as the dual mechanical port electric machine or four quadrant transducer [32] is basically a combination of two electrical machines which consists of 2 rotors and 1 stator (Fig. 1.1 (c)). The Permanent Magnet (PM) EVT that is considered in this PhD has 2 electrical ports and 2 mechanical ports. In case of a vehicle, the ICE could be connected to the inner rotor (shaft 1) and the wheels to the outer rotor (shaft 2). Both shafts are connected via the electrical ports by the DC-bus, slip rings and 2 inverters. The system in Fig. 1.1 also has a battery (optional) connected to the DC-bus making it possible to store energy while braking.

Different EVT topologies have been proposed and analyzed in literature. The fundamental operating principle of an induction machine based EVT is discussed in [33–35]. In this type of EVT, the outer rotor consists of a squirrel cage. Another feature of this EVT is that the magnetic field can be changed for optimal torque control [35, 36]. The main disadvantage is the limited power density compared to PM versions [37–39]. This makes the PM version as described in [40, 41] particularly interesting for HEVs.

In automotive applications, both an EVT or a CVT could be applied. It is clear from literature, that both have their advantages. However, to decide which technology is best given the application, a detailed comparative study is necessary. At this point, such a study both on component and system level is not available in literature.

1.2 Scientific goals

As explained in section 1.1, there is no comparison available in literature between mechanical and electrical variable transmissions that considers the entire operating range of the devices. To set up such a comparison, models of the toroidal CVT, belt CVT and EVT are required that are able to calculate the efficiency. The first goal is thus to set up these models and validate them based on data from literature or measurements. The efficiency of the variable transmissions is presented as function of 2 parameters: speed ratio and load torque for a given input speed. Hence, it is important that the structure of each model allows to use these parameters as input.

The second goal is related to the size and thus torque capacity of the variable transmissions. To have a fair comparison, the maximum output torque should be approximately the same for all variable transmissions. It is thus important to develop a design methodology for the variable transmissions. The belt CVT and its operating range are considered as a reference. Therefore, the focus is on the toroidal CVT and EVT. For the toroidal CVT, the maximum torque is described in terms of geometrical parameters that enable to study design modifications. This cannot be done for the EVT as the model depends on FE calculations. For the EVT, two design methodologies have been developed in scope of this thesis: a magnetic equivalent circuit model and scaling laws. These methods, especially the scaling laws, allow to modify the size of the EVT, with a reasonable computational effort.

The third goal is to compare the variable transmissions, with comparable maximum output torque, based on their efficiency both at component level and system level. The component level comes down to comparing the efficiency maps while the system level comparison will be done based on a CVT based vehicle. As the EVT has one degree of freedom more than the CVT, the electrical ports are not actively used during this comparison. Hence, the EVT is used as CVT, which means that no battery is used.

Finally, the forth goal is to compare an EVT based HEV with a well-known HEV drive train: the Toyota Hybrid System. Both drive trains are modeled and an optimal system level controller is defined based on dynamic programming. The main difference with the previous comparison is that due to installed storage capacity, i.e. battery, the capabilities of the EVT are now fully exploited.

1.3 Outline

In accordance with the research goals of the PhD, this work is structured as follows. The first part, chapters 2, 3, 4 and 5, are related to modeling and sizing of the variable transmissions (first and second goal). Chapter 2 focuses on the toroidal CVT while chapter 3 and 4 focus on the belt CVT and EVT respectively. In chapter 5, special attention is given to the scaling laws of the EVT. The second part of the thesis is the comparison itself (chapter 6). This comparison contains 2 parts: a comparison in CVT mode (goal 3) and a comparison in HEV mode (goal 4). Finally, chapter 7 concludes this work.

1.4 Publications

Articles in International SCI Journals

An overview of peer-reviewed journal papers that were published in the scope of this PhD:

- F. Verbelen, S. Derammelaere, P. Sergeant, K. Stockman, ”Half toroidal continuously variable transmission: trade-off between dynamics of ratio variation and efficiency", Mechanism and Machine theory, vol 107, 14 pages, 2017

- F. Verbelen, J. Druant, S. Derammelaere, H. Vansompel, F. De Belie, K. Stockman, P. Sergeant, "Benchmarking the permanent magnet electrical variable transmission against the half toroidal continuously variable transmission", Mechanism and Machine theory, vol 113, 17 pages, 2017

- F. Verbelen, S. Derammelaere, P. Sergeant and K. Stockman, "A comparison of the full and half toroidal continuously variable transmission in terms of dynamics of ratio variation and efficiency", Mechanisms and Machine Theory, vol 121, 23 pages, 2018

- F. Verbelen, A. Abdallh, H. Vansompel, K. Stockman, P. Sergeant, "Sizing methodology based on scaling laws for a permanent magnet electrical variable transmission, IEEE Transactions on Industrial Electronics, 11 pages, 2019

Articles in conference proceedings

An overview of the most important conference papers that were published in the scope of this PhD:

- F. Verbelen, S. Derammelaere, P. Sergeant and K. Stockman, "Visualizing the efficiency of a continuously variable transmission", Energy Efficiency in Motor Driven Systems, 10 pages, 2017

- F. Verbelen, M. Haemers, J. De Viaene, S. Derammelaere, K. Stockman, P. Sergeant, "Adaptive PI Controller for Slip controlled Belt Continuously Variable Transmission", PID conference (International Federation of Automatic Control), 6 pages, 2018

- M. Vafaeipour, M. Baghdadi, F. Verbelen, P. Sergeant, J. Van Mierlo, K. Stockman, O. Hegazy, "Technical Assessment of Utilizing an Electrical Variable Transmission System in Hybrid Electric Vehicles", IEEE Transportation electrification conference and expo, 8 pages, 2018

- S. Goyal, F. Verbelen, A. Abdallh, K. Stockman, P. Sergeant, "Energy management strategy for oscillating drive trains equipped with an electric variable transmission", International Conference on Electrical Machines and Systems, 6 pages, 2018

- F. Verbelen, J. Druant, A. De Kock, K. Stockman, P. Sergeant, "Magnetic Equivalent Circuit Model of a Permanent", International Conference on Electrical Machines, 7 pages, 2018

- M. Vafaeipour, M. Baghdadi, F. Verbelen, P. Sergeant, J. Van Mierlo, O. Hegazy, ”An ECMS-based Approach for Energy Management of a HEV Equipped with an Electrical Variable Transmission ”, International Conference on Ecological Vehicles and Renewable Energies, 8 pages, 2019
- M. Vafaeipour, D. Tran, M. Baghdadi, F. Verbelen, P. Sergeant, K. Stockman, J. Van Mierlo, O. Hegazy, ”Optimized Energy Management Strategy for a HEV Equipped with an Electrical Variable Transmission System”, Electric Vehicle Symposium, 12 pages, 2019
- F. Verbelen, H. Vansompel, A. Abdallh, K. Stockman and P. Sergeant, ”Design methodology for a PM electrical variable transmission used in HEV”, Energy Efficiency in Motor Driven Systems, 12 pages, 2019
- F. Verbelen, P. Defreyne, P. Sergeant and K. Stockman, ”Efficiency measurement strategy for a planetary gearbox with 2 degrees of freedom”, Energy Efficiency in Motor Driven Systems, 12 pages, 2019

Chapter 2

Toroidal Continuously Variable Transmission

In this chapter, the toroidal CVT is introduced. First, the key components and the operating principle of the CVT are discussed. Subsequently, the modeling techniques, control of the device and model validation are discussed. The general goal of this chapter is to present a model of a toroidal CVT that can be used to compare this variable transmission, in terms of efficiency, with alternative technologies. A model, capable of estimating the efficiency of the device is therefore an important requirement. Furthermore, it should be able to describe efficiency as function of the speed ratio (ratio of the output speed and input speed) and load torque.

2.1 Introduction

In order to compare the considered variable transmissions, models and subsystem control are needed. For these models, a set of model requirements have been defined: parametrized, following the physical causality, capable of analyzing dynamic events and incorporated losses.

The model needs to be parametrized to be able to analyze the effect of design changes on, for example, the output torque. The equations, defined in literature, are all based on a generalized description of the CVT. Commonly used parameters are the radius of a component, number of rollers, etc. More information on the geometrical parameters can be found in the next section.

Physical causality is important in order to obtain realistic results when doing a dynamic simulation. However, the models found in literature started with speed of the components as input. From speed, slip is deduced, which results in traction and thus torque. In this chapter, the relation has been reversed in order to obtain the speed based on the applied torque.

As this PhD discusses the performance of variable transmissions, the models need to be able to simulate dynamic events such as ratio variation. Although most of the models described in literature are perfectly capable of predicting what happens during these events, no research has been done on how the ratio should be varied. Therefore, in this chapter a detailed analysis is made of the ratio variation and how this process can be optimized resulting in a contribution to the state of the art.

Finally, losses need to be incorporated as the efficiency of the different variable transmissions will be compared. To that extend, only a small contribution is made by taking into account the speed dependency of the losses of the axial thrust bearings that support the intermediate rollers. Based on the defined models, efficiency can be calculated as function of speed ratio, load torque and speed. To visualize the efficiency a novel extrapolation method has been developed that is described in [42].

Apart from the models, the subsystem control needs to be defined. In case of a toroidal CVT, two controllers are needed: slip and ratio control. On the slip control, a lot of information is available related to the passive control. However, on the active control, the discussing is limited to patents that describe the general idea and advantages. No information can be found on how the control parameters can be derived. Therefore, in this chapter, a new method is applied based on the linearized slip dynamics of the CVT.

Concerning the ratio control, papers presenting experimental results can be found. However, as mentioned before, no detailed study is done on how optimal this ratio variation is performed. Therefore, a ratio variation algorithm has been designed in order to have the fastest ratio variation with minimal losses. This work resulted in 2 journal publications [43, 44]

2.2 Operating principle

In a toroidal CVT, power is transmitted from the input disc to the output disc via a set of intermediate rollers (see Fig. 2.1). To avoid metal to metal contact between the elements, a fluid known as traction fluid is used. This fluid separates the elements whereby contact and thus wear of the elements is avoided. As a toroidal CVT is a traction device, a certain amount of slip between the discs and rollers is necessary to transmit torque. However, to avoid excessive slip, the force, referred to as the clamping force, which presses all components together is to be controlled via a hydraulic cylinder [29, 45, 46] (see section 2.6) or a loading cam [47–49] (see section 2.7).

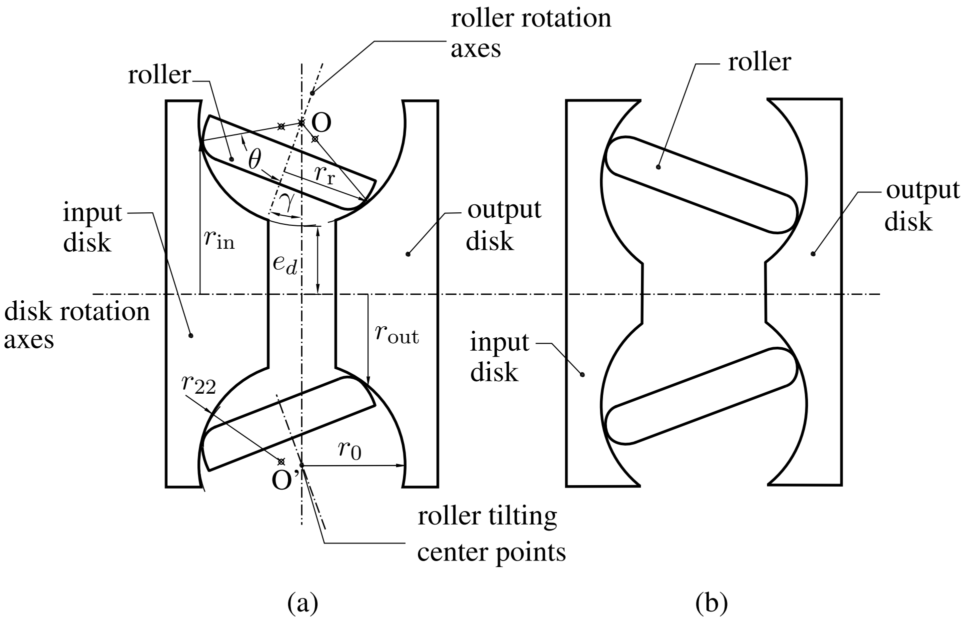

Figure 2.1: (a) Half toroidal CVT; (b) Full toroidal CVT.

The well known formula for the speed ratio τ_s, ignoring losses in the power transfer, is chosen as starting point to explain how the speed ratio of this CVT is varied:

$$\tau_s = \frac{\Omega_{out}}{\Omega_{in}} = \frac{T_{in}}{T_{out}} \tag{2.1}$$

in which the speed of the input disc and the output disc are denoted by Ω_{in} and Ω_{out} respectively and the torque generated by the input disc and output disc are characterized by T_{in} and T_{out} respectively. As torque equals force multiplied with the length of the lever arm, both the input and output torque, can be written in terms of the traction force Ft and contact radius r. If it is assumed that these traction forces at input Ft_{in} and output Ft_{out}, generated by shear stress in the oil film between the different components, are identical, it is possible to write:

$$\tau_{\text{s}} = \frac{Ft_{\text{in}} r_{\text{in}}}{Ft_{\text{out}} r_{\text{out}}} = \frac{r_{\text{in}}}{r_{\text{out}}} \tag{2.2}$$

By changing the orientation of the intermediate roller γ related to the symmetry line (see Fig. 2.1), the contact points between the input disc and roller r_{in} on the one hand and the roller and the output disc r_{out} on the other hand are changed and thus also the speed ratio is varied. Note that in (2.1) speed loss or slip ν has been ignored. The slip can be calculated as:

$$\nu = 1 - \frac{\frac{\Omega_{\text{out}}}{\Omega_{\text{in}}}}{\frac{r_{\text{out}}}{r_{\text{in}}}} \tag{2.3}$$

and if ν equals 0 (no slip), the following is true, which matches with (2.1) and (2.2):

$$\frac{\Omega_{\text{out}}}{\Omega_{\text{in}}} = \frac{r_{\text{out}}}{r_{\text{in}}} \tag{2.4}$$

Important to mention is that the ratio variation mechanism of the toroidal CVT can be considered as its Achilles heel. Hence, often multiple rollers are used to spread the traction forces over several contact points. However, a potential problem occurs if the rollers are not exactly oriented in the same manner. Take for example a 2 roller system, with a roller A and B. If both are not correctly aligned (both have different tilting angle γ and thus contact radii), roller A will strive for a different speed ratio as roller B (see (2.2)). The end result (actual speed ratio) will be a value in between which means that there will be a lot of slip (gross slip) under these conditions. In this operating point, the traction capabilities are inferior to what the controller expects. This can lead to damage inside the CVT. In toroidal CVTs, an attempt to avoid this is made by fixing the rollers to each other with a flexible cable. The flexible cable is needed as the components are moving but the cable also allows the components to shift relatively from each other over time. This phenomenon is not modeled as it is difficult to quantify how much the rollers go out of synchronization over time. The model that is discussed in the following sections of this chapter is thus only valid for toroidal CVTs of which the rollers move perfectly in synchronization.

There are 2 topologies of toroidal CVTs: the half toroidal and the full toroidal (see Fig. 2.1 (a) and (b)). Both topologies are clearly very similar and can therefore be defined by the same set of geometrical parameters. Both are operated in the same way. However, there are some significant differences concerning efficiency and dynamic behavior as will be shown in chapter 6.

The parameter that identifies a toroidal CVT as the half or full variant is the half cone-angle θ. This half cone-angle is defined as the angle between the axis of rotation and the line that goes through the center of the cavity O and the contact point between roller and input disc. In [46], the full toroidal CVT was defined as a toroidal CVT with a half cone-angle of $\frac{\pi}{2}$ rad. Later, many authors followed that definition [50–52]. The advantage of a half cone-angle of $\frac{\pi}{2}$ rad is that the normal forces on the roller are balanced out. Therefore, there is no resulting axial force on the rollers and consequently no axial bearing is necessary to support that roller. For the half toroidal CVT, the half cone-angle is less strictly defined and varies around $\frac{\pi}{3}$ rad [50, 53–57]. A half cone-angle between $\frac{\pi}{3}$ and $\frac{\pi}{2}$ rad is not interesting as this type of CVT does not benefit from the steep traction curve of a half toroidal CVT [46] nor will it benefit from low bearing losses in the rollers due to zero axial force.

To relate the slope of the traction curve to the half cone-angle, it is important to know which mechanisms influence the traction curve. One of those mechanisms is the spin velocity, or spin ratio σ in its dimensionless form. Higher spin means higher losses in the contact between the discs and the roller. As a consequence, more slip is needed to obtain the maximum traction coefficient. The slope is thus decreased for increasing spin ratio. According to [43], the spin ratio can be written as:

$$\sigma = \frac{\cos\gamma - (1+k)\cos\theta}{\sin\theta} \tag{2.5}$$

Based on (2.5) it is possible to deduce that for decreasing θ, the spin ratio decreases resulting in lower losses in the contact and a steeper traction curve. Moreover, the half toroidal CVT has thus the benefit of a steeper traction curve compared to the full toroidal CVT.

Another rather striking difference between both CVTs is the aspect ratio k which is mainly due to the difference in the eccentricity distance e_{d}. The aspect ratio k is defined as the ratio of the eccentricity e_{d} and the cavity radius r_0 (see Fig.

Table 2.1: Geometrical data of the half toroidal CVT

Cavity radius r_0	40 mm
Roller curvature r_{22}	32 mm
Half cone-angle θ	$\frac{\pi}{3}$ rad
Roller radius r_r	$r_0 \cos\theta = 20$ mm
Aspect ratio k	$\frac{e_\mathrm{d}}{r_0} = 0.625$
Speed ratio range τ_s	0.5-2
Number of roller per unit n	2
Number of units m	2

2.1). Like the half cone-angle, the aspect ratio also has an impact on the slope of the traction curve. The bigger k becomes, the steeper the traction curve.

The last difference between both CVTs is the conformity ratio CR:

$$CR = \frac{r_{22}}{r_0} \tag{2.6}$$

in which r_{22} is the curvature radius of the roller in the contact point with the disk and r_0 is the radius of the cavity (see Fig. 2.1). While in half toroidal CVTs values of 0.8 are common practice, the conformity ratio for a full toroidal CVT is much lower. In [51], it is shown that the optimal value for the CR of a full toroidal CVT, in terms of efficiency, is 0.5. However, as shown in [43], this has a negative effect on the torque capacity of the CVT. The higher the value for CR, the bigger the torque capacity, but the lower the efficiency.

The influence of CR on both efficiency as torque capacity can be explained by analyzing the contact. The higher the conformity ratio, the flatter the roller and consequently, the contact area will increase. If the contact area increases, for the same clamping force, the pressure will drop. As pressure is the limiting factor for the torque capacity (explained in detail in section 2.8), maximum torque increases with increasing CR. However, a bigger contact results in higher losses in that contact, which influences the efficiency. Therefore, there is an optimum value for CR if the efficiency is considered.

In the remaining part of this chapter, only the half toroidal CVT will be discussed. Hence, the half toroidal CVT outperforms the full toroidal CVT both during static as dynamic operation as shown in [50] and [43], respectively. The main geometrical parameters of the half toroidal CVT that is used for the discussion in this chapter are given in Table 2.1

2.3 Model structure

The model of the toroidal CVT consists of a contact model in which the traction coefficients are determined, a mechanical model which defines the relation between generated torque and speed but also the amount of slip ν, the equation for the loading cam or hydraulic cylinder and a load model (see Fig. 2.2). The inputs of the model are the driving torque coming for a source T_{S}, the load torque coming from an application T_{L} and the tilting angle γ of the toroidal CVT dictated from the control. To take the dynamic characteristics of the rotating elements into account the inertia of the input J_{in}, the rollers J_r and the output J_{out} respectively, are used in the model. Important internal variables are the clamping force F_{Din}, the input traction force $F_{\mathrm{t_{in}}}$, the input spin momentum $M_{\mathrm{s_{in}}}$, the output traction force $F_{\mathrm{t_{out}}}$ and the output spin momentum $M_{\mathrm{s_{out}}}$. The outputs of the model are the input speed Ω_{in} and output speed Ω_{out}. The same model can be used for the full toroidal CVT as the difference between both toroidal CVTs is limited to geometrical differences and the usage of an axial bearing.

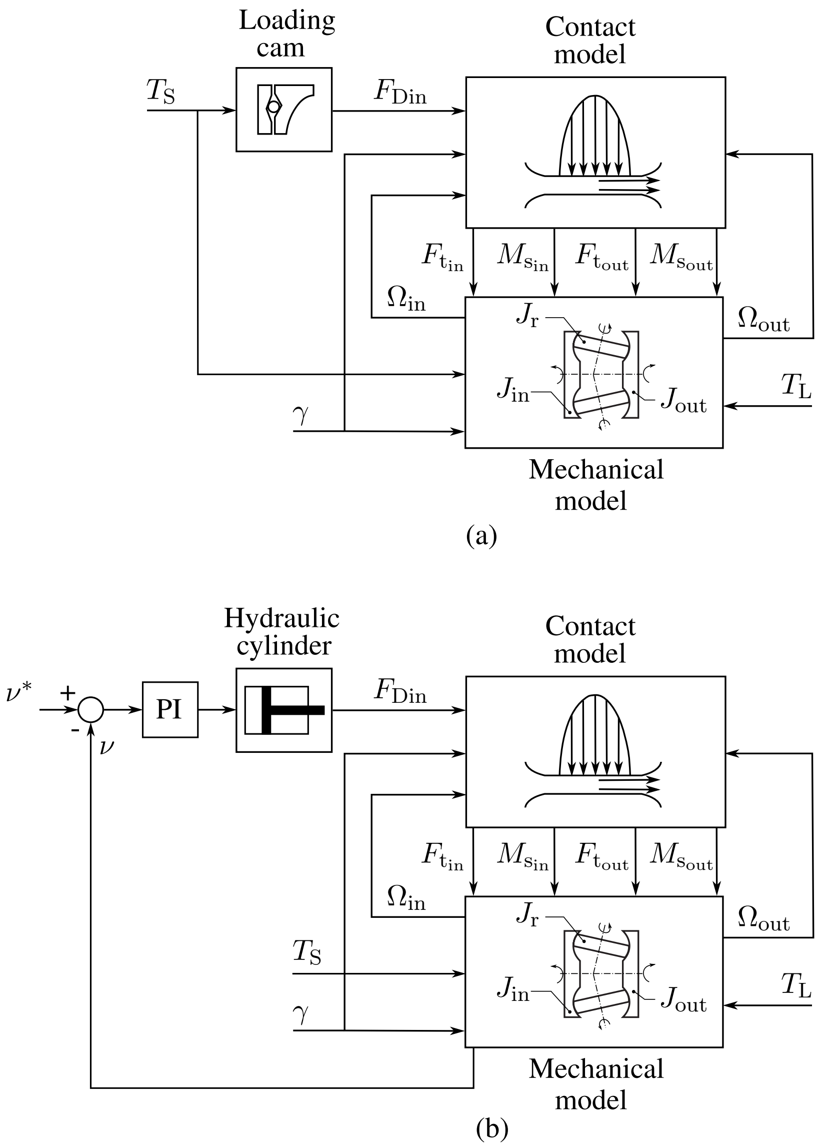

Figure 2.2: Model structure of the half toroidal CVT equipped with a loading cam (a) and a hydraulic cylinder (b).

2.4 Contact model

A toroidal CVT is a complex mechanism that demands high computational effort to simulate its behavior. Nikas [58] provides an extensive theoretical study on how to model the traction behavior of a CVT. Although the study in [58] yields accurate results, it requires pervasive computational effort that makes it unpractical for dynamic simulations. To counter this, researchers simplified the equations in order to approximate the behavior with less computational effort [21, 50, 59–62]. These adaptations are introduced in the contact model where phenomena as side slip or spin are simplified or neglected. In [21], the traction behavior is modeled with a fixed static and dynamic friction coefficient. Therefore, the influence of the geometry, tilting angle, pressure and fluid properties on the traction behavior is neglected. On the other hand, this approach results in a model that requires a low computational effort. Another property which is often simplified is the viscosity-temperature dependency of the traction fluid. As it is a certainty that the temperature in the contact (small area, high pressure) rises, the viscosity of the oil will drop in the contact zone. Neglecting temperature variations will thus have an impact although it is difficult to quantify as there is no experimental work on the subject. The main issue with the shear temperature rise in the contact (and drop of viscosity) is that there can be a mechanical contact between disc and roller. Consequently, the rotating elements of the CVT will be damaged and the lifetime will be reduced. As lifetime of the components is out of scope for this thesis, no further attention has been given to this issue. The main drawback of these simplifications is that the models are only valid in a strictly defined scope of applications as the parameters depend on the studied CVT or condition (traction fluid temperature).

Despite the mentioned limitations, the model of Carbone [50] is widely accepted as the reference model to study the toroidal CVT [51, 55, 57, 63, 64]. This is mainly due to the fairly accurate traction results which are comparable with the experimental results shown in [65] as long as the slip is smaller than 5%. For higher values of slip, the performance of a CVT will be slightly worse then modeled due to a lower traction coefficient than calculated.

Carbone [50] has adapted a model for fully flooded isothermal contacts to evaluate slip and spin losses. Because of the high pressures in the contact, it is necessary to describe the rheological behavior of the fluid. The model of Bair and Winer [66] is used for this. The impact of the pressure on the limiting shear stress is taken into account with the model of Roelands [66] as well as the dependency of the pressure on the viscosity. The film thickness is calculated with the model of Hamrock and Dowson [66, 67]. The effect of temperature gradients is not taken into account. The goal of the contact model is to calculate the friction and spin coefficient which enables the model to calculate the dynamic response of the system.

The first step is to calculate the pressure distribution in the contact. According to Hertz law, the maximum pressure is described as:

$$\tilde{p} = \tilde{p}_{\max}\sqrt{1 - X^2 - Y^2} \tag{2.7}$$

$$\tilde{p}_{\max} = \frac{3}{2}\frac{1}{\pi \tilde{a}_{\mathrm{x}} \tilde{a}_{\mathrm{y}}} \tag{2.8}$$

where $\tilde{p}$ is the dimensionless pressure distribution, $\tilde{p}_{\max}$ is the maximum dimensionless pressure, X and Y are the dimensionless coordinates of a point in the contact zone, $\tilde{a}_{\mathrm{x}}$ and $\tilde{a}_{\mathrm{y}}$ are the dimensionless semi-axes of the contact ellipse. The actual pressure distribution can now be calculated as:

$$p = \frac{\tilde{p} F_{\mathrm{N}}}{\wedge^2} \tag{2.9}$$

where F_{N} is the normal force on the contact and $\wedge$ is the contact length parameter [50]. Based on Fig. 2.1, it is possible to relate the clamping force to the normal forces:

$$F_{\mathrm{N}} = \frac{F_{\mathrm{Din}}}{n \sin(\theta + \gamma)} \tag{2.10}$$

Once the pressure distribution is known, the viscosity of the traction fluid can be determined throughout the contact area. Through viscosity, film thickness is calculated by which it is possible to determine the shear stress levels in the fluid film. The fluid properties which are included in [50] are used to solve the equations (see Table 2.2).

Table 2.2: Fluid properties.

Absolute viscosity at the atmospheric pressure η_0	3.25×10^{-3} Pa s
Viscosity-pressure index Z_1	0.85
Pressure-viscosity coefficient ζ	1.71×10^{-8} Pa^{-1}
Limiting shear stress at atmospheric pressure τ_{L0}	0.02×10^{9} Pa
Limiting shear stress coefficient a	0.085
Pole pressure constant of Roelands viscosity model c_{p}	1.96×10^{8} Pa
Pole viscosity of Roelands viscosity model η_∞	6.31×10^{-5} Pa s

The traction coefficients and the spin momentum values can now be found by solving the integrals written in (2.11)-(2.14).

$$\mu_{\mathrm{in}} = \tilde{a}_{\mathrm{X_{in}}} \tilde{a}_{\mathrm{Y_{in}}} \int_0^1 dR \int_0^{2\pi} \tilde{\tau}_{21\mathrm{X}} R d\psi \tag{2.11}$$

$$\mu_{\text{in}} = -\tilde{a}_{\text{X}_{\text{out}}}\tilde{a}_{\text{Y}_{\text{out}}} \int_0^1 dR \int_0^{2\pi} \tilde{\tau}_{23\text{X}} R d\psi \tag{2.12}$$

$$\begin{aligned}\chi_{\text{in}} =& \frac{\tilde{a}_{\text{X}_{\text{in}}}\tilde{a}_{\text{Y}_{\text{in}}}\wedge}{r_0 \tilde{r}_1} \int_0^1 dR \int_0^{2\pi} (\tilde{a}_{\text{X}_{\text{in}}}\tilde{\tau}_{21\text{Y}} \cos\phi \\ &-\tilde{a}_{\text{Y}_{\text{in}}}\tilde{\tau}_{21\text{X}} \sin\phi)\, R^2 d\psi\end{aligned} \tag{2.13}$$

$$\begin{aligned}\chi_{\text{out}} =& \frac{\tilde{a}_{\text{X}_{\text{out}}}\tilde{a}_{\text{Y}_{\text{out}}}\wedge}{r_0 \tilde{r}_3} \int_0^1 dR \int_0^{2\pi} (\tilde{a}_{\text{X}_{\text{out}}}\tilde{\tau}_{23\text{Y}} \cos\phi \\ &-\tilde{a}_{\text{Y}_{\text{out}}}\tilde{\tau}_{23\text{X}} \sin\phi)\, R^2 d\psi\end{aligned} \tag{2.14}$$

where μ_{in} and μ_{out} are the traction coefficients between input & roller and roller & output respectively. The spin coefficients between the contacts are given by χ_{in} and χ_{out}. The shear stress levels at input and output are defined as $\tilde{\tau}_{21\text{X}}$,$\tilde{\tau}_{21\text{Y}}$,$\tilde{\tau}_{23\text{X}}$ and $\tilde{\tau}_{23\text{Y}}$. X and Y are the result of the following coordinate transformation:

$$\begin{cases} X = R\cos(\psi) \\ Y = R\sin(\psi) \end{cases} \tag{2.15}$$

with $0 \leq R \leq 1$ and $0 \leq \psi \leq 2\pi$.

The traction forces, $F_{\text{t}_{\text{in}}}$ and $F_{\text{t}_{\text{out}}}$, as defined in Fig. 2.2 can be calculated as:

$$F_{\text{t}_{\text{in}}} = \mu_{\text{in}} F_{\text{N}} \tag{2.16}$$

$$F_{\text{t}_{\text{out}}} = \mu_{\text{out}} F_{\text{N}} \tag{2.17}$$

These forces have a positive effect on the generated torque as the direction of the forces aligns with the rolling direction (see Fig. 2.3). The spin momentum values, $M_{\text{s}_{\text{in}}}$ and $M_{\text{s}_{\text{out}}}$, on the other hand are determined as:

$$M_{\text{s}_{\text{in}}} = \chi_{\text{in}} F_{\text{N}} r_{\text{in}} \tag{2.18}$$

$$M_{\text{s}_{\text{out}}} = \chi_{\text{out}} F_{\text{N}} r_{\text{out}} \tag{2.19}$$

As the spin moment results in a drilling effect, the useful part of the traction force is partially consumed by the spin, which is considered as one of the disadvantages of a toroidal CVT.

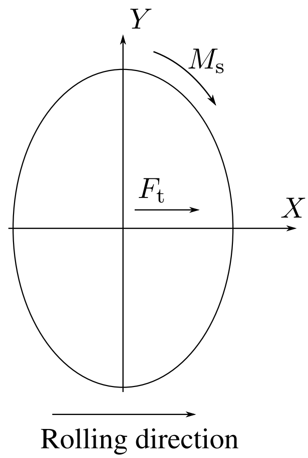

Figure 2.3: Hertzian contact ellipse and its coordinate system

2.5 Mechanical model

The mechanical model defines the relation between the generated torque (calculated based on the output of the contact model) and the resulting speed. The governing dynamic equations of the system (see (2.20-(2.21)) are written based on the free body diagram of Fig. 2.4. The negative effect of the spin momentum (term with χ in (2.21)) is clearly visible in the dynamic equations. Higher spin means less effective traction and thus reduced torque capacity. Moreover, it induces additional torque losses in the contact.

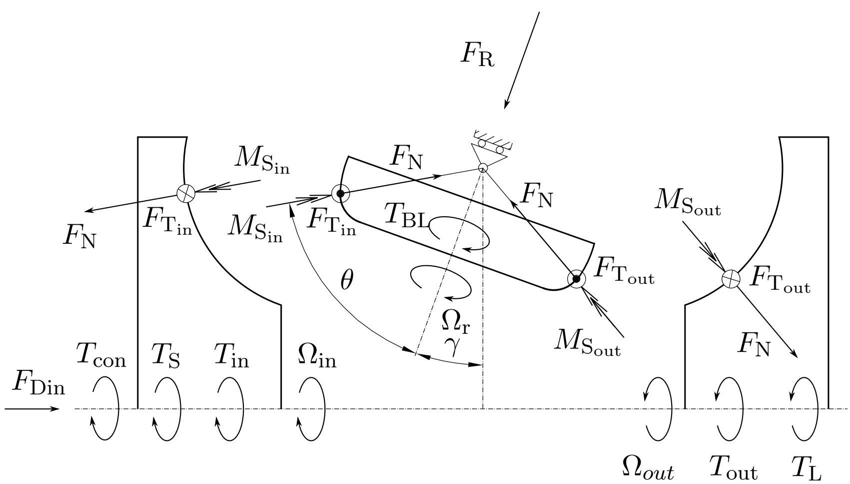

Figure 2.4: Free body diagram of half toroidal CVT. The symbol $\otimes$ is used for vectors pointing away from the reader. The symbol $\odot$ is used for vectors pointing towards the reader.

$$\begin{cases} J_{\mathrm{in}}\frac{d\Omega_{\mathrm{in}}}{dt} & = T_{\mathrm{S}} - T_{\mathrm{in}} - T_{\mathrm{con}} \\ J_{\mathrm{r}}\frac{d\Omega_{\mathrm{r}}}{dt} & = T_{\mathrm{r}} - T_{\mathrm{BL}} \\ J_{\mathrm{out}}\frac{d\Omega_{\mathrm{out}}}{dt} & = T_{\mathrm{out}} - T_{\mathrm{L}} \end{cases} \tag{2.20}$$

In (2.20), the torque applied to the input disc is denoted by T_{S} while the torque that is generated through traction is T_{in}. The torque loss linked to the device that controls the clamping force (loading cam or hydraulic cylinder) is denoted by T_{con}. Similarly, T_{L} is the load torque and T_{out} is the torque generated via traction at the output disc. Hence, in steady state, T_{S} equals T_{in} and T_{L} equals T_{out}. Finally, the torque on the roller and torque losses of the bearing supporting the roller are characterized by T_{r} and T_{BL}, respectively. The torque losses of that thrust bearing depend on the axial force F_{R} which is applied to the bearing due to the clamping force and the rotational speed of the intermediate rollers Ω_{r}. These torque losses have been defined based on data of SKF [68]. The bearing losses of the input and output disc are not considered in the analysis as their impact on the efficiency is negligible [50].

$$\begin{cases} J_{\mathrm{in}}\frac{d\Omega_{\mathrm{in}}}{dt} & = T_{\mathrm{S}} - m\,n\,\mu_{\mathrm{in}}F_{\mathrm{N}}r_{\mathrm{in}} - m\,n\,\chi_{\mathrm{in}}F_{\mathrm{N}}r_{\mathrm{in}}\sin(\theta+\gamma) - T_{\mathrm{con}} \\ J_{\mathrm{r}}\frac{d\Omega_{\mathrm{r}}}{dt} & = \mu_{\mathrm{in}}F_{\mathrm{N}}r_{\mathrm{r}} + \chi_{\mathrm{in}}F_{\mathrm{N}}r_{\mathrm{in}}\cos(\theta) - \mu_{\mathrm{out}}F_{\mathrm{N}}r_{\mathrm{r}} \\ & \quad +\chi_{\mathrm{out}}F_{\mathrm{N}}r_{\mathrm{out}}\cos(\theta) - T_{\mathrm{BL}}(\Omega_{\mathrm{r}}, F_{\mathrm{R}}) \\ J_{\mathrm{out}}\frac{d\Omega_{\mathrm{out}}}{dt} & = m\,n\,\mu_{\mathrm{out}}F_{\mathrm{N}}r_{\mathrm{out}} - m\,n\,\chi_{\mathrm{out}}F_{\mathrm{N}}r_{\mathrm{out}}\sin(\theta-\gamma) - T_{\mathrm{L}} \end{cases} \tag{2.21}$$

2.6 Active slip control

Slip ν (also know in literature as global sliding coefficient) defines the traction coefficient at input and output, μ_{in} and μ_{out}, which is an important parameter in the transfer of torque as shown in (2.21). Without slip there is no traction but too high values of slip will result in wear and high losses. In toroidal CVTs, slip can be controlled in an active or a passive way. The active control involves a hydraulic piston which regulates the force on the components. The torque loss related to that hydraulic component is denoted by T_{con}. To estimate this loss term, an empirical model has been set up based on measurement results provided in [69] that yields the torque loss as function of input speed and requested clamping force.

The main advantage of the active control is that the force can be changed as function of the operating conditions. An alternative is to use a loading cam. This passive device senses the torque on the input disc and transfers this into an axial force which presses the components together. More information concerning the passive control is given in section 2.7.

In the following sections, the control parameters of the active controller are derived based on the linearized slip dynamics.

2.6.1 Linearized slip dynamics

A hydraulic cylinder can be used to actively control the clamping force and thus the slip in a CVT. Slip, in any CVT, is defined by:

$$\nu = 1 - \frac{\tau_{\mathrm{s}}}{\tau_{\mathrm{t}}} \tag{2.22}$$

in which τ_{s} is the speed ratio based on the ratio of the output speed and input speed $\left(\frac{\Omega_{\mathrm{out}}}{\Omega_{\mathrm{in}}}\right)$ and τ_{t} is the speed ratio based on the ratio of the input contact radius and output contact radius $\left(\frac{r_{\mathrm{in}}}{r_{\mathrm{out}}}\right)$. As it is the objective to control the variations in slip, the time derivative of (2.22) is considered:

$$\frac{d\nu}{dt} = \frac{\frac{d\tau_{\mathrm{t}}}{dt}\tau_{\mathrm{s}} - \frac{d\tau_{\mathrm{s}}}{dt}\tau_{\mathrm{t}}}{\tau_{\mathrm{t}}^2} \tag{2.23}$$

Which can be rewritten as:

$$\frac{d\nu}{dt} = \frac{\frac{d\tau_{\mathrm{t}}}{dt}\frac{\Omega_{\mathrm{out}}}{\Omega_{\mathrm{in}}} - \frac{\frac{d\Omega_{\mathrm{out}}}{dt}\Omega_{\mathrm{in}} - \frac{d\Omega_{\mathrm{in}}}{dt}\Omega_{\mathrm{out}}}{\Omega_{\mathrm{in}}^2}\tau_{\mathrm{t}}}{\tau_{\mathrm{t}}^2} \tag{2.24}$$

Equation (2.24) can be redrafted in terms of torque and inertia considering (2.20):

$$\frac{d\nu}{dt} = \frac{\frac{d\tau_{\mathrm{t}}}{dt}\Omega_{\mathrm{out}}}{\tau_{\mathrm{t}}^2\Omega_{\mathrm{in}}} - \frac{T_{\mathrm{out}} - T_{\mathrm{L}}}{\Omega_{\mathrm{in}}J_{\mathrm{out}}\tau_{\mathrm{t}}} + \frac{\left(T_{\mathrm{S}} - T_{\mathrm{in}}\right)\tau_{\mathrm{s}}}{\Omega_{\mathrm{in}}J_{\mathrm{in}}\tau_{\mathrm{t}}} \tag{2.25}$$

which can be written in terms of the slip ν by using (2.22):

$$\frac{d\nu}{dt} = \frac{\frac{d\tau_{\mathrm{t}}}{dt}\Omega_{\mathrm{out}}}{\tau_{\mathrm{t}}^2\Omega_{\mathrm{in}}} - \frac{T_{\mathrm{out}} - T_{\mathrm{L}}}{\Omega_{\mathrm{in}}J_{\mathrm{out}}\tau_{\mathrm{t}}} + \frac{\left(T_{\mathrm{S}} - T_{\mathrm{in}}\right)(1-\nu)}{\Omega_{\mathrm{in}}J_{\mathrm{in}}} \tag{2.26}$$

By using (2.21), the equation describing the slip dynamics can be finalized:

$$\begin{aligned}\frac{d\nu}{dt} &= \frac{\frac{d\tau_{\mathrm{t}}}{dt}\Omega_{\mathrm{out}}}{\tau_{\mathrm{t}}^2\Omega_{\mathrm{in}}} - \frac{mnF_{\mathrm{t_{out}}}r_{\mathrm{out}} - mnM_{\mathrm{s_{out}}}\sin\left(\theta+\gamma\right) - T_{\mathrm{L}}}{\Omega_{\mathrm{in}}J_{\mathrm{out}}\tau_{\mathrm{t}}} \\ &+ \frac{\left(T_{\mathrm{S}} - mnF_{\mathrm{t_{in}}}r_{\mathrm{in}} - mnM_{\mathrm{s_{in}}}\sin\left(\theta+\gamma\right)\right)(1-\nu)}{\Omega_{\mathrm{in}}J_{\mathrm{in}}}\end{aligned} \tag{2.27}$$

in which the spin momentum at input $M_{\mathrm{s_{in}}}$ and output $M_{\mathrm{s_{out}}}$ equals:

$$M_{\mathrm{s_{in}}} = \chi_{\mathrm{in}} F_{\mathrm{N}} r_{\mathrm{in}} \tag{2.28}$$

$$M_{\mathrm{s_{out}}} = \chi_{\mathrm{out}} F_{\mathrm{N}} r_{\mathrm{out}} \tag{2.29}$$

For the control design, $M_{\mathrm{s_{in}}}$ and $M_{\mathrm{s_{out}}}$ are neglected, as they are small, which reduces (2.27) to:

$$\frac{d\nu}{dt} = \frac{\frac{d\tau_{\mathrm{t}}}{dt}\Omega_{\mathrm{out}}}{\tau_{\mathrm{t}}^2\Omega_{\mathrm{in}}} - \frac{mnF_{\mathrm{t_{out}}} r_{\mathrm{out}} - T_{\mathrm{L}}}{\Omega_{\mathrm{in}} J_{\mathrm{out}} \tau_{\mathrm{t}}} + \frac{\left(T_{\mathrm{S}} - mnF_{\mathrm{t_{in}}} r_{\mathrm{in}}\right)(1-\nu)}{\Omega_{\mathrm{in}} J_{\mathrm{in}}} \tag{2.30}$$

Which yields the following equation in terms of traction coefficients:

$$\frac{d\nu}{dt} = \frac{\frac{d\tau_{\mathrm{t}}}{dt}\Omega_{\mathrm{out}}}{\tau_{\mathrm{t}}^2\Omega_{\mathrm{in}}} - \frac{mnF_{\mathrm{N}}\mu_{\mathrm{out}} r_{\mathrm{out}} - T_{\mathrm{L}}}{\Omega_{\mathrm{in}} J_{\mathrm{out}} \tau_{\mathrm{t}}} + \frac{\left(T_{\mathrm{S}} - mnF_{\mathrm{N}}\mu_{\mathrm{in}}\tau_{\mathrm{t}} r_{\mathrm{out}}\right)(1-\nu)}{\Omega_{\mathrm{in}} J_{\mathrm{in}}} \tag{2.31}$$

The variation in slip is thus a function of 11 variables:

$$\frac{d\nu}{dt} = f\left(\nu, \frac{d\tau_{\mathrm{t}}}{dt}, \tau_{\mathrm{t}}, \Omega_{\mathrm{in}}, \Omega_{\mathrm{out}}, r_{\mathrm{out}}, F_{\mathrm{N}}, \mu_{\mathrm{in}}, \mu_{\mathrm{out}}, T_{\mathrm{S}}, T_{\mathrm{L}}\right) \tag{2.32}$$

Of these variables, only the normal force F_{N} (related to the clamping force F_{Din}, see (2.48)) can be used to actively control the slip. All other variables are controlled at a higher level by for example the energy management system which selects optimal operating points (T_{S}, Ω_{in}, …) or are induced by the considered load profile (T_{L}, Ω_{out}, …). Therefore, these variables are considered as disturbances D.

In the following paragraphs, the slip dynamics are linearized for control purposes (continuously for every time instant, i.e. adaptive control). However, the model of the CVT which is used to test the behavior of the elaborated controller, is not simplified to any extend. If (2.31) is linearized, ignoring the variables considered as disturbances D, the following equation is found:

$$\begin{aligned}\frac{d\nu}{dt} = &\left.\frac{\partial f}{\partial \nu}\right|_{*}(\nu-\nu^*) + D_{\frac{d\tau_{\mathrm{t}}}{dt}} + D_{\tau_{\mathrm{t}}} + D_{\Omega_{\mathrm{in}}} + D_{\Omega_{\mathrm{out}}} + D_{r_{\mathrm{out}}} \\ &+ \left.\frac{\partial f}{\partial F_{\mathrm{N}}}\right|_{*}(F_{\mathrm{N}} - F_{\mathrm{N}}^*) + D_{\mu_{\mathrm{in}}} + D_{\mu_{\mathrm{out}}} + D_{T_{\mathrm{S}}} + D_{T_{\mathrm{L}}}\end{aligned} \tag{2.33}$$

$$\frac{d\nu}{dt} = \left.\frac{\partial f}{\partial \nu}\right|_{*} (\nu - \nu^{*}) + \left.\frac{\partial f}{\partial F_{\mathrm{N}}}\right|_{*} (F_{\mathrm{N}} - F_{\mathrm{N}}^{*}) + D \tag{2.34}$$

Which can be rewritten as:

$$\frac{d\nu}{dt} = D - \underbrace{\left.\frac{\partial f}{\partial \nu}\right|_{*} \nu^{*} - \left.\frac{\partial f}{\partial F_{\mathrm{N}}}\right|_{*} F_{\mathrm{N}}^{*}}_{\mathrm{K}} + \underbrace{\left.\frac{\partial f}{\partial \nu}\right|_{*}}_{\mathrm{L}} \nu + \underbrace{\left.\frac{\partial f}{\partial F_{\mathrm{N}}}\right|_{*}}_{\mathrm{M}} F_{\mathrm{N}} \tag{2.35}$$

In which the partial derivative of ν equals:

$$\left.\frac{\partial f}{\partial \nu}\right|_{*} = \frac{mnF_{\mathrm{N}}\mu_{\mathrm{in}}r_{\mathrm{out}}\tau_{\mathrm{t}} - T_{\mathrm{S}}}{\Omega_{\mathrm{in}}J_{\mathrm{in}}} = L \tag{2.36}$$

And the partial derivative of F_{N}:

$$\left.\frac{\partial f}{\partial F_{\mathrm{N}}}\right|_{*} = -\frac{mn\mu_{\mathrm{out}}r_{\mathrm{out}}}{\Omega_{\mathrm{in}}J_{\mathrm{out}}\tau_{\mathrm{t}}} - \frac{(mn\mu_{\mathrm{in}}\tau_{\mathrm{t}}r_{\mathrm{out}})(1-\nu)}{\Omega_{\mathrm{in}}J_{\mathrm{in}}} = M \tag{2.37}$$

The next step is to take the Laplace of (2.35):

$$\nu(s)\,s = K + L\nu(s) + MF_{\mathrm{N}}(s) \tag{2.38}$$

Note that the disturbance term has been removed as it has no impact on the actual linearized transfer function. The term K can also be removed as it is merely an offset which can be ignored for control purposes. Therefore, the following transfer function is found:

$$\frac{\nu(s)}{F_{\mathrm{N}}(s)} = \frac{-\frac{M}{L}}{-\frac{1}{L}s + 1} \tag{2.39}$$

2.6.2 Slip controller

Equation (2.39) shows that the complex nonlinear behavior of the slip dynamics is now converted to a first order system that can be easily controlled with a PI controller (see Fig. 2.2 (b)). The transfer function of a PI controller is written as:

$$TF_{\mathrm{PI}} = K_{\mathrm{p}}\left(\frac{T_{\mathrm{i}}s + 1}{T_{\mathrm{i}}s}\right) \tag{2.40}$$

with the proportional term K_{p} and the integral term T_{i}. The integral term should be equal to the time constant of the first order system depicted by (2.39). If the system pole is canceled by the controller zero, the dynamical behavior can be uniquely defined by the control parameter K_p. T_i is therefore equal to:

$$T_\mathrm{i} = \frac{-1}{L} \tag{2.41}$$

with L defined in (2.36). Note that this can only be done if the pole is in the left half plane (see Fig. 2.5 (a)) which means that L needs to be negative. This will be the case if $T_\mathrm{S} > T_\mathrm{in}$ which is valid for almost all operating conditions. Only during stages where the source torque is 0 while the CVT still rotates (= still slip and thus traction), the control method could become unstable. To calculate the proportional term, the closed loop system is taken into account:

$$TF_{CL} = \frac{\frac{-M}{L}K_p}{T_i s + \frac{-M}{L}K_p} \tag{2.42}$$

Which means that the closed loop pole defining the closed loop dynamics can be found at:

$$s = \frac{\frac{M}{L}K_p}{T_i} \tag{2.43}$$

By which the proportional gain of the controller can be defined with one degree of freedom α:

$$K_p = \frac{\alpha T_i}{\frac{M}{L}} = \frac{-\alpha}{M} \tag{2.44}$$

The value α defines the position of the closed loop pole as demonstrated in Fig. 2.5 (red line) and is related to the ability to handle disturbances. The higher α is chosen, the better the system can handle disturbances but the more demanding these setpoints for the clamping force will become for the hydraulic system. Based on [70] it is possible to deduce that the force setpoint may vary with a maximum slope of 250 kN per second. This value depends on the compressibility of the oil, the enclosed volume of oil and the chosen control architecture for the hydraulic circuit. These elements are considered out of scope of this thesis. Based on simulation, α equal to -0.2 is chosen as optimal value. The black cross in Fig. 2.5 resembles the system pole while the blue cross and circle resemble the pole and zero of the PI controller respectively. Only case (a) is discussed in this thesis because of the previously mentioned reason.

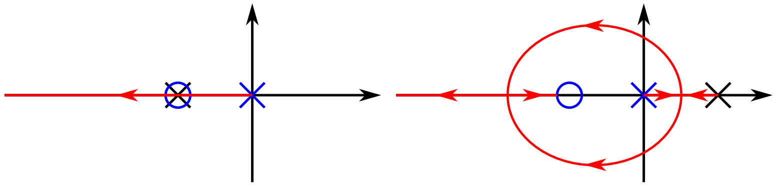

Figure 2.5: (a) Root locus for the case in which $T_{\mathrm{S}} > T_{\mathrm{in}}$: left half plane system pole. (b) Root locus for the case in which $T_{\mathrm{S}} < T_{\mathrm{in}}$: right half plane system pole (potential unstable operation).

Determining the controller proportional gain and integral gain requires a lot of variables (see Fig. 2.6 (a)). However, many of these variables can be replaced by constants. If the slip controller performs well, slip and thus the traction coefficient will be fairly constant. Furthermore, the difference in traction coefficient between input and output is rather low. As a consequence, both traction coefficients are chosen to be constant and identical. Based on the geometry of the CVT, it is possible to determine the output radius based on the theoretical speed ratio. At last, slip can be replaced by the desired value.

Due to these changes, only 2 measurements remain: speed of the input disc Ω_{in} and the torque applied by the source T_{S}. Of these variables speed is easily measured and torque of the ICE could be estimated based on engine characteristics [71, 72] to avoid an expensive torque sensor.

Analysis of these simplifications showed that there is no significant difference between the controller implementation based on Fig. 2.6 (a) and (b). Only during start up, version (a) clearly performs better.

2.6.3 Results

To analyze the effectiveness of the control, 2 load cycles are defined: varying load at constant speed and varying speed ratio at constant load. In order to compare the active and passive control, the same load cycle is used.

Varying load at constant speed ratio

Fig. 2.7 shows the response of the controlled system. The slip is controlled at a value of 2% (nominal setpoint values between 2% and 4% according to [55]). If the load torque T_{L} increases, the torque coming from the source T_{S} increases as well to maintain a constant input speed Ω_{in}. Subsequently, the generated input torque T_{in} needs to increase as well or slip will increase between input and output. To counter this, the clamping force F_{Din} needs to increase.

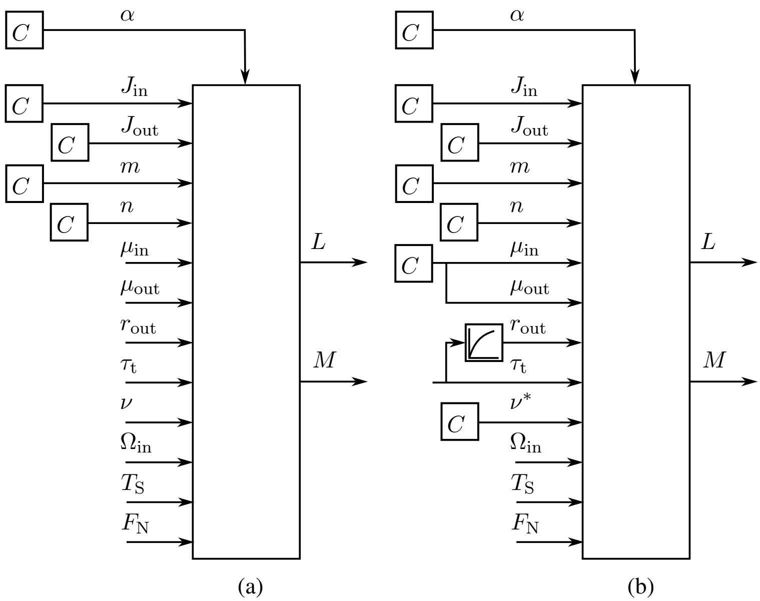

Figure 2.6: (a) Overview on the inputs to calculate L and M. (b) Overview on the strictly necessary inputs to calculate L and M. The value C stands for a constant.

It is clear from the results that the sudden load variations result in increased slip, after which the clamping force indeed increases to control the slip back to the desired value.

Varying speed ratio at constant load

Fig. 2.8 shows that the slip controller has no problem with maintaining constant slip during ratio variation. During ratio variation at constant load T_L, the source torque T_S will vary as function of the speed ratio variation. Higher speed ratio τ_s results in higher source torque to maintain a constant input speed Ω_{in}. The clamping force F_{Din} will thus increase with the speed ratio to control the slip at its constant value.

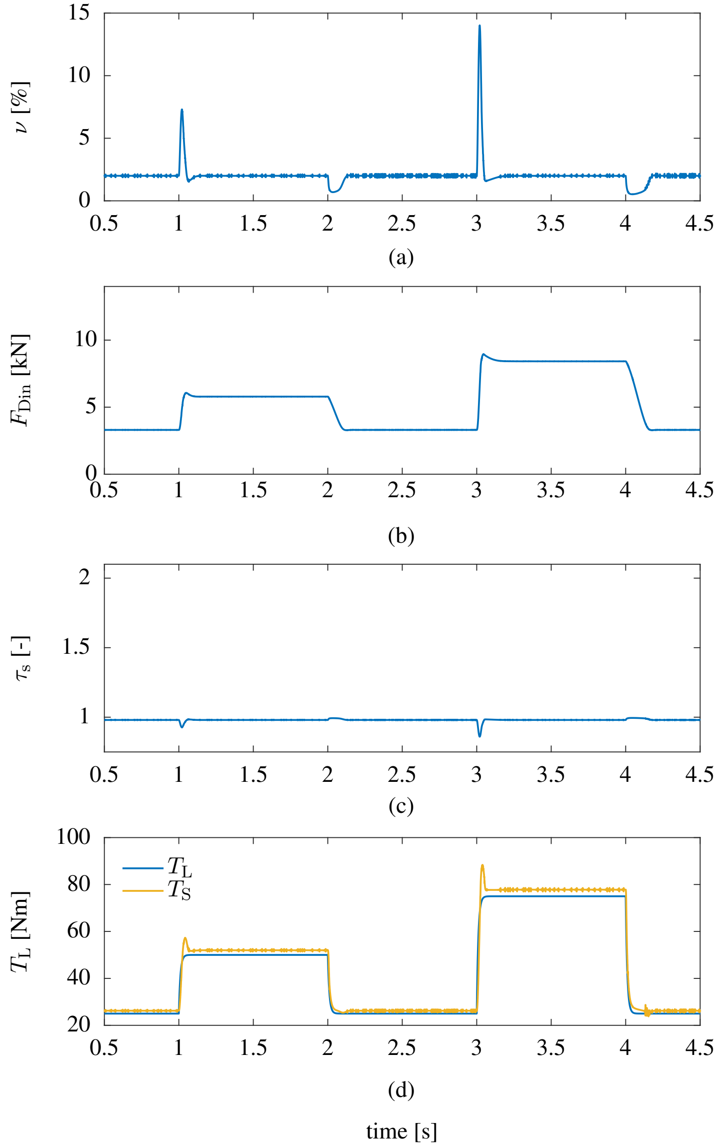

Figure 2.7: Slip ν [%] (a) and clamping force F_{Din} [kN] (b) as function of time for varying load torque T_{L} (d), constant input speed of 1500 rpm and speed ratio of 1 (c). Valid for active clamping force control (hydraulic cylinder).

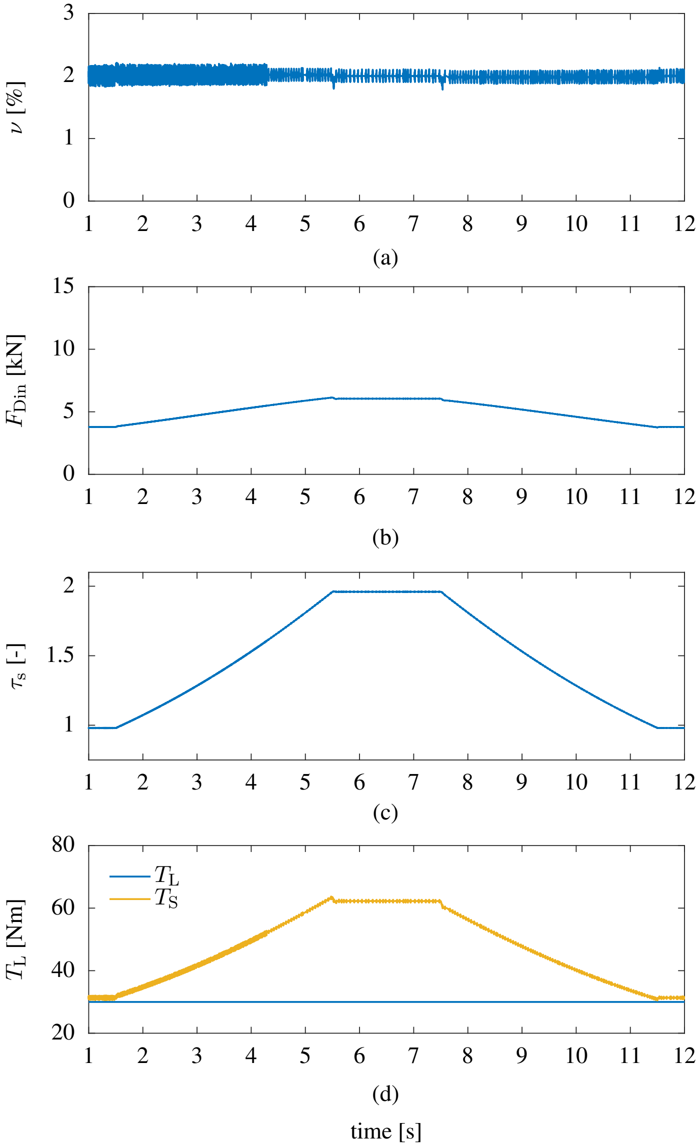

Figure 2.8: Slip ν [%] (a) and clamping force F_{Din} [kN] (b) as function of time for varying speed ratio τ_{s} (c), constant input speed of 1500 rpm and constant load torque of 25 Nm (d). Valid for active clamping force control (hydraulic cylinder).

2.7 Passive slip control

The advantage of the loading cam is that it does not need a controller. The loading cam senses the torque at the input and translates it to a clamping force. This means that only the input torque has an impact on the clamping force. However, slip depends on much more variables than just the torque applied to the input disc. To counter the influence of for example the input speed, the force obtained at the input disc, is overrated (the device is over clamped). This is done by the design of the loading cam but also by adding a spring that provides a preload of the system.

Like the active control, the loading cam also has its losses, which are related to friction and bearing losses. Based on the analysis made in [48], it is possible to conclude that the total loss can be split in a torque (linear function) and speed dependent (quadratic function) part. The torque dependent part is dominant. Only at low torque (below 25 Nm) and high input speed (above 4000 rpm), the speed dependent losses are dominant. As these operating points seldom occur, it is decided to model the losses in the loading cam strictly as a linear function of the input torque.

The loading cam is designed in such a way that stable operating is ensured. This means that the slip is retained to a value of maximum 5% in steady state. The nominal values for the slip, as mentioned earlier, are between 2% and 4% [55]. Measurements of the clamping force on a toroidal CVT equipped with a loading cam given by Yamamoto [48] show that the clamping force F_{Din} can be approximated as:

$$F_{\mathrm{Din}} = k_{\mathrm{s}} T_{\mathrm{S}} + b \tag{2.45}$$

where k_{s} is a constant gain which describes the influence of the input torque on the clamping force and b is the preload of the spring. Slip is not mentioned in (2.45) and will thus vary slightly depending on the torque applied to the input disc T_{S}. Equation (2.45) seems to be independent from the speed ratio. However, during ratio variation, T_{S} will vary as well. Therefore, the clamping force will be adapted to constrain the slip.

To calculate the values for k_{s} and b, the steady state version of (2.21) can be used:

$$0 = T_{\mathrm{S}} - m\,n\,\mu_{\mathrm{in}} F_{\mathrm{N}} r_{\mathrm{in}} - m\,n\,\chi_{\mathrm{in}} F_{\mathrm{N}} r_{\mathrm{in}} \sin\left(\theta + \gamma\right) \tag{2.46}$$

which can be rewritten as (2.47) by ignoring the term related to the spin:

$$T_{\mathrm{S}} = m\,n\,\mu_{\mathrm{in}} F_{\mathrm{N}} r_{\mathrm{in}} \tag{2.47}$$

Based on Fig. 2.1, it is possible to relate the clamping force to the normal forces (see (2.48)) and the input radius to the tilting angle (see (2.49)):

$$F_{\mathrm{N}} = \frac{F_{\mathrm{Din}}}{n\,\sin(\theta+\gamma)} \tag{2.48}$$

$$r_{\mathrm{in}} = r_0 + e_{\mathrm{d}} - r_0\cos(\theta+\gamma) \tag{2.49}$$

By using (2.48) and (2.49), (2.47) can be rewritten as:

$$T_{\mathrm{S}} = m\,\mu_{\mathrm{in}} F_{\mathrm{Din}} \frac{r_0 + e_{\mathrm{d}} - r_0\cos(\theta+\gamma)}{\sin(\theta+\gamma)} \tag{2.50}$$

Equation (2.50) is a function of the clamping force, the tilting angle, the friction coefficient and geometrical properties. To express the clamping force as function of the input torque, an operating point for the tilting angle and friction coefficient needs to be chosen. For the tilting angle, a value of 0 rad is chosen, i.e. a speed ratio of 1. The friction coefficient is equal to 0.095 which is the peak value shown in Fig. 2.20 (b). By filling in these values together with the geometrical parameters in (2.50, the following expression is found:

$$T_{\mathrm{S}} = 0.01 F_{\mathrm{Din}} \Rightarrow F_{\mathrm{Din}} = 100 T_{\mathrm{S}} \tag{2.51}$$

This means that k_{s} equals 100. The preload b has been set to 5000N and ensures stable operation at low torque values [49].

2.7.1 Results

To analyze the effectiveness of the control, 2 load cycles are defined: varying load at constant speed and varying speed ratio at constant load. In order to compare the active and passive control, the same load cycle is used. In addition to the result section of the active slip control, a comparison of the energy efficiency of both methods has been added.

Varying load at constant speed ratio

Fig. 2.9 shows again that if the load torque T_{L} increases, clamping force F_{Din} needs to increase as well. The robustness against load variations is much higher when a loading cam is used. This is due to the fast response via the loading cam, i.e. a variation in torque is immediately translated in a variation in clamping force. The downside of the method is that the slip cannot be controlled to a specific value and that can have a negative impact on the efficiency (see 2.7.1).

Varying speed ratio at constant load

Similar to the active control, the clamping force increases with the speed ratio (see Fig. 2.10). The loading cam does not allow to control the slip at a specific value, which explains the slightly varying value for the slip in Fig. 2.10.

Note that the obtained slip, approximately 0.6%, is significantly lower compared to the setpoint value (2% slip) of the active control. This is primarily due to the low load torque, 25Nm, and the high preload. The system is basically overclamped at low torque to ensures stable operation at low torque values. As a result, the slip is low

Comparison of the efficiency for active and passive slip control

As already mentioned, the biggest side-effect of the loading cam is that the slip cannot be actively controlled. The ideal slip for a given operating point cannot be pursued as the clamping force and thus the slip is merely a function of the input torque. This has consequences in terms of efficiency, which is shown in Fig. 2.11. Fig. 2.11 shows that the efficiency of the actively controlled system is fairly constant. The main reason for this is the constant value for the slip as function of time. For the passive control, the slip depends of the chosen operating point which is reflected in the efficiency variations. However, it is predominantly during part load (low load torque) that the passive solution performs significantly worse compared to the active solution. Moreover, at higher torque values, there is hardly any difference in steady state efficiency. The active control is thus mainly an asset in optimizing the efficiency during part load. Note that for the active controller, the losses of the hydraulic components have been taken into account while for the loading cam losses due to friction are considered.

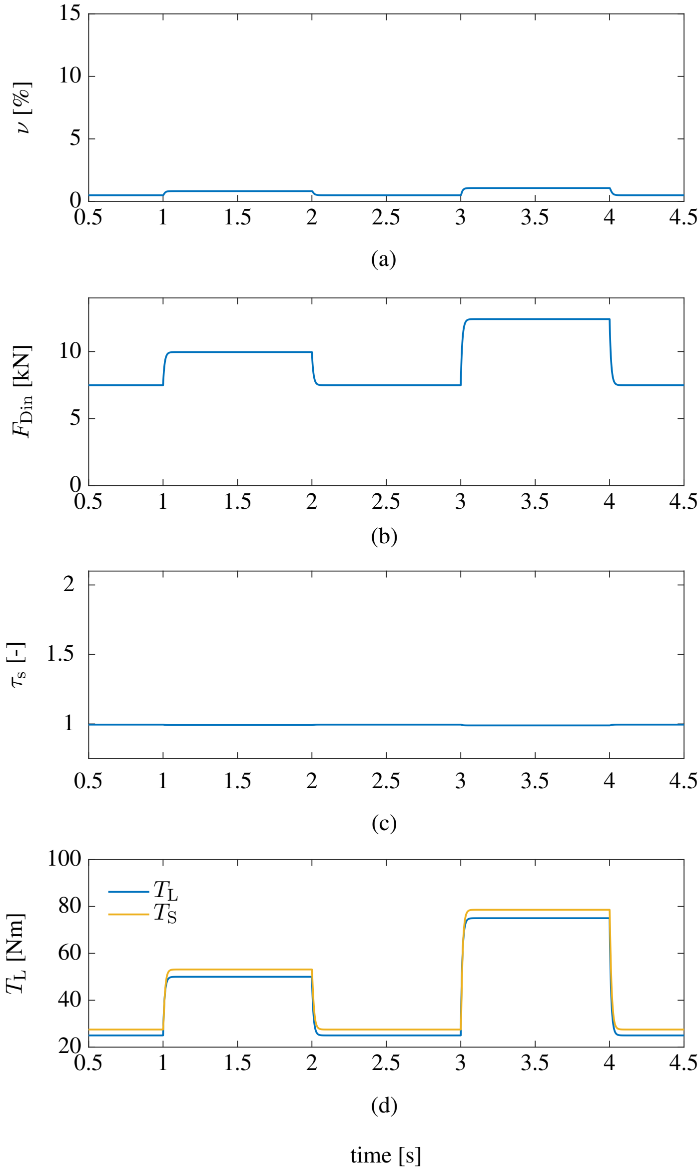

Figure 2.9: Slip ν [%] (a) and clamping force F_{Din} [kN] (b) as function of time for varying load torque T_{L} (d), constant input speed of 1500 rpm and speed ratio of 1 (c). Valid for passive clamping force control (loading cam).

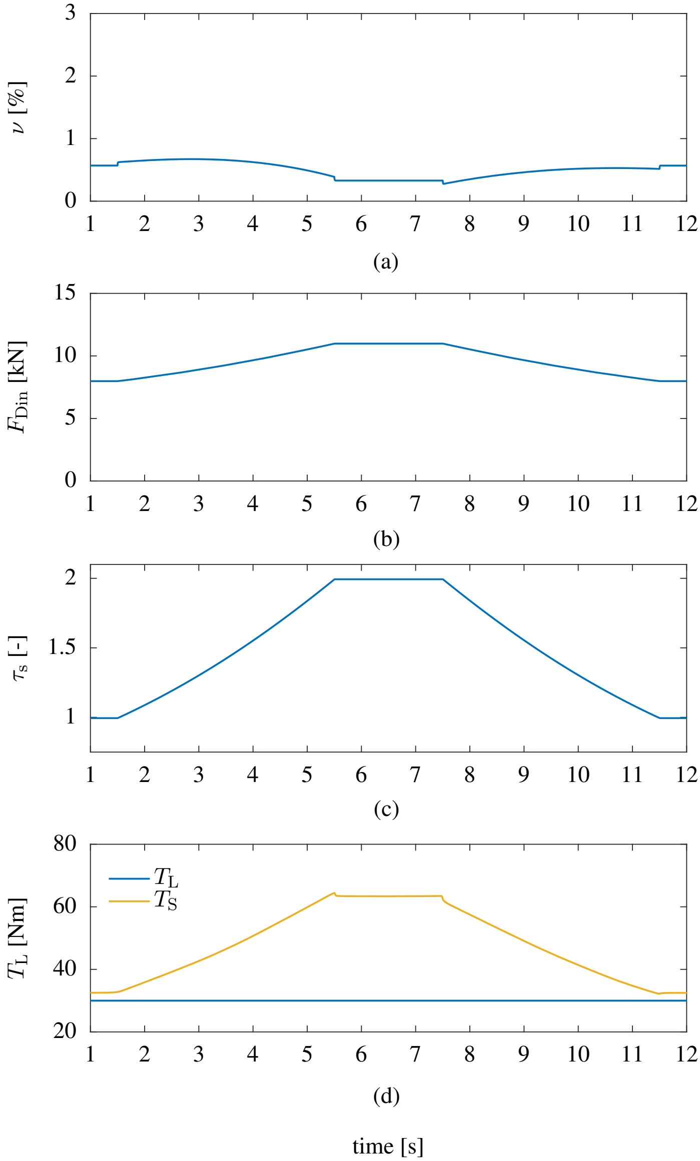

Figure 2.10: Slip ν [%] (a) and clamping force F_{Din} [kN] (b) as function of time for varying speed ratio τ_{s} (c), constant input speed of 1500 rpm and constant load torque of 25 Nm (d). Valid for passive clamping force control (loading cam).

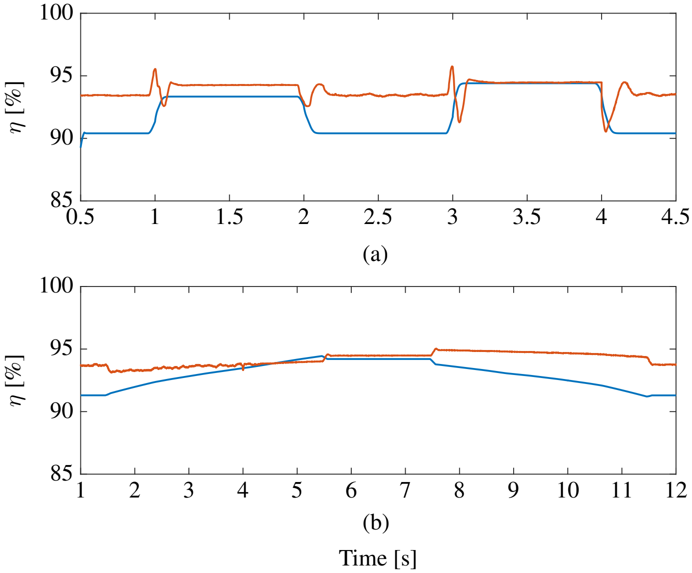

Figure 2.11: Comparison of the efficiency when active control (red) or passive control (blue) is used. (a) Efficiency η [%] as function of time for varying load torque at constant speed ratio (identical operating points as in Fig. 2.7 and 2.9). (b) Efficiency η [%] as function of time for varying speed ratio at constant load torque (identical operating points as in Fig. 2.8 and 2.10).

2.8 Control of the speed ratio

2.8.1 Output torque

A CVT enables the user to regulate the output speed and thus torque in a stepless way. This is done by varying the tilting angle as previously discussed. The dynamic equation of the output disc (see (2.52)) is rewritten here for convenience.

$$J_{\mathrm{out}}\frac{d\Omega_{\mathrm{out}}}{dt} = m\,n\,\mu_{\mathrm{out}}F_{\mathrm{N}}r_{\mathrm{out}} - m\,n\,\chi_{\mathrm{out}}F_{\mathrm{N}}r_{\mathrm{out}}\sin\left(\theta-\gamma\right) - T_{\mathrm{L}} \qquad (2.52)$$

In this equation, the output torque is defined by the traction force $F_{\mathrm{N}}\mu_{\mathrm{out}}$ and the spin momentum $F_{\mathrm{N}}r_{\mathrm{out}}\chi_{\mathrm{out}}$.

$$T_{\mathrm{out}} = m\,n\,\mu_{\mathrm{out}}F_{\mathrm{N}}r_{\mathrm{out}} - m\,n\,\chi_{\mathrm{out}}F_{\mathrm{N}}r_{\mathrm{out}}\sin\left(\theta-\gamma\right) \qquad (2.53)$$

In Fig. 2.12 (a), the output torque T_{out} is presented as function of the slip ν. The highest output torque is found for high values of slip for which χ_{out} goes to zero as displayed in Fig. 2.12 (b).

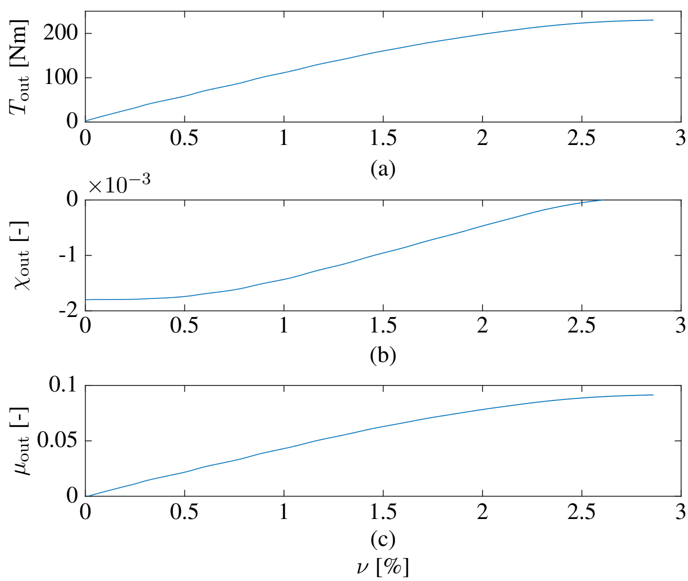

Figure 2.12: (a) Output torque T_{out} [Nm] as a function of the slip ν [%]. (b) Output spin coefficient χ_{out} [-] as a function of the slip ν [%] (c) Friction coefficient at the output μ_{out} [-] as a function of the slip ν [%].

Therefore, it is possible to neglect the term with χ_{out} if the maximum output torque is considered. Consequently (2.53) can be rewritten as:

$$T_{\text{out}_{\max}} = m\, n\, F_{\text{N}_{\max}} r_{\text{out}} \mu_{\text{out}_{\max}} \tag{2.54}$$

Equation (2.54), which is similar to (2.47), means that the maximum torque that can be delivered by the output, depends only on the number of rollers n, the number of units m, the maximum normal force $F_{\text{N}_{\max}}$, the contact radius r_{out} and a maximum value of the friction coefficient at the output $\mu_{\text{out}_{\max}}$. Less convenient is that the maximum torque also depends on the tilting angle as it influences the contact radius $r_{\text{out}}(\gamma)$. The normal force can be rewritten as the clamping force $F_{\text{Din}_{\max}}$ based on (2.48).

As discussed in section 2.6 and 2.7, this clamping force is derived by a controller or based on a loading cam. During load variations, the passive control (with loading cam), clearly performed best. In terms of efficiency, the active control showed potential, but mainly during part load operation. Therefore, further analysis of the speed ratio variation is done based on a passively controlled CVT.

As the clamping force depends on the design of the loading cam, this design is of primordial importance for the torque capacity of the CVT. A stiffer design (higher k_{s}) will result in higher forces and thus a higher maximum output torque. Higher forces will also result in higher pressure levels in the contact zone which forms the actual limit of the torque capacity.

The maximum pressure is defined in the design phase as it is a measure for the material strength of the CVT but it is also related to the capabilities of the chosen traction fluid. Modern CVTs are designed in order to withstand pressures up to 3GPa [50, 73, 74]. The relationship between force and pressure is derived starting from (2.8) and (2.9):

$$\tilde{p}_{\max} = \frac{3}{2}\frac{1}{\pi \tilde{a}_{\text{x}}\tilde{a}_{\text{y}}} = \frac{p_{\max}\wedge^2}{F_{\text{N}}} \tag{2.55}$$

Which can be redrafted as:

$$F_{\text{N}} = \frac{2}{3}\pi \tilde{a}_{\text{x}}\tilde{a}_{\text{y}} \wedge^2 p_{\max} \tag{2.56}$$

Which can be rewritten in final form as:

$$F_{\mathrm{N_{max}}} = \frac{32}{3}\pi r_0^2 p_{\mathrm{max}}^3 \tilde{a}_{\mathrm{x}}^3 \tilde{a}_{\mathrm{y}}^3 \frac{1}{E_{\mathrm{eff}}} \tag{2.57}$$

where E_{eff} is the effective elastic modulus. All parameters defined in (2.57), except the maximum pressure p_{max}, depend purely on geometrical parameters and are thus fixed for a given CVT. With (2.48) and (2.57), it is possible to plot the maximum clamping force for a selected maximum pressure which is defined in the design stage (see Fig. 2.13). The blue line shows how the maximum clamping force is influenced by the tilting angle if the contact between input disc and roller is considered. The red line shows the same for the contact between roller and output disc. Because there can only be one limit, the most limiting curve for each side is chosen (shown as the thicker line). Fig. 2.13 is particularly useful to check the validity the design of the loading cam as for all input torques, the resulting clamping forces should be below the thicker line.

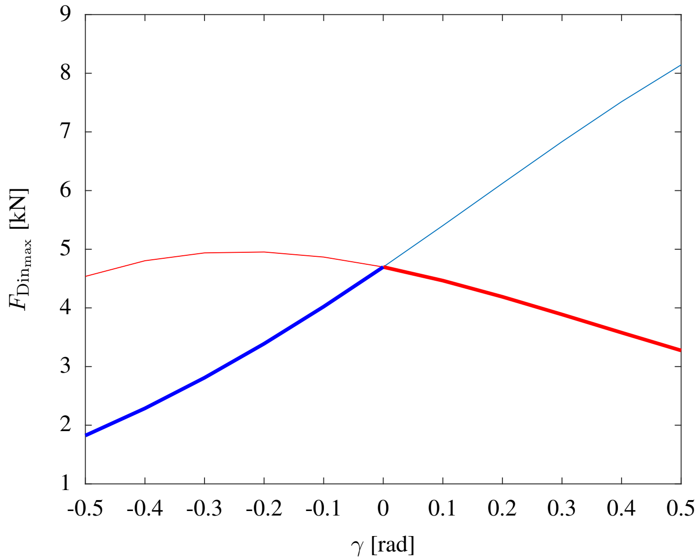

Figure 2.13: Maximum clamping force $F_{\mathrm{Din_{max}}}$ [kN] as a function of tilting angle γ [rad] for a maximum pressure of 2.6GPa. Input oriented (blue), output oriented (red).

The maximum output torque can now be calculated based on (2.54) and (2.48). Fig. 2.14 plots the maximum torque as function of the tilting angle for various maximum pressure levels. The continuous red lines are purely based on the output of (2.54). The blue asterisks are the actual maximum output torque values reached in the model. These values have been determined by slowly increasing the load torque and thus the output torque. Above the critical torque values, slip increases dramatically and synchronization between input and output is lost. Fig. 2.14 shows great resemblance between both calculation techniques and thus proves that the assumption to neglect the spin coefficient is valid in case the maximum output torque is considered. As the contact model is also valid for the full toroidal CVT, it is worth to notice that (2.53) and thus the results of this section, are applicable on full toroidal CVTs as well.

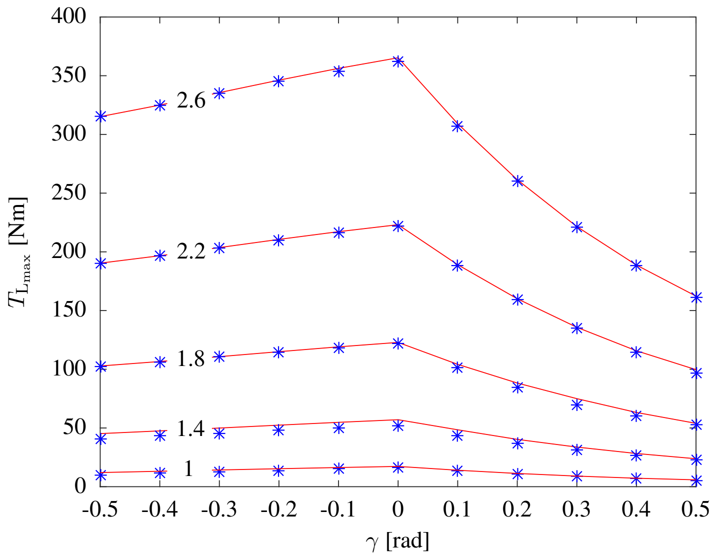

Figure 2.14: Maximum load torque $T_{\mathrm{L_{max}}}$ [Nm] as function of tilting angle γ [rad] for pressures between 1 and 2.6GPa (Δ P=0.4GPa). Maximum load torque computed by (2.54) (blue asterisks), computed by the model (red line).

2.8.2 Maximum acceleration

In the previous paragraphs an expression has been derived for the maximum output torque of the half toroidal CVT. This output torque is the torque which is used to drive the output disc and the load. Moreover, the output torque defines how fast the load can be accelerated and thus how dynamic the speed ratio can be changed. The dynamic equation of the output disc is given by:

$$T_{\mathrm{out}} = T_{\mathrm{L}} + J_{\mathrm{out}} \frac{d\Omega_{\mathrm{out}}}{dt} \tag{2.58}$$

The acceleration of the output can therefore be written as:

$$\frac{d\Omega_{\text{out}}}{dt} = \frac{T_{\text{out}} - T_{\text{L}}}{J_{\text{out}}} \tag{2.59}$$

In (2.59) the acceleration will reach its maximum value if the maximum output torque is considered:

$$\frac{T_{\text{out}_{\text{max}}} - T_{\text{L}}}{J_{\text{out}}} = \left\{ \frac{d\Omega_{\text{out}}}{dt} \right\}_{\text{max}} \tag{2.60}$$

The speed ratio of the CVT is written as follows:

$$\tau_{\text{s}}(\gamma) = \frac{\Omega_{\text{out}}}{\Omega_{\text{in}}} \tag{2.61}$$

If the derivative of the output speed is taken, an expression is found for the output acceleration as function of input acceleration and tilting angle:

$$\frac{d\Omega_{\text{out}}}{dt} = \frac{d\tau_{\text{s}}(\gamma)}{dt}\Omega_{\text{in}} + \frac{d\Omega_{\text{in}}}{dt}\tau_{\text{s}}(\gamma) \tag{2.62}$$

Considering maximum acceleration of the output shaft $\left\{\frac{d\Omega_{\text{out}}}{dt}\right\}_{\text{max}}$, (2.60) and (2.62) are equal which yields the following expression:

$$\frac{d\Omega_{\text{in}}}{dt}\left\{\tau_{\text{s}}(\gamma)\right\}_{\text{max}} + \Omega_{\text{in}}\left\{\frac{d\tau_{\text{s}}(\gamma)}{dt}\right\}_{\text{max}} = \frac{T_{\text{out}_{\text{max}}} - T_{\text{L}}}{J_{\text{out}}} \tag{2.63}$$

When the differential equation (2.63) is solved, the maximum speed at which the speed ratio $\left\{\frac{d\tau_{\text{s}}(\gamma)}{dt}\right\}_{\text{max}}$ may be varied is obtained. By integrating the solution, the desired speed ratio τ_{s} is found at a certain moment. The last step is to calculate the tilting angle based on the desired speed ratio. Neglecting slip at input and output ($\nu = 0$), it is possible to deduce the equation for the speed ratio in terms of the geometrical parameters (based on Fig. 2.1):

$$\tau_{\text{s}}(\gamma) = \frac{1}{\tau_{\text{t}}} = \frac{r_1}{r_3} = \frac{e_d + r_0 - r_0\cos(\theta + \gamma)}{e_d + r_0 - r_0\cos(\theta - \gamma)} \tag{2.64}$$

This provides the tilting angle via the inverse of this function (given by [75]):

$$\gamma = -\,2\arctan\left\{\frac{-\left(\tau_{\mathrm{s}}+1\right)\sin\left(\theta\right)}{\left(\tau_{\mathrm{s}}-1\right)\left[\left(k+1\right)+\cos\left(\theta\right)\right]}+\frac{\sqrt{\left(\tau_{\mathrm{s}}+1\right)^{2}\sin^{2}\left(\theta\right)-\left[\left(\tau_{\mathrm{s}}-1\right)\left(k+1\right)\right]^{2}+\left[\left(\tau_{\mathrm{s}}-1\right)\cos\left(\theta\right)\right]^{2}}}{\left(\tau_{\mathrm{s}}-1\right)\left[\left(k+1\right)+\cos\left(\theta\right)\right]}\right\} \tag{2.65}$$

2.8.3 Control procedure

Based on the previously mentioned equations the optimal speed ratio variation can be imposed to the CVT. As (2.63) depends on $T_{\mathrm{out}_{\mathrm{max}}}(p_{\mathrm{max}}, \gamma)$, this solution will vary constantly as for each new time step a new optimal tilting angle and thus a new $T_{\mathrm{out}_{\mathrm{max}}}$ is reached. This means that the optimal trajectory will be calculated step by step during the ratio variation.

The first step is to calculate the maximum output torque according to (2.54). The next step is to derive the maximum achievable acceleration given this output torque (2.58). With (2.63) the fastest rate of change at which the speed ratio may be varied can be determined based on the maximum acceleration. By integrating the previous solution and solving (2.65) the actual tilting angle is found. What is done here is a step by step calculation of the optimal tilting angle which results in maximum acceleration of the output.

The necessary inputs for the procedure can be found in Fig. 2.15. Almost all inputs are easily accessible in the case of a car. Speed of the input (rotational speed of the ICE) and speed of the output (wheels) are measured while driving. The maximum friction coefficient and inertia of the load are well known. Even the source torque which is generated by the ICE and the load torque are available in modern cars through observers [71,72].

Fig. 2.16 gives an example of the method described in the previous paragraph. The method is initiated at a tilting angle of 0 rad ($\tau_{\mathrm{s}} = 1$) and is ended at a tilting angle of 0.5 rad ($\tau_{\mathrm{s}} = 2.1$). The maximum output torque is shown as the red line in Fig. 2.16 (a). The blue line is the actual output torque. Before the ratio variation procedure is initiated ($T_{\mathrm{simulation}} < 2s$), this output torque is equal to the load torque ($T_{\mathrm{L}} = 110Nm$) as the CVT is in steady state ($\Omega_{\mathrm{out}} = $ constant). The difference between the actual output torque and the maximum output torque which may be demanded from the CVT is a measure for the maximum potential acceleration of the output of the CVT. Fig. 2.16 indicates that after the command is given to vary the speed ratio, the tilting angle starts to increase in such a way that the actual output torque increases up to the maximum output torque. This strategy

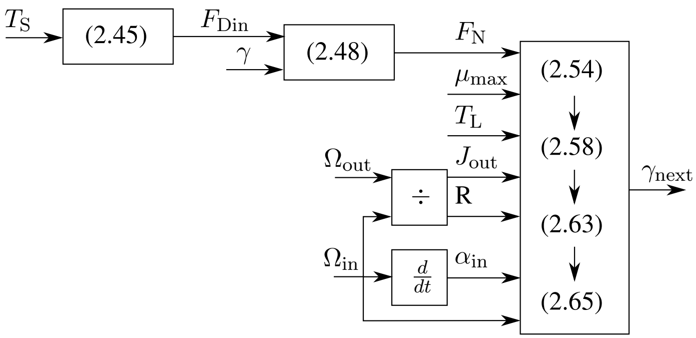

Figure 2.15: Work flow and necessary inputs for the proposed procedure.

produces the optimal tilting angle. After approximately 0.2s, the desired speed ratio is obtained.

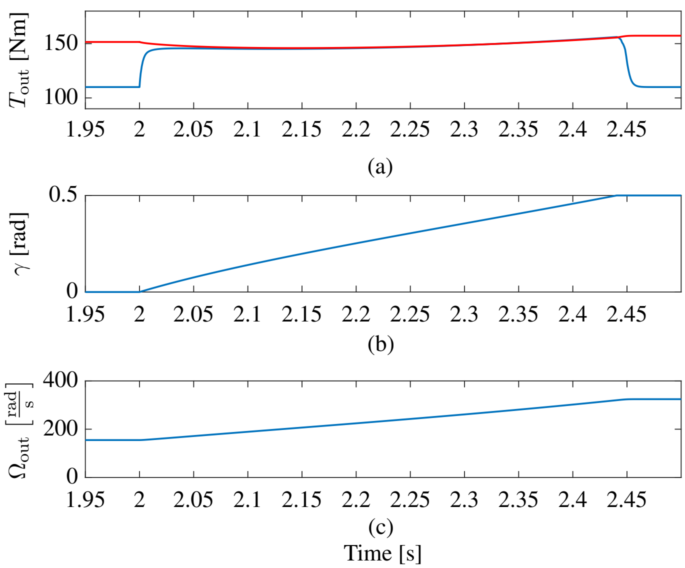

Figure 2.16: (a) Output torque T_{out} [Nm] during ratio variation. Actual T_{out} (blue), calculated $T_{out_{max}}$ (red). (b) Tilting angle γ [rad]. (c) Output speed Ω_{out} $\left[\frac{rad}{s}\right]$.

2.8.4 Discussion on the optimality of the trajectory of the tilting angle during ratio variation

Despite the fact that Fig. 2.16 shows that the maximum output torque is correctly persued, no evidence is given so far that this is indeed the best way to control the speed ratio. As there are no trajectories defined in literature, 3 possible paths for the tilting angle are proposed to make a comparison (see Fig. 2.17). The first one is the considered optimal path (method described in this section). The second path is an s-curve trajectory. This path is chosen because it is known to give smooth and energy efficient results in motion control systems [76]. In those applications, the s-curve is used as trajectory for the speed setpoint by which jerk is minimized. The last path is a linear approximation of the optimal path. All paths vary the tilting angle from start angle to final angle in the same period of time.

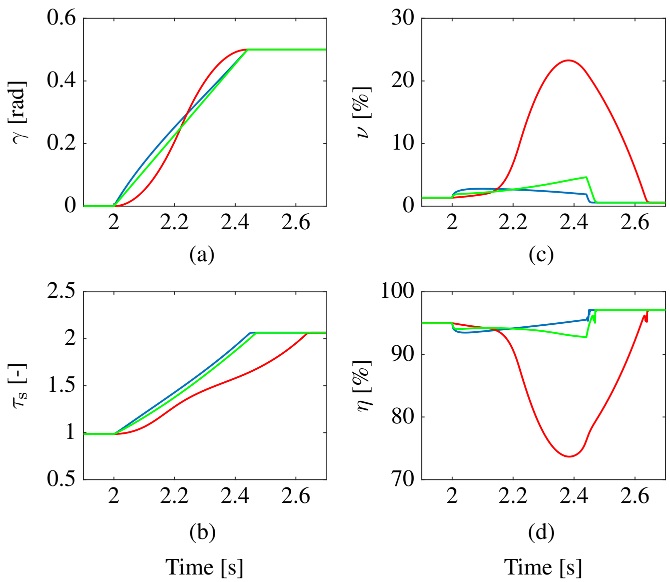

Figure 2.17: a) Tilting angle γ [rad] during ratio variation. (b) Actual speed ratio τ_t [-] during ratio variation. (c) Slip ν [%] during ratio variation. (d) Efficiency η [%] during ratio variation. All properties are visualized for 3 different trajectories: optimal path (blue), s-curve path (red), linear path (green).

In Fig. 2.17 (b) the actual speed ratio τ_s is visualized. What is striking is that the desired speed ratio of 2.1 is not reached at the same time for the different paths although the tilting angle reaches its final value in exactly the same time for all cases. The linear trajectory is relatively close to the optimal path but the s-curve trajectory takes almost 30% longer to reach the desired speed ratio. This means that there is a significant difference between the geometrical speed ratio τ_t and the actual speed ratio τ_s. Difference between τ_t and τ_s can be explained by an increase in slip as can be seen in Fig. 2.17 (c).

Fig. 2.17 (c) shows that the linear path and s-curve lead to less slip in the starting phase. This is due to a smaller acceleration of the tilting angle in that phase. As all trajectories have to reach the final value in the same amount of time, acceleration has to increase eventually to make up for lost time. For the s-curve this increase in acceleration of the tilting angle occurs after 2.05 s. As a result slip raises to a maximum of 21.5%. This phenomenon is less prominent for the linear case due to a smaller increase in acceleration. However, the increase in slip towards the end of the ratio variation trajectory is still clearly visible in comparison with the optimal path. Fig. 2.17 (d) shows the efficiency of the CVT during ratio variation. The same reasoning as for the slip holds for the efficiency. During ratio variation, the CVT with the optimal trajectory has an average efficiency of 93.7% while this is 93.2% for the linear trajectory and only 86.3% for the s-curve. The optimal trajectory is once again the best option to chose from in terms of dynamics and efficiency.

Fig. 2.17 has shown an important characteristic of the CVT: the dynamics and efficiency of the CVT during ratio variation are highly dependent on the trajectory of the tilting angle. The optimal path, described in this section, leads to optimal results in performance (fastest response) and efficiency (lowest losses). Therefore, it is vital to control the actual position of the tilting angle according to the procedure discussed in section 2.8.3.

A question that remains is whether the transient period of ratio variation can be decreased. In other words: is it possible to vary the speed ratio faster compared to the optimal path? This is simulated by adding a gain after the optimal ratio control. Therefore the tilting angle is not varied at the optimal pace but at a higher pace set by the gain. The gain was chosen to be 1.2. The result can be found in Fig. 2.18.

Fig. 2.18 (a) shows the trajectory of the tilting angle for both cases. If it is possible to vary the ratio faster than optimal, the faster case (red line) should reach the final speed ratio faster compared to the optimal case (blue line). However, Fig. 2.18 (b) shows that the opposite is true. This phenomenon can be explained in a similar way as in Fig. 2.17. The faster case induces a larger acceleration (above the maximum value) causing slip to increase dramatically (Fig. 2.18 (c)), resulting in a slower response with higher losses than the optimal case.

The limit that restraints the optimal path is set in the design phase: the loading cam. The loading cam sets the relation between input torque and clamping force (see (2.45)). If the speed ratio is increased, the input torque has to increase as well because the impact of the equivalent load torque increases. As a result higher

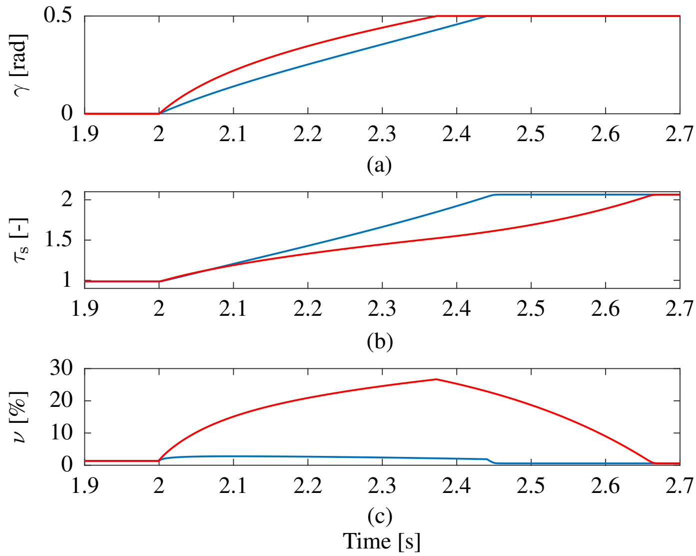

Figure 2.18: (a) Tilting angle γ [rad] during ratio variation for 2 different trajectories: optimal path (blue), faster than optimal path (red). (b) Actual speed ratio τ_{s} [-] during ratio variation. (c) Slip ν [%] during ratio variation.

clamping forces are applied on the CVT and thus higher normal forces. As depicted in (2.54) the maximum output torque, which forms the base of the method, depends on the normal force. From that equation it is trivial to see that higher normal forces result in higher output torque and thus a higher potential acceleration.

If a higher acceleration is required, the loading cam should be redesigned in order to have a larger normal force for a given input torque. This procedure is limited by the maximum pressure which is also defined in the design stage. Higher normal forces will induce higher pressure levels in the contact zone. Continuing to increase the clamping force will eventually lead to mechanical breakdown or problems with the contact fluid.

In order to obtain a higher clamping force for a given input torque, the gain k_s (see (2.45)) is increased. The parameters of the initial and updated loading cam can be found in Table 2.3.

Fig. 2.19 shows the results of the calculated optimal path for the 2 loading cams. The blue line is the initial case as discussed in Fig. 2.17 and 2.18 (blue line), the red line is the updated case. The trajectory of the tilting angle with the updated loading cam is clearly faster then the initial case (see Fig. 2.19 (a)). Something similar was shown in Fig. 2.18 but the vital difference is that in Fig. 2.19 the

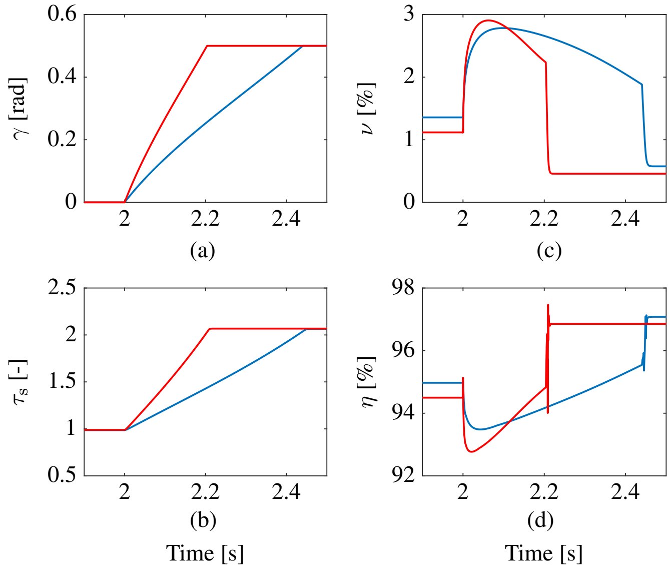

Figure 2.19: (a) Tilting angle γ [rad] during ratio variation for the initial loading cam (blue) and updated - which means increased clamping force - loading cam (red). (b) Actual speed ratio τ_s [-] during ratio variation. (c) Slip ν [%] during ratio variation. (d) Efficiency η [%] during ratio variation.

design is adapted to result in a new (faster) optimal trajectory while in Fig. 2.18 the output of the procedure was adapted to obtain faster ratio variation. The effect of this updated design is visible in Fig. 2.19 (c): the speed ratio setpoint is reached faster compared to the initial case. Because the speed ratio is able to follow the geometrical speed ratio imposed by the roller, slip remains relatively small (see Fig. 2.19 (b)). The slip peaks at approximately 3% which is a lot better than the 21.5% from Fig. 2.18.

The last parameter to be discussed is the efficiency (see Fig. 2.19 (d)). The figure shows that the efficiency of the updated case is lower than the initial case. This is as expected because the updated loading cam results in higher clamping forces which induce bigger reaction forces (F_R see Fig. 2.4) in the bearings which support the rollers. Because the losses in the bearings are influenced by the axial force, higher losses are expected.

In Fig. 2.19, it is shown that by adapting the loading cam, the dynamics of the CVT can be increased. It is also proven that there is a trade-off between performance and efficiency. Higher potential acceleration comes with higher steady state losses and thus lower efficiency.

Table 2.3: Design of the loading cam.

	Initial loading cam	Updated loading cam
k_s $\left[\frac{\mathrm{N}}{\mathrm{Nm}}\right]$	100	140
b [N]	5000	5000

2.9 Validation of the model

The model was originally presented in [50] and provided the opportunity to study the effects of one variable on another. During this analysis, other parameters that have an impact on the studied variable are kept constant, which is useful to study steady state phenomena. An example given in the original paper [50] is the relation between the dimensionless input torque and the efficiency (reproduced in Fig. 2.20 (c)). Parameters which are held constant during the analysis are the speed ratio, the input speed and the dimensionless load parameter (function of the normal force).

What is not possible due to the original model structure is the analysis of the impact of multiple variables on a single property. This occurs for example if the efficiency has to be calculated during ratio variation. In case of ratio variation, the efficiency has to be determined for varying dimensionless input torque and varying ratio. This limitation has to be overcome to be able to calculate the impact of the ratio variation on efficiency and overall dynamics.

By programming the equations according to the previously given structure (see Fig. 2.2), it is possible to study the dynamic behavior of the CVT. As a consequence, outputs can be studied as function of time for multiple time varying inputs. To validate the Simulink version of the original model, Fig. 10, 12 and 15 of the original publication ([50]) have been reproduced (see Fig. 2.20).

Fig. 2.20 (a) shows the impact of the dimensionless input torque t_{in} on the spin coefficient χ_{in}. χ_{in} is calculated based on (2.13) and t_{in} as:

$$t_{\mathrm{in}} = \frac{T_{\mathrm{in}}}{mnF_{\mathrm{N}}r_{\mathrm{in}}} \tag{2.66}$$

Fig. 2.20 (b) shows the impact of the slip ν on the dimensionless output torque t_{out} with t_{out} calculated as:

$$t_{\mathrm{out}} = \frac{T_{\mathrm{out}}}{mnF_{\mathrm{N}}r_{\mathrm{out}}} \tag{2.67}$$

Fig. 2.20 (c) shows the impact of the dimensionless input torque t_{in} on the efficiency η with η calculated as:

$$\eta = \frac{P_{\mathrm{out}}}{P_{\mathrm{in}}} = \frac{\Omega_{\mathrm{out}} T_{\mathrm{out}}}{\Omega_{\mathrm{in}} T_{\mathrm{in}}} \tag{2.68}$$

in which the input and output torque can be written in terms of traction coefficients based on (2.21):

$$\eta = \frac{\Omega_{\mathrm{out}} \left(\mu_{\mathrm{out}} - \chi_{\mathrm{out}} \sin\left(\theta - \gamma\right)\right) r_{\mathrm{out}}}{\Omega_{\mathrm{in}} \left(\mu_{\mathrm{in}} + \chi_{\mathrm{in}} \sin\left(\theta + \gamma\right)\right) r_{\mathrm{in}}} \tag{2.69}$$

Note that the losses related to the actuation system (hydraulic cylinder or loading cam) are not taken into account in (2.69). This is the case as in [50], these losses have not been considered.

The comparison presented in Fig. 2.20 shows great resemblance between the model and the original data notwithstanding the difference in model structure. This proves that the developed model is capable of reproducing the results presented in [50].

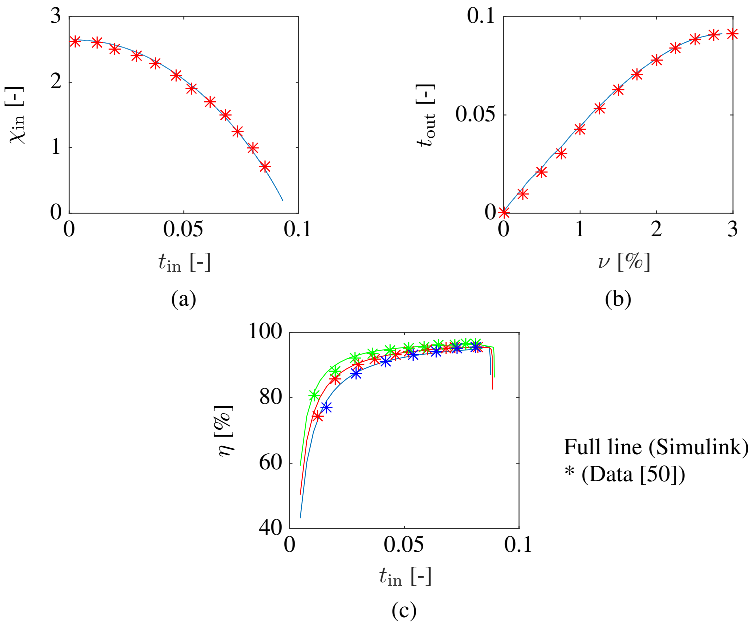

Figure 2.20: (a) Input spin coefficient χ_{in} as a function of the dimensionless input torque t_{in} (comparison with Fig. 10 in [50]). (b) Dimensionless output torque t_{out} as a function of the slip (ν) (comparison with Fig. 12 in [50]). (c) Efficiency η as function of the dimensionless input torque t_{in} for different values of speed ratio τ_{t} (comparison with Fig. 15 in [50]). $\tau_{\text{t}} = \frac{2}{3}$ (blue), $\tau_{\text{t}} = 1$ (red) and $\tau_{\text{t}} = 1.5$ (green).

2.10 Conclusion

In this chapter, the toroidal CVT is introduced. The operating principle has been discussed and it is shown how the speed ratio of the device is changed. Furthermore, the control of slip is discussed based on 2 methods: active control via a hydraulic cylinder or passive control via a loading cam. The active control has been defined based on the slip dynamics. This is an entirely new method for the toroidal CVT based on a method that is designed for a belt CVT. For the design of the loading cam, standard design procedures are used.

Analysis of the results shows that the passive control can handle load variations better than the active control. The side effect is that slip cannot be controlled to a specific value which has an impact on the traction coefficient and thus also on the efficiency. However, during load variations, the passive control (with loading cam), clearly performed best. Therefore, further on in this thesis, the comparison between the different variable transmissions will be done based on a toroidal CVT with loading cam. The efficiency of the considered toroidal CVT thus depends on losses in the contact, loading cam and thrust bearings.

The presented comparison between the active and passive control has shown that the model can calculate the efficiency throughout simultaneous ratio and load variation. It is thus possible to visualize the efficiency in terms of speed ratio and load torque. Therefore, the first research goal, defined in section 1.2, has been realized. This is important as the different variable transmissions will be compared in terms of efficiency as function of speed ratio and load torque.

Thereafter, the ratio control has been optimized compared to the state of the art by relating speed ratio variation to the maximum output torque. It is shown that the design of the loading cam has a significant impact on the dynamics. If the stiffness is increased, faster dynamics are possible but at the cost of increased steady state losses. This trade-off between efficiency and dynamics has not been presented before and resulted in 2 journal publications.

Besides its use to optimize the ratio variation, the equation to calculate the maximum output torque can also be used to redesign the toroidal CVT. Therefore, the second research goal, as specified in section 1.2, has also been accomplished. Finally, the model is validated based on the available literature.

Chapter 3

Belt Continuously Variable Transmission

In this chapter, the belt CVT is introduced. First, the key components and the operating principle of the CVT are discussed. Subsequently, the modeling techniques, control of the device and model validation are discussed. The general goal of this chapter is to present a model of a belt CVT that can be used to compare this variable transmission, in terms of efficiency, with alternative technologies. Like the toroidal CVT, it has to be possible to calculate the efficiency as function of the speed ratio (ratio of the output speed and input speed) and load torque.

3.1 Introduction

In correspondence with the toroidal CVT, the model is subjected to the same requirements: parametrized, following the physical causality, capable of analyzing dynamic events and incorporated losses.

The model needs to be parametrized to be able to analyze the effect of design changes. Although the equations used to calculate, for example the torque, are parametrized, no analytical traction model, depending on geometrical parameters, was found in literature. Hence, the traction model used in this chapter depends on measurements and is thus not parametrized. Changing the dimensions could thus result in erroneous results. To avoid this, the belt CVT considered in this chapter will not be redesigned. The design of the toroidal CVT and EVT will thus be changed in order to match the performance of the belt CVT.

Physical causality is important in order to obtain realistic results when doing a dynamic simulation. In contrast to the toroidal CVT, this is not related to torque and speed but to the dynamic model of the belt. The model used to evaluate this originally started with the rate of change of the running radius. Based on this input, the corresponding clamping forces can be calculated. However, in reality, forces are applied to the pulleys and that results in a changing running radius of the belt. Therefore, in this chapter a method is elaborated to invert the relationship and to have a fast assessment of the effect of clamping forces on the rate of change of the running radius of the belt.

Both on the dynamics and the losses of the belt CVT, an abundance of models is available. In this chapter, a selection of these models is used to finalize the component model of the belt CVT.

Apart from the models, the subsystem control needs to be defined. Similar to the toroidal CVT, two controllers are needed: slip and ratio control. On the slip control, a contribution is made based on a method that uses the linearized slip dynamics of the CVT (identical to the method used for the toroidal CVT) [77]. Concerning ratio control, a standard PI controller is used.

3.2 Operating principle

In a belt CVT, power is transmitted from the input pulley to the output pulley via a V-shaped belt. The pulleys are composed of a fixed half and a movable half (sheave). By adapting the position of the movable sheaves, the belt will run on another radius and as a result the speed ratio τ_s is altered. Movement of the sheaves and thus control of the speed ratio is done via 2 hydraulic cylinders that deliver a force on the primary and secondary pulley, F_p and F_s respectively. Like the toroidal CVT, the belt CVT is also a traction device in which slip between belt and pulley is necessary to deliver torque. The slip in a belt CVT is typically controlled via the secondary pulley, while the ratio of both forces determines the speed ratio.

3.3 Model structure

The model of the belt CVT has a similar layout as the toroidal CVT (see Fig. 3.1): a contact model, mechanical model and transient variator model are combined to describe the behavior of the CVT. In the contact model, the relation between slip and traction coefficient is determined while in the mechanical model the speed, speed ratio and slip are calculated based on the applied torque. The transient variator model, which is a new block compared to the toroidal CVT, describes the relation between the applied forces, derived by a controller, and the resulting speed ratio.

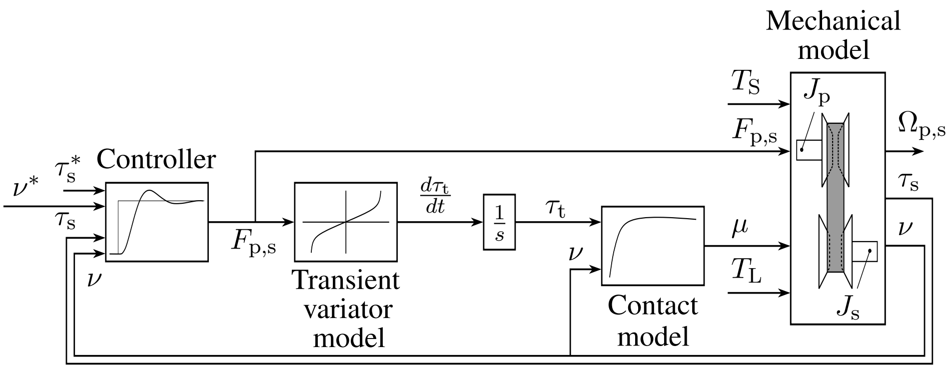

Figure 3.1: Model structure of the belt CVT.

3.4 Contact model

In contrast to the toroidal CVT, traction curves of the belt CVT are discussed on the basis of measurements, not theory. In [78], it is concluded, based on measurements, that the traction curve is mostly dependent on the speed ratio $\tau_s = \frac{\Omega_s}{\Omega_p}$. As it is not the aim of this thesis to define new models, the measurement data provided in [25,69] is used to make a Look-up Table based traction model. The traction data allows to relate the slip and speed ratio to the achieved traction coefficient.

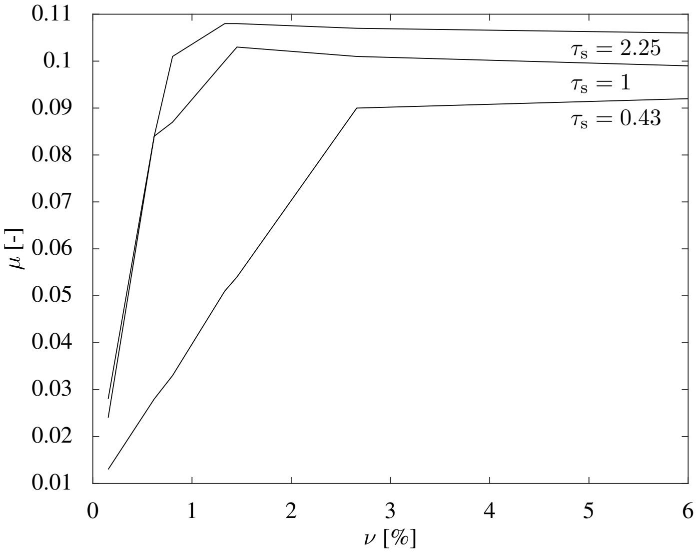

Figure 3.2: Friction coefficient μ [-] as function of the slip ν [%] for varying speed ratio τ_{s} [-]. Data acquired from [25, 69].

3.5 Mechanical model

The governing equations of motion for the primary and secondary pulley, derived based on Fig. 3.3, are written as follows:

$$\begin{cases} J_{\mathrm{p}} \frac{d\Omega_{\mathrm{p}}}{dt} & = T_{\mathrm{S}} - T_{\mathrm{p}} - T_{\mathrm{hyd}} \\ J_{\mathrm{s}} \frac{d\Omega_{\mathrm{s}}}{dt} & = T_{\mathrm{s}} - T_{\mathrm{l}} - T_{\mathrm{L}} \end{cases} \tag{3.1}$$

in which J_{p} and J_{s} are the inertia values for primary and secondary pulley, respectively. The speed of the primary and secondary pulley is denoted by Ω_{p} and Ω_{s}, respectively. The torque which is delivered by the source is T_{S} while the load torque coming from an application is T_{L}. T_{l} represents the torque loss in the bearings and belt [69] while T_{hyd} is the torque needed to drive the hydraulics that are used to generate the clamping forces. This torque loss T_{hyd} is function of the input speed (coupled with the oil flow) and the requested clamping force (related to the pressure in the system) [79]. The torque that is generated by primary and secondary pulley is T_{p} and T_{s}, respectively, and can be written in terms of the slip ν, the secondary clamping force F_{s}, the running radius $R_{\mathrm{p,s}}$ and the half cone angle β:

$$T_{p,s} = \frac{2F_s \mu\left(\tau_{\mathrm{s}}, \nu\right) R_{p,s}}{\cos\beta} \tag{3.2}$$

When (3.1) and (3.2) are combined, the following set of equations is found:

$$\begin{cases} J_\mathrm{p}\frac{d\Omega_\mathrm{p}}{dt} & = T_\mathrm{S} - \frac{2F_\mathrm{s}\mu(\tau_\mathrm{s},\nu)R_\mathrm{p}}{\cos\beta} - T_\mathrm{hyd} \\ J_\mathrm{s}\frac{d\Omega_\mathrm{s}}{dt} & = \frac{2F_\mathrm{s}\mu(\tau_\mathrm{s},\nu)R_\mathrm{s}}{\cos\beta} - T_\mathrm{l} - T_\mathrm{L} \end{cases} \tag{3.3}$$

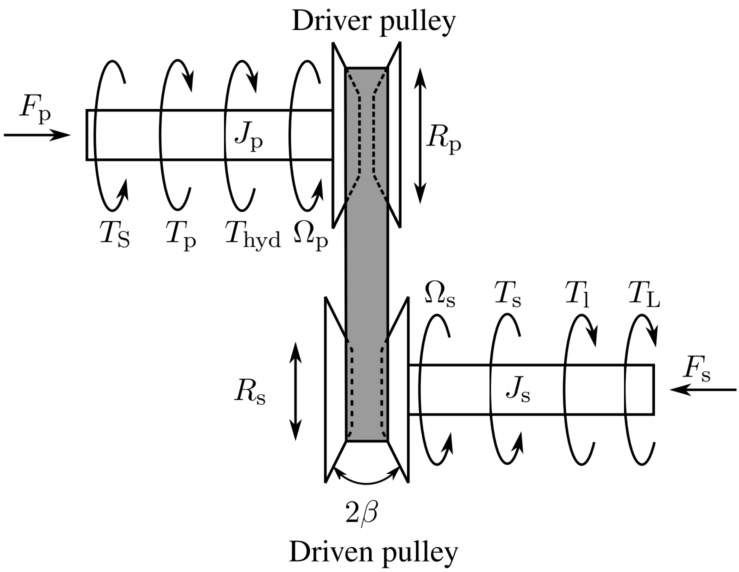

Figure 3.3: Belt CVT

3.6 Transient variator model

The transient variator model describes the dynamical behavior of the belt for given clamping forces, input speed and load torque. This model is thus used to calculate the variation in speed ratio for the given inputs. Several models are available in literature [22, 80–83]. Safai [80] concluded that there is a linear relation between the clamping force and the velocity at which the primary pulley sheave is moving. The model showed that the change in clamping force ratio resulted in a change in speed ratio.

Ide [81] proposed a model that describes the relation between the clamping force ratio and the speed ratio variation:

$$\frac{d\tau_\mathrm{t}}{dt} = \Omega_\mathrm{p}\sigma_\mathrm{Ide}\left[\left(\frac{F_\mathrm{p}}{F_\mathrm{s}}\right) - \left(\frac{F_\mathrm{p}}{F_\mathrm{s}}\right)_\mathrm{eq}\right] \tag{3.4}$$

in which τ_t is the theoretical speed ratio that equals the ratio of R_p and R_s, σ_Ide is determined based on measurements and subscript eq refers to the clamping force ratio in steady state. In other words: if the applied clamping force ratio $\left(\frac{F_\mathrm{p}}{F_\mathrm{s}}\right)$ matches the calculated steady state clamping force ratio, the derivative of the speed ratio becomes 0, i.e. the speed ratio stabilizes. The validation presented in [82] proves the applicability of the model, however some deviation between model and measurements is observable particularly at low speed ratio values.

In contrast to Shafai and Ide, Carbone started from a theoretical basis to derive the relation between speed ratio variation and clamping force ratio [84]. Based on his theoretical findings, a model is derived and validated [22]. The main equation is similar to the model of Ide, except for the logarithmic relation:

$$\frac{d\tau_\mathrm{t}}{dt} = \Omega_\mathrm{p}\Delta\frac{1+\cos^2(\beta)}{\sin(2\beta)}\sigma_\mathrm{Carbone}\left[\ln\left(\frac{\mathrm{F_p}}{\mathrm{F_s}}\right) - \ln\left(\frac{\mathrm{F_p}}{\mathrm{F_s}}\right)_\mathrm{eq}\right] \tag{3.5}$$

in which Δ inherits the pulley deformation in rad which can be calculated based on FEM or which can be estimated based on the following equation [22]:

$$\Delta = 0.001\left[1 + 0.02\left(F_\mathrm{s} - 20\right)\right] \tag{3.6}$$

The clamping force F_s in (3.6) is denoted in kN. It is interesting to see that the first term of the Taylor series expansion of (3.5) is closely related to the model of Ide (3.4):

$$\begin{aligned}\ln\left(\frac{\mathrm{F_p}}{\mathrm{F_s}}\right) - \ln\left(\frac{\mathrm{F_p}}{\mathrm{F_s}}\right)_\mathrm{eq} =& \frac{1}{\left(\frac{F_\mathrm{p}}{F_\mathrm{s}}\right)_\mathrm{eq}}\left[\left(\frac{F_\mathrm{p}}{F_\mathrm{s}}\right) - \left(\frac{F_\mathrm{p}}{F_\mathrm{s}}\right)_\mathrm{eq}\right] \\ & -\frac{1}{2}\frac{1}{\left(\frac{F_\mathrm{p}}{F_\mathrm{s}}\right)^2_\mathrm{eq}}\left[\left(\frac{F_\mathrm{p}}{F_\mathrm{s}}\right) - \left(\frac{F_\mathrm{p}}{F_\mathrm{s}}\right)_\mathrm{eq}\right]^2 \\ & + \ldots\end{aligned} \tag{3.7}$$

It is thus possible to state that the model of Ide is a first order representation of the model of Carbone and that the difference between both representations is proportional with the higher order terms [22]:

$$\left.\frac{d\tau_\mathrm{t}}{dt}\right|_\mathrm{Ide} - \left.\frac{d\tau_\mathrm{t}}{dt}\right|_\mathrm{Carbone} \sim \frac{1}{2}\frac{1}{\left(\frac{F_\mathrm{p}}{F_\mathrm{s}}\right)^2_\mathrm{eq}}\left[\left(\frac{F_\mathrm{p}}{F_\mathrm{s}}\right) - \left(\frac{F_\mathrm{p}}{F_\mathrm{s}}\right)_\mathrm{eq}\right]^2 + \ldots \tag{3.8}$$

As the force ratio increases with increasing speed ratio, the higher order terms become less important at high speed ratio. That explains the increasing accuracy of the Ide model or why it is less accurate at low speed ratio values.

The model of Carbone, referred to as the CMM (Carbone-Mangialardi-Mantriota) model in literature, has been widely accepted as the reference model to describe the dynamic behavior of the belt. Therefore, this model is chosen to model the transient behavior of the belt. In the following section the CMM model is briefly discussed.

3.6.1 CMM variator model

The objective of the CMM variator model is to describe the ratio variation dynamics in function of the driving parameters of a belt CVT which comes down to determining $\sigma_{\mathrm{Carbone}}$ as mentioned in (3.5). In (3.5) it is thus assumed that there is a linear relation between the logarithm of the clamping force ratio and the ratio variation itself. However, as it is the purpose to use this model for varying inputs (clamping forces, load torque, input speed, ...), finding this $\sigma_{\mathrm{Carbone}}$ could become a cumbersome task. Moreover, no analysis on the accuracy of this linearized model and its driving parameter $\sigma_{\mathrm{Carbone}}$ for a wide range of varying inputs has been done. Therefore, in this thesis a slightly different representation for (3.5) is used. that is closer to the original governing equation:

$$\left.\frac{d\tau_{\mathrm{t}}}{dt}\right|_{\mathrm{CMM}} = \Omega_{\mathrm{p}}\Delta\frac{1+\cos^2(\beta)}{\sin(2\beta)}Ag \tag{3.9}$$

in which g and h are calculated as:

$$g = (h\tau + 1)\,\tau \tag{3.10}$$

$$h = \frac{\pi - 2\arcsin\left(\frac{R_{\mathrm{p}}(1-\tau)}{\tau}\right)}{\pi + 2\arcsin\left(\frac{R_{\mathrm{p}}(1-\tau)}{\tau}\right)} \tag{3.11}$$

In this formulation of the CMM variator model, the dimensionless parameter A is the unknown value which needs to be found and that resembles the ratio of change of the pitch radius. This dimensionless parameter depends on the speed ratio τ_{t}, the torque at the secondary pulley T_{s}, the clamping force at the primary pulley F_{p}, the clamping force at the secondary pulley F_{s} and the speed of the secondary pulley Ω_{s}. As it is not possible to solve the relation between force ratio and ratio variation in a forward way, the inverse problem is solved. The dimensionless value A is thus considered known and the clamping force ratio is searched for. By solving this problem for various input values (speed ratio, torque, clamping force,

...), it is possible to reverse the solution in order to obtain speed ratio variation as function of the driving parameters. This also means that the model is not fixed to a linear representation as it is solved for numerous combinations of inputs.

The first step in solving the inverse problem is calculating the dimensionless radial $\tilde{v}_{\mathrm{r}}$ and tangential velocity of the belt $\tilde{v}_{\theta}$, given A:

$$\tilde{v}_{\mathrm{r}} = A - \cos\left(\theta - \theta_{\mathrm{c}} + \frac{\pi}{2}\right) \tag{3.12}$$

$$\tilde{v}_{\theta} = \tilde{v}_{\theta,0} - A\theta - 2\sin\left(\frac{\theta}{2}\right)\sin\left(\frac{\theta}{2} - \theta_{\mathrm{c}}\right) \tag{3.13}$$

in which θ_{c} is the position of the center of the wedge, θ is the angular coordinate and $\tilde{v}_{\theta,0}$ is the initial value for the tangential speed. These parameters are also depicted on Fig. 3.4.

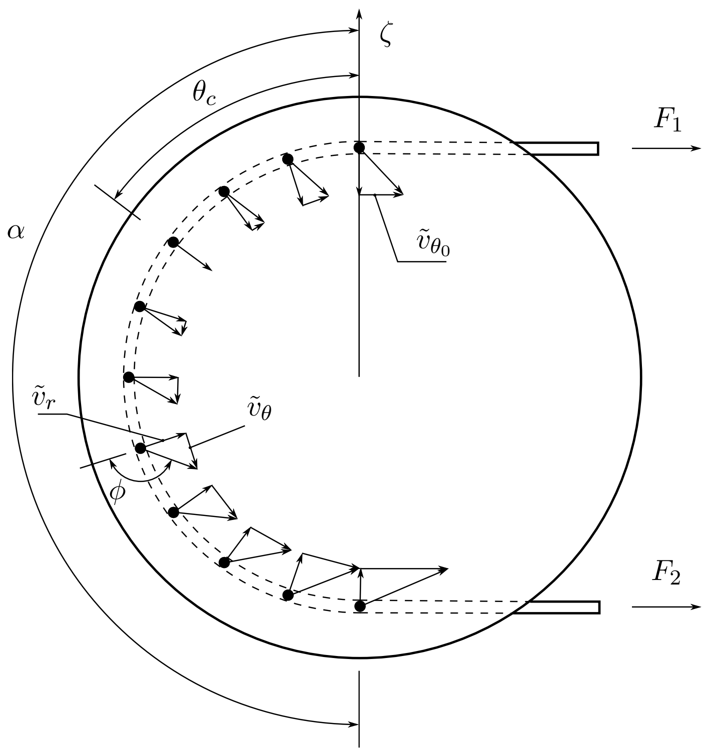

Figure 3.4: Belt CVT in motion [84].

The next step is to calculate the wrap angle α and the dimensionless force ratio ζ:

$$\alpha_{\mathrm{p,s}} = \pi - 2\arcsin\left(\frac{R_{\mathrm{p,s}}\,(1-\tau)}{\tau}\right) \tag{3.14}$$

$$\gamma_{\mathrm{p,s}} = \int_0^{\alpha_{\mathrm{p,s}}} \frac{\mu \sin\phi}{\sin\beta_0\sqrt{1+\tan^2\beta_0\cos^2\phi} - \mu\cos\phi} \tag{3.15}$$

$$\zeta_{\mathrm{p,s}} = \gamma_{\mathrm{p,s}}\left(\alpha_{\mathrm{p,s}}\right) \tag{3.16}$$

Once ζ_{s} is known, the following equations can be solved to obtain the resulting clamping force.

$$\kappa_{\mathrm{p,s}} = e^{\gamma}_{\mathrm{p,s}} \tag{3.17}$$

$$\tilde{p}_{\mathrm{p,s}} = \frac{\sqrt{1+\tan^2\beta_0\cos^2\phi}}{\sin\beta_0\sqrt{1+\tan^2\beta_0\cos^2\phi} - \mu\cos\phi}\,\frac{\kappa_{\mathrm{p,s}}}{2} \tag{3.18}$$

$$F_{2,1} = \frac{T_{\mathrm{p,s}}}{\left|1-\zeta_{\mathrm{p,s}}\right| R_{\mathrm{p,s}}} + \sigma\Omega^2_{\mathrm{p,s}}R^2_{\mathrm{p,s}} \tag{3.19}$$

$$F_{\mathrm{p,s}} = \int_0^{\alpha_{\mathrm{p,s}}} \left[\cos\beta_0 + \frac{\mu\tan\beta_0\cos\phi}{\sqrt{1+\tan^2\beta_0\cos^2\phi}}\right]\tilde{p}_{\mathrm{p,s}}\left(F_{2,1} - \sigma\Omega^2_{\mathrm{p,s}}R^2_{\mathrm{p,s}}\right) \tag{3.20}$$

As the clamping force is an input, the question may arise why this property needs to be calculated. To answer that question, (3.12) and (3.13) need to be reconsidered. The variables θ_{c} and $\tilde{v}_{\theta,0}$ need to be known to solve that equation. Both variables are related to ζ which in turn is related to F_{s}. The main principle of the solving method is thus to choose a ζ value as reference and iteratively search for that combination of θ_{c} and $\tilde{v}_{\theta,0}$ which results in the same ζ as the one which was chosen. However, the chosen ζ will then result in a F_{s} value that also needs to match with the input clamping force. Finding that ζ for which the model results in the correct clamping force is thus another iterative process. When the calculated clamping force matches the input clamping force, the correct ζ is found for the secondary pulley. A schematic of both iterative processes is presented in Fig. 3.5.

A similar procedure has to be followed for the primary pulley. However, as both pulleys are connected via the belt, it is possible to derive ζ_{p} from the value of the secondary pulley:

$$\zeta_{\mathrm{p}} = \frac{1}{\zeta_{\mathrm{s}}} \tag{3.21}$$

Also the A value needs to be matched:

$$A_{\mathrm{p}} = \frac{A_{\mathrm{s}}}{h} \tag{3.22}$$

Knowing ζ_{p} reduces the complexity of solving the equations for the primary side as no additional iterations are necessary to find the correct dimensionless force. The necessary steps are summarized in Fig. 3.6.

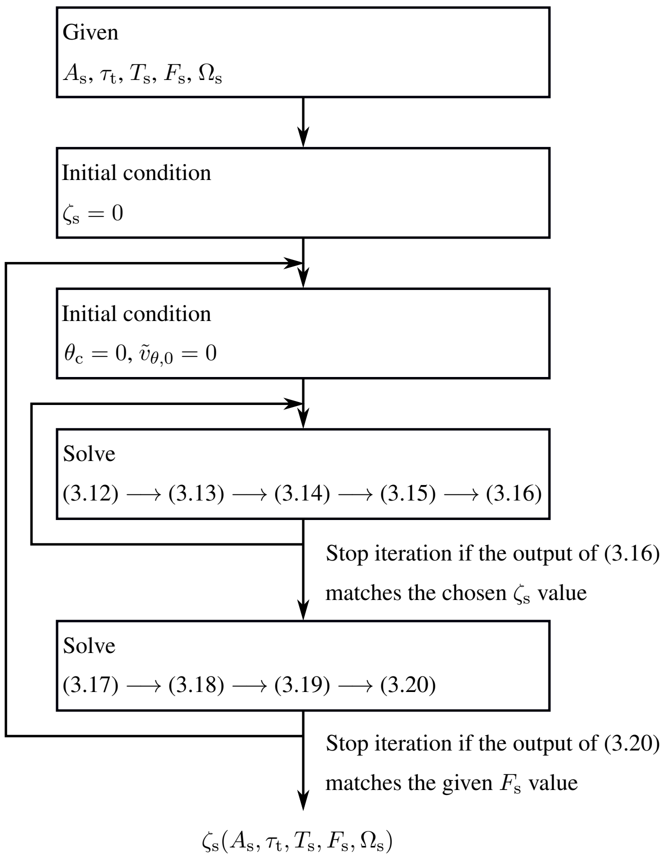

Figure 3.5: Numerical calculation of dimensionless force ratio at the secondary pulley ζ_{s} of a belt CVT as function of the speed ratio τ_{t}, secondary torque T_{s}, secondary clamping force F_{s}, rate of change of the pitch radius A_{s} and secondary speed Ω_{s}.

The output of this procedure is thus a matching secondary clamping force for the given input values. Calculating the clamping force ratio for these inputs is trivial. If this procedure is repeated for several inputs, the obtained array can be

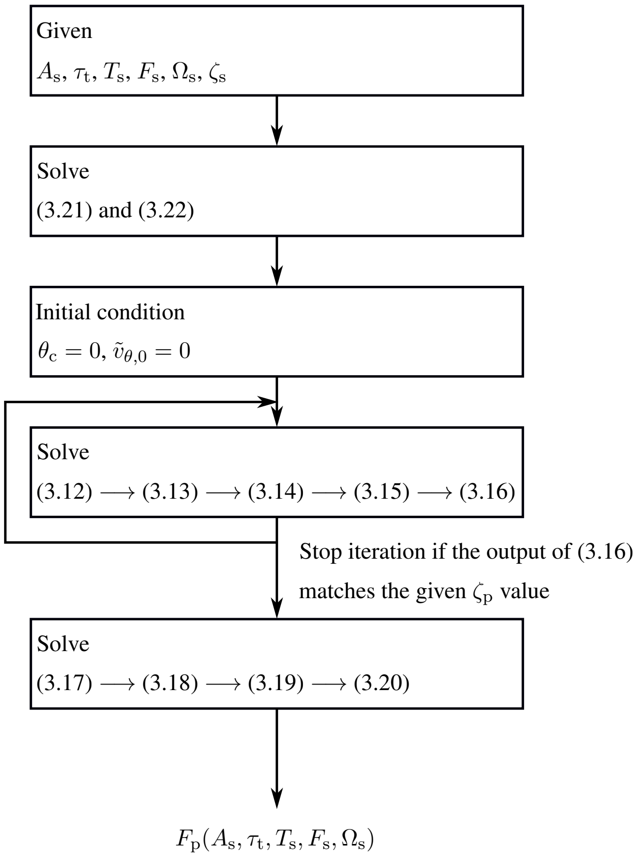

Figure 3.6: Numerical calculation of the primary clamping force F_p of a belt CVT as function of the speed ratio τ_t, secondary torque T_s, secondary clamping force F_s, rate of change of the pitch radius A_s and secondary speed Ω_s.

inverted on a predefined grid of clamping force values. The final result is a multi dimensional look-up table which can be used to solve (3.9) for all possible inputs (T_s,Ω_s,F_s,F_p,τ).

3.6.2 Validation of the CMM variator model

The CMM variator model is extensively validated in literature [22, 85, 86]. To verify if the described procedure to solve the equations is correctly programmed, a comparison between the output of the used model and data from [22] is compared. Fig. 3.7 shows great resemblance between both datasets, which means the CMM variator model is correctly programmed.

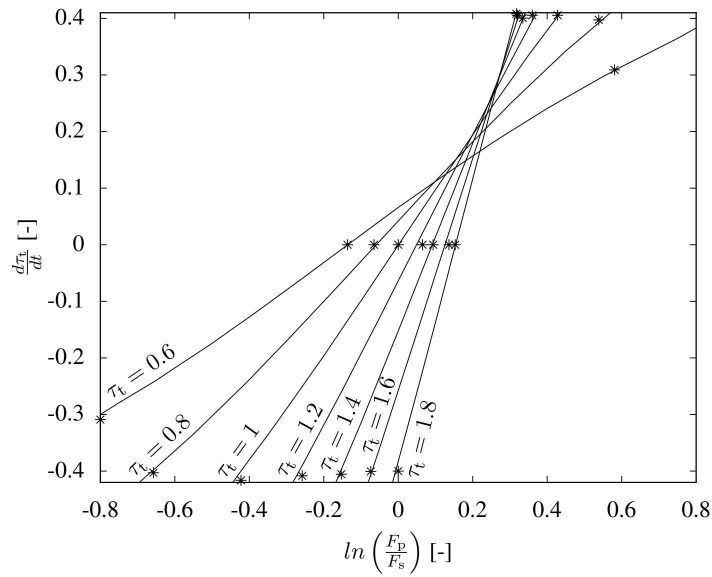

Figure 3.7: Speed ratio variation $\frac{d\tau_t}{dt}$ [-] as function of the clamping force ratio $ln\left(\frac{F_p}{F_s}\right)$ [-] for a speed of the secondary pulley of 1000 rpm, clamping force at the secondary pulley of 20 kN and varying speed ratio. Full lines are the results of the model used in this thesis, stars are based on data acquired from [22].

3.7 Active slip control

In contrast to the toroidal CVT, only belt CVTs with active control are made. The reason for this is fairly straightforward: the position of the pulleys determines the speed ratio. Therefore, the position needs to be controlled and not just merely the force. The method to derive the controller parameters however, is the same as for the toroidal CVT. Hence, as the parameters are different, the necessary steps to calculate the controller parameters are repeated in this section. Note that due to this slip controller, the minimal clamping force to transfer a specific load torque, will be applied to the system. In literature, this is called a safety factor of 1 (ratio of applied clamping force and minimum clamping force). However, in reality, often a value of 1.3 is chosen, which means the device is over-clamped and that reduces the efficiency [87]. This safety factor is used to obtain stable operation and to increase the robustness against load variations. The robustness, while using a safety factor of 1, will be tested in this section.

3.7.1 Linearized slip dynamics

As demonstrated by [88], it is vital to model the slip dynamics in order to design a proper slip controller. When the speed ratio is varied or during load disturbance or variation, slip variations will occur. Slip ν is defined by the ratio of the actual speed ratio τ_s and the theoretical or geometrical speed ratio τ_t, see (3.23). In (3.23), the actual speed ratio τ_s is calculated as the ratio of the secondary Ω_s and primary speed Ω_p while the theoretical speed ratio τ_t is defined by the ratio of the primary R_p and secondary radius R_s.

$$\nu = \frac{-\tau_\mathrm{s}}{\tau_\mathrm{t}} + 1 = \frac{-\frac{\Omega_\mathrm{s}}{\Omega_\mathrm{p}}}{\frac{R_\mathrm{p}}{R_\mathrm{s}}} + 1 \tag{3.23}$$

As it is the objective to control the variations in slip, the derivative is considered similar to (2.23) for the toroidal CVT:

$$\frac{d\nu}{dt} = \frac{\frac{d\tau_\mathrm{t}}{dt}\tau_\mathrm{s} - \frac{d\tau_\mathrm{s}}{dt}\tau_\mathrm{t}}{\tau_\mathrm{t}^2} \tag{3.24}$$

Which can be rewritten as:

$$\frac{d\nu}{dt} = \frac{\frac{d\tau_\mathrm{t}}{dt}\frac{\Omega_\mathrm{s}}{\Omega_\mathrm{p}} - \frac{\frac{d\Omega_\mathrm{s}}{dt}\Omega_\mathrm{p} - \frac{d\Omega_\mathrm{p}}{dt}\Omega_\mathrm{s}}{\Omega_\mathrm{p}^2}\tau_\mathrm{t}}{\tau_\mathrm{t}^2} \tag{3.25}$$

Considering (3.3) and ignoring the losses, (3.25) can be redrafted in terms of torque and inertia:

$$\frac{d\nu}{dt} = \frac{\frac{d\tau_\mathrm{t}}{dt}\Omega_\mathrm{s}}{\tau_\mathrm{t}^2\Omega_\mathrm{p}} - \frac{T_\mathrm{s} - T_\mathrm{L}}{\Omega_\mathrm{p} J_\mathrm{s}\tau_\mathrm{t}} + \frac{(T_\mathrm{S} - T_\mathrm{p})(1-\nu)}{\Omega_\mathrm{p} J_\mathrm{p}} \tag{3.26}$$

By using (3.2), the equation describing the slip dynamics can be finalized:

$$\begin{aligned} \frac{d\nu}{dt} = {} & \frac{\frac{d\tau_\mathrm{t}}{dt}\Omega_\mathrm{s}}{\tau_\mathrm{t}^2\Omega_\mathrm{p}} + \frac{1}{\Omega_\mathrm{p}}\left(-\frac{2F_\mathrm{s}\mu R_\mathrm{s}}{J_\mathrm{s}\cos\beta\tau_\mathrm{t}} + \frac{T_\mathrm{L}}{J_\mathrm{s}\tau_\mathrm{t}}\right) \\ & + \frac{1-\nu}{\Omega_\mathrm{p}}\left(-\frac{2F_\mathrm{s}\mu R_\mathrm{s}\tau_\mathrm{t}}{J_\mathrm{p}\cos\beta} + \frac{T_\mathrm{S}}{J_\mathrm{p}}\right) \end{aligned} \tag{3.27}$$

The variation in slip is thus a function of 10 variables:

$$\frac{d\nu}{dt} = f\left(\nu, \frac{d\tau_{\mathrm{t}}}{dt}, \tau_{\mathrm{t}}, \Omega_{\mathrm{s}}, \Omega_{\mathrm{p}}, F_{\mathrm{s}}, R_{\mathrm{s}}, T_{\mathrm{S}}, T_{\mathrm{L}}, \mu\right) \tag{3.28}$$

Of these variables, only the secondary clamping force F_{s} can be used to actively control the slip. All other variables are controlled at a higher level by for example the energy management system which selects optimal operating points (T_{S}, Ω_{p}, ...) or are induced by the considered load profile (T_{L}, Ω_{s}, ...). Therefore, these variables are considered as disturbances D.

Notice that the primary clamping force F_{p} does not appear in the equation. However, this does not mean that F_{p} has no impact on the slip. As shortly mentioned in section 3.2, the speed ratio τ_{t} of the CVT depends on the ratio of the clamping forces. Consequently, an increase of F_{p} will lead to a variation in speed ratio τ_{t}. As the speed ratio has an impact on the slip dynamics (see (3.27)), F_{s} will also have to change to maintain the desired slip value. The secondary clamping force has thus an indirect effect on the slip.

If (3.27) is linearized (continuously for every time instant, i.e. adaptive control), ignoring the variables considered as disturbances D, the following equation is found:

$$\begin{aligned}\frac{d\nu}{dt} &= D_{\frac{d\tau_{\mathrm{t}}}{dt}} + D_{\tau_{\mathrm{t}}} + D_{\Omega_{\mathrm{s}}} + D_{\Omega_{\mathrm{p}}} + \left.\frac{\partial f}{\partial F_{\mathrm{s}}}\right|_{*} (F_{\mathrm{s}} - F_{\mathrm{s}}^{*}) + D_{\mathrm{R_s}} \\ &+ D_{\mathrm{T_L}} + D_{\mathrm{T_S}} + \left.\frac{\partial f}{\partial \nu}\right|_{*} (\nu - \nu^{*}) + D_{\mu}\end{aligned} \tag{3.29}$$

$$\frac{d\nu}{dt} = D + \left.\frac{\partial f}{\partial F_{\mathrm{s}}}\right|_{*} (F_{\mathrm{s}} - F_{\mathrm{s}}^{*}) + \left.\frac{\partial f}{\partial \nu}\right|_{*} (\nu - \nu^{*}) \tag{3.30}$$

Which can be rewritten as:

$$\frac{d\nu}{dt} = \underbrace{D - \left.\frac{\partial f}{\partial F_{\mathrm{s}}}\right|_{*} F_{\mathrm{s}}^{*} - \left.\frac{\partial f}{\partial \nu}\right|_{*} \nu^{*}}_{\mathrm{K}} + \underbrace{\left.\frac{\partial f}{\partial F_{\mathrm{s}}}\right|_{*}}_{\mathrm{L}} F_{\mathrm{s}} + \underbrace{\left.\frac{\partial f}{\partial \nu}\right|_{*}}_{\mathrm{M}} \nu \tag{3.31}$$

In which the partial derivative of F_{s} equals:

$$\left.\frac{\partial f}{\partial F_{\mathrm{s}}}\right|_{*} = -\frac{2\mu R_{\mathrm{s}}}{\Omega_{\mathrm{p}} J_{\mathrm{s}} \cos\beta \tau_{\mathrm{t}}} - \frac{(1-\nu)\, 2\mu R_{\mathrm{s}} \tau_{\mathrm{t}}}{\Omega_{\mathrm{p}} J_{\mathrm{p}} \cos\beta} = L \tag{3.32}$$

And the partial derivative of ν:

$$\left.\frac{\partial f}{\partial \nu}\right|_{*} = \frac{2F_{\mathrm{s}}\mu R_{\mathrm{s}}\tau_{\mathrm{t}}}{\Omega_{\mathrm{p}}J_{\mathrm{p}}\cos\beta} - \frac{T_{\mathrm{S}}}{\Omega_{\mathrm{p}}J_{\mathrm{p}}} = M \tag{3.33}$$

The next step is to take the Laplace of (3.31):

$$\nu(s)s = K + LF_{\mathrm{s}}(s) + M\nu(s) \tag{3.34}$$

Note that the disturbance term has been removed as it has no impact on the actual linearized transfer function. The term K can also be removed as it is merely an offset which can be ignored for control purposes. Therefore, the following transfer function is found:

$$\frac{\nu(s)}{F_{\mathrm{s}}(s)} = \frac{\frac{-L}{M}}{\frac{-1}{M}s + 1} \tag{3.35}$$

This means that the complex nonlinear behavior of the slip dynamics is now converted to a first order system which can be easily controlled.

3.7.2 Slip controller

Based on section 3.7.1, it is known that the slip dynamics can be described as a first order system. Therefore a PI controller should result in acceptable slip behavior. According to section 2.6.2, it is possible to write the proportional term T_{i} and the integral term K_{p} of the PI controller in terms of M and L:

$$T_{\mathrm{i}} = \frac{-1}{M} \tag{3.36}$$

$$K_{\mathrm{p}} = \frac{\alpha T_{\mathrm{i}}}{\frac{L}{M}} = \frac{-\alpha}{L} \tag{3.37}$$

The value α defines again the position of the closed loop pole.

To implement the PI controller, L and M need to be determined. Parameter L is calculated based on (3.32) while parameter M can be determined with (3.33).

The many parameters in those equations define the operating point based on which the linearization is done. As all inputs of (3.32) and (3.33) are constantly varying, the equations need to be solved repeatedly during simulation to feed the PI controller with the optimal K_{p} and T_{i} at all times. However, the computational effort of solving these static relations is negligible.

Another complexity of the determination of L and M is the number of parameters which need to be obtained to solve the equations, see Fig. 3.8 (a). This is of course not an issue in simulation but when tested on a test bench this becomes important. To counter this concern, some simplifications are proposed to reduce the number of variables.

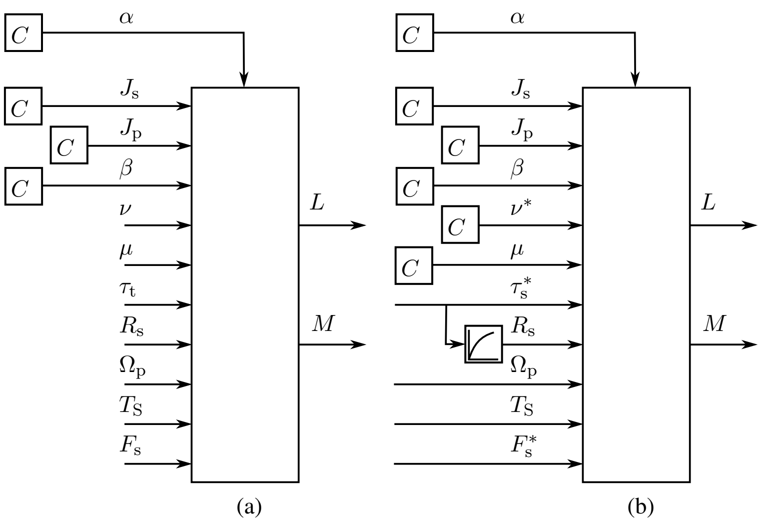

Figure 3.8: (a) Overview on the inputs to calculate L and M. (b) Overview on the strictly necessary inputs to calculate L and M. The value C stands for a constant.

As constant slip is expected due to proper control, the friction coefficient μ will be fairly stable. The first adaptation is thus to consider a fixed friction coefficient μ. Furthermore, on the hypothesis of proper slip control, the slip is presumed equal to the setpoint. Based on the assumption of proper slip control and low values for slip it is also possible to equalize the theoretical and the actual speed ratio (see (3.23)). Combined with an appropriate ratio controller it is possible to obtain τ_t and the running radii $R_{\text{p,s}}$ directly from the speed ratio setpoint. The last simplification is to use the output of the slip controller to estimate the force on the secondary pulley F_{s} instead of measuring the clamping force.

Due to these changes, only 2 measurements remain: speed of the primary pulley Ω_{p} and the torque on the primary pulley T_{S}. Of these variables speed is easily measured, while the torque of the ICE could be estimated based on engine characteristics [71, 72] to avoid an expensive torque sensor.

3.7.3 Results

Varying load at constant speed ratio

Fig. 3.9 shows that the magnitude of the load variation has no significant impact on the settling time of the controller. Only the overshoot increases for increasing load. This also means that the robustness against load variation is good enough, despite the safety factor of 1. Fig. 3.9 also shows that not only the force on the secondary pulley changes due to the load variations but also the force on the primary pulley. The reason for this effect is that the speed ratio of the CVT is defined by the ratio of both forces on the pulleys. As the secondary force needs to be changed to maintain a constant value for the slip, the primary force needs to change as well to maintain the desired, constant, value for the speed ratio.

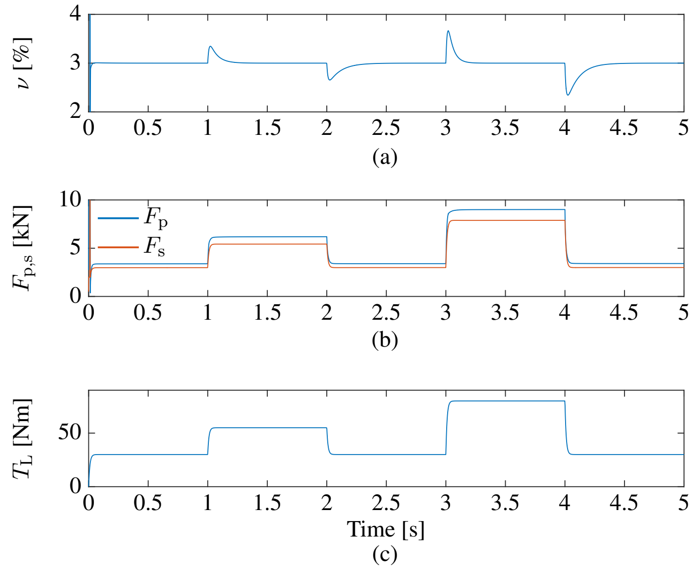

Figure 3.9: Slip ν [%] (a) and clamping forces $F_{\mathrm{p,s}}$ [kN] (b) as function of time for load torque T_{L} [Nm] variations in function of time at constant speed ratio τ_{s} of 1.

Varying speed ratio at constant load

According to (3.29), the speed ratio could also be a disturbance for the slip controller. However, Fig. 3.10 shows that the proposed control architecture has no difficulties with sustaining constant slip values while the speed ratio is following a desired curve. Note that there are 2 peaks in the profile of the secondary clamping force. By increasing the force on the secondary clamping force, the torque T_s developed by that pulley increases. As a result the secondary pulley is accelerated by which the imposed speed ratio τ_s^* value is maintained.

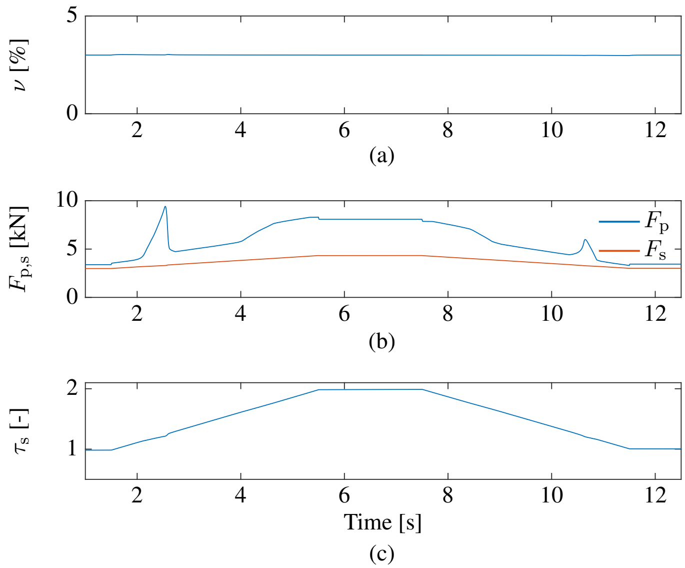

Figure 3.10: Slip ν [%] (a), clamping forces $F_{\rm p,s}$ [kN] (b) and speed ratio $\tau_{\rm s}$ [-] (c) as function of time for a constant load torque $T_{\rm L}$ of 30Nm.

3.8 Control of the speed ratio

As control algorithm, a PI controller is chosen, which has been tuned based on the work of [28]. A differential action is not necessary as the shifting process exhibits a sufficient amount of damping [28]. The implementation of this PI controller with fixed K_p and T_i is rather trivial and is therefore not further discussed.

3.9 Validation of the model

The model of the belt CVT is validated based on the efficiency. The efficiency η is calculated as:

$$\eta = \frac{P_{\rm out}}{P_{\rm in}} = \frac{P_{\rm in} - P_{\rm l} - P_{\rm hyd}}{P_{\rm in}} \tag{3.38}$$

in which $P_{\rm l}$ are the losses in the belt and bearings, $P_{\rm hyd}$ are the losses in the hydraulic actuation system. For $P_{\rm l}$, an empirical model has been set up based on measurement results provided in [69] (see Fig. 1 in [69]). For the losses in the hydraulic actuation system, the efficiency map provided in [79] has been used (see Fig. 4.10 [79]).

Fig. 3.11 presents the comparison of the efficiency obtained via the model described in this thesis and the measured efficiency presented in [89]. The differences between the 2 results remains restricted to 2%. The main reason for these differences, besides model uncertainties, is related to the chosen operating points for the slip throughout the map (not provided in the original paper) which has an impact on both the losses related to traction and the losses related to the belt and hydraulics. Note that the figure shows the efficiency of the belt CVT and a fixed gear combined. That explains the speed ratio range which is rather low. The ratio of the fixed gear τ_{fg} equals 0.19 and is modeled as a constant efficiency of 98%.

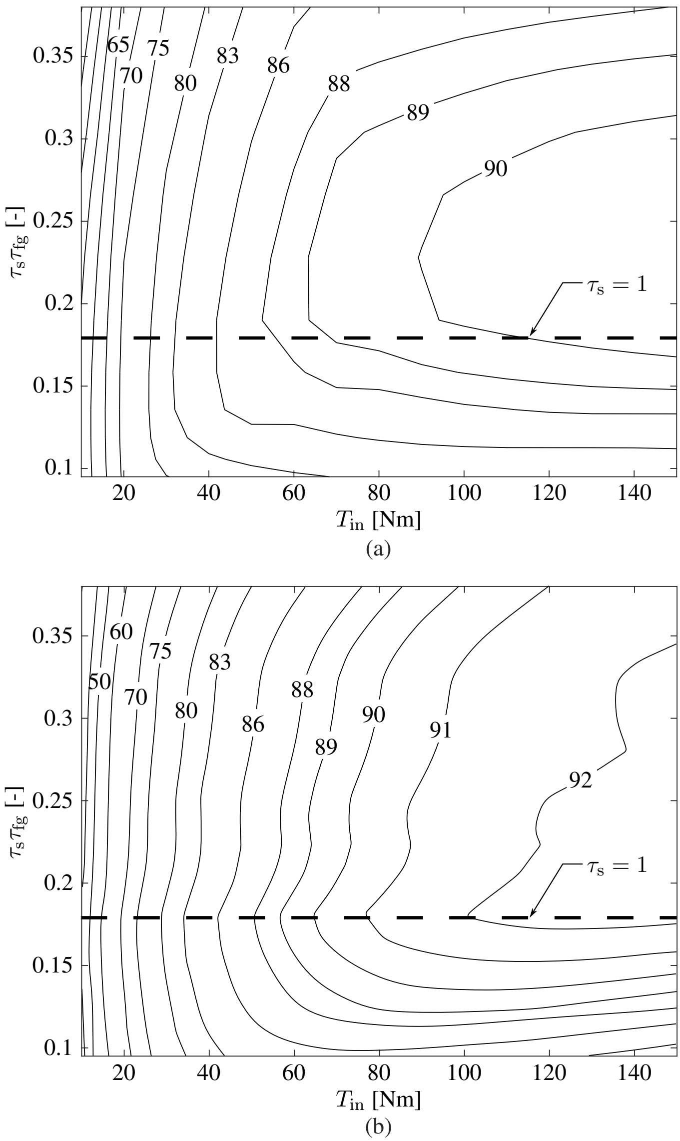

Figure 3.11: Efficiency η [%] as function of input torque T_{in} and speed ratio τ_s. A final gear with a speed ratio τ_{fg} of 0.19 and an efficiency of 98% has been taken into consideration. (a) Efficiency calculated based on (3.38). (b) Efficiency data from [89].

3.10 Conclusion

In this chapter, the belt CVT is introduced. The operating principle has been discussed and it is shown how the clamping force influences the ratio variation characteristic of the belt. The variator model, that inherits the ratio variation characteristics, is validated based on the available literature. Furthermore, a new method to control the slip, similar as the one used for the active slip control of a toroidal CVT, is elaborated. This is important as proper slip control can significantly increase the efficiency of the belt CVT. This efficiency depends on the losses in the contact, losses in belt and bearings and hydraulic losses. Finally, the model is validated in terms of efficiency based on the available literature. The concept of the efficiency map that is used for this comparison (efficiency in terms of speed ratio and load torque) is important as it will be used to compare the belt CVT with other variable transmissions. Moreover, this also shows that the first research goal, as defined in section 1.2, has been realized.

Chapter 4

Permanent Magnet Electrical Variable Transmission

In this chapter, the permanent magnet EVT is introduced. First, the key components and operating principle of the EVT are discussed. Subsequently, the modeling techniques, control of the device and a comparison of the different model structures is presented. Finally, the experimental setup and model validation are discussed. Again, for the comparison of the variable transmissions it is important that the efficiency can be expressed as function of the speed ratio (ratio of the output speed and input speed) and load torque.

4.1 Introduction

In correspondence with the previously discussed CVT models, the EVT model is subjected to the same requirements: parametrized, following the physical causality, capable of analyzing dynamic events and incorporated losses.

The model used in this PhD has been developed by Joachim Druant [90] and matches all requirements. However, the need of FE evaluations imposes limitations on how fast design changes can be analyzed. Therefore, an alternative for these FE calculations based on a Magnetic Equivalent Circuit (MEC) model is being defined [91]. This MEC model is solved faster and still produces acceptable results. Moreover, it is still completely parametrized, which makes it ideal for design purposes. Later on, in chapter 5, an additional and even faster design methodology is discussed.

4.2 Operating principle

In this section the operating principle of the permanent magnet EVT is discussed. As mentioned in the introduction, many types of EVT exist. However, the PM version has a higher power density, which makes them more interesting for HEV applications than concurrent topologies. As automotive is by far the most important application for an EVT, the decision is made to focus on the PM-EVT as described in [40, 41]

4.2.1 Topology

A cross section of the EVT considered in this thesis is shown in Fig. 4.1. The inner rotor and stator each consist of a distributed three-phase winding. The outer rotor is equipped with a single layer of permanent magnets and a DC-field winding which are separated by a flux bridge. The shafts of the inner and outer rotor form the two mechanical ports while the windings of both the inner rotor and stator form the two electrical ports. To provide power to the inner rotor, slip rings are used.

The impact of the flux bridge and the DC-field winding on the general behavior of the EVT is explained via Fig. 4.2. Fig. 4.2 (a) shows the field density of the EVT for all currents set to zero. The only MMF sources come thus from the magnets. Due to the flux bridge, only a small fraction of the permanent magnet flux is linked with the stator. This unique aspect of the considered EVT reduces the stator torque but also reduces the losses in the stator induced by the permanent magnet field. However, this stator flux linkage can be manipulated. If a negative DC-field current is applied, the path of the permanent magnet flux changes (Fig. 4.2 (b)) and thus the stator flux linkage is increased. Notice that this variation in DC-field current has no significant effect on the field in the inner rotor due to the

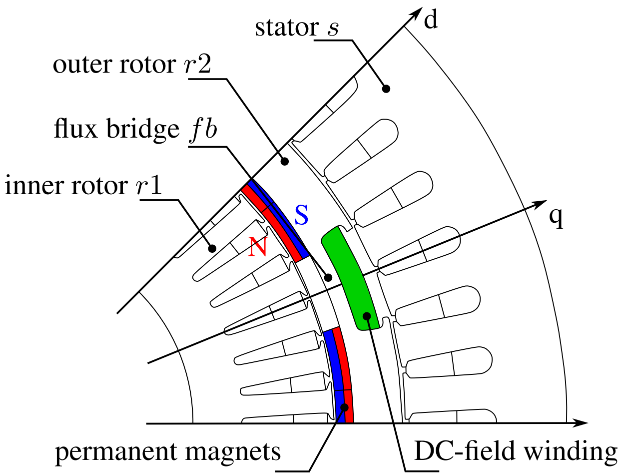

Figure 4.1: Cross section of the considered PM-EVT with hybrid excitation.

low recoil permeability of the magnets μ_{rec}. For a more detailed analysis on the impact of this DC-field winding on both losses and generated torque the reader is referred to [92] and [41] respectively. Some machine parameters are given in Table 4.1 for clarity.

Table 4.1: Machine parameters of the considered EVT

	stator	outer rotor	inner rotor
rated mechanical power [kW]	-	120	75
maximal speed $\Omega_{\text{r1,2,max}}$ [rpm]	-	6000	6000
number of slots [-]	48	-	48
number of pole pairs N_p [-]	4	4	4
outer radius [mm]	175	123.5	102
inner radius [mm]	124.5	103	57
PM thickness [mm]	-	5	-
active axial length [mm]	87	87	87
width flux bridge [mm]	-	5	-

One of the main advantages of the EVT is that there is no mechanical connection between the inner rotor and the outer rotor. Moreover, if applied in a HEV, the EVT can be used to decouple the ICE (connected to the inner rotor) and the wheels (connected to the outer rotor) in terms of speed and torque (see Fig. 4.3). This makes it possible to operate the ICE independently from the wheels. Consequently, the ICE can be operated at its operating point of maximum efficiency at all times. Why the EVT is decoupled in terms of speed is rather trivial: there is no mechanical link between both shafts and as a consequence they can rotate at different

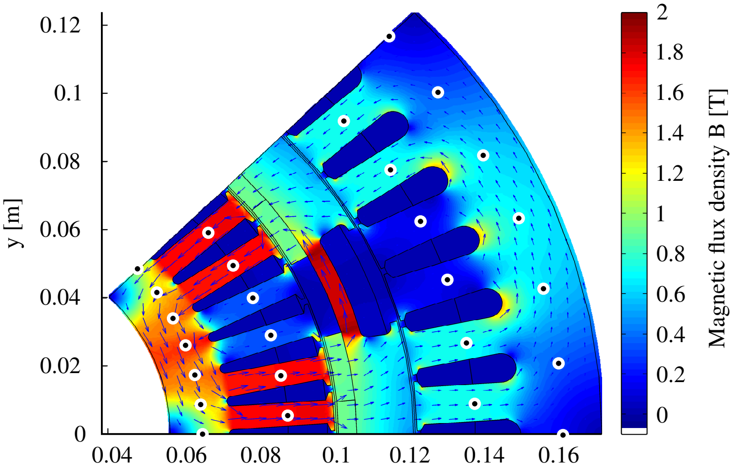

(a)

x [m]

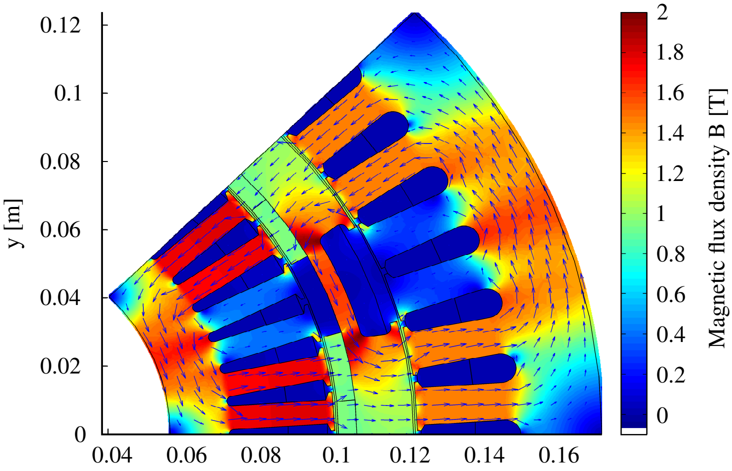

(b)

x [m]

Figure 4.2: Influence of the DC-field current on the stator flux linkage for (a) a DC-field current of 0A and (b) a DC-field current of -10A. All other currents in stator and inner rotor are set to 0A. The markers are used for a validation step presented in section 4.4.2.

speed. To explain why the EVT also decouples input and output in terms of torque, the EVT is first considered without stator. Suppose that the ICE is operating at the following operating point: T_{ICE} and Ω_{ICE}. Then the inner rotor should, in steady state, produce a torque equal to the opposite of the ICE torque in order to maintain the speed:

$$T_{\mathrm{r1}} = -T_{\mathrm{ICE}} \tag{4.1}$$

In order to produce this torque, currents need to be applied to the windings of the inner rotor:

$$T_{\mathrm{r1}} = \frac{3}{2} N_{\mathrm{p}} \left(\Psi_{\mathrm{r1q}} I_{\mathrm{r1d}} - \Psi_{\mathrm{r1d}} I_{\mathrm{r1q}} \right) \tag{4.2}$$

in which flux Ψ and current I are related to the dq reference frame (related to the outer rotor) and N_{p} is the number of pole pairs. Note that the factor $\frac{3}{2}$ is related to Clarke's transformation. Due to action-reaction, the electromagnetic torque on the outer rotor will produce the opposite torque. Therefore the following is true:

$$T_{\mathrm{r2}} = T_{\mathrm{ICE}} \tag{4.3}$$

The torque at the wheels is thus the same as the torque generated by the ICE. To be able to modify the torque at the outer rotor, the stator is added. By applying currents through the stator windings, an electromagnetic torque is added to the outer rotor. Since the sum of the torque values on all components needs to be 0, the torque on the outer rotor T_{r2} can be determined by:

$$T_{\mathrm{r2}} = -T_{\mathrm{s}} - T_{\mathrm{r1}} = -T_{\mathrm{s}} + T_{\mathrm{ICE}} \tag{4.4}$$

in which the stator torque T_{s} is calculated as:

$$T_{\mathrm{s}} = \frac{3}{2} N_{\mathrm{p}} \left(\Psi_{\mathrm{sq}} I_{\mathrm{sd}} - \Psi_{\mathrm{sd}} I_{\mathrm{sq}} \right) \tag{4.5}$$

The fluxes (stator flux in the d-axis Ψ_{sd}, stator flux in the q-axis Ψ_{sq}, inner rotor flux in the d-axis Ψ_{r1d} and inner rotor flux in the q-axis Ψ_{r1q}) in (4.5) and (4.2) depend on 5 independent current setpoints: stator current in the d-axis I_{sd}, stator current in the q-axis I_{sq}, current in the DC-field winding of the outer rotor I_{r2d}, inner rotor current in the d-axis I_{r1d} and inner rotor current in the q-axis I_{r1q}. The relation between flux and current is determined based on FE calculations (see section 4.4). The FE model, which forms the backbone of the model, has been validated on a prototype [41]. More information on the experimental setup is given in section 4.9.

4.2.2 Ideal power flows

Based on the operating principle, it is possible to discuss the ideal power flows (power flows without losses). These power flows (electrical, mechanical and electro-magnetic) are drawn on the overall schematic, in Fig. 4.3. If the example of the HEV is chosen, the mechanical power of both shafts equals:

$$\begin{aligned} P_{\mathrm{m,r1}} &= T_{\mathrm{r1}}\Omega_{\mathrm{r1}} = -T_{\mathrm{ICE}}\Omega_{\mathrm{r1}} \\ P_{\mathrm{m,r2}} &= T_{\mathrm{r2}}\Omega_{\mathrm{r2}} \end{aligned} \tag{4.6}$$

The mechanical power of the outer rotor can be rewritten based on (4.4) as:

$$P_{\mathrm{m,r2}} = \underbrace{-T_{\mathrm{r1}}\Omega_{r2}}_{P_{\mathrm{a,r1}}}\underbrace{-T_{\mathrm{s}}\Omega_{r2}}_{P_{\mathrm{a,s}}} \tag{4.7}$$

$P_{\mathrm{a,r1}}$ and $P_{\mathrm{a,s}}$ are the power flows that cross the airgap between the inner rotor - outer rotor and outer rotor - stator respectively. If the losses are neglected, the sum of both mechanical powers equals the battery power P_{bat}:

$$P_{\mathrm{bat}} = P_{\mathrm{m,r1}} + P_{\mathrm{m,r2}} \tag{4.8}$$

As the battery power flows via both inverters, the following has to be true:

$$P_{\mathrm{bat}} = P_{\mathrm{e,r1}} + P_{\mathrm{e,s}} \tag{4.9}$$

Neglecting losses, the electrical power of the stator $P_{\mathrm{e,s}}$ is equal to the airgap power $P_{\mathrm{a,s}}$ (see Fig. 4.3):

$$P_{\mathrm{e,s}} = -T_{\mathrm{s}}\Omega_{\mathrm{r2}} = \left(T_{\mathrm{r2}} + T_{\mathrm{r1}}\right)\Omega_{\mathrm{r2}} = \left(T_{\mathrm{r2}} - T_{\mathrm{ICE}}\right)\Omega_{\mathrm{r2}} \tag{4.10}$$

The electrical power converted by the stator is thus proportional with the speed of the outer rotor and the difference between inner rotor and outer rotor torque (i.e. stator torque).

The electrical power of the inner rotor equals the sum of the mechanical power $P_{\mathrm{m,r1}}$ and airgap power $P_{\mathrm{s,r1}}$ (see Fig. 4.3):

$$P_{\mathrm{e,r1}} = P_{\mathrm{m,r1}} + P_{\mathrm{a,r1}} = T_{\mathrm{r1}}\Omega_{\mathrm{r1}} - T_{\mathrm{r1}}\Omega_{\mathrm{r2}} = -T_{\mathrm{r1}}\left(\Omega_{\mathrm{r2}} - \Omega_{\mathrm{r1}}\right) \tag{4.11}$$

Equation (4.11) shows thus that the electrical power of the inner rotor depends on the speed difference between both rotors and the inner rotor torque.

Besides the equations which explain the power flows in the EVT, a graphical way of expressing the power flows (see Fig. 4.4) has been presented in [90]. The main idea is to make it easier to qualitatively understand the sign and magnitude of the different power flows within the EVT for all possible mechanical operating points of both rotors. In the case of a HEV, the inner rotor is connected to an

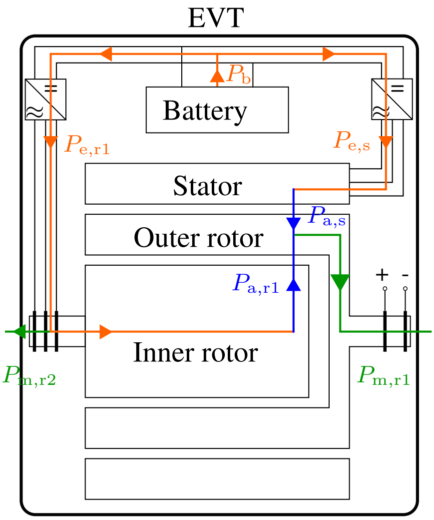

Figure 4.3: Principle scheme of the EVT and sign convention for different power paths within the EVT.

ICE. Therefore, the operating point of the inner rotor will stay in the first quadrant (except during engine braking). The figure clearly shows that if the inner rotor speed is lower than the outer rotor speed, the electrical power of the inner rotor will be positive which is in line with (4.11). If both speed values are the same, the electrical power of the inner rotor is zero (vertical line). If the torque values are the same for both rotors, the electrical power of the stator is zero (horizontal line). Finally, also the line corresponding to zero battery power P_{bat} is shown, given by $T_{\mathrm{r2}} = -\frac{\Omega_{\mathrm{r1}}}{\Omega_{\mathrm{r2}}} T_{\mathrm{r1}}$. When the EVT is operated on this line, it basically acts as a CVT. In the area above this line, the battery power is positive (power flow from battery to the EVT). Below the line, the battery power is negative (power flow from EVT to battery).

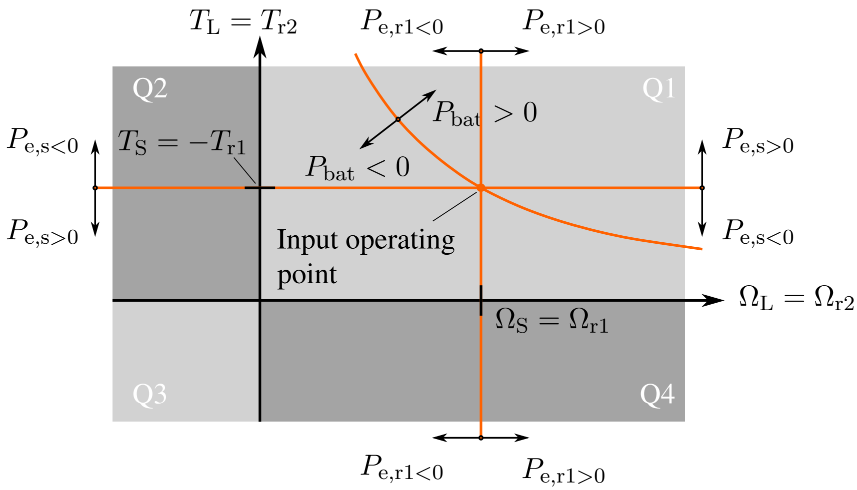

Figure 4.4: Power flow as function of torque and speed at inner and outer rotor [90].

4.3 Model structure

Different models can be used depending on the minimum time step required to model the load correctly or the requested simulation speed. For a fast check of the losses for a given load cycle, the static model can be used (section 4.3.1). If it is important to take the dynamics of the rotors into account, then the hybrid model can be used (section 4.3.2). If the load cycle is highly dynamic, which means in the order of a few ms, then it is required to use the dynamic model (section 4.3.3).

4.3.1 Static model

The model structure of the static model is given in Fig. 4.5. In this model, both mechanic and electrical dynamics are ignored. This means that torque (i.e. current) and speed are obtained instantly. Therefore, this model can be classified as a backward model of the EVT, ideal for use in system level analysis. The inputs are the torque and the speed of both the source and load denoted by T_S, Ω_S, T_L and Ω_L, respectively. As current dynamics are ignored, the inner rotor torque T_{r1} equals the applied torque by the source at the input side, T_S. Moreover, the torque at the outer rotor T_{r2} equals the load torque T_L. The speed imposed by the source Ω_S equals the inner rotor speed Ω_{r1} and the speed of the outer rotor Ω_{r2} equals the setpoint value of the load Ω_L. Assuming that the efficiency can be calculated using this model (shown in chapter 6), it is possible to express that efficiency as function of speed ratio and load torque. Hence, for a given input speed Ω_S, the output speed can be defined based on a desired speed ratio. Moreover, fixing the load torque, will define the torque at the input (if no power is exchanged with the battery).

The first step in solving the model is to check whether or not the desired torque values can be generated by the EVT. Therefore, it is important to know what the maximum torque is, which is discussed in section 4.5. The mechanical losses (bearing losses and slip ring losses) can also be determined as these only depend on the speeds of both rotors (see section 4.6.4). The next step is to calculate the currents based on the chosen operating points OP. More details concerning this step are given in section 4.7, which discusses the optimal control. As the electrical dynamics are ignored, set values for the current and actual currents are the same. Therefore, it is possible to calculate the flux (more information given in section 4.4) and iron losses (see section 4.6.2). Now the flux is known, the voltage can be calculated based on (4.12) which also includes copper losses in the power balance [90]. Note that the electrical speed on the inner and outer rotor is denoted by ω_{r1} and ω_{r2}, respectively.

$$\begin{cases} V_{\mathrm{sq}} = R_{\mathrm{s}} I_{\mathrm{sq}} - \omega_{\mathrm{r2}} \Psi_{\mathrm{sd}} \\ V_{\mathrm{sd}} = R_{\mathrm{s}} I_{\mathrm{sd}} + \omega_{\mathrm{r2}} \Psi_{\mathrm{sq}} \\ V_{\mathrm{r2d}} = R_{\mathrm{r2}} I_{\mathrm{r2d}} \\ V_{\mathrm{r1q}} = R_{\mathrm{r1}} I_{\mathrm{r1q}} - \left(\omega_{\mathrm{r2}} - \omega_{\mathrm{r1}}\right) \Psi_{\mathrm{r1d}} \\ V_{\mathrm{r1d}} = R_{\mathrm{r1}} I_{\mathrm{r1d}} + \left(\omega_{\mathrm{r2}} - \omega_{\mathrm{r1}}\right) \Psi_{\mathrm{r1q}} \end{cases} \tag{4.12}$$

A last set of losses are the inverter losses. These depend on the currents and voltages, which are used but also on the DC-bus voltage and switching frequency (see section 4.6.3). The last step before the battery power can be calculated is to determine the electrical power of both stator and rotor which can be calculated based on (4.13) and (4.14).

$$P_{\mathrm{e,s}} = \frac{3}{2} \left(V_{\mathrm{sd}} I_{\mathrm{sd}} + V_{\mathrm{sq}} I_{\mathrm{sq}} \right) \tag{4.13}$$

$$P_{\mathrm{e,r1}} = \frac{3}{2} \left(V_{\mathrm{r1d}} I_{\mathrm{r1d}} + V_{\mathrm{r1q}} I_{\mathrm{r1q}} \right) \tag{4.14}$$

The battery power itself is thereafter calculated as follows:

$$P_{\mathrm{bat}} = P_{\mathrm{e,s}} + P_{\mathrm{e,r1}} + P_{\mathrm{m,l}} + P_{\mathrm{fe}} + P_{\mathrm{inv}} \tag{4.15}$$

4.3.2 Hybrid model

As mentioned in the introduction of this section, the difference between the static and hybrid model is that mechanical dynamics are taken into account (see Fig.

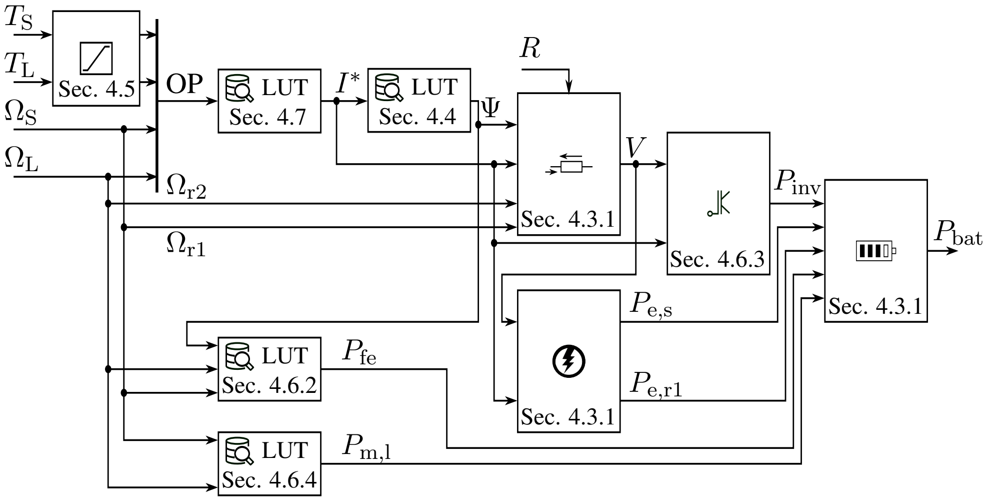

Figure 4.5: Model structure of the EVT (static version).

4.6). This means that the speed of the rotors varies as function of the applied and generated torque:

$$\begin{cases} J_{r1}\frac{d\Omega_{r1}}{dt} & = T_S + T^*_{r1} \\ J_{r2}\frac{d\Omega_{r2}}{dt} & = T^*_{r2} + T_L \end{cases} \tag{4.16}$$

in which J_{r1} and J_{r2} are the inertia of the inner and outer rotor, respectively. Torque applied by a source at the inner rotor, for example the ICE, is denoted by T_S while the torque, which is applied to the outer rotor, is depicted as T_L. T^*_{r1} and T^*_{r2} are the setpoint values for the electromagnetic torque generated by the inner and outer rotor respectively. These torque values are the output of the speed controllers, which maintain the speed at the desired value.

4.3.3 Dynamic model

The dynamic model has a similar layout as the previous models (see Fig. 4.7). However, for the dynamic model, also the current dynamics are taken into account. This means that the currents will have to be controlled with a PI controller. To derive the relation between voltage and current, (4.12) is rewritten in matrix notation:

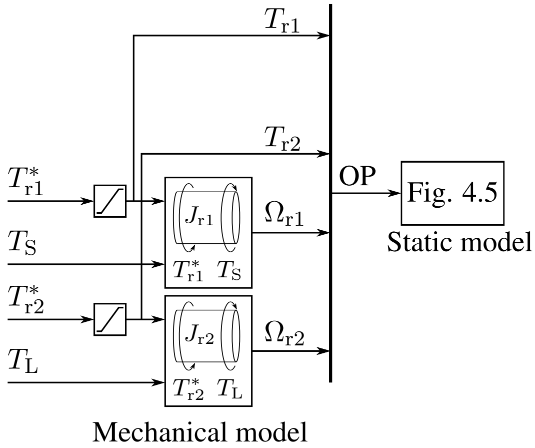

Figure 4.6: Model structure of the EVT (hybrid version).

$$\begin{bmatrix} V_{sq} \\ V_{sd} \\ V_{r2d} \\ V_{r1q} \\ V_{r1d} \end{bmatrix} = \underbrace{\begin{bmatrix} R_s & 0 & 0 & 0 & 0 \\ 0 & R_s & 0 & 0 & 0 \\ 0 & 0 & R_{r2} & 0 & 0 \\ 0 & 0 & 0 & R_{r1} & 0 \\ 0 & 0 & 0 & 0 & R_{r1} \end{bmatrix}}_{\mathbf{R}} \begin{bmatrix} I_{sq} \\ I_{sd} \\ I_{r2d} \\ I_{r1q} \\ I_{r1d} \end{bmatrix} + \frac{d}{dt} \begin{bmatrix} \Psi_{sq} \\ \Psi_{sd} \\ \Psi_{r2d} \\ \Psi_{r1q} \\ \Psi_{r1d} \end{bmatrix} + \begin{bmatrix} -\omega_{r2}\Psi_{sd} \\ \omega_{r2}\Psi_{sq} \\ 0 \\ -\left(\omega_{r2} - \omega_{r1}\right)\Psi_{r1d} \\ \left(\omega_{r2} - \omega_{r1}\right)\Psi_{r1q} \end{bmatrix} \tag{4.17}$$

The first term on the right hand side is the resistance matrix **R**. The elements of this diagonal matrix can be found by measuring the winding resistances, or by calculating the winding resistance using electrical resistance models. The derivative of the flux is not known beforehand but using the chain rule, it can be rewritten as:

$$\frac{d}{dt} \begin{bmatrix} \Psi_{sq} \\ \Psi_{sd} \\ \Psi_{r2d} \\ \Psi_{r1q} \\ \Psi_{r1d} \end{bmatrix} = \underbrace{\begin{bmatrix} \frac{\partial \Psi_{sq}}{\partial I_{sq}} & \frac{\partial \Psi_{sq}}{\partial I_{sd}} & \frac{\partial \Psi_{sq}}{\partial I_{r2d}} & \frac{\partial \Psi_{sq}}{\partial I_{r1q}} & \frac{\partial \Psi_{sq}}{\partial I_{r1d}} \\ \frac{\partial \Psi_{sd}}{\partial I_{sq}} & \frac{\partial \Psi_{sd}}{\partial I_{sd}} & \frac{\partial \Psi_{sd}}{\partial I_{r2d}} & \frac{\partial \Psi_{sd}}{\partial I_{r1q}} & \frac{\partial \Psi_{sd}}{\partial I_{r1d}} \\ \frac{\partial \Psi_{r2d}}{\partial I_{sq}} & \frac{\partial \Psi_{r2d}}{\partial I_{sd}} & \frac{\partial \Psi_{r2d}}{\partial I_{r2d}} & \frac{\partial \Psi_{r2d}}{\partial I_{r1q}} & \frac{\partial \Psi_{r2d}}{\partial I_{r1d}} \\ \frac{\partial \Psi_{r1q}}{\partial I_{sq}} & \frac{\partial \Psi_{r1q}}{\partial I_{sd}} & \frac{\partial \Psi_{r1q}}{\partial I_{r2d}} & \frac{\partial \Psi_{r1q}}{\partial I_{r1q}} & \frac{\partial \Psi_{r1q}}{\partial I_{r1d}} \\ \frac{\partial \Psi_{r1d}}{\partial I_{sq}} & \frac{\partial \Psi_{r1d}}{\partial I_{sd}} & \frac{\partial \Psi_{r1d}}{\partial I_{r2d}} & \frac{\partial \Psi_{r1d}}{\partial I_{r1q}} & \frac{\partial \Psi_{r1d}}{\partial I_{r1d}} \end{bmatrix}}_{\boldsymbol{J}\left(\boldsymbol{\Psi}\right)} \frac{d}{dt} \begin{bmatrix} I_{sq} \\ I_{sd} \\ I_{r2d} \\ I_{r1q} \\ I_{r1d} \end{bmatrix} \tag{4.18}$$

In the latter equation, $\boldsymbol{J}\left(\boldsymbol{\Psi}\right)$ represents the Jacobi matrix of the function $\boldsymbol{\Psi}$ defined as:

$$\begin{bmatrix} \Psi_{\mathrm{sq}} \\ \Psi_{\mathrm{sd}} \\ \Psi_{\mathrm{r2d}} \\ \Psi_{\mathrm{r1q}} \\ \Psi_{\mathrm{r1d}} \end{bmatrix} = \begin{bmatrix} \Psi_{\mathrm{sq}}\left(I_{\mathrm{sq}}, I_{\mathrm{sd}}, I_{\mathrm{r2d}}, I_{\mathrm{r1q}}, I_{\mathrm{r1d}}\right) \\ \Psi_{\mathrm{sd}}\left(I_{\mathrm{sq}}, I_{\mathrm{sd}}, I_{\mathrm{r2d}}, I_{\mathrm{r1q}}, I_{\mathrm{r1d}}\right) \\ \Psi_{\mathrm{r2d}}\left(I_{\mathrm{sq}}, I_{\mathrm{sd}}, I_{\mathrm{r2d}}, I_{\mathrm{r1q}}, I_{\mathrm{r1d}}\right) \\ \Psi_{\mathrm{r1q}}\left(I_{\mathrm{sq}}, I_{\mathrm{sd}}, I_{\mathrm{r2d}}, I_{\mathrm{r1q}}, I_{\mathrm{r1d}}\right) \\ \Psi_{\mathrm{r1d}}\left(I_{\mathrm{sq}}, I_{\mathrm{sd}}, I_{\mathrm{r2d}}, I_{\mathrm{r1q}}, I_{\mathrm{r1d}}\right) \end{bmatrix} = \boldsymbol{\Psi}\left(I_{\mathrm{sq}}, I_{\mathrm{sd}}, I_{\mathrm{r2d}}, I_{\mathrm{r1q}}, I_{\mathrm{r1d}}\right) \tag{4.19}$$

with $\boldsymbol{\Psi} : \mathbb{R}^5 \to \mathbb{R}^5$ a non-linear vector function of the currents. Using this notation, the governing dynamical equations can also be written as:

$$\boldsymbol{J}\frac{d}{dt}\begin{bmatrix} I_{\mathrm{sq}} \\ I_{\mathrm{sd}} \\ I_{\mathrm{r2d}} \\ I_{\mathrm{r1q}} \\ I_{\mathrm{r1d}} \end{bmatrix} = \begin{bmatrix} V_{\mathrm{sq}} \\ V_{\mathrm{sd}} \\ V_{\mathrm{r2d}} \\ V_{\mathrm{r1q}} \\ V_{\mathrm{r1d}} \end{bmatrix} - \boldsymbol{R}\begin{bmatrix} I_{\mathrm{sq}} \\ I_{\mathrm{sd}} \\ I_{\mathrm{r2d}} \\ I_{\mathrm{r1q}} \\ I_{\mathrm{r1d}} \end{bmatrix} - \begin{bmatrix} -\omega_{\mathrm{r2}}\Psi_{\mathrm{sd}} \\ \omega_{\mathrm{r2}}\Psi_{\mathrm{sq}} \\ 0 \\ -\left(\omega_{\mathrm{r2}} - \omega_{\mathrm{r1}}\right)\Psi_{\mathrm{r1d}} \\ \left(\omega_{\mathrm{r2}} - \omega_{\mathrm{r1}}\right)\Psi_{\mathrm{r1q}} \end{bmatrix} \tag{4.20}$$

Solving (4.20) thus provides the dynamic relation between applied voltage and current through the windings of the EVT. All other steps to solve the model are identical to the ones taken to solve the static and hybrid model.

Due to the fact that dynamic model is organized according to the physical causality (i.e. integral causality), it is a forward model.

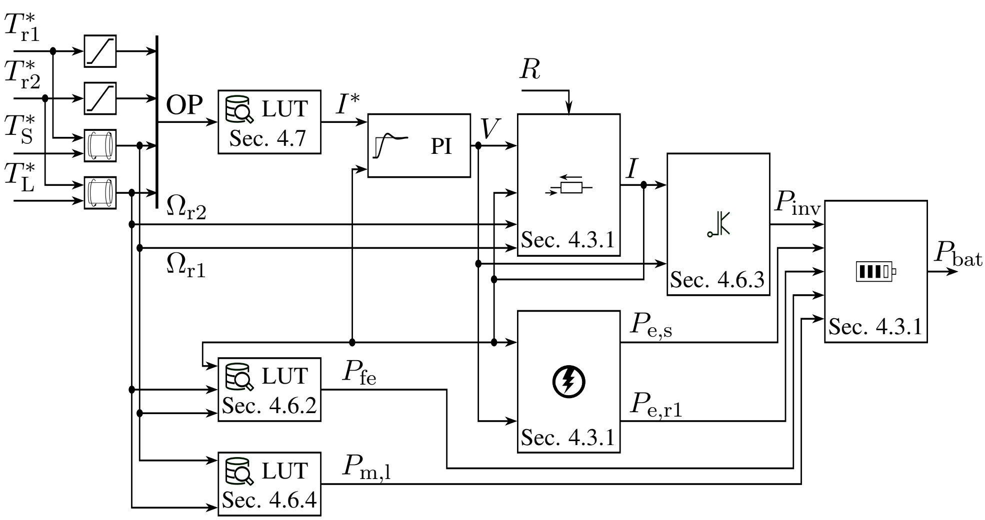

Figure 4.7: Model structure of the EVT (dynamic version).

4.4 Current to flux relation

4.4.1 Based on a Finite Element model

The relation between current and flux needs to be known to solve the model of the EVT. Therefore, a Finite Element (FE) model has been developed. To validate the model, measurements have been performed for varying currents. Fig. 4.8 shows that the estimated flux based on the FE model matches closely with the measured result. More information about the current to flux relations can be found in chapter 3 of [90].

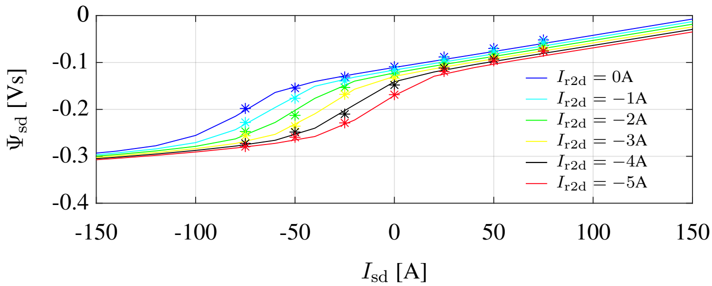

(a)

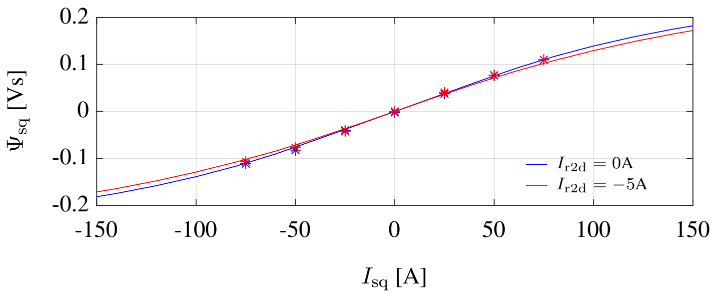

(b)

Figure 4.8: (a) Stator flux in the d-axis Ψ_{sd} as function of the stator current in the d-axis I_{sd} for varying DC-field current I_{r2d}. The d-axis flux remains negative due to the chosen orientation of the d-axis. (b) Stator flux in the q-axis Ψ_{sq} as function of the stator current in the q-axis I_{sq} for varying DC-field current I_{r2d}. All other current setpoints are 0. Full lines are obtained via FE calculations while the stars are based on measurements.

Although FE models are accurate as shown in Fig. 4.8, the side effect is that the computational effort is high. As a consequence, FE models cannot be used directly in the model. To solve this, the relation between current and flux is calculated a priori and the data is stored in Look-Up Tables (LUT). According to [90], the flux values of stator and inner rotor in both q-axis and d-axis depend on a set of 5 currents. This means that the LUTs are constructed in 5 dimensions.

4.4.2 Based on a Magnetic Equivalent Circuit model

Magnetic Equivalent Circuits (MEC) of various electrical machines such as induction machines [93], DC machines [94] or permanent magnet synchronous machines [95] are available in literature. The main advantage of this modeling technique, compared to FE calculations, is the reduced computational effort. This makes the use of MEC models highly interesting for design purposes [96–99].

There are 2 ways to define the MEC of a system or machine: based on nodal equations or mesh equations as used in this thesis. A detailed comparison between both methods is given in [100]. Once the MEC is defined, it is solved using, for example, Newton-Raphson. In this thesis a toolbox is used to solve the MEC [101].

In Fig. 4.9, a fragment of the MEC model of the EVT is shown. It is composed of source terms (blue circles), non-linear reluctances (red bars) for the yoke and teeth, linear reluctances (green bars) representing leakage and linear reluctances (orange bars) for the airgaps, which depend on the relative position of the inner rotor - outer rotor and outer rotor - stator. In the following paragraphs, all these reluctances, which characterize the behavior of the inner rotor, outer rotor, stator and both airgaps are discussed.

Inner rotor $r1$

The inner rotor is represented by a non-linear reluctance for the yoke R_{y} and the teeth R_{t}. These reluctances are calculated based on (4.21) and take saturation of the material into account.

$$R_{\mathrm{y,t}}\left(B\right) = \frac{l_{\mathrm{y,t}}}{\mu_0 \mu_{\mathrm{r}}(B) A_{\mathrm{y,t}}} \tag{4.21}$$

in which μ_0 is the permeability of air, $l_{\mathrm{y,t}}$ is the length of the yoke or teeth respectively while $A_{\mathrm{y,t}}$ is the cross-sectional surface of the yoke or teeth. The relation between the relative permeability μ_{r} and the flux density B has been defined based on [102] and is validated as shown in Fig. 4.10.

The windings of the inner rotor are added through source terms F_{r1} which depend on the currents that flow through the three-phase distributed winding $I_{\mathrm{r1_{a,b,c}}}$:

$$F_{\mathrm{r1}} = \frac{I_{\mathrm{r1_{a,b,c}}} W_{\mathrm{d}}}{a} \tag{4.22}$$

with W_{d} the winding distribution matrix and a the number of parallel branches.

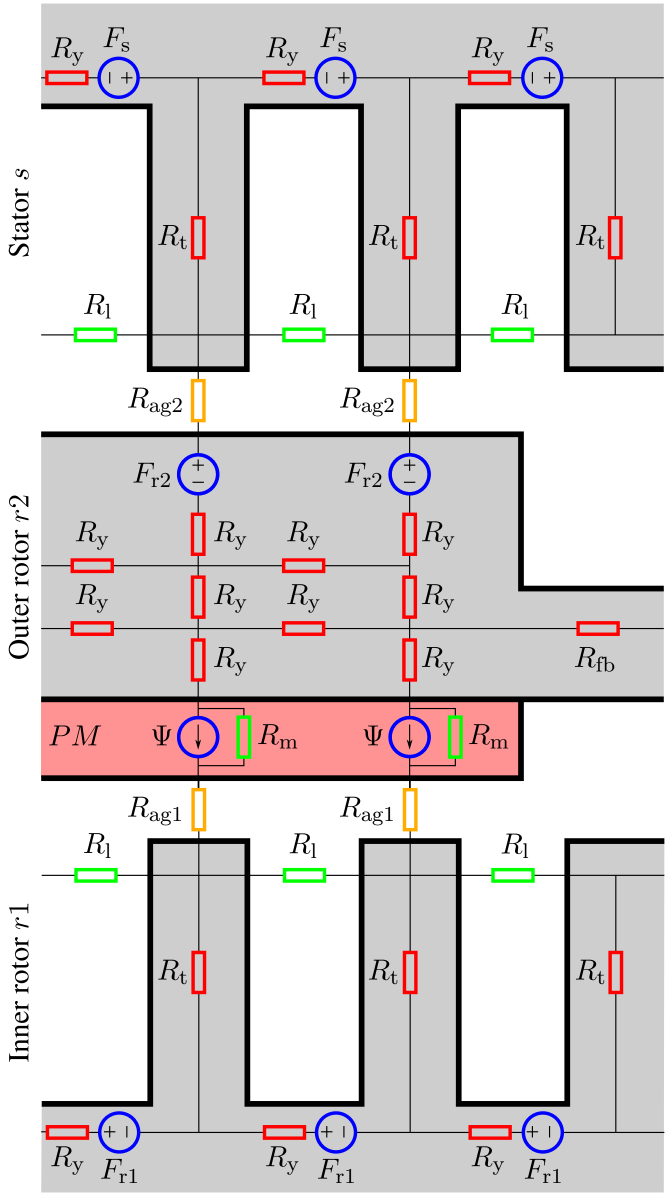

Figure 4.9: Structure of the proposed MEC model.

To model the leakage from one tooth to the other, a closer look is taken to these teeth (see Fig. 4.11). The figure shows that there are 2 different paths defined. The first path and the corresponding permeance P_1 include the part below the tooth tip while the second path P_2 includes only the tooth tip.

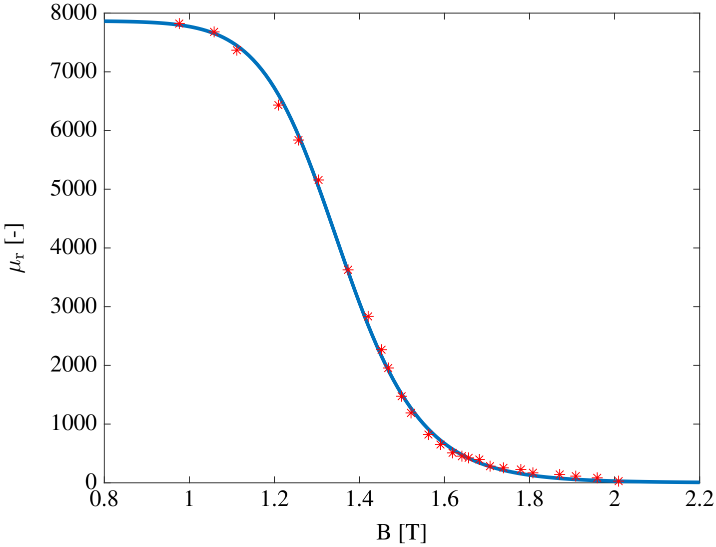

Figure 4.10: Relative permeability μ_r of the core material M400-50A. Full line represents the fitted model, the red stars are measurements.

The permeance of path 1, P_1, can be calculated as follows:

$$P_1 = \mu_0 L \int_{r_{oy}}^{r_0 - T_{th}} \frac{dx}{\theta_{bs} x} \tag{4.23}$$

Therefore, the tooth to tooth leakage permeance of path 1 can be described as:

$$P_1 = \frac{\mu_0 L}{\theta_{bs}} ln\left(\frac{r_0 - T_{th}}{r_{oy}}\right) \tag{4.24}$$

with L the axial length of the machine, r_o the outer radius of the inner rotor, T_{th} the tooth tip height, r_{oy} the outer radius of the inner rotor yoke and θ_{bs} the angle span at the bottom of the slot opening. An analog derivation leads to the expression for the permeance of path 2:

$$P_2 = \frac{\mu_0 L}{\theta_{ts}} ln\left(\frac{r_o}{r_o - T_{th}}\right) \tag{4.25}$$

with θ_{ts} the angle span at the top of the slot opening. As these permeances are in parallel, the total tooth to tooth leakage reluctance R_l is:

$$R_l = \frac{1}{P_1 + P_2} \tag{4.26}$$

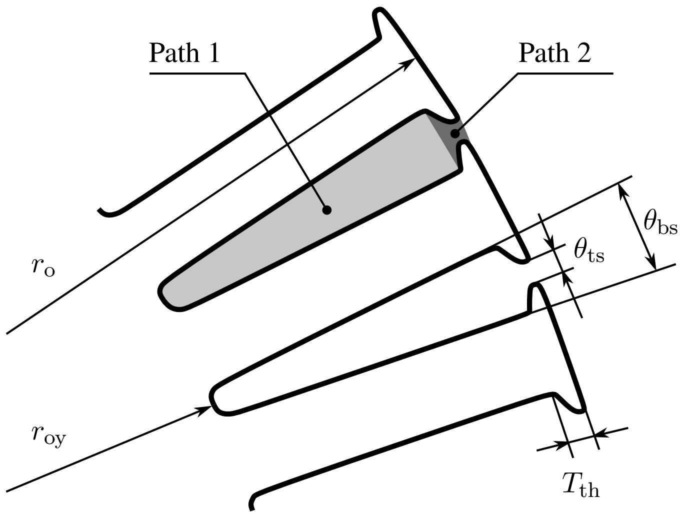

Figure 4.11: Different paths for tooth to tooth leakage.

Air gap between inner rotor and outer rotor $ag1$

The airgap is represented by multiple airgap permeances which are denoted by $P_{\text{ag1,1}}$, $P_{\text{ag1,2}}$, $P_{\text{ag1,3}}$ (Fig. 4.12). The reluctance value for the airgap R_{ag1} is then calculated as follows:

$$R_{\text{ag1}} = \frac{1}{Sf\left(P_{\text{ag1,1}} + P_{\text{ag1,2}} + P_{\text{ag1,3}}\right)} \tag{4.27}$$

with Sf the stacking factor. Notice that these permeances are not always defined and depend on the position of the inner rotor teeth compared to the outer rotor permanent magnets. In order to incorporate this in the model, three cases are examined (case (a)-(c)) which consider a different type of overlap between a tooth and a permanent magnet.

Case (a) is characterized by overlap with region 1 and 2. In case (b) the whole tooth is below the permanent magnet and in case (c) there is overlap with region 2 and 3. In the following paragraphs, case (a) and (b) will be discussed. Case (c) is not addressed due to the similarity with case (a).

In case (a) there is only partial overlap between the tooth tip and the considered permanent magnet. The angle w of this overlap can be characterized as:

$$w = \theta_2 - \theta_1 \tag{4.28}$$

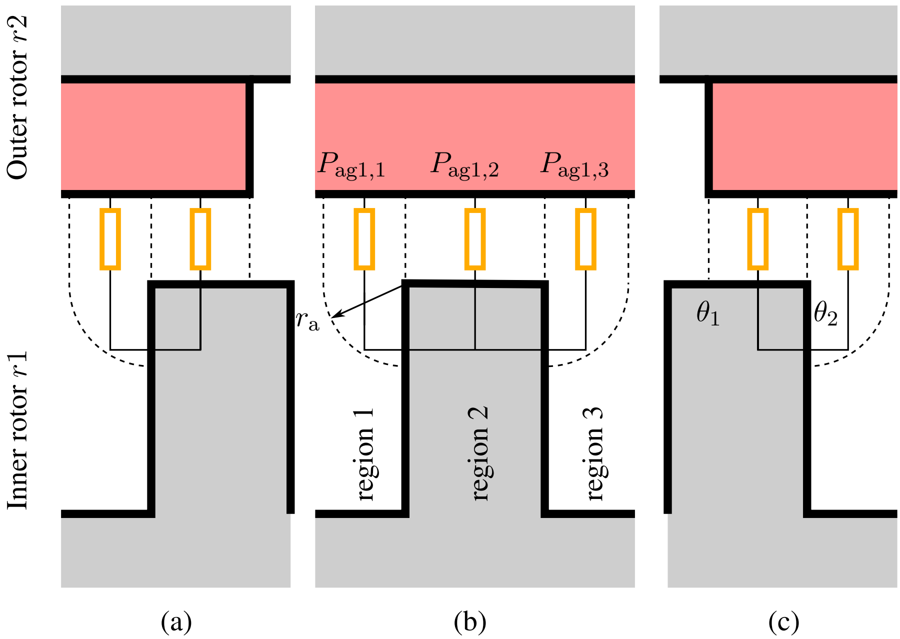

Figure 4.12: Reluctances for airgap between inner rotor and outer rotor.

with θ_1 the angular position which indicates the start of overlap and θ_2 the end of overlap. The permeance of the direct path can thus be calculated as:

$$P_{\mathrm{ag1,2}} = \frac{\mu_0 A}{l_{\mathrm{ag1}}} = \frac{\mu_0 w r_{\mathrm{ag1}} L}{l_{\mathrm{ag1}}} \tag{4.29}$$

with r_{ag1} the average airgap radius and l_{ag1} the width of the airgap. Besides the direct path there is also a path to accommodate fringing fluxes ($P_{\mathrm{ag1,1}}$ and $P_{\mathrm{ag1,3}}$). The length of this path is equal to:

$$l = l_{\mathrm{ag1}} + \frac{\pi}{2} r_\mathrm{a} \tag{4.30}$$

Which means that the flux density B can be written as:

$$B(r_\mathrm{a}) = \mu_0 \frac{F}{l_{\mathrm{ag1}} + \frac{\pi}{2} r_\mathrm{a}} \tag{4.31}$$

with F the source term. Based on the flux density, the flux Ψ can be determined by integration:

$$\Psi = \int_0^{r_{\mathrm{sc,1}}} B(r_\mathrm{a}) L dr_\mathrm{a} \tag{4.32}$$

$$r_{\mathrm{sc},1} = (\theta_2 - \theta_1)\, r_{\mathrm{ag1}} \tag{4.33}$$

Equation (4.32) now resolves in:

$$\Psi = \frac{2\mu_0 F L}{\pi} ln \left(\frac{2 l_{\mathrm{ag1}} + \pi r_{\mathrm{sc},1}}{2 l_{\mathrm{ag1}}} \right) \tag{4.34}$$

and thus the permeance equals

$$P_{\mathrm{ag1},1} = \frac{2\mu_0 L}{\pi} ln \left(1 + \frac{\pi r_{\mathrm{sc},1}}{2 l_{\mathrm{ag1}}} \right) \tag{4.35}$$

The permeance for the second fringing flux path $P_{\mathrm{ag1},3}$ is due to symmetry equal to $P_{\mathrm{ag1},1}$.

If case (b) in Fig. 4.12 is valid, there is overlap in all regions. As the permeance of the direct path will then be significantly bigger than the permeances for the fringing paths, the reluctance for the airgap can be simplified to:

$$R_{\mathrm{ag1}} = \frac{1}{S f P_{\mathrm{ag1},2}} \tag{4.36}$$

As mentioned earlier, case (c) is not addressed due to the similarity with case (a).

Outer rotor $r2$

The outer rotor is represented by non-linear reluctances for the yoke and flux bridge and source terms are added to take the effect of the permanent magnets and the DC winding into account. The determination of the reluctances in the outer rotor is analogous to those in the inner rotor which means that (4.21) remains valid. This can also be applied to the reluctance of the permanent magnets R_{m}:

$$R_{\mathrm{m}} = \frac{L_{\mathrm{m}}}{\mu_{\mathrm{rec}} A_{\mathrm{m}}} \tag{4.37}$$

with μ_{rec} the recoil permeability of the magnets and A_{m} the surface of the magnets. The source term can be expressed as:

$$\Psi = A_{\mathrm{m}} B_{\mathrm{r}} \tag{4.38}$$

with B_{r} the remanent flux density of the magnets. Finally, the source term linked to the DC winding F_{r2} is calculated as follows:

$$F_{\mathrm{r2}} = \pm I_{\mathrm{r2d}} N \tag{4.39}$$

with I_{r2d} the DC-field current and N the number of turns in the winding per pole and of which the sign depends on the orientation of the nearby magnet.

Air gap between outer rotor and stator $ag2$

The airgap between outer rotor and stator shows a lot of analogy with the airgap between inner rotor and outer rotor. However, a new path with radius r_{b} needs to be introduced to accommodate an additional fringing flux path (see Fig. 4.13). This path does not exist in $ag1$ as the flux does not leave permanent magnets in the normal direction. In case of $ag2$, there are no permanent magnets and thus fringing via path b is possible.

Equations (4.40), (4.41) and (4.42) respectively yield the permeances for the direct path and the 2 fringing flux paths if case (a) is considered.

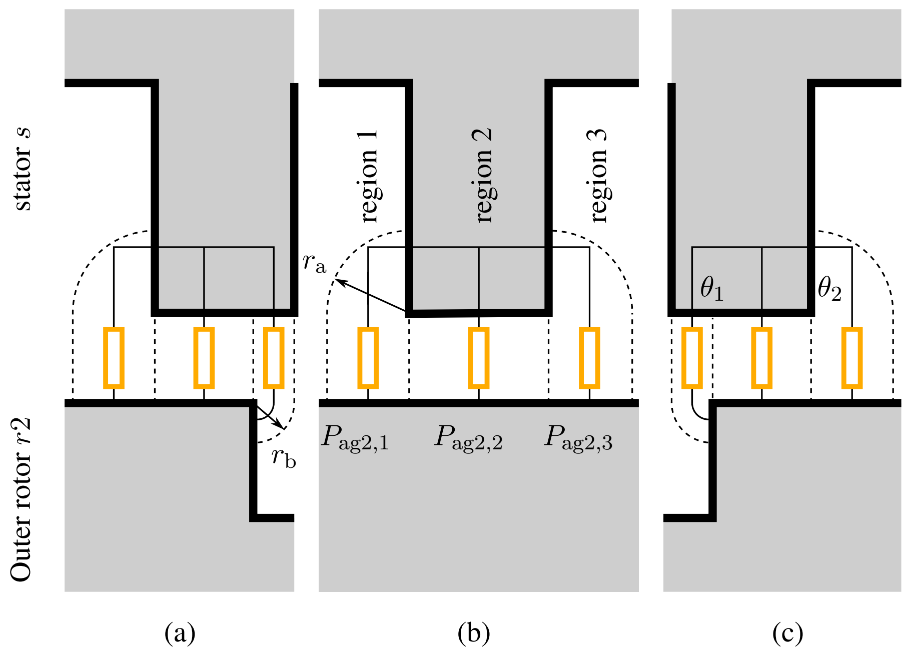

Figure 4.13: Reluctances for airgap between outer rotor and stator.

$$P_{\mathrm{ag2,2}} = \frac{\mu_0 A}{l_{\mathrm{ag2}}} = \frac{\mu_0 w r_{\mathrm{ag2}} L}{l_{\mathrm{ag2}}} \tag{4.40}$$

$$P_{\mathrm{ag2,1}} = \frac{2\mu_0 L}{\pi} ln\left(1 + \frac{\pi r_{\mathrm{sc,2}}}{2 l_{\mathrm{ag2}}}\right) \tag{4.41}$$

$$P_{\mathrm{ag2,3}} = \frac{2\mu_0 L}{\pi} ln\left(1 + \frac{\pi\left(r_{\mathrm{o}} - r_{\mathrm{fbo}}\right)}{l_{\mathrm{ag2}}}\right) \tag{4.42}$$

with r_{o} the outer radius of the outer rotor and r_{fbo} the outer flux bridge radius. The resulting reluctance is again calculated as follows:

$$R_{\mathrm{ag2}} = \frac{1}{Sf\left(P_{\mathrm{ag2,1}} + P_{\mathrm{ag2,2}} + P_{\mathrm{ag2,3}}\right)} \tag{4.43}$$

which simplifies to (4.44) if case (b) is considered.

$$R_{\mathrm{ag2}} = \frac{1}{Sf P_{\mathrm{ag2,2}}} \tag{4.44}$$

Stator s

As for the inner rotor, the stator is also represented by a non-linear reluctance for the yoke R_{y} and the teeth R_{t} which are also calculated based on (4.21). The windings are again added through a source term F_s that is calculated according to (4.22). Only the winding distribution matrix is different as there is a small difference in the number of windings per slot. Finally, the leakage is again incorporated by 2 paths. This leads to the following expressions for the permeances of both paths:

$$P_1 = \frac{\mu_0 L}{\theta_{\mathrm{bs}}} ln\left(\frac{r_{\mathrm{iy}}}{r_{\mathrm{iy}} - T_{\mathrm{l}} + T_{\mathrm{th}}}\right) \tag{4.45}$$

with r_{iy} the inner radius of the stator yoke, T_{th} the stator tooth tip height, T_{l} the stator tooth length and θ_{bs} the angle span of one slot at the bottom.

$$P_2 = \frac{\mu_0 L}{\theta_{\mathrm{ts}}} ln\left(\frac{r_{\mathrm{iy}} - T_{\mathrm{l}} + T_{\mathrm{th}}}{r_{\mathrm{iy}} - T_{\mathrm{l}}}\right) \tag{4.46}$$

with θ_{ts} the angle span at the top of the slot opening. As these permeances are in parallel, the total tooth to tooth leakage reluctance can again be calculated based on (4.26).

Results and validation

In order to validate the MEC model, it will be compared with FE calculations which have been validated on a prototype [41]. Additionally to the results in terms of, for example, flux density, it is also useful to compare the computation time for one evaluation of the FE and MEC model. A single evaluation of the FE model takes on average 2s, while the MEC is solved in only 0.2s (single processor, just to indicate the speed difference). This step thus yields the fluxes for a unique set of 5 currents. However, if the performance of the EVT should be analyzed this will be done for a range of currents and due to the dependency of flux on 5 current components, the computation time and the potential reduction by using the MEC becomes substantial. Therefore it is evident that this considerable reduction in computational effort offers a lot of opportunities in terms of design optimization.

Fig. 4.2 (a) shows the permanent magnet field as all currents are set to zero and the only sources of MMF come from the magnets. To investigate if the MEC can predict this behavior, the flux densities of the indicated points (black dots in Fig. 4.2) in stator and inner rotor yoke and teeth are calculated by a FE model and compared with the results of the MEC.

Fig. 4.14 clearly shows that the MEC model is able to estimate the flux densities almost as good as the FE calculations. Note that the angular position in Fig. 4.14 varies from 0 to $\frac{\pi}{2}$rad (1 pole pair) while Fig. 4.2 only shows results until $\frac{\pi}{4}$rad.

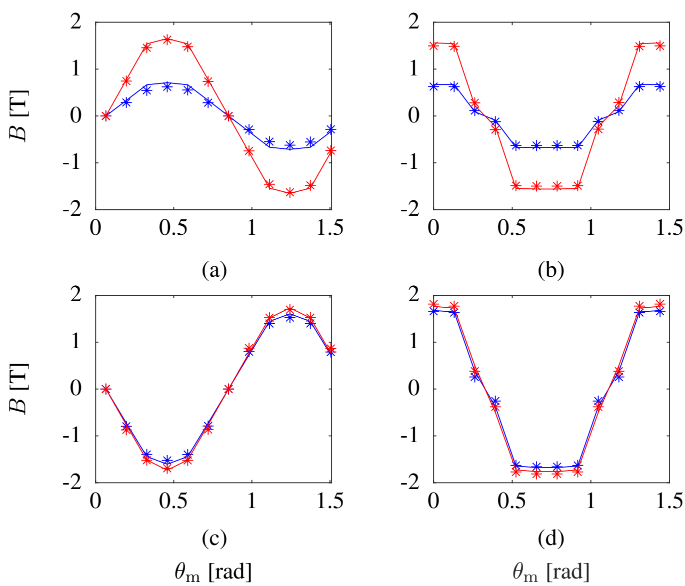

Figure 4.14: Flux density as function of mechanical position for (a) the stator yoke, (b) the stator teeth, (c) the inner rotor yoke and (d) the inner rotor teeth. The continuous lines are based on MEC data while the stars are based on FE calculations. The blue signals represents a DC-field current of 0A while the red signals are valid for a DC-field current of -10A. All other currents in stator and inner rotor are set to 0A.

Besides the flux density, the flux itself is also to be validated. This is done for the stator flux in the direction of the d- and q-axis for varying current. Fig. 5.1 shows that the MEC and FE calculations result in similar values for the flux.

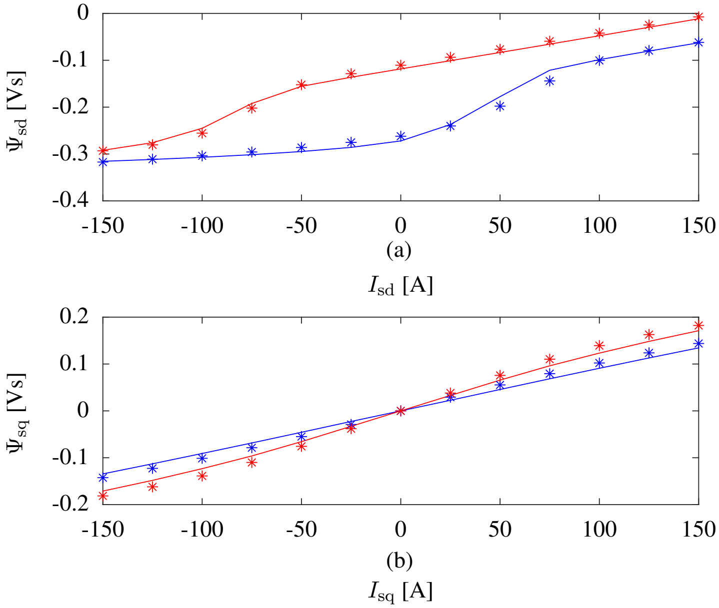

Figure 4.15: Flux as function of stator current for (a) the stator in the d-axis and (b) the stator in the q-axis. The continuous lines are based on MEC data while the stars are based on FE calculations. The blue signals represents a DC-field current of 0A while the red signals are valid for a DC-field current of -10A. All other currents in stator and inner rotor are set to 0A.

In this final validation step, the stator torque T_s calculated based on the MEC is compared with FE calculations. This torque is calculated based on (4.5). Fig. 4.16 shows that the difference between the MEC and FE calculations remains restricted to 7%. Extensive calculations throughout the complete operating range showed that the discrepancy between torque calculated based on MEC or FE rarely exceeded 10% (the higher the torque, the bigger the difference between FE and MEC results). Besides the accuracy which is shown on Fig. 4.16, the impact of the DC-field winding is clearly visible: low DC-field currents result in low stator flux linkage and thus a lower stator torque.

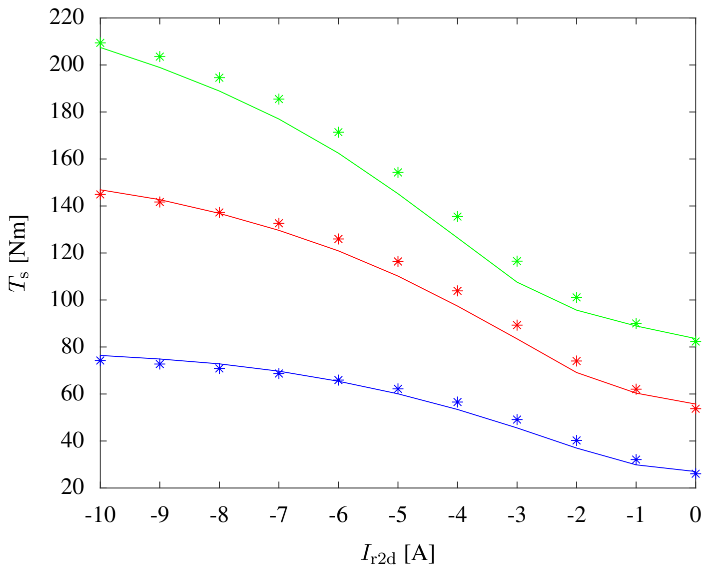

Figure 4.16: Stator torque T_s as function of DC-field current I_{r2d} for a fixed current in the stator d-axis I_{sd} of -50A and varying q-axis stator current I_{sq}. The continuous lines are based on MEC data while the stars are based on FE calculations. The blue signals are valid for I_{sq} equal to 50A, the red signal for I_{sq} equal to 100A and the green signal for I_{sq} equal to 150A.

4.5 Limitations of the EVT

Knowledge of the limits of the EVT is of high importance for the design of the EVT but also for the operating range of the model. There are 3 torque limiting factors for the EVT: mechanical, electrical and thermal of which the thermal limits are out of scope for this thesis due to the lack of a model. Mechanical limits are related to the maximum speed of the bearings. These maximum values are mentioned in Table 4.1. The maximum values for the torque (continuous, not in peak) are related to the maximum voltage. For a space vector modulation control scheme, the maximum voltage is given by [103]:

$$|V_{\mathrm{r1,max}}| = |V_{\mathrm{s,max}}| = \frac{V_{\mathrm{DC}}}{\sqrt{3}} \tag{4.47}$$

The voltage of the inner rotor in the dq-reference frame, is written as:

$$V_{\mathrm{r1d}} = R_{\mathrm{r1}} I_{\mathrm{r1d}} + \frac{d\Psi_{\mathrm{r1d}}}{dt} + (\omega_{\mathrm{r2}} - \omega_{\mathrm{r1}})\, \Psi_{\mathrm{r1q}} \tag{4.48}$$

$$V_{\mathrm{r1q}} = R_{\mathrm{r1}} I_{\mathrm{r1q}} + \frac{d\Psi_{\mathrm{r1q}}}{dt} - \left(\omega_{\mathrm{r2}} - \omega_{\mathrm{r1}}\right) \Psi_{\mathrm{r1d}} \tag{4.49}$$

By combining (4.47), (4.48) and (4.49), the following equation is found:

$$\begin{aligned} V_{\mathrm{r1d}}^2 + V_{\mathrm{r1q}}^2 &= \left(\omega_{\mathrm{r2}} - \omega_{\mathrm{r1}}\right)^2 \left(\Psi_{\mathrm{r1d}}^2 + \Psi\mathrm{r1q}^2\right) \\ &+ 2R_{\mathrm{r1}} \left(\omega_{\mathrm{r2}} - \omega_{\mathrm{r1}}\right) \left(I_{\mathrm{r1d}} \Psi_{\mathrm{r1q}} - I_{\mathrm{r1q}} \Psi_{\mathrm{r1d}}\right) \\ &+ R_{\mathrm{r1}}^2 \left(I_{\mathrm{r1q}}^2 + I_{\mathrm{r1d}}^2\right) \\ &= \frac{V_{\mathrm{DC}}^2}{3} \end{aligned} \tag{4.50}$$

Note that in (4.50), the following terms are neglected: $\frac{d\Psi_{\mathrm{r1d}}}{dt}$ and $\frac{d\Psi_{\mathrm{r1q}}}{dt}$ as the maximum value is considered in steady state.

The same equation can be derived for the stator:

$$\begin{aligned} V_{\mathrm{sd}}^2 + V_{\mathrm{sq}}^2 &= \omega_{\mathrm{r2}}^2 \left(\Psi_{\mathrm{sd}}^2 + \Psi\mathrm{sq}^2\right) \\ &+ 2R_{\mathrm{s}} \omega_{\mathrm{r2}} \left(I_{\mathrm{sd}} \Psi_{\mathrm{sq}} - I_{\mathrm{sq}} \Psi_{\mathrm{sd}}\right) \\ &+ R_{\mathrm{s}}^2 \left(I_{\mathrm{sq}}^2 + I_{\mathrm{sd}}^2\right) \\ &= \frac{V_{\mathrm{DC}}^2}{3} \end{aligned} \tag{4.51}$$

Note that in (4.50) and (4.51), the following terms are neglected: $\frac{d\Psi_{\mathrm{r1d}}}{dt}$, $\frac{d\Psi_{\mathrm{r1q}}}{dt}$, $\frac{d\Psi_{\mathrm{sd}}}{dt}$ and $\frac{d\Psi_{\mathrm{sq}}}{dt}$ as the maximum value is considered in steady state.

For a given DC-bus voltage and inner rotor torque that results in a certain I_{r1q} and I_{r1d}, (4.50) can be solved to a speed difference. The result is thus the maximum speed difference at which the torque can still be generated.

Fig. 4.17 shows how the inner rotor torque and stator torque are related to the speed difference and speed of the outer rotor, respectively. These relations are stored in look-up tables that are used in the model to check whether the requested torque can be generated or not (see saturation block in Fig. 4.5).

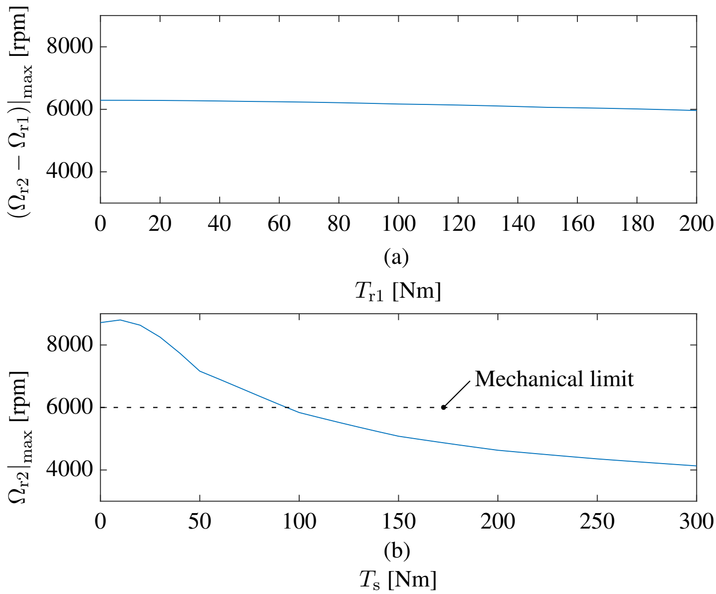

Figure 4.17: (a) Maximum speed difference as function of the inner rotor torque. (b) Maximum outer rotor speed as function of the stator torque.

4.6 Losses

4.6.1 Copper losses

Copper losses are included in the power balance when (4.12) is solved. They can be calculated as:

$$P_{\mathrm{cu}} = \frac{3}{2}R_{\mathrm{s}}\left(I_{\mathrm{sd}}^2 + I_{\mathrm{sq}}^2\right) + R_{\mathrm{r2}}I_{\mathrm{r2d}}^2 + \frac{3}{2}R_{\mathrm{r1}}\left(I_{\mathrm{r1d}}^2 + I_{\mathrm{r1q}}^2\right) \tag{4.52}$$

The value for the resistance is considered constant (independent of temperature).

4.6.2 Iron losses

The magnetic flux density B, which is necessary to calculate the iron losses, can be estimated based on the magnetic flux linkage Ψ. As explained in section 4.4, the magnetic flux linkage depends on 5 currents. The relation between the flux and currents is stored in LUT. In order to calculate the flux density based on the known flux linkage, the magnetic induction waveform in the iron is assumed to vary sinusoidal:

$$B(t) = \hat{B}\cos(\omega t + \delta) \tag{4.53}$$

in which $\omega = 2\pi f$ equals the outer rotor electrical speed if the stator is considered. If the iron losses in the inner rotor are considered, ω equals the speed difference of both rotors. Based on (4.53), it is possible to calculate the iron losses in [W/kg] [104]:

$$p_{\mathrm{fe}}(t) = \left[a\hat{B}^{\alpha}f + b\hat{B}^{2}f^{2}c\hat{B}f\left(\sqrt{1 + d\hat{B}f} - 1\right)\right] \tag{4.54}$$

with a, b, c, d and α magnetic core material parameters, $\hat{B}$ the amplitude of the magnetic flux density in the iron. The values for the material properties are determined via measurements.

Apart from the presented iron losses above, there are also PWM induced iron losses $P_{\mathrm{fe,PWM}}$. These losses are caused by the current ripple that is always present. The higher harmonics of the current induce additional losses as the iron is periodically magnetizing and demagnetizing represented by small secondary loops on the BH-curve [90]. To measure these iron losses they need to be separated from the other losses. This can be done by measuring the losses in stator and inner rotor at standstill (no speed-dependent iron losses, bearing losses or slip ring losses) and with current setpoints equal to 0 (no copper losses). By varying the DC-bus voltage while measuring the losses, a linear relation was observed. Therefore, it was possible to define an empirical model to estimate the PWM induced iron losses

$$P_{\mathrm{fe,PWM}} = \frac{5}{7}V_{\mathrm{DC}} \tag{4.55}$$

4.6.3 Inverter losses

Losses in the inverter occur in the switches and diodes. Each inverter has 6 switches and diodes. As the current and voltage characteristics for the identical switches are identical (but shifted in time), it is sufficient to calculate the losses in a single leg of the inverter and multiply the losses with 6. Hence, also the losses in the diodes are identical. The method described in the following paragraphs is described in detail in [105] and is valid under the following assumptions:

- Transistor and diode switching times are neglected;
- junction temperatures are temporally constant;
- linear modulation;
- the switching frequency ripple of the AC current (sinusoidal current) is neglected;

- $f_{\mathrm{sw}} >> f_{\mathrm{out}}$.

The parameters that are presented in Table 4.2, 4.3 and 4.4 are valid for the used SKiM459GD12E4 module made by Semikron.

To control the current in the windings, a pulse pattern is generated by comparing the sinusoidal reference voltage V_{ref} with a triangular shaped control voltage V_{h} (see Fig. 4.18). The switching frequency f_{sw} is defined by the control voltage while the fundamental frequency f_{out} is related to the reference voltage. By varying the amplitude of V_{ref}, the degree of converter modulation is changed. As long as $V_{\mathrm{ref}} \leq V_{\mathrm{h}}$, this is called linear modulation ($m \leq 1$). The modulation factor m equals:

$$m = \frac{\hat{V}}{\frac{V_{\mathrm{DC}}}{2}} \tag{4.56}$$

in which $\hat{V}$ is the amplitude of the output voltage and V_{DC} is the DC-bus voltage. This voltage amplitude is easily calculated based on the internal variables of the model as:

$$\hat{V} = \sqrt{V_{\mathrm{d}}^2 + V_{\mathrm{q}}^2} \tag{4.57}$$

According to [105], the on-state power dissipation $P_{\mathrm{con,T}}$ in a switch can be calculated as:

$$P_{\mathrm{con,T}} = \left(\frac{1}{2\pi} + m\cos(\phi)\right) V_{\mathrm{ce0}}\hat{I} + \left(\frac{1}{8} + \frac{m\cos(\phi)}{3\pi}\right) r_{\mathrm{ce}}\hat{I}^2 \tag{4.58}$$

in which V_{ce0} is the temperature-dependent threshold voltage of the on-state characteristic, $\hat{I}$ is the amplitude of the current, r_{ce} is the temperature-dependent bulk resistance of the on-state characteristic. The $\cos(\phi)$ is calculated as:

$$\cos(\phi) = \frac{V_{\mathrm{q}}I_{\mathrm{q}} + V_{\mathrm{d}}I_{\mathrm{q}}}{\hat{V}\hat{I}} \tag{4.59}$$

Note that the values for constants, V_{ce0} and r_{ce}, can be found in Table 4.2.

The total switching loss $P_{\mathrm{sw,T}}$ is calculated as:

$$P_{\mathrm{sw,T}} = f_{\mathrm{sw}}\left(E_{\mathrm{on}} + E_{\mathrm{off}}\right)\frac{\hat{I}}{\pi I_{\mathrm{ref}}}\left(\frac{V_{\mathrm{DC}}}{V_{\mathrm{ref}}}\right)^{K_{\mathrm{V,T}}}\left(1 + TC_{\mathrm{esw}}\left(T_{\mathrm{j,T}} - T_{\mathrm{ref}}\right)\right) \tag{4.60}$$

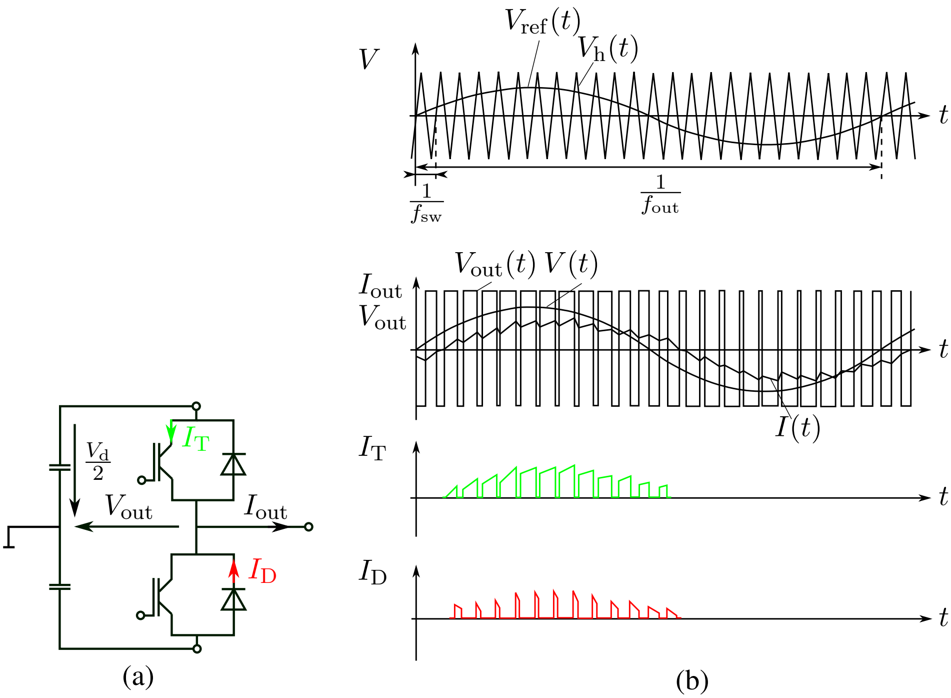

Figure 4.18: (a) Phase module of a PWM inverter. (b) Pulse pattern generation by means of the intersection method, output voltages and currents. Source: [105].

with E_{on} the turn-on power dissipation, E_{off} the turn-off power dissipation, I_{ref} the current for which the datasheet values are valid, V_{ref} the voltage for which the datasheet values are valid, $K_{V,T}$ the exponent for the voltage dependency of switching losses, TC_{esw} the temperature coefficient of the switching losses, $T_{j,T}$ the junction temperature, T_{ref} the temperature for which the datasheet values are valid.

The on-state power dissipation of the diodes $P_{con,D}$ can be calculated according to:

$$P_{con,D} = \left(\frac{1}{2\pi} - m\cos(\phi)\right) V_{f0}\hat{I} + \left(\frac{1}{8} - \frac{m\cos(\phi)}{3\pi}\right) r_f \hat{I}^2 \tag{4.61}$$

in which V_{f0} is the temperature-dependent threshold voltage of the on-state characteristic and r_f is the temperature-dependent bulk resistance of the on-state characteristic. The values for these constants are given in Table 4.3. The total switching loss $P_{sw,D}$ is calculated as:

Table 4.2: Typical values to calculate the losses related to the switches (IGBT) valid for a junction temperature of 150°C.

V_{ce0}	0.75V
r_{ce}	$3.55 \times 10^{-3}\Omega$
f_{sw}	10kHz
E_{on}	22×10^{-3}J
E_{off}	57×10^{-3}J
I_{ref}	450A
V_{ref}	600V
T_{ref}	150°C
TC_{esw}	$0.003\frac{1}{K}$
$K_{\text{V,T}}$	1.35
V_{CES}	1200V
I_{F}	450A

$$P_{\text{sw,D}} = f_{\text{sw}} E_{\text{rr}} \left(\frac{\hat{I}}{\pi I_{\text{ref}}}\right)^{K_{\text{I,D}}} \left(\frac{V_{\text{DC}}}{V_{\text{ref}}}\right)^{K_{\text{V,D}}} \left(1 + TC_{\text{err}}\left(T_{\text{j,D}} - T_{\text{ref}}\right)\right) \quad (4.62)$$

in which E_{rr} is the turn-off power dissipation of the inverse diode used as a free-wheeling diode, $K_{\text{I,D}}$ is the exponent for the current dependency of switching losses, $K_{\text{V,D}}$ is the exponent for the voltage dependency of switching losses, TC_{err} is the temperature coefficient of the switching losses and $T_{\text{j,D}}$ the junction temperature.

Table 4.3: Constants to calculate the losses related to the diodes.

V_{f0}	1V
r_{f}	$2.7 \times 10^{-3}\Omega$
E_{rr}	40×10^{-3}J
TC_{err}	$0.006\frac{1}{K}$
$K_{\text{V,D}}$	0.6
$K_{\text{I,D}}$	0.6

To calculate the junction temperatures in (4.60) and (4.62), a thermal network is used that is solved iteratively:

$$T_{\text{j,T}} = R_{\text{th,T}}\left(P_{\text{con,T}} + P_{\text{sw,T}}\right) + T_{\text{cw}} \quad (4.63)$$

$$T_{\text{j,D}} = R_{\text{th,D}}\left(P_{\text{con,D}} + P_{\text{sw,D}}\right) + T_{\text{cw}} \quad (4.64)$$

in which $R_{\mathrm{th,T}}$ and $R_{\mathrm{th,T}}$ are the thermal resistance of a switch and diode respectively, T_{cw} is the temperature of the cooling water. See Table 4.4 for the values of the constants.

Table 4.4: Constants for the thermal network.

$R_{\mathrm{th,T}}$	$0.08\frac{K}{W}$
$R_{\mathrm{th,D}}$	$0.17\frac{K}{W}$
T_{cw}	16°C
$T_{\mathrm{j,T}}\,(t=0)$	20°C
$T_{\mathrm{j,D}}\,(t=0)$	20°C

The total power loss of the inverter is than calculated as:

$$P_{\mathrm{inv}} = 6\left(P_{\mathrm{con,T}} + P_{\mathrm{sw,T}} + P_{\mathrm{con,D}} + P_{\mathrm{sw,D}} + P_0\right) \tag{4.65}$$

in which $P_0 = 30\mathrm{W}$ are the no load losses of the module.

4.6.4 Mechanical losses

Bearing losses and slip ring losses are identified as mechanical losses. In the EVT, 2 sets of slip rings are used: an AC unit sr_1 and a DC unit sr_2. Moreover, 4 bearings are used to constrain the shafts.

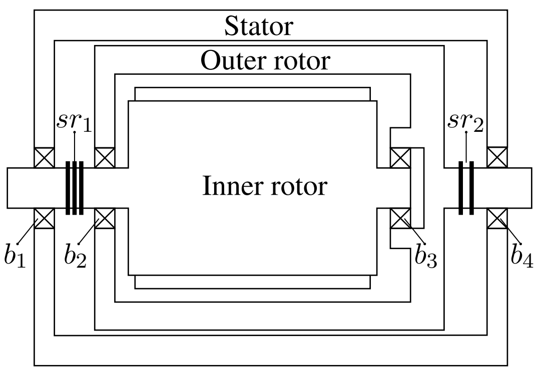

Figure 4.19: Bearing and slip ring configuration.

Slip ring losses

The losses due to the slip rings have been identified on the setup by measuring the torque losses with and without the brushes. These experiments have been conducted for varying speed. The results show that the torque loss related to the slip rings of the inner rotor sr_1 (AC slip ring unit) is constant (independent of the speed) and is approximately equal to 0.12Nm [106]. For the DC slip ring unit sr_2, the difference in measured torque between the experiment with and without brushes was smaller than the accuracy of the torque sensors (accuracy class 0.1%, rated torque 100Nm). The torque losses of sr_2 are thus ignored.

Bearing losses

Bearing b_1 is a double row angular contact ball bearing which supports the inner rotor onto the stator housing. Bearing b_2 and b_3 support the inner rotor onto the outer rotor. Finally, bearing b_4 supports the outer rotor onto the stator housing. To identify the losses of each bearing, experiments have been designed in which only the losses of the bearing under consideration change. As a result, the losses of the other bearings can be canceled out. The torque loss for each bearing is given in Table 4.5. Note that the losses of bearing b_2 and b_3 cannot be separated as they are mounted on the same shaft. Moreover, the sum of the losses of both bearings is given in Table 4.5. Measurements on the EVT setup have shown that these torque losses can be considered independent of the rotational speed of the shafts [107]. More details concerning the experiments which have to be conducted to find the bearing losses can be found in [106].

Table 4.5: Bearing losses

	torque loss [Nm]
bearing b_1	0.3
bearing $b_2 + b_3$	0.7
bearing b_4	0.3

4.7 Control - selection of optimal currents

The control of the EVT is related to the selection of the optimal current setpoint to achieve a given operating point. As there are 2 independent torque setpoints and 5 different current setpoints, an infinite number of current combinations will result in the same generated torque. Of course, only one of these combinations will result in the lowest losses. To find this set of optimal currents, an optimization routine has been developed and validated on a prototype [92]. This optimization routine can be written as:
Find:

$$I^* = \left[I^*_{\mathrm{sq}}, I^*_{\mathrm{sd}}, i^*_{\mathrm{r2d}}, I^*_{\mathrm{r1q}}, I^*_{\mathrm{r1d}}\right] \in \mathbb{R}^5 \tag{4.66}$$

with:

$$I^* = \arg\min\left(P_{\mathrm{loss}}\left(I, \Omega_{\mathrm{r1}}, \Omega_{\mathrm{r2}}\right)\right) \tag{4.67}$$

subjected to:

$$T_{\mathrm{s}}\left(I^{*}\right)=T_{\mathrm{s,set}}\ \&\ T_{\mathrm{r1}}\left(I^{*}\right)=T_{\mathrm{r1,set}} \tag{4.68}$$

The generated torque is calculated based on (4.5) and (4.2), P_{loss} is equal to the sum of iron P_{fe} (4.54) and copper losses P_{cu} (4.52). As solving this routine takes some time, the optimization is carried out offline after which the results are stored in a LUT which is consulted during operation. The LUT thus basically yields the optimal current setpoints given an OP defined by a stator T_{s} and inner rotor T_{r1} torque setpoint and inner and outer rotor speed denoted by Ω_{r1} and Ω_{r2} respectively.

4.8 Comparison between static, hybrid and dynamic model structures

4.8.1 Static versus hybrid model

The difference between the static and hybrid model is purely related to the use of the dynamic equations of motion for the inner and outer rotor. A comparison between both models for a given load cycle (varying torque and speed at the outer rotor) is presented in Fig. 4.20. Fig. 4.20 (a) clearly shows that the static model assumes a stepwise variation in speed. This is, due to the inertia of the outer rotor, of course not possible.

The speed of the hybrid model depends on the requested dynamics, the inertia and the bandwidth of the speed controller. Besides the speed, the torque is also affected by the speed controller. The speed controller defines the torque setpoint to obtain the stepwise variation in speed. In the considered case, maximum torque is requested from the outer rotor to obtain the speed variation. As a consequence there is a difference between the fixed input torque that is used in the static model and the calculated torque (output controller) that is used as input in the dynamic model. Hence, the static model assumes that the speed variation occurs instantly and without any variation in torque to achieve that speed variation. If torque and speed show differences, it makes sense that also the battery power (see Fig. 4.20 (c)) will be different if the static or hybrid model is used.

Fig. 4.20 showed a worst case scenario (stepwise variation in speed) to enlarge the possible differences between the static and hybrid model. However, this does not mean that the static model is useless. Fig. 4.21 shows for example a part of a driving cycle (NEDC) for which the differences are clearly a lot smaller. The figure shows that the static and hybrid model are comparable as long as the requested variations in speed can be achieved without significant error. When a highly dynamic speed variation is requested (inner rotor speed change after 138s), the speed controller cannot follow and differences in battery power will occur. At first sight,

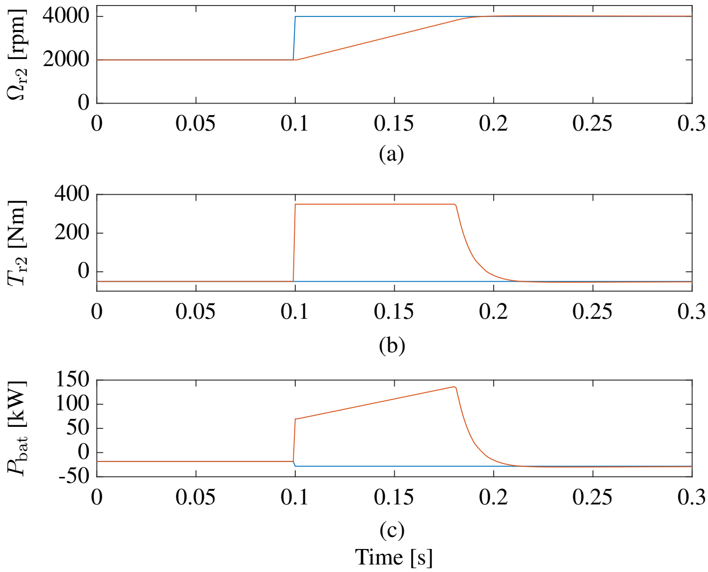

Figure 4.20: (a) Speed of the outer rotor based on the static (blue) and hybrid model (red). (b) Torque of the outer rotor based on the static (blue) and hybrid model (red). (c) Battery power based on the static (blue) and hybrid model (red). The torque and speed setpoint of the inner rotor are constant during the simulation. Moreover, the load torque of the outer rotor is constant as well.

this seems relevant, but translated to the state of charge of the battery this would result in a difference of less than 0.1%.

To summarize: typical vehicle simulations with low dynamic speed and load variations (i.e. NEDC) can be executed based on the static model. However, if faster variations in speed and torque are imposed (i.e. WLTC, see Fig. 6.14 (d)) small differences are noticeable, i.e. a difference of 4% in the state of charge of the battery. For dynamic load patterns, the hybrid model will thus yield more accurate results.

4.8.2 Hybrid versus dynamic

The previous section showed that demanding speed variations resulted in erroneous results if the static model was used. Fig. 4.22 shows that highly dynamic torque variations result in differences between the hybrid and dynamic model. The reason for this is straightforward: to cope with a fast increase or decrease in torque, current needs to change accordingly. In the hybrid model, the current is changed instantly. Therefore, the requested torque (output of the speed controller) equals the torque

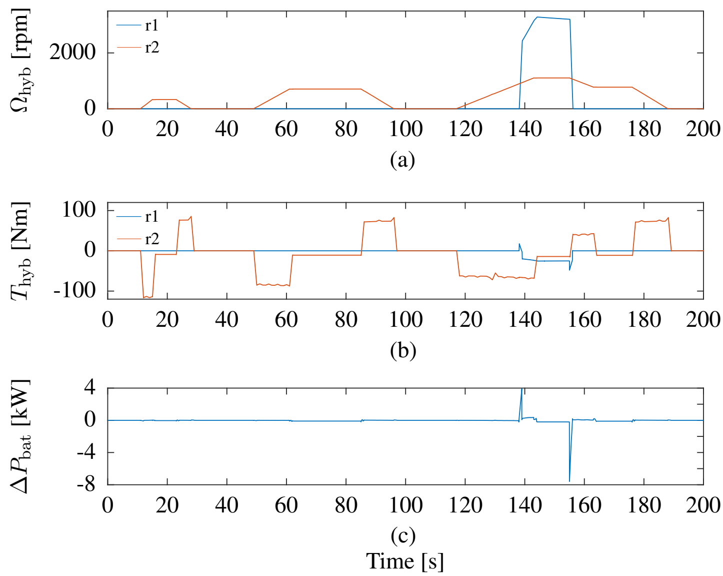

Figure 4.21: (a) Speed of the inner (blue) and outer rotor (red) based on the hybrid model. (b) Torque of the inner (blue) and outer rotor (red) based on the hybrid model. (c) Difference between the battery power obtained via the static and hybrid model.

which is being generated. In the dynamic model, current dynamics are taken into account which has its effect on the torque. The overshoot, which is noticeable in Fig. 4.22 (b), is thus due to the current controller.

For vehicle applications, no differences are observed between the hybrid and dynamic model. Moreover, the dynamic model has a high computational effort due to the small sample time which makes it unfeasible to perform simulations of 1800s (length of the WLTC). The dynamic model should thus only be used if one is interested in highly dynamic applications (EVT in weaving loom) or phenomena. An example where highly dynamic phenomena play an important role is if one would like to investigate the impact of torque peaks coming from the ICE on the behavior of the EVT.

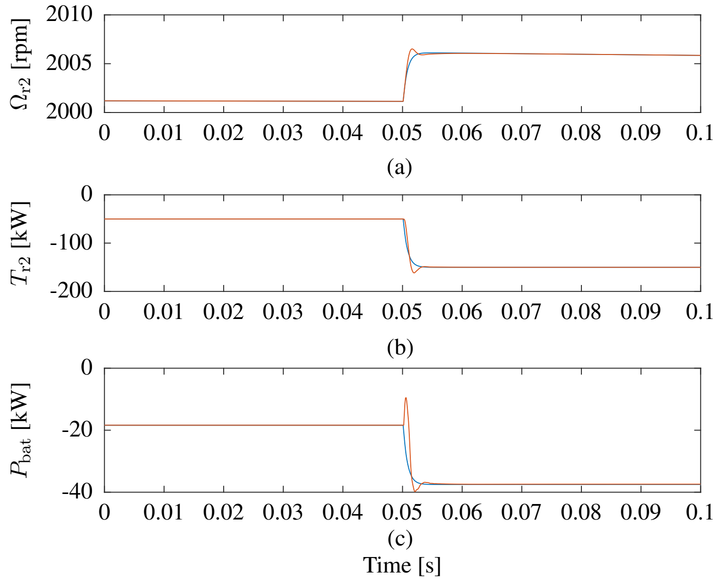

Figure 4.22: (a) Speed of the outer rotor based on the hybrid (blue) and dynamic model (red). (b) Torque of the outer rotor based on the hybrid (blue) and dynamic model (red). (c) Battery power based on the static (blue) and hybrid model (red). The torque and speed setpoint of the inner rotor are constant during the simulation. Moreover, the load torque of the outer rotor is constant as well.

4.9 Validation of the model

The FE model and the models which are used to predict the losses are thoroughly validated on a setup [90]. One of the figures which is used in [90] to show the accuracy of the developed loss models is Fig. 4.23. Fig. 4.23 compares the fractions of all losses (except the inverter losses) with the total measured power loss $P_{\mathrm{l,meas}}$.

An overview of the experimental setup is given in Fig. 4.24. Two induction machines are speed or torque controlled and load the inner and outer rotor of the EVT. Between the shafts of the induction machines and EVT, a torque sensor is mounted with a maximum measurable torque of 100Nm. This torque is quite low considering the maximum torque of the EVT. However, this was done to be able to perform torque measurements with high accuracy in order to evaluate the losses.

Besides the induction machines, two custom made inverters are used to control the currents in the inner rotor and the stator. The DC-supply is used to control the current in the DC-field winding. A schematic overview on all the inputs and measured properties is given in Fig. 4.25.

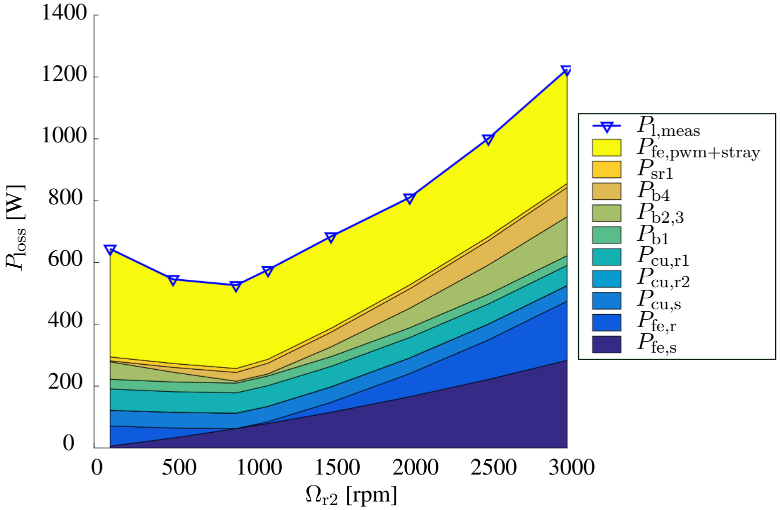

Figure 4.23: Measured loss and calculated loss separation. Inner rotor torque $T_{\text{r1}} = -40$Nm, outer rotor torque $T_{\text{r2}} = 70$Nm, and inner rotor speed $\Omega_{\text{r1}} = 1000$rpm. The DC-bus voltage V_{DC} of the inverters equals 400 V. Source: [90].

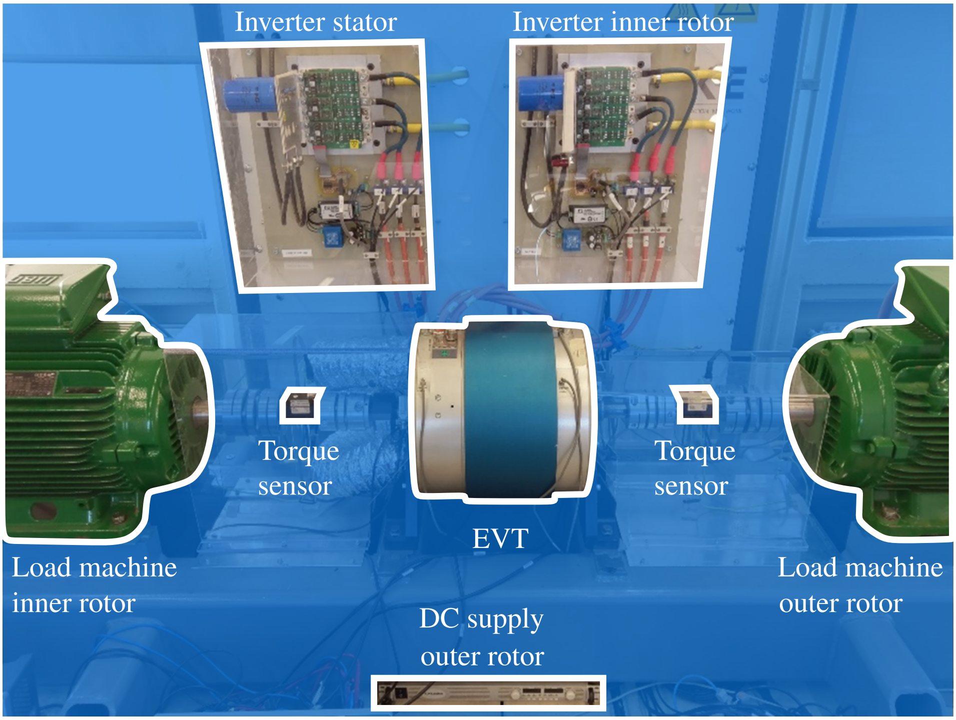

Figure 4.24: Experimental setup.

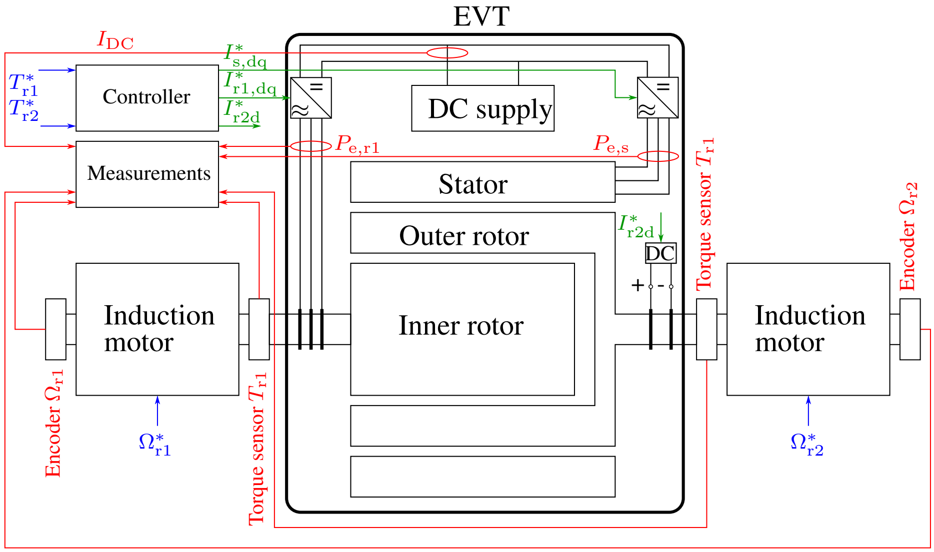

Figure 4.25: Schematic of the experimental setup. Blue: user defined inputs. Green: setpoint values for the current (see section 4.7). Red: measurements.

4.10 Conclusion

In this chapter, the permanent magnet EVT is introduced. The operating principle has been discussed and it is shown how the behavior of the EVT can be modeled based on three degrees of accuracy: a static, hybrid and dynamic model. The static model can be used if torque and speed vary at a low pace. If higher dynamics occur the hybrid model is the best option. The dynamic model should only be used when it is for example the objective to study the impact of torque pulses coming from an ICE on the EVT. All these models have a similar structure that allows to express the efficiency, later on, as function of the speed ratio and the load torque. As explained in the chapters of the toroidal and belt CVT, this is important for the comparison of the variable transmissions. Furthermore, it shows that the first research goal, as defined in section 1.2, has been completed.

The presented models rely on the current to flux relationships which are stored in look-up tables as FE calculations are too slow. However, an alternative is given with a lower computational effort: the magnetic equivalent circuit model. Besides the current to flux relations, the reader is introduced with the loss models, the limitations of the EVT and optimal control that is used. These losses will be used later on to calculate the efficiency of a given operating point. Finally, the experimental setup is shortly discussed at which the validation of the models has been performed.

Chapter 5

Design methodology for EVT

In this chapter, scaling laws for a permanent magnet EVT are introduced. First the scaling laws are derived after which they are validated based on FE results. Next, scalable optimal control is derived based on which a design methodology is presented. To demonstrate the work flow, a case study is considered at the end of this chapter.

5.1 Introduction

The design process of any EVT offers challenges due to the many degrees of freedom. In [108] the optimal stator-slot/outer-rotor-pole/inner-rotor-slot number has been determined for a synchronous PM-EVT. The optimal combination was distinguished by low voltage harmonics in the back-EMF, high average torque with low ripple and low iron loss. In [109], changes in height, span and position of the PM material are considered together with changes in PM layers and shapes. Cheng [13] applied a system level approach where the overall dimensions for the PM-EVT are defined according to the main design equations for a normal, i.e. one rotor, PM synchronous machine (PMSM) as formulated in [110].

The methods proposed in [13, 108, 109] provide insight, to some extend, in design modifications but require a lot of Finite Element (FE) calculations. Such methods are accurate but rather time-consuming to determine the complex relation between current and flux. Although the MEC model, as presented in 4.4.2 is faster, the computational effort is still rather high for a first general assessment of the size of a design.

To solve the issues with the FE simulations (or MEC model), scaling laws defined for a PMSM will be used as defined in [111] to optimize the general size of the EVT. A brief survey on scaling laws is given in section 5.2. These scaling laws allow to scale a well-known EVT design, later called the reference design, of which all current to flux relations are known, in both axial and radial directions. In order to fit the voltage requirements of the scaled EVT with the power supply, a winding scaling factor can be used. Note that it is not the objective, nor is the matter discussed, to derive scaling laws for the inverters.

This ultra-fast scaling method will be combined with the validated optimal control of a PM-EVT [92] to obtain a method which can optimize the topology, in terms of copper and iron losses, in any given Operating Point (OP). This OP is defined by the torque developed by the inner rotor and stator and the speed of both rotors. The methodology is thus applicable for any kind of application. However, the method developed in this chapter will most likely be used to optimize the drive train of a Hybrid Electrical Vehicle (HEV) equipped with an EVT. Similar optimization routines based on scaling laws developed for electrical vehicles with PMSM have already shown a great potential [112, 113].

The novelty of the method described in this chapter is in applying the scaling law strategy to an EVT, not in the scaling law strategy itself as this has already been published in [111]. Furthermore, the scalable optimal control, which is developed in this chapter, is one of the main contributions. Finally, the combination of simultaneously optimizing geometry and control of a PM-EVT via scaling laws is entirely new.

5.2 General scaling laws

5.2.1 Theoretical background

Scaling laws have been used in the past to provide a prediction of the average specific torque of a scaled machine based on a reference machine. The advantage of these scaling laws is the simplicity of the method and the fact that they can be applied at an early design stage. Examples can be found in literature for switched reluctance machines [114] and induction machines [115]. The work presented in [114] has later been used by Stipetic [111] to derive scaling laws for a PMSM.

There are 3 scaling parameters: rewinding K_W, axial scaling K_A and radial scaling K_R. Rewinding is done to meet the voltage requirements of the power supply system [111] and has no impact on the dimensions of the scaled EVT. Changing K_W is done by modifying the number of turns per coil N_c, the number of parallel paths a_p or a combination of both:

$$K_\mathrm{W} = \frac{a_\mathrm{p,0}}{a_\mathrm{p}} \frac{N_\mathrm{c}}{N_\mathrm{c,0}} \tag{5.1}$$

in which subscript 0 is used to refer to the reference machine. Axial scaling K_A is carried out by varying the axial core length l_a while the lamination cross-section is preserved:

$$K_\mathrm{A} = \frac{l_\mathrm{a}}{l_\mathrm{a,0}} \tag{5.2}$$

Radial scaling considers a proportional change of all dimensions of the cross-section. The radial scaling factor K_R is therefore equal to the ratio of the diameter of the scaled D and reference D_0 EVT respectively:

$$K_\mathrm{R} = \frac{D}{D_0} \tag{5.3}$$

As reported by [111], the presented method is valid for any PM machine. Therefore, the objective of this section is to check whether the scaling laws are still applicable if a PM-EVT is considered.

According to [111], the scaling laws are only valid if the magnetic flux densities in the core of the scaled machine are preserved. To find the conditions for which this statement holds, the Poisson's equation is written for the reference machine [111]:

$$\frac{\partial}{\partial x_0}\left(\frac{1}{p_0}\frac{\partial A_\mathrm{z,0}}{\partial x_0}\right) + \frac{\partial}{\partial y_0}\left(\frac{1}{p_0 u}\frac{\partial A_\mathrm{z,0}}{\partial y_0}\right) = -J_\mathrm{z,0} \tag{5.4}$$

and the scaled machine:

$$\frac{\partial}{\partial x}\left(\frac{1}{p}\frac{\partial A_{\mathrm{z}}}{\partial x}\right)+\frac{\partial}{\partial y}\left(\frac{1}{p}\frac{\partial A_{\mathrm{z}}}{\partial y}\right)=-J_{\mathrm{z}} \tag{5.5}$$

in which the slot current density scales with K_{J}, $A_{\mathrm{z},0}$ and A_{z} resemble the cross-sectional surface of the reference and the scaled machine respectively, and x, y are dimensions, which scale with the radial scaling factor K_{R}. In order to preserve the exact same saturation, i.e. $p_0 = p$, the terms in the parentheses must be equal for both the reference and scaled machine [111].

$$\frac{1}{K_{\mathrm{R}}}\frac{\partial}{\partial x}\left(\frac{1}{\mu}\frac{\partial A_{\mathrm{z}}}{\partial x}\right)+\frac{1}{K_{\mathrm{R}}}\frac{\partial}{\partial y}\left(\frac{1}{\mu}\frac{\partial A_{\mathrm{z}}}{\partial y}\right)=-K_{\mathrm{J}}J_{\mathrm{z}} \tag{5.6}$$

This is true if:

$$K_{\mathrm{J}}=\frac{1}{K_{\mathrm{R}}} \tag{5.7}$$

As the cross-section scales with K_{R}^2, the scaled current will be proportional to the radial scaling factor. When combined with the winding factor (see [111]), the current in the scaled machine should meet the following equation:

$$I=\frac{K_{\mathrm{R}}}{K_{\mathrm{W}}}I_0 \tag{5.8}$$

with I an array composed of the 5 currents which flow in the scaled machine and I_0 an array of currents flowing in the reference machine. If the relation in (5.8) is met, then the flux linkage in the machine will scale as [111]:

$$\Psi\left(I\right)=K_{\mathrm{A}}K_{\mathrm{R}}K_{\mathrm{W}}\Psi_0\left(I_0\right) \tag{5.9}$$

Based on (5.9), it is now possible to derive the scaling law for the generated torque:

$$T=\frac{3}{2}N_{\mathrm{p}}\left(\Psi_{\mathrm{q}}I_{\mathrm{d}}-\Psi_{\mathrm{d}}I_{\mathrm{q}}\right) \tag{5.10}$$

which can be rewritten in terms of the reference EVT based on (5.8) and (5.9):

$$\begin{aligned}
T &= \frac{3}{2}N_\mathrm{p}\left(K_\mathrm{A}K_\mathrm{R}K_\mathrm{W}\Psi_{\mathrm{q},0}\frac{I_{\mathrm{d},0}K_\mathrm{R}}{K_\mathrm{W}}\right.\\
&\left.-K_\mathrm{A}K_\mathrm{R}K_\mathrm{W}\Psi_{\mathrm{d},0}\frac{I_{\mathrm{q},0}K_\mathrm{R}}{K_\mathrm{W}}\right)\\
&= K_\mathrm{A}K_\mathrm{R}^2\frac{3}{2}N_\mathrm{p}\left(\Psi_{\mathrm{q},0}I_{\mathrm{d},0}-\Psi_{\mathrm{d},0}I_{\mathrm{q},0}\right)\\
&= K_\mathrm{A}K_\mathrm{R}^2T_0\left(I_0\right)\\
&= K_\mathrm{A}K_\mathrm{R}^2T_0\left(\frac{K_\mathrm{W}}{K_\mathrm{R}}I\right)
\end{aligned} \tag{5.11}$$

with $T=[T_\mathrm{s}\ T_\mathrm{r2}\ T_\mathrm{r1}]$ and $T_0=[T_{\mathrm{s},0}\ T_{\mathrm{r2},0}\ T_{\mathrm{r1},0}]$ the electromagnetic torque of the scaled machine and the reference machine, respectively.

5.2.2 Validation based on FE

To validate the scaling law depicted in (5.9), a new FE based model is made for an EVT which is 20% longer and 30% wider ($K_\mathrm{A}=1.2$ and $K_\mathrm{R}=1.3$). No winding scaling is applied ($K_\mathrm{W}=1$).

To demonstrate how the scaling law needs to be applied, the stator flux in the d-axis will be calculated based on the scaling laws. The considered currents which flow in the scaled design are: $I_\mathrm{r2d}=-6.5$ A, $I_\mathrm{sd}=-50$ A, all other currents are equal to 0 A. To calculate the flux, the following steps need to be taken:

1. Scale the currents based on (5.8): $I_{\mathrm{r2d},0}=-5.0$ A, $I_{\mathrm{sd},0}=-38.5$ A.
2. Determine $\Psi_{\mathrm{sd},0}$ in the reference machine for these currents: -0.256 Vs (see Fig. 4.8 (a), red line)
3. Scale the flux according to (5.9): -0.399 Vs

Fig. 5.1 (a) shows that the same result is found via the FE model. Moreover, the figure compares the results of all current setpoints which were originally presented in Fig. 4.8. The figure clearly shows that the scaling laws are valid. Furthermore, we can conclude that recalculating the current to flux relations that cover 5 dimensions is not necessary if a scaled version of the reference EVT is considered.

Besides the validation of the scaling law for flux, Fig. 5.1 shows that the scaling law for the generated torque is also applicable. The following example is chosen to demonstrate the method: $I_\mathrm{r2d}=-6.5$A and $I_\mathrm{sq}=130$ A, all other currents are equal to 0 A. To calculate the torque, the following steps need to be taken:

1. Scale the currents based on (5.8): $I_{\mathrm{r2d},0}=-5$ A, $I_{\mathrm{sq},0}=100$ A.

2. Determine $T_{s,0}$ in the reference machine for these currents: 93 Nm (see Fig. 4.8 (c), red line)

3. Scale the torque according to (5.11): 188.6 Nm

When this is compared with the torque calculated based on FE (red curve in Fig. 5.1 (c)), a torque of 188.6 Nm is found that justifies the scaling law. A similar analysis has been carried out to analyze the back-EMF of the scaled machine. From that analysis it is concluded that the scaling law for the voltage depicted in [111] holds for a PM-EVT as well.

Fig. 5.1 showed that the scaling laws are accurate for the considered scaling factors, i.e. $K_{\mathrm{A}} = 1.2$ and $K_{\mathrm{R}} = 1.3$. To demonstrate that the method stays accurate for multiple scaling factors, Fig. 5.2 has been added. The same conclusions can be drawn for varying axial scaling factors.

5.2.3 Validation based on literature

In the previous subsection, the scaling laws were validated based on FE calculations. However, applying the scaling laws on an EVT prototype which is described in literature can prove the applicability of the method in real life as well. A similar methodology has been applied for PM machines used in wind generator systems [116, 117]. The EVT which is used to perform the validation is described by Pisek [108]. It is also a PM-EVT but without DC-field winding and flux bridge. To eliminate the behavior of this part, the current in the DC-field winding is chosen in such a way that the flux through the flux bridge is 0. The main reasons for the choice of this paper are the comprehensive description of the geometry and the results which describe the relation between generated torque and current.

Based on the dimensions of the EVT described by Pisek, it is possible to derive the following scaling factors: $K_{\mathrm{A}} = 1.15$, $K_{\mathrm{R}} = 0.55$ and $K_{\mathrm{W}} = 1$. When these scaling factors are applied to the EVT described in this thesis the results in Fig. 5.3 are obtained. For the inner rotor, a close match is obtained while the scaled stator torque deviates from the measured torque presented in [108] at higher currents. As the relation between current and torque is strictly linear in the case of the Pisek EVT, the saturation level remains constant. This could be due to the perforation in the outer rotor which is likely to be saturated while the field in the stator yoke remains limited. In contrast to the Pisek EVT, the stator yoke and teeth of the EVT presented in this thesis are saturated for higher currents which results in lower torque as shown in Fig. 5.3 (b).

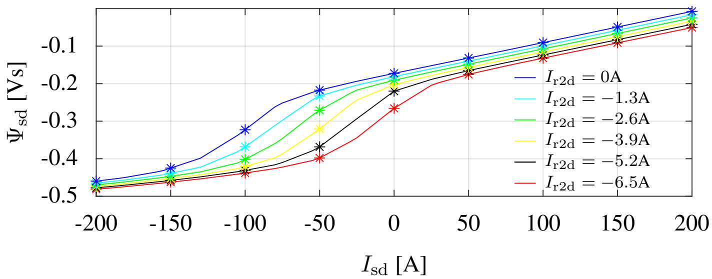

(a)

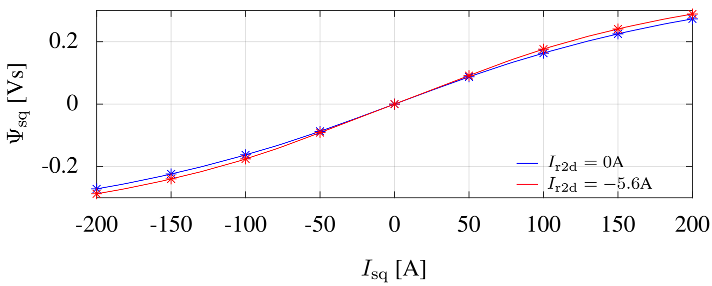

(b)

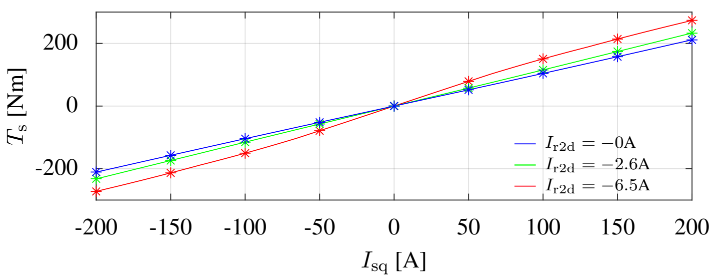

(c)

Figure 5.1: (a) Stator flux in the *d*-axis Ψ_{sd} as function of the stator current in the *d*-axis I_{sd} for varying DC-field current I_{r2d}. (b) Stator flux in the *q*-axis Ψ_{sq} as function of the stator current in the *q*-axis I_{sq} for varying DC-field current I_{r2d}. (c) Stator torque T_{s} as function of stator current in the *q*-axis I_{sq} for varying DC-field current I_{r2d}. All other current setpoints are 0. Full lines are obtained via FE calculations of a design characterized by a length which is 1.2 times the reference length ($K_{\mathrm{A}} = 1.2$) and a diameter which is 1.3 times the reference diameter ($K_{\mathrm{R}} = 1.3$). The stars are obtained by using the presented scaling laws.

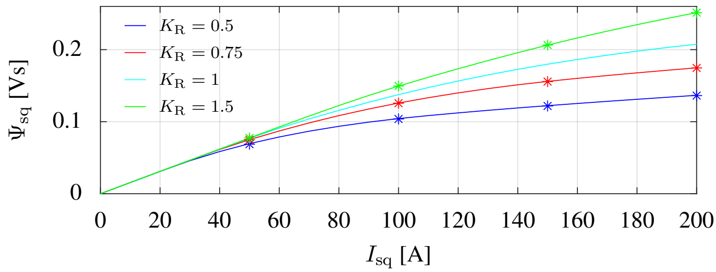

Figure 5.2: Stator flux in the q-axis Ψ_{sq} as function of the stator current in the q-axis I_{sq}. All other current setpoints are 0. Full lines are obtained via FE calculations of a design characterized by the specified scaling factors ($K_A = 1$ and K_R varies between 0.5 and 1.5). The stars are obtained by using the presented scaling laws (no scaling for the cyan curve, i.e. $K_A = K_R = 1$).

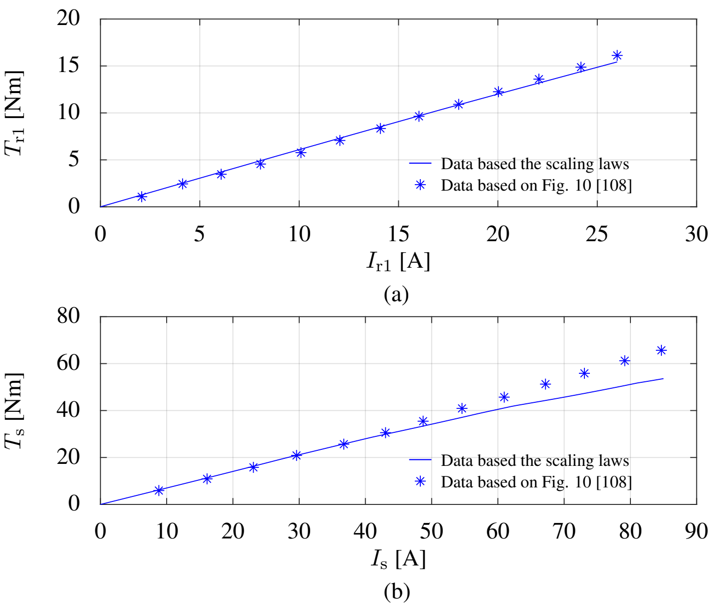

Figure 5.3: Comparison between measured and scaled torque for the inner rotor (a) and stator (b) respectively. The measure torque values are obtained via [108] in Fig. 10 and 11 respectively.

5.3 Scalable optimal control

Fig. 5.1 (c) shows that an infinite number of current combinations will result in the same generated torque. If a stator torque of 200 Nm and inner rotor torque of 0 Nm are considered, then the green line shown in Fig. 5.1 (c) offers the lowest losses (see Table 5.1, case ②). However, if the optimal set of currents is searched for via the algorithm described in [92], it is shown that the losses can be further reduced with 30%. It is thus not enough to scale the current to flux relations based on (5.9), the control needs to be scaled as well. To establish this optimal control, the optimal set of currents resulting in the desired OP, need to be found. As mentioned in the introduction, this OP is defined by the torque developed by the inner rotor and stator and the speed of both rotors. To find this optimal set of currents per OP, the optimization routine as described in section 4.7 is solved. Of course, it is not feasible to have to repeat this optimization routine for every new design. Therefore, the following paragraphs will discuss the scalable control. As a result, the time-consuming method will only have to be computed once, i.e. for the reference EVT.

Scalable control has recently been developed to scale the efficiency map of a PMSM [113, 118]. In these papers, maximum torque per ampere and field weakening algorithms in fmincon functions (nonlinear solver in Matlab ®) are used to determine the optimal currents of the scaled machine based on the reference machine and its LUTs. However, this has not been discussed in literature for a PM-EVT so far. Therefore, compared to the State-of-the-Art, this scalable control for an EVT is a new and crucial step in the scaling law based sizing methodology of an EVT.

The first step in obtaining the desired scalable control is to scale the torque setpoint for the OP at the input side of the LUT containing the optimal control of

Table 5.1: Comparison of the losses obtained for various current combinations results in the same operating point: stator torque of 200 Nm, inner rotor torque of 0 Nm, inner rotor speed of 0 rpm and an outer rotor speed of 1000 rpm.

Case	①	②	③	Optimal
I_{sq} [A]	189.4	172	138.9	-133.6
I_{sd} [A]	0	0	0	79.6
I_{r2d} [A]	0	-2.6	-6.5	-1.1
I_{r1q} [A]	0	0	0	-0.4
I_{r1d} [A]	0	0	0	-14.5
P_{cu} [W]	886	803	926	570
P_{fe} [W]	357	353	340	238
P_{loss} [W]	1243	1156	1266	808

the reference EVT (see Fig. 5.4, scaled variables are indicated with superscript s). Hence, the second step is to scale the current back towards the scaled EVT based on (5.8). Validation of this scalable optimal control is done on the earlier introduced reference EVT and the rescaled EVT. The results of this methodology are shown in Fig. 5.5. The continuous lines show the actual optimal currents for the scaled EVT which are determined based on the method presented in [92] while the stars represent the results based on the scalable optimal control. The figure shows that there is only a minimal difference between the currents that are acquired via both methods. Moreover, the difference in losses is negligible (see Fig. 5.5 (d)). Note that the inner rotor current in the *d*-axis is close to zero. This is because the inner rotor has no saliency. I_{r1d} will thus have no effect on the torque, but will only increase the copper losses.

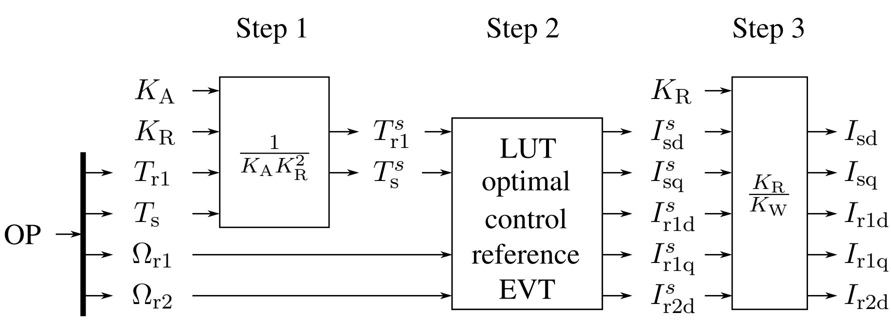

Figure 5.4: Methodology to obtain the optimal control for a scaled EVT based on the optimal control of the reference EVT. Step 1: scale the desired torque that needs to be delivered by the scaled design. Step 2: find the optimal current, given the scaled operating points. Step 3: use the scaling law for the current to scale the currents back to the scaled design. Note that scaled variables are indicated with superscript s.

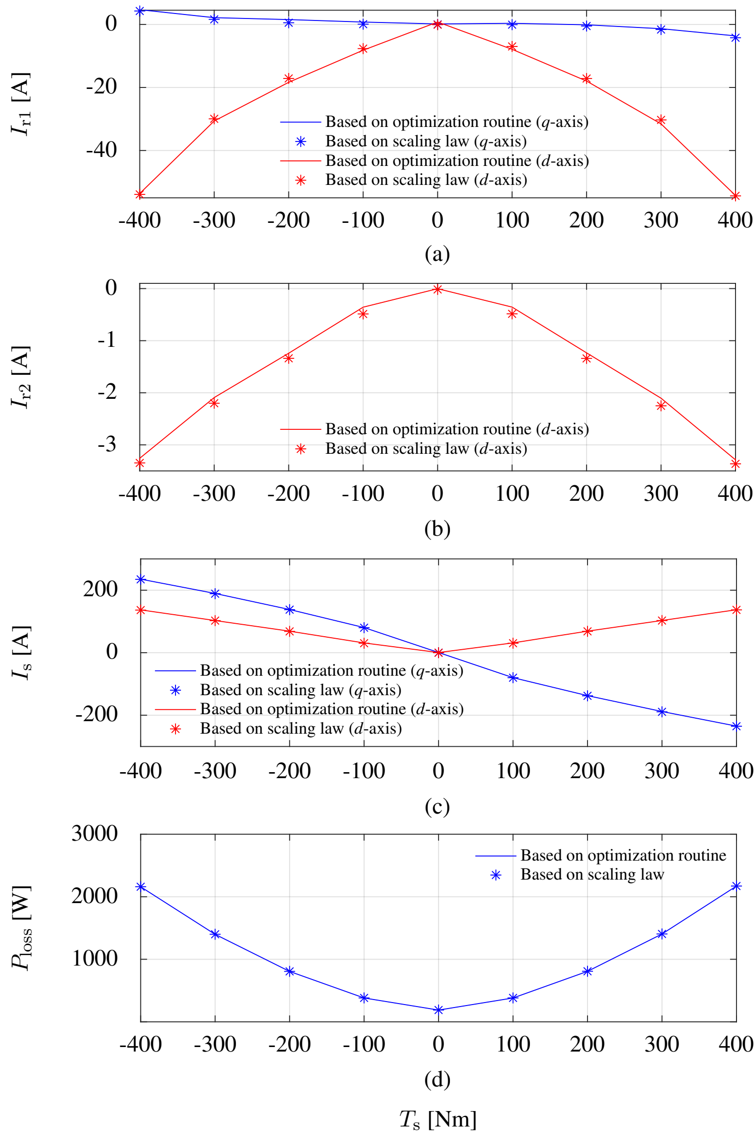

Figure 5.5: (a)-(c) Optimal currents for varying stator torque T_s and inner rotor torque T_{r1} of 0 Nm. (d) Losses for the calculated optimal current set. The speed of the inner rotor Ω_{r1} is 0 rpm while the outer rotor speed Ω_{r2} is 1000 rpm.

5.4 Sizing methodology

The proposed sizing methodology uses the elaborated scaling laws and the scalable optimal control to graphically assess the feasibility of a design. Feasibility is defined by the losses of the design and whether the design fits the demanded constraints such as torque or weight limitations. To graphically combine all this information, a performance map is used. This map shows the losses P_{loss}, composed of copper and iron losses, as a function of the axial and radial scaling factor for a given OP. The following subsections provide a method to set up a performance map and demonstrate how limitations can be visualized.

5.4.1 Step 1: performance map boundaries and design constraints

The first step in setting up the performance map is to define the boundaries and stepsize for the considered scaling factors. This results in a grid of axial and radial scaling factors that characterize the considered designs (Fig. 5.6). Note that a third axis can be added for the winding factor. In the remainder of this chapter, the winding factor is set to 1.

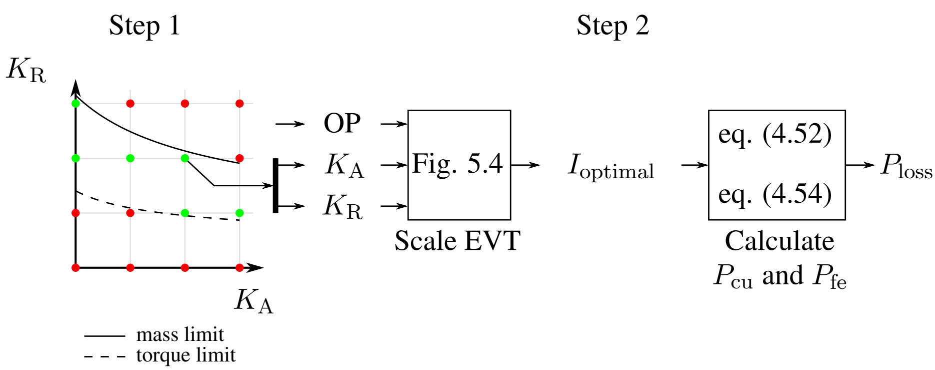

Figure 5.6: Necessary steps in setting up a performance map. Step 1: define a grid of possible designs and add the constraints. Green dots are in agreement with the constraints while the red dots violate the constraints. Step 2: determine the losses for each design that fits the constraints.

The grid thus defines a set of designs for which the losses could be determined (visualized by the green and red dots in Fig. 5.6). As not all combinations of K_A and K_R are realistic, it is essential to add constraints, at least concerning weight and required torque. Those constraints are the solid and dashed line in Fig. 5.6, respectively. The applicable range for the scaling factors is restricted due to thermal and technological reasons. However, if an axial and radial scaling factor of 1.25 is chosen, the output torque will already be approximately 200% higher [118].

To determine the maximum torque limit, the force density is used. The force density F_d is a measure for the force developed per square meter of an active air gap surface area. This parameter is rather constant over a wide range of machine power values [119, 120] (29.1kN/m^2 for the stator and 23.9 kN/m^2 for the inner rotor, see section 5.5). This makes the force density particularly suitable to estimate the torque boundaries for designs with varying power ranges. The maximum torque T_max (inner rotor or stator torque) can be calculated as:

$$T_\mathrm{max} = 2\pi r^2 l_\mathrm{a} F_\mathrm{d} \tag{5.12}$$

in which r is the airgap radius, l_a is the active length and F_d is the force density. The value for F_d can be theoretically obtained as elaborated in [121, 122] or can be based on measurements. Measuring F_d comes down to determining the maximum continuous torque of the EVT for which there is still an acceptable thermal equilibrium.

As the required torque is typically one of the design criteria and thus a known property, it is more useful to relate the torque to the chosen radius of the stator or inner rotor:

$$r = \sqrt{\frac{T_\mathrm{max}}{2\pi F_\mathrm{d} l_\mathrm{a}}} \tag{5.13}$$

Based on the definitions of the scaling laws, (5.2) and (5.3), it is possible to rewrite (5.13) as:

$$K_\mathrm{R} r_0 = \sqrt{\frac{T_\mathrm{max}}{2\pi F_\mathrm{d} K_\mathrm{A} l_\mathrm{a,0}}} \tag{5.14}$$

$$K_\mathrm{R} = \frac{1}{r_0}\sqrt{\frac{T_\mathrm{max}}{2\pi F_\mathrm{d} K_\mathrm{A} l_\mathrm{a,0}}} \tag{5.15}$$

in which r_0 is the airgap radius and $l_\mathrm{a,0}$ is the active length, both of the reference machine. Equation (5.15) can now be used to calculate the relation between the axial and radial scaling factors given a maximum required torque T_max (defined by the considered application). Fig. 5.7 shows this relation for several torque values (dotted lines). Any design, defined by a given K_A and K_R value, which is located under the design line, will be overloaded during operation. This design torque could for example be the rms value of the load profile of the considered application. However, if the load torque is not periodic, which is for example the case when HEVs are considered, the average torque could be used.

As stated at the beginning of this subsection, there are other restrictions which could be important as well. Such constraints are related to maximum weight or

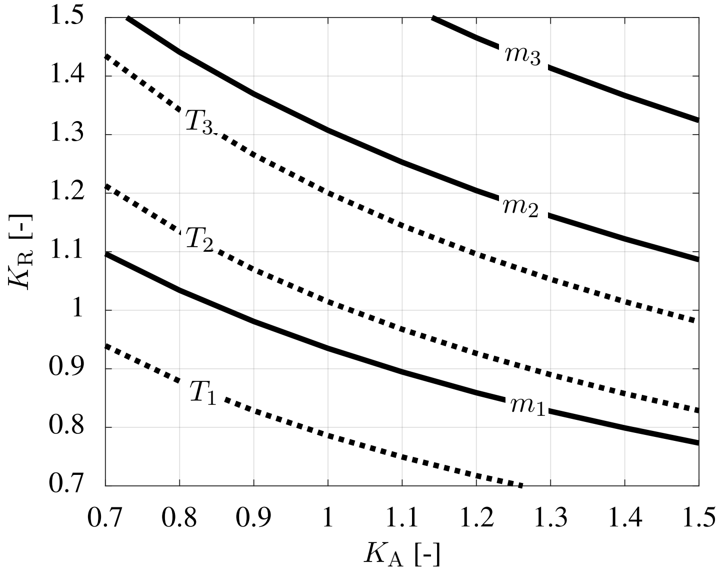

Figure 5.7: Torque and mass as function of scaling factors. Any solution below the design lines for maximum stator torque ($T_1 = 150$ Nm, $T_2 = 250$ Nm and $T_3 = 350$ Nm) will result in overload for the specified torque. Solutions above the design lines for maximum mass ($m_1 = 50$ kg, $m_2 = 100$ kg and $m_3 = 150$ kg) leads to a heavier solution than the specified mass.

volume which is for example very important in HEVs. Based on the sizing of the EVT, it is possible to calculate boundary conditions for these quantities as shown in Fig. 5.7 for the weight (full lines). Any design above the line will be heavier than the specified maximum value.

It is thus possible to visually analyze which designs in the considered set can be excluded based on the specified design constraints. This simplifies the design problem as shown in Fig. 5.6 where the designs that meet the constraints are colored green and the designs that do not meet the constraints are colored red.

5.4.2 Step 2: optimal currents and losses

Step 2, as demonstrated in Fig. 5.6, is to determine the optimal current set for a design at a specific OP. Note that only one OP is considered per performance map. However, it is possible to integrate the losses of multiple performance maps over time if one wants to analyze a cycle (see section 5.5). The method for a single OP is summarized in Fig. 5.4. Once the currents are known, the copper losses are easily determined based on (4.52). Note that the resistance of the inner rotor, outer rotor and stator scale as well:

Table 5.2: Comparison of the computational effort to analyze 10000 OP of a scaled EVT.

	Computational effort (FE calculations) [s]	Computational effort (scaling laws) [s]
Current to flux	350000	200
Optimal control	60000	0 (*)
Total	410000	200

(*) Happens simultaneously with the calculation of the current to flux relations.

$$R = \frac{K_{\mathrm{W}}^2}{K_{\mathrm{R}}^2}\left(K_{\mathrm{A}} R_{\mathrm{co},0} + K_{\mathrm{R}} R_{\mathrm{ew},0}\right) \tag{5.16}$$

in which $R_{\mathrm{co},0}$ is the resistance of the reference EVT in the core region, while $R_{\mathrm{ew},0}$ is the resistance of the end winding. In addition to the copper losses, the iron losses need to be determined. Assuming a sinusoidal air gap induction waveform, it is possible to calculate the iron losses in [W/kg] based on (4.54). Now the losses are determined, the procedure above is repeated for every design in the grid that meets the criteria, i.e. green dots. For a detailed analysis of the separation of the losses, the authors refer to [107].

5.4.3 Computational effort of FE vs. scaling laws

One of the main advantages of the scaling laws is the sheer drop in the computational effort compared to FE calculations. If the scaling laws are applied, an OP of a scaled design is evaluated in 0.02 s (Core i7 processor, 2.9 GHz). As already stated in section 4.4.2, it takes 2s per FE calculation and approximately 175000 FE calculations are necessary to take all the current to flux relations correctly into account. This results in a calculation time of roughly 4 days. The next step is to search for the optimal control. This takes 6 s per OP, which seems negligible. However, the more detail that is required from the load pattern (higher number of considered OP), the more significant this part will become. Table 5.2 gives an additional example when 10000 OP are considered (10 possible values for inner rotor torque, stator torque, inner rotor speed and outer rotor speed). Note that the scaling has no impact on the accuracy: an FE model would yield the exact same results as long as it is a scaled version of the original design.

5.5 Case study

To demonstrate the method, a generic load profile as depicted in Table 5.3 has been chosen. This profile is periodically executed (OP ① starts again after OP ④

Table 5.3: Generic load profile

Operating point	T_{s} [Nm]	T_{r1} [Nm]	Ω_{r1} [rpm]	Ω_{r2} [rpm]	Δt [%]
①	150	80	1000	2000	30
②	200	20	750	2000	10
③	50	70	500	1000	40
④	80	50	750	1000	20

is finished). Here, an additional constraint is a maximum weight of 200 kg. Note that the optimization routine will result in a design which is able to execute the load cycle from an electromagnetic point of view with minimal losses. However, the thermal aspect is not considered and is out of scope for this dissertation as no scalable thermal model for this type of PM-EVT exist. The main difficulty in setting up a thermal model is in quantifying how much heat can be evacuated from the air gap and how the rotational speed of both shafts influences this behavior. As a prototype is available, measurements could be done to model this heat flow.

The first step is again to define a grid and to visually represent the limitations on the performance map. All designs that are above the mass limit or below the torque limit do not need to be considered, which reduces the computational effort.

To determine the maximum torque line, the force density of the reference EVT and the rms torque of the profile need to be known. To obtain the force density, the maximum torque values on stator and inner rotor are considered. For the reference EVT, these maximum torque values are 200 Nm and 300 Nm respectively (both rotors at standstill). Given the geometrical parameters of the EVT, this translates to a force density of 29.1 kN/m^2 for the stator and 23.9 kN/m^2 for the inner rotor. The difference in force density between the stator and inner rotor is related to the type of cooling. The inner rotor is cooled with air while the stator is cooled via a water jacket allowing a higher current density and thus a higher torque. The rms torque of the profile is calculated based on Table 5.3 and equals 134.2 Nm for the stator and 66.4 Nm for the inner rotor. The stator torque is thus more critical and is taken into account for the maximum torque line. The mass limitation is purely related to geometry (which needs to be scaled) and mass density values of the used materials. Details considering the scalable geometrical model are considered out of scope for this publication.

The second step is to calculate the losses for each OP for a grid defined by axial and radial scaling factors. Based on these losses the total energy consumption for one cycle can be obtained by integrating the losses (Fig. 5.8). The limitations based on the stator torque of 134.2 Nm (dashed line Fig. 5.8) and a maximum mass of 200 kg (full line Fig. 5.8) are plotted on this graph to eliminate designs which do not match with the constraints. The white regions in Fig. 5.8 represent designs which are not considered (below the dashed line or above the full line) or which do not suffice (not acceptable although within the constraints). These insufficient designs are related to OP ② for which a rather high torque is demanded in comparison with the rms torque for which the application is designed. The white area above the torque limit in Fig. 5.8 thus represents designs which are able to produce the rms torque but not the peak torque related to OP ②. As the optimal design is defined as the design with the lowest energy consumption, the minimum of the values shown in the performance map is the optimal design (yellow circle Fig. 5.8).

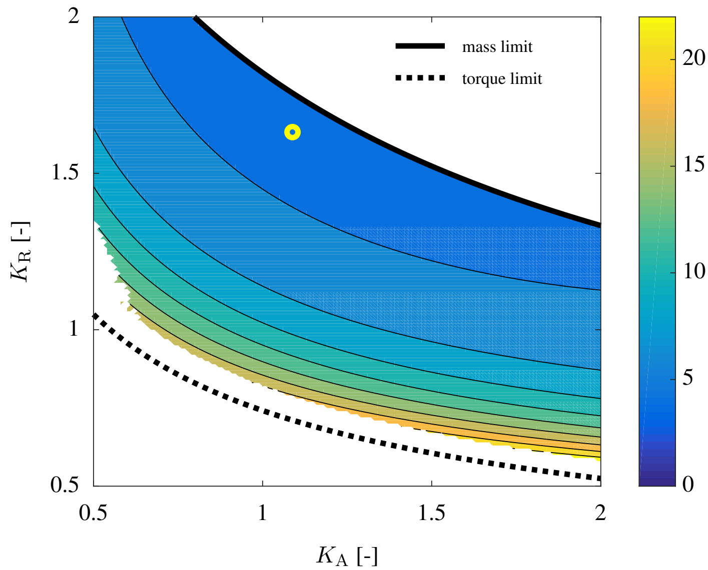

Figure 5.8: Performance map displaying the energy consumption [kJ] over a cycle. The period of one cycle has been arbitrarily chosen equal to 10 seconds. The optimal design is highlighted as the yellow circle.

In the previous paragraphs, a method is demonstrated to size the EVT based on constraints. However, it is also interesting to investigate the impact of those constraints on the optimal design. It is, for example, possible to investigate how the energy consumption changes as a function of the maximum considered weight, which is an important feature in automotive applications. The torque limit is less suited for this as the torque is linked with the load profile which usually cannot be changed easily.

Fig. 5.9 shows how the energy consumption ΔE changes as the restriction on the allowed weight changes. To set up this figure, the demonstrated method in this section has to be repeated for a range of mass values. Each of them will result in a different solution with different losses and thus energy consumption. The red dot on the figure clearly shows that, for the given load cycle, it is possible to design an EVT which, is roughly 50 kg lighter than the optimum without having a significant increase in the energy consumption (an increase of 0.7 %). This is valuable information as less weight can reduce losses at system level as well (for example in a HEV). Note that if the weight needs to reduce drastically, for example towards 100 kg, then the energy consumption will increase by 15.2 %.

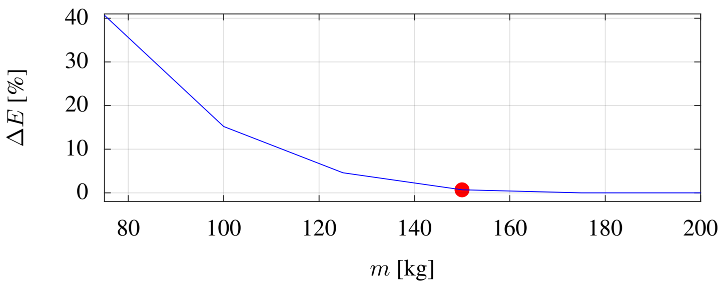

Figure 5.9: Difference in energy consumption between optimal solutions for varying mass with as a reference the optimal solution at a mass of 200 kg.

5.6 Conclusion

In this chapter, a methodology is presented to design the EVT and its control by using a reference EVT and scaling laws for the flux linkage, torque and control algorithm. Although the concept of the scaling laws is not new, it has not been presented before applied to an EVT. Moreover, the combination between the scalable design and scalable control is entirely new. Therefore, in this chapter, the second research goal, given in section 1.2, has been accomplished.

Based on the scaling laws and an accurate description of the influence of the 5 independent current components on the flux linkage with the stator and inner rotor of a reference machine, it is possible to calculate copper and iron losses of a scaled EVT in about 0.02 s. This is more than 2000 times faster compared to the FE based method (if 10000 OP are taken into account). The shear drop in computational effort allows for a fast assessment of design modifications via axial and radial scaling in terms of losses, maximum torque and weight, volume or inertia. All this information is combined on a single performance map. Because the performance map shows both losses and limits, it can be used easily to visually select the optimal design for a specific OP or a load cycle. Whether this load cycle comes from a highly dynamic application, such as a weaving loom or a less dynamically demanding vehicle application, does not have an impact on the applicability of the method. The method can thus be used as part of a general optimization routine, which selects the optimal components of a drive train with an EVT. As an EVT is developed for HEV applications, the primary use of the presented method is in the optimization of such drive trains. Without scaling laws, studying the impact of design changes of the EVT on the complete drive train is almost impossible to research due to the computational effort. Future developments will mainly focus on applying the method in optimization strategies. The main limitation of the method is that it can only optimize the overall dimensions and not details such as the width of the teeth or the radius of for example the inner rotor. The performance of the scaled machine depends thus on how well the electromagnetic design of the reference EVT is done.

Chapter 6

Benchmark studies

In this chapter, a benchmark analysis is performed to compare the EVT with the two considered CVT technologies. This comparison is split in 2 main topics: a component level analysis and a system level analysis. In the component level analysis, the comparison is done based on the operating range and the efficiency. To compare the EVT and CVT, the EVT is used as CVT. In the system level analysis, 2 cases are considered. The first case considers a classical vehicle with variable transmission. The second example compares the performance of a HEV drive train (Toyota Prius) with an EVT based HEV.

6.1 Component level

In this section, the operating range and efficiency of the different technologies will be compared.

6.1.1 Operating range

The first step to benchmark the EVT with other variable transmission is to define the size of the considered components. This size mainly depends on the application for which the variable transmission will be used. As a variable transmission is used in automotive to optimize the system level efficiency, it makes sense to consider a vehicle as application. As the considered belt CVT is designed for automotive applications, its operating range is used as reference. Moreover, the traction model is not parametrized, which could introduce errors in the model of the redesigned belt CVT. To match the maximum torque of the toroidal CVT with the belt CVT small design changes were necessary. The EVT on the other hand had already a comparable maximum output torque as the belt CVT.

Maximum torque of the belt CVT

Based on the model of the belt CVT described in chapter 3, it is possible to set up an efficiency map that will reveal the maximum torque, i.e. the model becomes unstable for a load torque bigger than the maximum torque. In contrast to the toroidal CVT where maximum pressure defined maximum torque, in a belt CVT it is the maximum force generated by the hydraulic cylinders that defines the maximum torque. As there are 2 cylinders, 2 forces need to be controlled within their limits. The force at the secondary pulley defines the slip and the ratio of both forces is related to the speed ratio.

Due to the slip controller, the slip can be controlled actively which also means that the setpoint of the slip can be changed depending on the speed ratio. Hence, for low speed ratio, the slope of the traction curve is less steep (see Fig. 3.2). Consequently, the optimal setpoint for the slip will be higher compared to the ideal slip at high speed ratio. Based on Fig. 3.2, it is possible to deduce that for low speed ratio, the traction curve peaks around 2.5% slip. For safety reasons, the slip is controlled at 2%. If the speed ratio is increased until 1, a linear change of the slope and thus optimal slip is assumed. For a further increase towards a speed ratio of 2, no significant change in the optimal slip value is noticeable. Moreover, the optimal slip is kept at 1% which is in accordance with [69].

Note that to perserve the lifetime of the belt CVT, often a safety factor is used. This safety factor increases the strictly necessary clamping force with a certain percentage. According to literature, a safety factor of 1.3 is often used [18, 123, 124]. As the clamping forces are set too high, higher losses occur which compromises the efficiency [124]. In this thesis, an optimal slip controller is used. The safety factor is thus 1 which optimizes the efficiency to the limit.

Slip thus defines the force on the secondary pulley. The force on the primary pulley, however, depends on the dynamics of the belt and can be calculated based on the CMM model.

Maximum torque of the toroidal CVT

The maximum torque of a toroidal CVT has already been thoroughly discussed in section 2.8 and is presented as function of the tilting angle γ and the maximum pressure in Fig. 2.14. However, the maximum torque of the considered toroidal CVT is rather low compared to the torque of the belt CVT. As the belt CVT is the reference, the toroidal CVT has been modified to fit the requirements. Based on the equation for the maximum torque, (2.54), it is decided to increase the number of rollers per unit n from 2 to 3. At a contact pressure of 2.4GPa, this yields approximately the same peak torque as the belt CVT, as shown later on in Fig. 6.2.

Maximum torque of the EVT

Using an EVT in CVT mode comes down to controlling the setpoints of both shafts in such a way that the power to a fictitious battery becomes 0. Therefore, the electrical port is not used and 1 degree of freedom is lost. To understand how the maximum torque will vary with the speed ratio, it is necessary to take the maximum torque of the stator and inner rotor into account.

The maximum torque on the stator is limited at 300Nm:

$$|T_{\mathrm{s}}| \leq 300 \tag{6.1}$$

which can be written in terms of inner and outer rotor torque as:

$$|-T_{\mathrm{r1}} - T_{\mathrm{r2}}| \leq 300 \tag{6.2}$$

The outer rotor is connected to the load, T_{r2} equals thus T_{L}. Moreover, in lossless conditions the relation between input torque T_{r1} and load torque T_{L} can be written as:

$$\tau = \frac{T_{\mathrm{in}}}{T_{\mathrm{out}}} = \frac{-T_{\mathrm{r1}}}{T_{\mathrm{L}}} \rightarrow T_{\mathrm{r1}} = -\tau T_{\mathrm{L}} \tag{6.3}$$

If (6.2) and (6.3) are combined, the following equation is found:

$$|(\tau - 1)\, T_{\mathrm{L}}| \leq 300 \tag{6.4}$$

which can be solved as:

$$T_{\mathrm{L}} \leq \frac{-300}{\tau - 1} \text{ for } \tau < 1 \tag{6.5}$$

$$T_{\mathrm{L}} \leq \frac{300}{\tau - 1} \text{ for } \tau > 1 \tag{6.6}$$

Apart from the stator, the inner rotor can produce a maximum torque of 200Nm. The same strategy can be followed as above to derive the following equation:

$$T_{\mathrm{L}} \leq \frac{200}{\tau} \tag{6.7}$$

When (6.5), (6.6) and (6.7) are plotted, Fig. 6.1 is obtained. Fig. 6.1 clearly shows that the relations described by (6.5) and (6.7) constrain the torque.

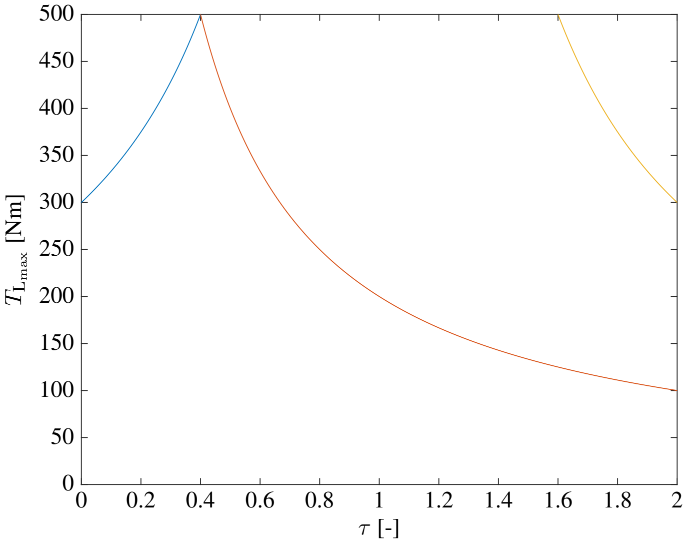

Figure 6.1: Maximum torque of the EVT in lossless condition as function of the speed ratio. Blue: based on (6.5), orange: based on (6.6) and red: based on (6.7).

Comparison

Fig. 6.2 shows the difference in maximum torque for the different variable transmissions. The figure shows that the maximum torque of the EVT is lower than predicted by Fig. 6.1. However, this could be expected, as due to the losses, higher torque is needed to balance the power of both input and output. Note that now design changes were necessary to obtain these results. The reference EVT has thus a similar maximum output torque, in CVT mode, as the considered belt CVT.

Fig. 6.2 reveals 2 important differences between the EVT used as CVT and a mechanical variable transmission. The first one is the EVT can be used at speed ratio values close to zero. In literature, this is called an Infinitely Variable Transmission. Classical CVTs can also be used as IVT but then they need to be combined with a planetary gear which further reduces the efficiency of the transmission. The second difference is the location of the maximum torque. The maximum torque of the toroidal CVT is clearly located at a speed ratio of 1 while for the belt CVT the maximum torque is fairly constant at low speed ratio. The EVT, however, has a maximum torque at way lower speed ratio.

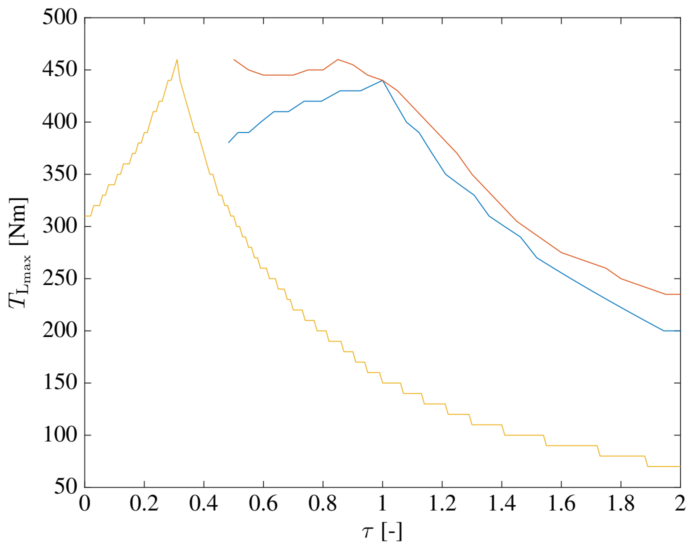

Figure 6.2: Maximum output torque of the toroidal CVT (blue), belt CVT (red) and EVT (orange) as function of the speed ratio for a constant input speed of 2000 rpm.

6.1.2 Efficiency

Based on the comparison of the maximum torque and by extension of the operating range, it is decided to compare the efficiency of the technologies between a speed ratio of 0.5 and 2. The efficiency for a speed ratio of 0.5, 1 and 2 is presented in Fig. 6.3. Based on this figure it is possible to conclude that the toroidal CVT performs best at low speed ratio, while the belt CVT is the best technology at speed ratios above 1. The EVT, however, is inferior to its mechanical variants. Only at a speed ratio of 1 or at low load torque, it can compete with the toroidal and belt CVT.

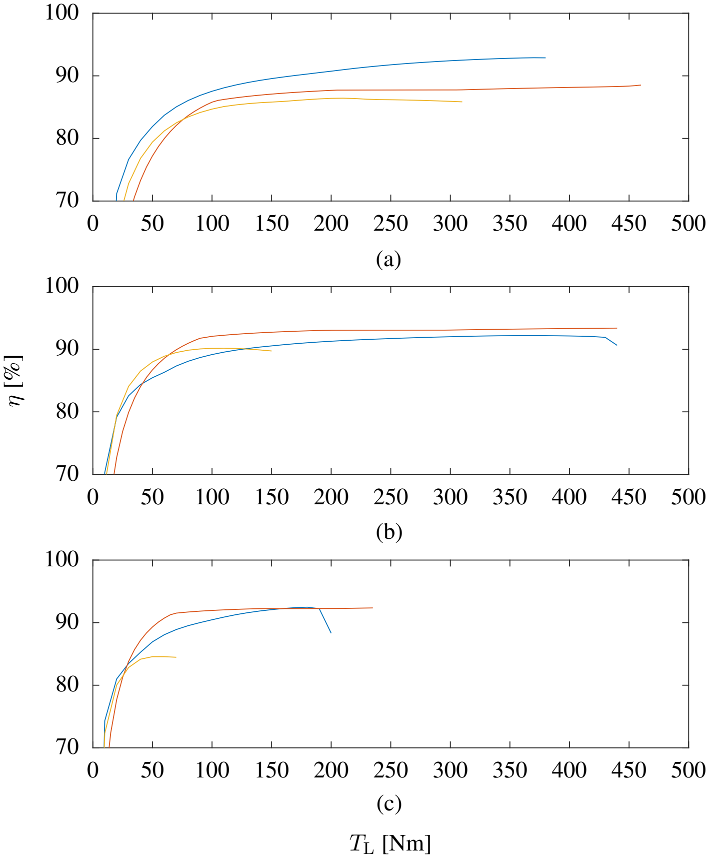

Figure 6.3: Efficiency of the toroidal CVT (blue), belt CVT (red) and EVT (orange) as function of the load torque for a constant input speed of 2000 rpm. (a) speed ratio of 0.5, (b) speed ratio of 1 and (c) speed ratio of 2.

Fig. 6.4 gives an overview on the differences between the 3 technologies throughout the operating range. Fig. 6.4 (a), (b) and (c) present the difference in efficiency in the common operating range while (d), (e) and (f) strictly state which technology is best. An important remark which can be made based on Fig. 6.4 is that the different technologies are relatively close to each other. Although the EVT has a lower efficiency, the difference never exceeds 4%, except for very low torque values.

The high efficiency of the belt CVT is somewhat surprising. Therefore, it is important to highlight again that the safety factor for the clamping force equals 1. Hence, in reality, a safety factor of 1.3 is often used, which means that the device is over-clamped and that reduces the efficiency [87].

For the toroidal CVT, it is important to stress that loss of synchronization between the rollers has not been taken into account. Moreover, in reality the efficiencies of both the belt and toroidal CVT are slightly lower causing the differences to be even smaller.

6.1.3 Conclusion

The comparison between the different variable transmissions has shown that the belt CVT is performing excellent compared to the toroidal CVT and EVT in CVT mode. Only at low torque, the EVT is able to compete with the belt CVT. The toroidal CVT on the other hand performs also better than the belt CVT in part load and a low speed ratio values. Despite these statements, the differences in terms of efficiency are limited to 4% in a large area of the operating range. Only at low torque, differences tend to become bigger. Note that the belt CVT is operated at ideal clamping forces and the toroidal CVT is simulated for perfectly synchronized rollers. This means that in reality the efficiency of both variable transmissions will be lower causing the differences between the technologies to be even smaller.

As the differences in terms of efficiency are not that significant, the operating range of the CVT is of high importance as it defines the flexibility at which the drive train can be used. Comparing the belt and toroidal CVT, not much of a difference can be noted as both have similar maximum torque values and the same ratio spread. The EVT however can reduce the ratio up to, in theory, 0. This is a huge advantage compared with the other 2 variable transmissions, as will be shown in the system level comparison.

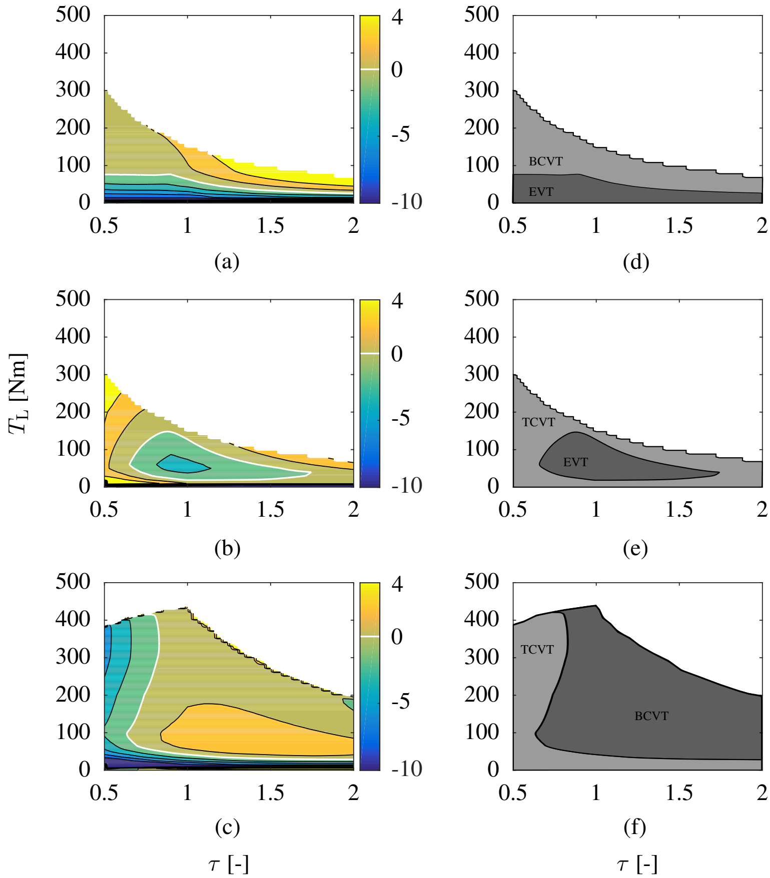

Figure 6.4: Comparison between different variable transmissions based on their efficiency [%] in the common operating area as function of speed ratio and load torque for a fixed input speed of 2000 rpm. (a) and (d) Comparison between belt CVT and EVT ($\eta_{\mathrm{BCVT}} - \eta_{\mathrm{EVT}}$). (b) and (e) Comparison between toroidal CVT and EVT ($\eta_{\mathrm{TCVT}} - \eta_{\mathrm{EVT}}$). (c) and (f) Comparison between belt an toroidal CVT ($\eta_{\mathrm{BCVT}} - \eta_{\mathrm{TCVT}}$). Whereas the figures in the left column present the actual difference in efficiency between the considered variable transmissions, the column on the right strictly visualizes in which area a variable transmission outperforms the one with which it is compared.

6.2 System level - CVT based vehicle

The component analysis showed that the belt CVT performs well compared to the EVT and toroidal CVT. However, a component is seldom used as a stand alone device. Therefore, it is important to study the behavior of the component at system level, i.e. the application in which it is used. As variable transmissions are used in vehicles, the system level comparison will focus on a CVT based vehicle.

The chosen drive train is depicted in Fig. 6.5. It consists of a Internal Combustion Engine (ICE), a clutch, a variable transmission and a final drive.

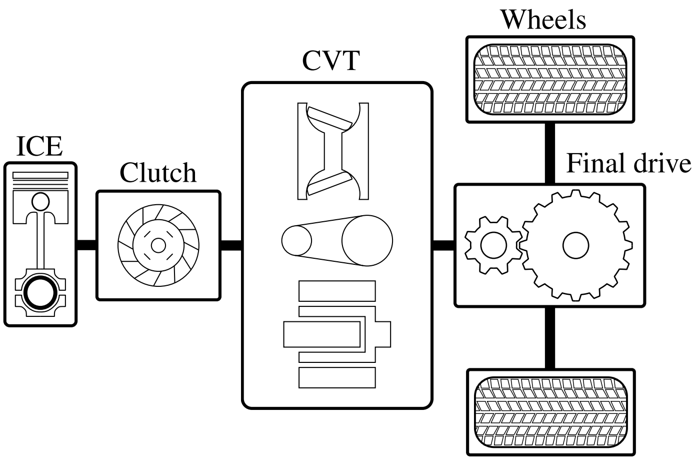

Figure 6.5: Schematic of a CVT based drive train.

To model this drive train, a backward approach has been used. The required torque T_{w} (see (6.8)) and speed at the wheels Ω_{w} are a function of the chosen driving cycle (WLTC, Fig. 6.6 (a)) and vehicle parameters (Table 6.1). Note that (6.8) considers a flat road.

$$T_{\mathrm{w}} = r_{\mathrm{w}} \left(m \frac{\mathrm{d}v_{\mathrm{car}}}{\mathrm{d}t} + mgf + \frac{1}{2} v_{\mathrm{car}}^2 \rho A_{\mathrm{f}} c_{\mathrm{d}} \right) \tag{6.8}$$

$$\Omega_{\mathrm{w}} = \frac{v_{\mathrm{car}}}{r_{\mathrm{w}}} \tag{6.9}$$

Table 6.1: Vehicle parameters

Mass m [kg]	1200
Aerodynamic drag coefficient c_{d}[-]	0.24
Frontal cross sectional area A_{f} [m^2]	2.16
Rolling resistance coefficient f [-]	0.008
Wheel radius r_{w} [m]	0.29
Mass density of the air ρ [kg/m^2]	1.204

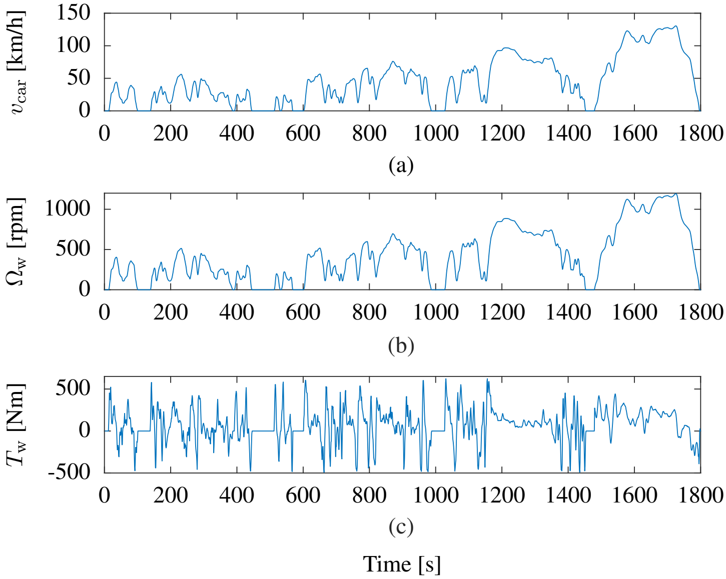

Figure 6.6: (a) Imposed vehicle speed [km/h] as function of time. (b) Wheel speed [rpm] as function of time. (c) Wheel torque [Nm] as function of time based on (6.8). Valid for the WLTC.

Based on the fixed gear ratio τ_{FG} and a fixed efficiency ($\eta_{\mathrm{FG}} = 97\%$) of the final drive, the necessary output torque $T_{\mathrm{CVT_{out}}}$ and speed $\Omega_{\mathrm{CVT_{out}}}$ of the variable transmission are determined:

$$T_{\mathrm{CVT_{out}}} = \frac{T_{\mathrm{w}}\tau_{\mathrm{FG}}}{\eta_{\mathrm{FG}}} \tag{6.10}$$

$$\Omega_{\mathrm{CVT_{out}}} = \frac{\Omega_{\mathrm{w}}}{\tau_{\mathrm{FG}}} \tag{6.11}$$

Note that the case in which power would flow from the wheels to the ICE (during braking) does not occur as it is assumed that all braking torque (negative wheel torque) is generated by the mechanical brakes.

Once the speed ratio of the variable transmission τ_{CVT} is chosen, it is possible to obtain the operating points at the input of the variable transmission which equal the outputs of the clutch. As the clutch is considered as an ideal component (no losses included), the output properties of the clutch model equal the setpoint values for the ICE:

$$T_{\mathrm{ICE}} = \frac{T_{\mathrm{CVT_{out}}} \tau_{\mathrm{CVT}}}{\eta_{\mathrm{CVT}}} \tag{6.12}$$

$$\Omega_{\mathrm{ICE}} = \frac{\Omega_{\mathrm{CVT_{out}}}}{\tau_{\mathrm{CVT}}} \tag{6.13}$$

The final step in the backward model is to use the setpoint for the ICE to calculate the fuel consumption based on Fig. 6.7.

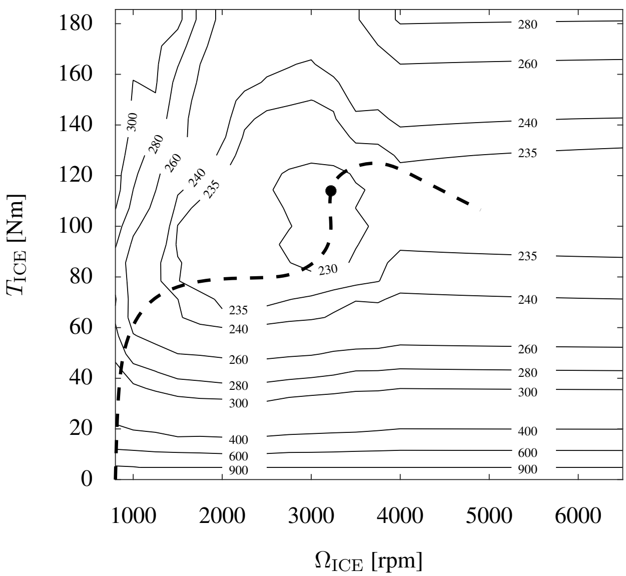

Figure 6.7: Fuel consumption $[g/kWh]$ of a turbocharged gasoline engine (direct injection) running on a Miller cycle. The black dot indicates the optimal operating point of the ICE. The optimal operating line (optimal point for varying power) is visualized by the dashed line.

Note that the slip has been ignored in (6.13). The correct equation would be:

$$\Omega_{\mathrm{ICE,real}} = \frac{\Omega_{\mathrm{CVT_{out}}} (1 - \nu)}{\tau_{\mathrm{CVT}}} \tag{6.14}$$

As the slip ν is low, typically not more than 2%, the impact on the final fuel consumption of using $\Omega_{\mathrm{ICE,real}}$ instead of Ω_{ICE} is negligible. Moreover, slip is incorporated in the efficiency term η_{CVT} that is used:

$$\eta_{\mathrm{CVT}} = \eta_{\Omega}\eta_{\mathrm{T}} = (1-\nu)\,\eta_{\mathrm{T}} \tag{6.15}$$

in which η_{T} stands for the torque loss in the traction-contact, bearings, belt and hydraulics.

To have a fair comparison between the different variable transmissions, an optimization routine has been written that optimizes the gear ratio of the final drive and speed ratio of the variable transmission throughout the driving cycle. The first step in this routine is to pick a gear ratio for the final drive. For this given drive train, it is the purpose to optimize the speed ratio given a driving cycle. This can be done by optimizing time instant by time instant which means that for a given time instant, the backward model is solved for n possible speed ratio values of which the one that results in the lowest fuel consumption is saved (Fig. 6.8).

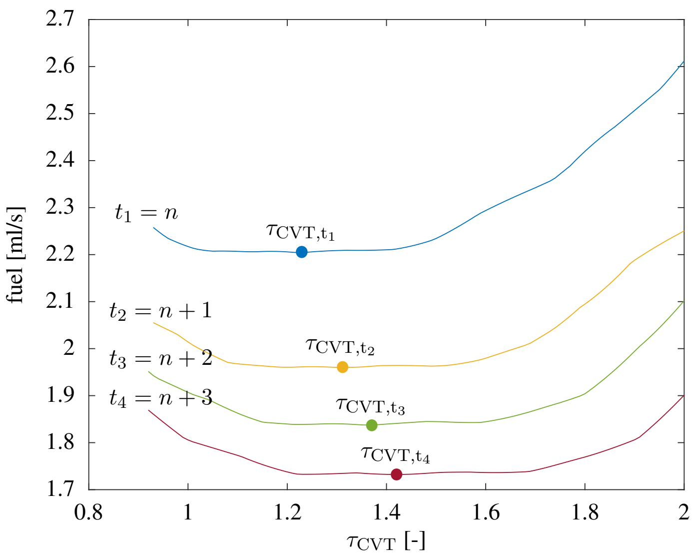

Figure 6.8: Optimization of the chosen speed ratio of the variable transmission given the time instant.

By doing this for the complete driving cycle, an array with optimal speed ratio values $[\tau_{\mathrm{CVT,t1}}\ \tau_{\mathrm{CVT,t2}}\ \tau_{\mathrm{CVT,t3}}\ \ldots]$ is found that optimizes the fuel consumption of the entire driving cycle. In order to find the optimal gear ratio value of the final drive, this procedure is thereafter repeated for m possible gear ratio values.

The results of the optimization routine are combined in Table 6.2. It is shown that, the EVT performs best. To explain this, some background insight is given on the chosen operating points in the following paragraphs.

Table 6.2: Results of the optimization routine.

	Belt CVT	Toroidal CVT	EVT as CVT
Optimal gear ratio τ_{FG} [-]	0.34	0.37	0.40
Fuel consumption [l/100km]	5.20	5.26	5.17

The optimal speed ratio variation for the variable transmission, given the optimal value for the fixed gearbox, are presented in Fig. 6.9. The time series of the speed ratio variation of the 3 variable transmission are similar. Logically, the belt and toroidal CVT are quite similar. This makes sense as their speed ratio range is the same and the efficiency of both technologies is comparable. The EVT follows the same trend, with one important exception: at low vehicle speeds, the speed ratio can drop to near zero. Theoretically, it is possible to go to 0 but this induces a huge amount of losses and therefore, the algorithm is constraint to speed ratios above 0.05.

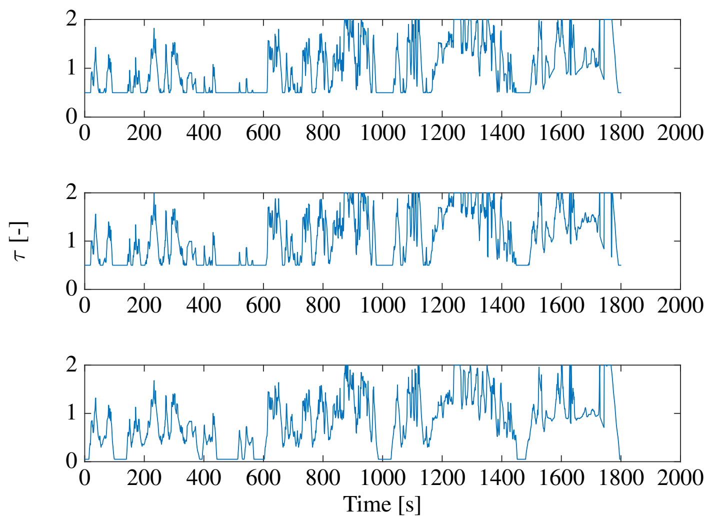

Figure 6.9: Speed ratio variation as function of time for (a) toroidal CVT, (b) belt CVT and (c) EVT. Valid for the WLTC.

The chosen operating points for the toroidal CVT, belt CVT and EVT as CVT are presented in Fig. 6.10, Fig. 6.11 and Fig. 6.12, respectively. Although these maps look different at first sight, they have a lot in common. If the operating points below a speed ratio of 0.5 are excluded from the EVT map, the result (chosen operating points) is similar to the one that is used in the toroidal and belt CVT. This is within the expectations as the variation in speed ratio was also similar.

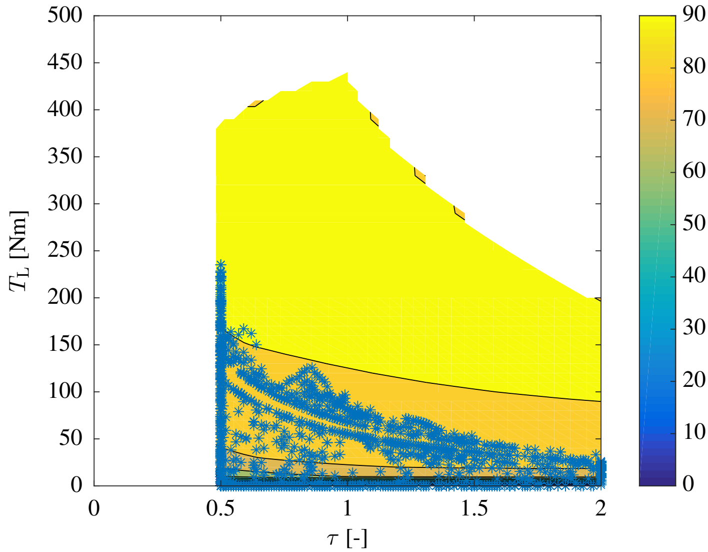

Figure 6.10: Chosen operating points (blue stars) of the toroidal CVT plotted on top of the efficiency map [%]. Valid for the WLTC.

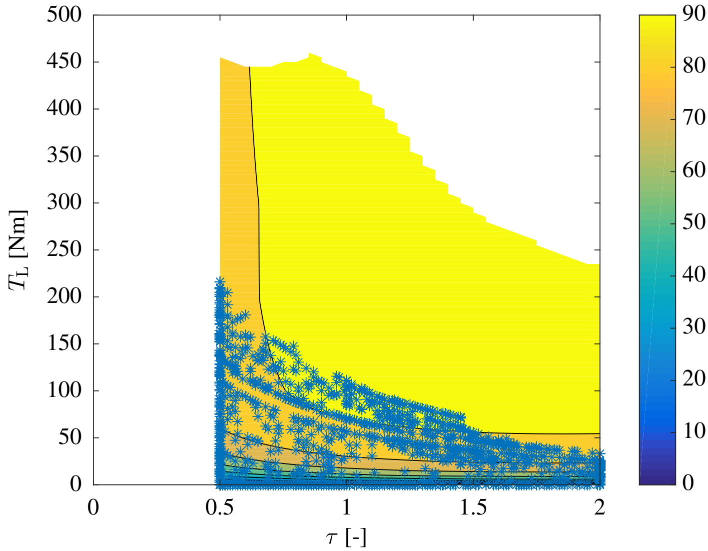

Figure 6.11: Chosen operating points (blue stars) of the belt CVT plotted on top of the efficiency map [%]. Valid for the WLTC.

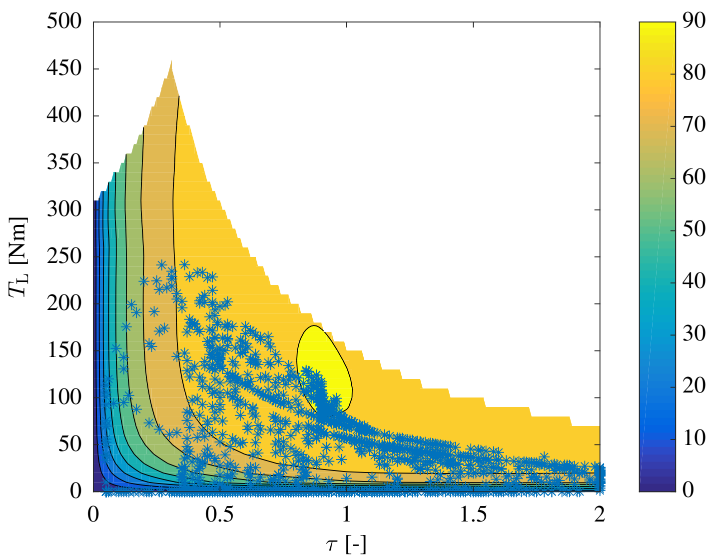

Figure 6.12: Chosen operating points (blue stars) of the EVT plotted on top of the efficiency map [%]. Valid for the WLTC.

However, the ability of the EVT to go to low values in speed ratio is also visible and is a great advantage. This means that when the vehicle accelerates from standstill, the clutch is closed faster. When (6.11) and (6.13) are combined it is possible to calculate the minimal speed of the vehicle $v_{\mathrm{car,min}}$ at which the clutch is fully closed:

$$v_{\mathrm{car,min}} = \Omega_{\mathrm{ICE,min}} r_{\mathrm{CVT,min}} r_{\mathrm{FG}} r_{\mathrm{w}} \tag{6.16}$$

For a minimal speed of the ICE of 800 rpm, the following minimal vehicle speeds are found: 16.2 km/h for the toroidal CVT, 14.9 km/h for the belt CVT and 1.7 km/h for the EVT. The values found for the toroidal and belt CVT are relatively high and that is due to the loss-less clutch. If losses in the clutch would be modeled, the optimization routine would pick a lower speed ratio value for the fixed gear in order to close the clutch faster which would optimize the behavior. However, by adding losses to the clutch, especially the belt and toroidal CVT driven vehicle will suffer from that resulting in a conclusion even more in favor of the EVT.

This, however, does not explain why the EVT based vehicle performs better than the other vehicles. The clutch is basically considered slip mode as long as the vehicle speed is below the minimum vehicle speed. In that case, the ICE is run at its minimal speed of 800 rpm. As there are no losses, it is assumed that the requested torque coming from the wheels is generated by the ICE. At start-up, often high torque is required at low speed, which means that the ICE is operating in a highly inefficient operating area (see Fig. 6.13). As the EVT is able to operate at much lower speed ratios, the optimal operating line (dashed line Fig. 6.13) can be tracked much more accurately. The wide speed ratio range allows the system thus to overcome the lower efficiency of the EVT.

6.2.1 Conclusion

In the conclusion on the component based comparison (section 6.1.3) it was highlighted that the EVT has a, in theory, infinite ratio spread. The system level comparison has shown that the impact of this property has a positive impact on the overall losses of the system and thus the fuel consumption of the vehicle. The EVT based vehicle shows to have the lowest fuel consumption, followed by the belt and toroidal CVT. Note that the losses in the clutch, which have not been taken into account, will mainly increase the fuel consumption of the belt and toroidal based vehicles. This results in a conclusion even more in favor of the EVT.

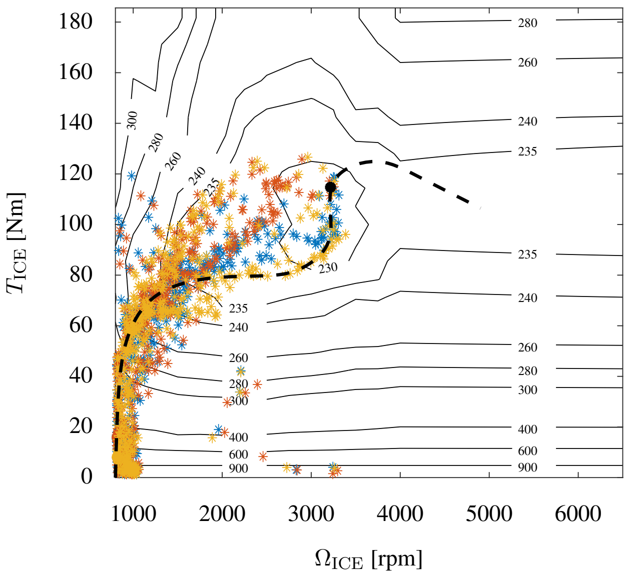

Figure 6.13: Chosen operating points of the ICE during the WLTC. Blue: toroidal CVT, red: belt CVT, orange: EVT.

6.3 System level - series-parallel HEV

In the previous analysis, the operating points of the EVT were limited in order to obtain a fair comparison. However, it is important to know how well the EVT can perform if all degrees of freedom are optimally used. When the EVT is used with the ability to exchange power with a battery, the ICE and wheels are completely decoupled which allows to optimize the operating points of the ICE even further compared to CVT mode. This step is called hybridization and the vehicles with such a drive train are called Hybrid Electrical Vehicles (HEV). One of the most competitive hybrid drive trains is the Toyota Prius. Therefore, in the following sections, the Toyota Prius will be compared with an EVT based HEV. To have a broad comparison, 4 different driving cycles are considered: Artemis urban cycle (Fig. 6.14 (a)), Artemis rural cycle (Fig. 6.14 (b)), Artemis highway cycle (Fig. 6.14 (c)) and WLTC (Fig. 6.14 (d)). More information on the Artemis cycles and the WLTC can be found in [125] and [126], respectively.

6.3.1 Toyota Hybrid System

Figure 6.21 presents the Toyota Hybrid System (THS) used in the second generation of the Toyota Prius. This is a well known series-parallel architecture which consists of an ICE and 2 electrical machines ($M/G1$ and $M/G2$) which are linked via a planetary gear. The wheels are connected, through the final drive with $M/G1$

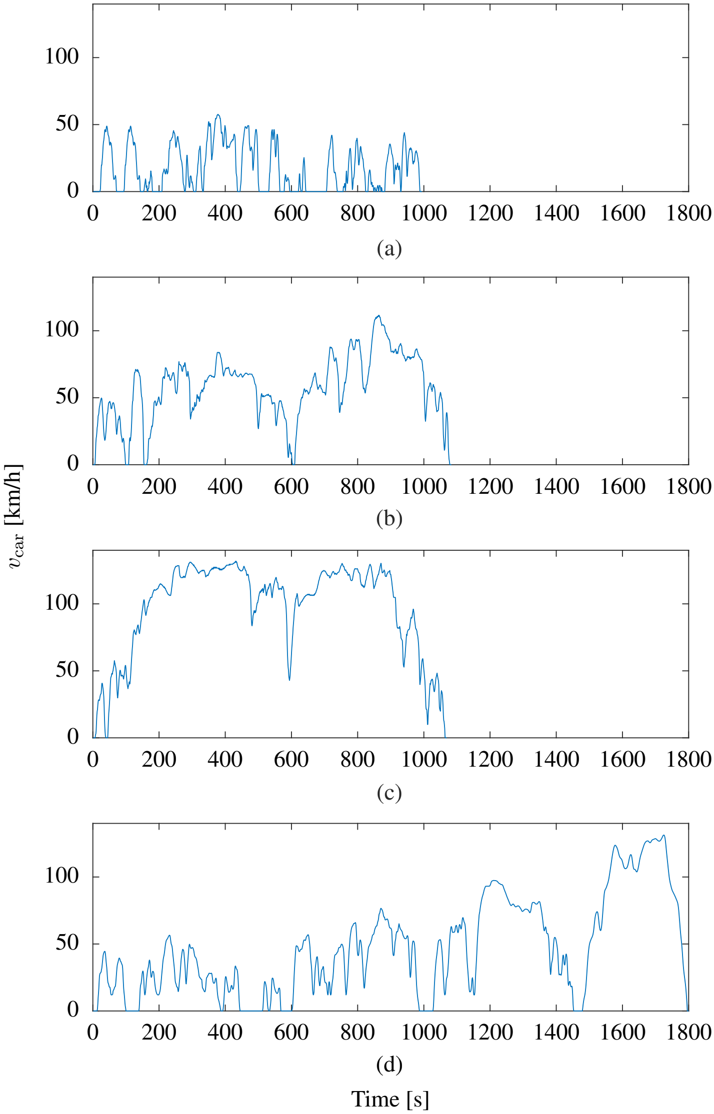

Figure 6.14: Vehicle speed [km/h] as function of time for the following driving cycles: (a) Artemis urban cycle, (b) Artemis rural cycle, (c) Artemis highway cycle and (d) WLTC.

and the ring gear while the $M/G2$ is connected to the sun gear. Finally, the shaft of the ICE is connected to the carrier gear.

In the following subsections, more information is presented on the overall dimensions, planetary gear, final drive, the electrical machines, battery, ICE and cho-

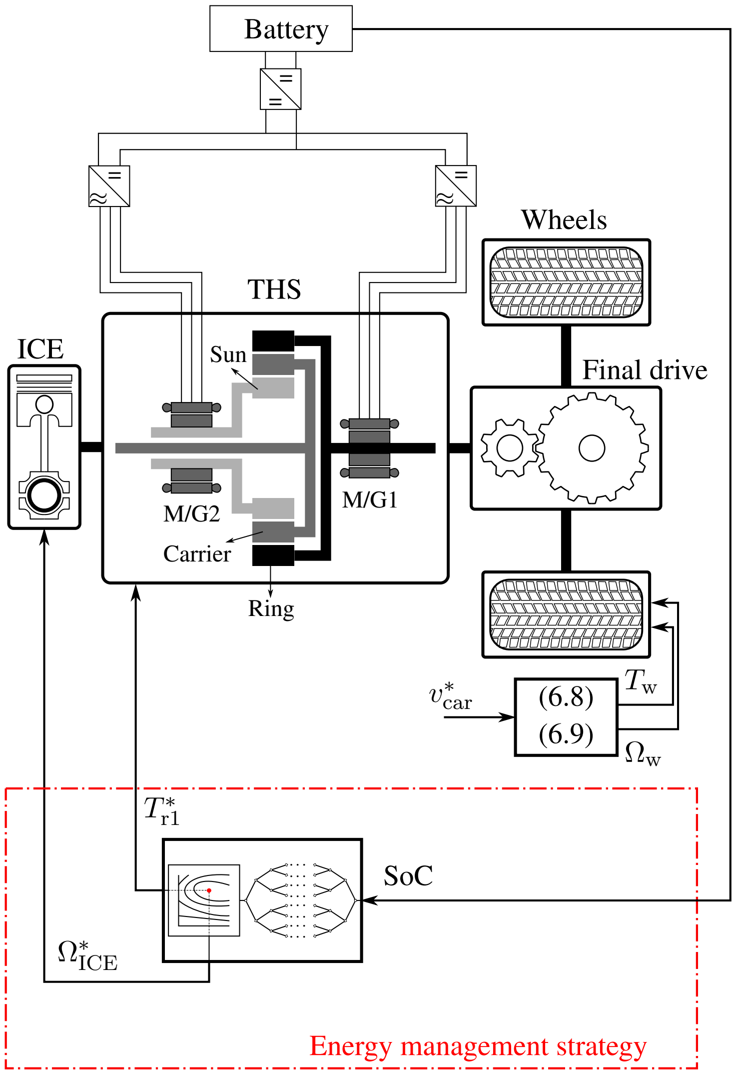

Figure 6.15: Schematic of the Toyota Hybrid System.

sen vehicle parameters.

Overall dimensions

The total length of the THS is approximately 310 mm while the diameter can be estimated to be 270 mm [14] (without housing). These dimensions will be used as benchmark size for the EVT.

Planetary gear and final drive

The planetary gear is modeled based on the Willis equations and a fixed efficiency value of 97% [127, 128]. Dynamic effects have been ignored. According to the Willis equations, the relation between the torque on sun T_s, carrier T_c and ring T_r can be denoted as:

$$T_\mathrm{r} = -T_\mathrm{c}\frac{Z_\mathrm{r}}{Z_\mathrm{r}+Z_\mathrm{s}}\eta_\mathrm{PG}^{\mathrm{sign}(T_\mathrm{c})} \tag{6.17}$$

$$T_\mathrm{s} = -T_\mathrm{c}\frac{Z_\mathrm{s}}{Z_\mathrm{r}+Z_\mathrm{s}} \tag{6.18}$$

in which Z_r and Z_s are the number of teeth on the ring and sun, respectively. All properties can be found in Table 6.3. Note that all the losses are assigned to the gear-meshing between the ring and planets. Moreover, a constant value is assumed, although the efficiency varies with torque and speed. However, it is common practice to take a constant value for the efficiency [128]. Measurements in the lab have confirmed that this assumption is valid, although the measurements have been conducted on lower rated power (see Appendix A).

Based on the fact that the sum of the torque on a shaft needs to be zero (in steady state), it is possible to derive that the torque on the carrier equals the opposite of the generated torque of the ICE T_ICE:

$$T_\mathrm{c} = -T_\mathrm{ICE} \tag{6.19}$$

Combining (6.17), (6.18) and (6.19) now yields the following equations which relate the torque on the ring and sun with the generated ICE torque:

$$T_\mathrm{r} = T_\mathrm{ICE}\frac{Z_\mathrm{r}}{Z_\mathrm{r}+Z_\mathrm{s}} \tag{6.20}$$

$$T_\mathrm{s} = T_\mathrm{ICE}\frac{Z_\mathrm{s}}{Z_\mathrm{r}+Z_\mathrm{s}} \tag{6.21}$$

Besides the torque, the speed of the different components needs to be determined. Therefore, the Willis equation for the speed relationships is used:

$$Z_\mathrm{s}\Omega_\mathrm{s} + Z_\mathrm{r}\Omega_\mathrm{r} = \left(Z_\mathrm{s}+Z_\mathrm{r}\right)\Omega_\mathrm{c} \tag{6.22}$$

in which the speed of the sun, carrier and ring are denoted by Ω_s, Ω_c and Ω_r, respectively.

Table 6.3: Characteristics of the Toyota Prius II [128].

Planetary gear	Number of teeth ring Z_{r} [-]	78
	Number of teeth planets Z_{p} [-]	23
	Number of teeth sun Z_{s} [-]	30
	Overall ratio τ_{PG} [-]	2.6
	Efficiency η_{PG} [%]	97
Final drive	Speed ratio τ_{FG} [-]	0.243
	Efficiency η_{FG} [%]	97
M/G1 (PMSM)	Maximum power [kW]	30
	Maximum speed [rpm]	10000
	DC-bus voltage [V]	500
	Maximum torque [Nm]	160
M/G2 (PMSM)	Maximum power [kW]	50
	Maximum speed [rpm]	6000
	DC-bus voltage [V]	500
	Maximum torque [Nm]	400
NiMh battery	NiMh module number [-]	28
	Nominal energy [kWh]	1.3
	Nominal voltage [V]	201.6

M/G1 and M/G2

Based on the Willis equations, the torque on ring and sun could be related to the generated torque of the ICE. The next step is to relate the torque values of the planetary gear to the electrical machines. Both of these electrical machines are 3 phase PMSM.

The first electrical machine $M/G1$ is mounted on the ring and is also connected to the input of the final drive. Balancing the torque values thus yields:

$$T_{\mathrm{r}} + T_{\mathrm{M/G1}} = T_{\mathrm{GB_{in}}} \tag{6.23}$$

in which $T_{\mathrm{M/G1}}$ is the torque of $M/G1$ and $T_{\mathrm{GB_{in}}}$ is the input torque of the fixed gearbox that can be written as function of the wheel torque T_{w}:

$$T_{\mathrm{GB_{in}}} = \frac{\tau_{\mathrm{FG}} T_{\mathrm{w}}}{\eta_{\mathrm{FG}}} \tag{6.24}$$

By using (6.20) and (6.24), (6.23) can be written as function of T_{ICE}:

$$T_{\mathrm{M/G1}} = \frac{\tau_{\mathrm{FG}} T_{\mathrm{w}}}{\eta_{\mathrm{FG}}} - T_{\mathrm{ICE}} \frac{Z_{\mathrm{r}}}{Z_{\mathrm{r}} + Z_{\mathrm{s}}} \tag{6.25}$$

A similar methodology can be followed to write the torque of $M/G2$, $T_{\mathrm{M/G2}}$, as function of the generated torque of the ICE:

$$T_{\mathrm{M/G2}} = -T_{\mathrm{ICE}} \frac{Z_{\mathrm{s}}}{Z_{\mathrm{r}} + Z_{\mathrm{s}}} \tag{6.26}$$

According to Fig. 6.15, $M/G1$ is mounted on the ring and is connected, via the final drive, to the wheels. As the vehicle speed and thus the speed of the wheels is known apriori, the speed of $M/G1$, can thus be written as:

$$\Omega_{\mathrm{M/G1}} = \Omega_{\mathrm{r}} = \frac{\Omega_{\mathrm{w}}}{\tau_{\mathrm{GB}}} \tag{6.27}$$

Based on the speed relationship of the Willis equation, it is possible to derive the speed of $M/G2$ which is mounted on the sun:

$$\Omega_{\mathrm{M/G2}} = \Omega_{\mathrm{s}} = \frac{(Z_{\mathrm{r}} + Z_{\mathrm{s}})\, \Omega_{\mathrm{ICE}} - \Omega_{\mathrm{M/G1}} Z_{\mathrm{r}}}{Z_{\mathrm{s}}} \tag{6.28}$$

in which the speed of the ICE and $M/G1$ equal the speed of the carrier and ring, respectively.

Based on the equations mentioned above, it is possible to determine the operating points of both electrical machines. The efficiency of both $M/G1$ and $M/G2$ is taken into account on the basis of their efficiency map, see Fig. 6.16 and 6.17. Note that these efficiency maps present results of models, no actual measurements have been done to verify these results. However, a comparison between the efficiency maps and the measurement results presented in [10] show that model and measurements are approximately the same. Only at high speed and low torque, the model overestimates the efficiency, which is important to keep in mind.

Battery

The battery (NiMh) is used to balance the power flows between inner and outer rotor but also to store braking energy, which can be used later on to accelerate the vehicle when needed. As mentioned in Table 6.3, 28 cells connected in series are used. To model the behavior of the battery, a simplified equivalent model is used (Fig. 6.18).

Based on Fig. 6.18, the terminal voltage V_{bat} (equal to the input of the DC/DC converter) can be written as:

$$V_{\mathrm{bat}} = V_{\mathrm{oc}} - V_{\mathrm{R}} \tag{6.29}$$

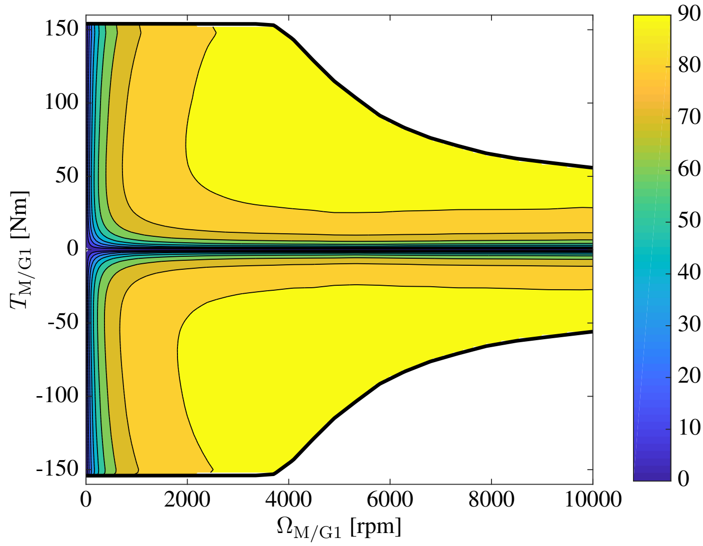

Figure 6.16: Efficiency map [%] of M/G1. Source: [127].

in which V_{oc} is the open circuit voltage and V_{R} is the voltage drop over the internal resistance R_{int}. Equation (6.29) can be written in terms of the battery power P_{bat}:

$$V_{\mathrm{oc}} = \frac{P_{\mathrm{bat}}}{i_{\mathrm{bat}}} + V_{\mathrm{R}} \tag{6.30}$$

which can be rewritten as:

$$i_{\mathrm{bat}} = \frac{V_{\mathrm{oc}} - \sqrt{V_{\mathrm{oc}}^2 - 4R_{\mathrm{int}}P_{\mathrm{bat}}}}{2R_{\mathrm{int}}} \tag{6.31}$$

Note that the power to or from the battery P_{bat} equals the sum of the electrical power of both electrical machines increased with the losses in the DC/DC converter and the auxiliary power (Fig. 6.15). In case of the EVT, the electrical power of the electrical machines is replaced by the electrical power of the stator and inner rotor. Moreover, the impact of the State of Charge (SoC) on the open circuit voltage V_{oc} has been modeled based on a LUT.

The SoC, which needs to be controlled, is calculated as:

$$SoC = SoC_0 - \int \frac{i_{\mathrm{bat}}}{3600C_{\mathrm{bat}}} \tag{6.32}$$

Finally, the losses of the battery $P_{\mathrm{l,bat}}$ can be calculated as:

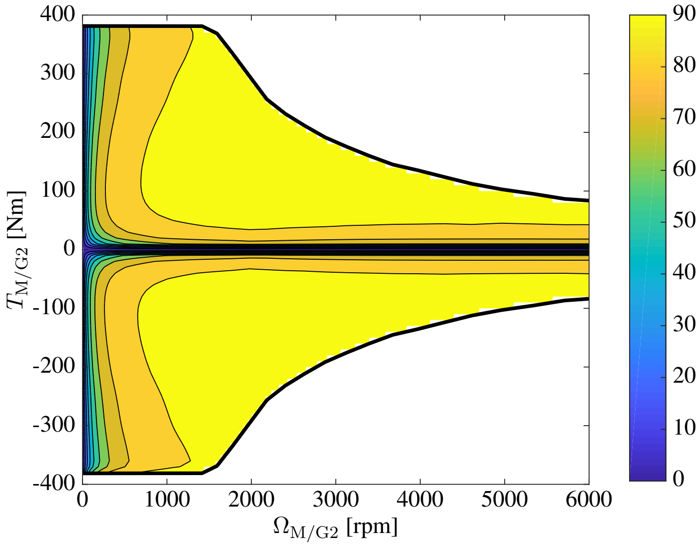

Figure 6.17: Efficiency map [%] of M/G2. Source: [127].

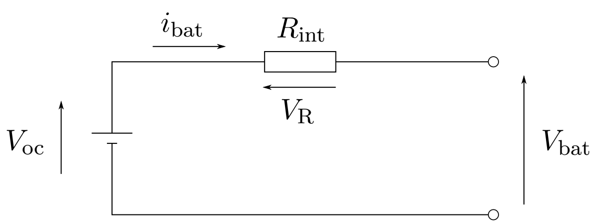

Figure 6.18: Thevenin equivalent circuit model of the battery.

$$P_{\mathrm{l,bat}} = R_{\mathrm{int}} i_{\mathrm{bat}}^2 \tag{6.33}$$

ICE

The fuel map of this ICE is shown in Fig. 6.19. The black dot represents the operating point which results in the lowest fuel consumption. In the analysis, the dynamics of the ICE are ignored. Only the fuel consumption of the ICE is taken into account together with its boundary conditions in terms of operating range.

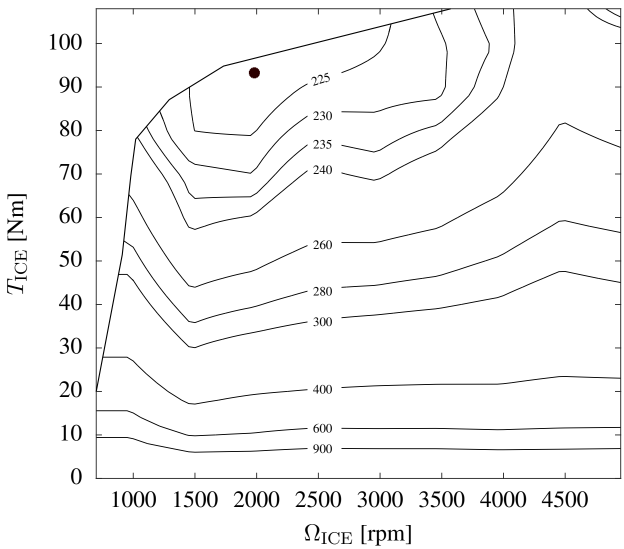

Figure 6.19: Fuel consumption [g/kWh] of the ICE used in a Toyota Prius (1497 cc, 57kW@5000 rpm). The black circle indicates the optimal operating point of the ICE. Source: [127].

DC/DC converter

The purpose of the DC/DC converter is to boost the battery voltage in order to be able to work on a fixed DC-bus voltage of 500V. The model that is used to calculate the DC/DC converter losses is made by Flanders Make and is based on a component loss model of KU Leuven (IGBT as switching technology). Both are developed to support the EMTechno project. To accelerate the computation, a map with the losses as a function of battery power $P_{\rm bat}$ and DC-bus voltage $V_{\rm DC}$ is generated (see Fig. 6.20). The input voltage (battery voltage) is considered fixed. This is not entirely correct as the battery voltage will vary with the SoC. However, the variation of the battery voltage is so small that it has no significant effect on the losses of the DC/DC converter.

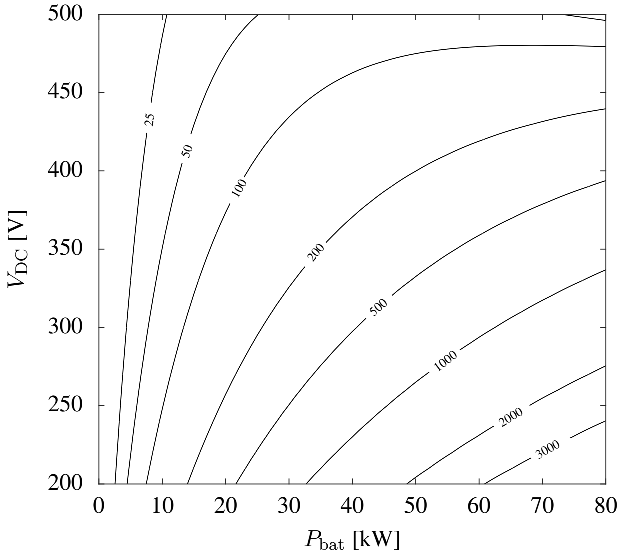

Figure 6.20: Power losses [W] in the DC/DC converter.

Vehicle

Both the wheel speed and the wheel torque are imposed by the driving cycle. The wheel speed is directly related to the vehicle speed and the wheel torque is related to the acceleration, speed of the vehicle (due to the speed dependency of for example the aerodynamic drag), vehicle parameters (see Table 6.4) but also the road gradient (ignored in (6.8)). Finally, the auxiliary power P_{aux} is a constant loss term that takes the power consumption into account of the fuel pump, water pump, ...

Table 6.4: Vehicle parameters of the Toyota Prius II.

Mass m [kg]	1360
Aerodynamic drag coefficient c_d [-]	0.24
Frontal cross sectional area A_f [m^2]	2.16
Rolling resistance coefficient f [-]	0.008
Wheel radius r_w [m]	0.29
Mass density of the air ρ [kg/m^2]	1.204
Power to drive the auxiliaries P_{aux} [W]	250

6.3.2 EVT based HEV

Fig. 6.21 gives a schematic overview of the EVT based HEV drive train. In accordance with previously published literature [92, 129], the inner rotor of the EVT is connected to the Internal Combustion Engine (ICE) while the outer rotor is connected, via the final drive, to the wheels of the vehicle. The purpose of this final drive is to change the speed ratio and deliver torque to both wheels.

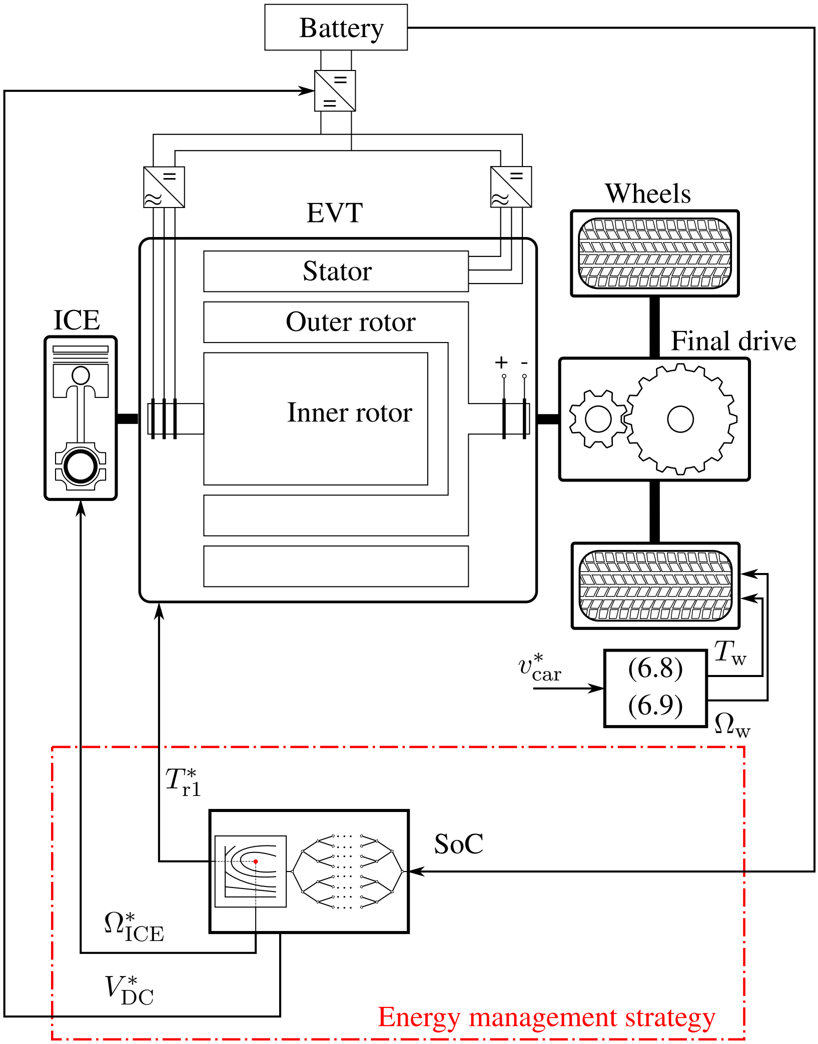

Figure 6.21: Schematic of an EVT based HEV.

In the following subsections, some information is presented on the sizing, the gears and the DC/DC converter. As the ICE has a dominant effect on the fuel consumption, the fuel map of the ICE used in the Toyota Prius II has been used (see section 6.3.1). Logically, the vehicle parameters (see section 6.3.1) and battery characteristics (see section 6.3.1) are also identical.

Overall dimensions

The total length of the reference EVT (EVT available in the lab of Ghent University) is 363.5 mm and the diameter is 338 mm (without housing). This means that the EVT is significantly bigger than the THS. Taking the size of the THS as a measure for the available space in a car, the EVT needs to be scale down. Otherwise, it might not fit.

In radial direction, the scaling factor K_{R} equals $\frac{270}{338} = 0.8$. These dimensions have been determined based on confidential construction drawings, no further information can be presented on this topic.

For the axial scaling factor, it is important to state that only a fraction of the total length is actively used. The length of the stack is only 87 mm, while the end winding takes 95 mm of the space (sum of both sides). The remaining 181.5 mm is used for slip rings (largest portion), bearings and spacing. Moreover, as shown in [130], the slip rings can be mounted inside the rotor. This results in a shorter device and therefore makes it possible to make the stack longer. Hence, if the active length is doubled ($K_{\mathrm{A}} = 2$), the total length becomes $2 \times 87 + 95 = 269$ mm. As slip rings are inside the rotor, this leaves 51 mm for the bearings and spacing. Scaling the EVT with $K_{\mathrm{A}} = 2$ will thus result in a device with a compareable length as the THS.

Gears

With the driving cycle as input, the wheel torque and speed are known as function of time. These properties can be translated towards the outer rotor based on the following expressions:

$$\Omega_{\mathrm{r2}} = \frac{\Omega_{\mathrm{w}}}{\tau} \tag{6.34}$$

$$T_{\mathrm{r2}} = \frac{T_{\mathrm{w}}\tau}{\eta^{\mathrm{sign}(T_{\mathrm{w}})}} \tag{6.35}$$

in which η is the efficiency of the final drive (fixed value of 97%) and τ is the speed ratio which equals 0.2. Note that during braking, the efficiency term goes to the numerator as power flows from the wheels to the outer rotor. In the comparison of the CVT based vehicles, this was not the case as all braking torque was produced by mechanical brakes. Finally, the relation between the operating points of the ICE and inner rotor are written as follows:

$$\Omega_{\mathrm{r1}} = \Omega_{\mathrm{ICE}} \tag{6.36}$$

$$T_{\mathrm{r1}} = -T_{\mathrm{ICE}} \tag{6.37}$$

DC/DC converter

In contrast to the DC/DC converter that is used in the Prius, the converter in the EVT is not only used to boost the battery voltage to a fixed DC-bus voltage. The component is also used to actively control the DC-bus voltage in order to optimize the energy efficiency of the EVT subsystem (EVT and its inverters). This is possible as the switching losses in the inverter are dependent on the used DC-bus voltage, see (4.62). Moreover, PWM induced iron losses also clearly depend on the DC-bus voltage (see (4.55)). Decreasing the DC-bus voltage will thus have a positive effect on the losses.

The question is: how much can the DC-bus be decreased? As explained in section 4.5, the maximum torque of the stator and inner rotor can be calculated for a given DC-bus voltage as function of the outer rotor speed and the difference in speed of both rotors, respectively. By inverting this relation, it is possible to calculate the minimal DC-bus voltage as function of the operating point. To avoid instability, the minimum desired DC-bus voltage is fixed at the nominal battery voltage.

To have a fair comparison with the Toyota Prius II, the same DC/DC converter model is used to calculate the losses of the component.

6.3.3 Optimal control - Dynamic programming

Dynamic Programming (DP) allows to find the optimal solution of a control problem and is commonly used to optimize the energy management problem of HEVs. It is able to optimize the power flows in the system by using an a priori known driving cycle [14, 131, 132]. Therefore, this method cannot be used in an online controller. However, as DP optimizes the system, it is ideal to benchmark different topologies of comparable drive trains.

The DP algorithm is based on the principle of optimality (optimal substructure) defined by Bellman which states that an optimal solution can be constructed from optimal solutions of its sub-problems [133, 134]. Or in other words: a large problem can be solved given the solution of its smaller sub-problems.

To explain how it works, a simple example is executed (see Fig. 6.22). Assume there is a system with a state X that needs to be controlled during a period in time while the cost is minimized. The state is constrained in such a way that it should never exceed X_{max} nor be lower than X_{min}. In addition, the value of the state at the beginning and end should be the same. The first step is to discretize the problem in time. The result is a set of sub-problems that define the system each on one time instant. According to the principle of optimality, optimizing these sub-problems will optimize the system. The second step is to define a grid to determine the space in which the state can vary.

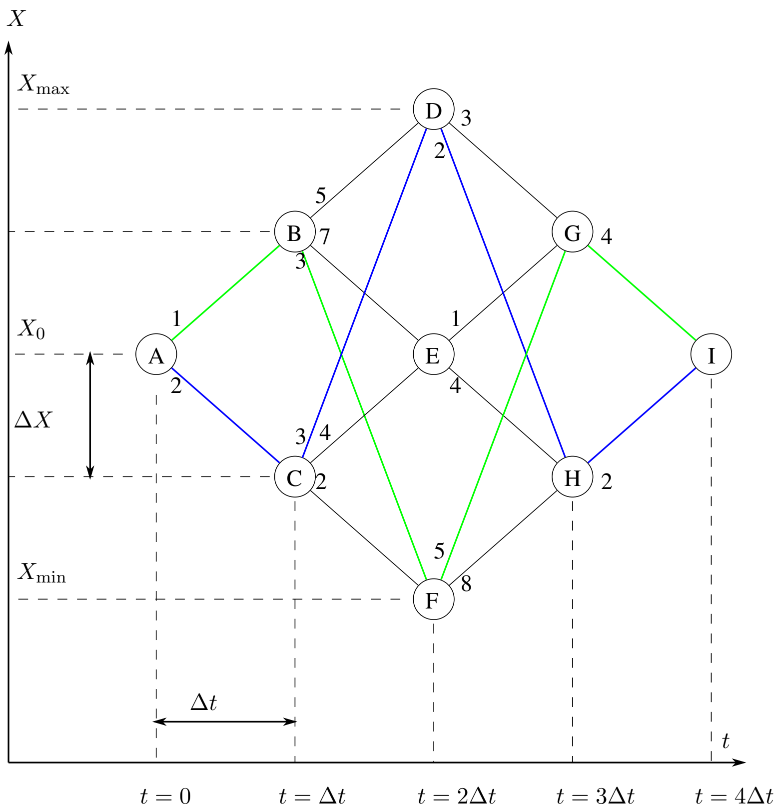

Figure 6.22: Optimization problem used as example to explain dynamic programming.

In Fig. 6.22, all possible paths are drawn and the cost of each action is mentioned on the path. To find the optimum, the sub-problems need to be optimized. However, this does not mean that the optimal solution is defined by following the path with the lowest cost from node to node (see green line in Fig. 6.22: total cost equals 13). Hence, a path with a higher cost at time instant n could lead to a lower overall cost. The actual meaning of optimality is that once you have found an optimal path between, for example A and D (Z_{D}), all paths going through D towards I will have followed Z_{D}.

Table 6.5: Optimal path

Cost z	Followed route Z
$z(A) = 0$	$Z(A) = A$
$z(B) = z(A) + 1 = 1$	$Z(B) = AB$
$z(C) = z(A) + 2 = 2$	$Z(C) = AC$
$z(D) = z(C) + 3 = 5$	$Z(D) = ACD$
$z(E) = z(C) + 4 = 6$	$Z(E) = ACE$
$z(F) = z(C) + 2 = 4$	$Z(F) = ACF$
$z(G) = z(E) + 1 = 7$	$Z(G) = ACEG$
$z(H) = z(D) + 2 = 7$	$Z(H) = ACDH$
$z(I) = z(H) + 2 = 9$	$Z(I) = ACDHI$

To find the solution of this problem, the cost of the route towards a node ($z(A)$, $z(B)$, $z(C)$, $z(D)$, $\dots$), needs to be calculated. By keeping track of the cost of each path, the optimal paths can be saved (see Table 6.5). By starting each new section of the path with the previously found optimal path, the solution of the problem is found which equals 9 as cost (see blue line in Fig. 6.22). More important, besides the fact that the optimal solution is found, is the number of calculations it took to find the solution. Here, it took 8 sums to find the optimal path. In contrast, if all possible paths would have been analyzed to select the optimal one, 32 sums would have been required (4 sums for each of the 8 possible paths). This difference in computational effort may seem negligable but is of great importance when more complex systems are analyzed over a much bigger time horizon.

Of course, the drive train of a HEV is more complex than the example presented above. But in essence, the same principle is used to optimize the power flows. The state is in this case the SoC of the battery which may vary between 2 fixed values. Identical to the example, the SoC at the beginning and end of the driving cycle should be the same. The input variables, that define the cost of a path are the torque and speed of the wheels and the chosen operating points of the ICE. As a matter of fact, as the driving cycle is a priori known and imposed to the system, the torque and speed of the wheels are not considered as controllable variables.

To find a solution in a computationally efficient manner, the open source toolbox provided by Sundström and Guzella has been used as framework for the DP structure [132]. The framework requires a Matlab model of the considered drive train and definitions in terms of cost and discretization step. The chosen discretization step for the SoC, operating points of the ICE and time are shown in Table 6.6. Note that the initial value for the SoC, SoC_0, and the final value SoC_{end} are slightly different. This is to give the algorithm a bit of freedom as it is not possible to have exactly the same value SoC_0 and SoC_{end}.

Table 6.6: Chosen parameters for the DP algorithm.

State of Charge SoC	Number of values n_{SoC}	100
	Maximum value SoC_{max} [%]	60
	Minimum value SoC_{min} [%]	30
	Initial value SoC_0 [%]	50
	Final value SoC_{end} [%]	51
Speed of the ICE Ω_{ICE}	Number of values $n_{\mathrm{ICE,N}}$	50
	Maximum value $\Omega_{\mathrm{ICE,max}}$ [rpm]	3500
	Minimum value $\Omega_{\mathrm{ICE,min}}$ [rpm]	700
Torque of the ICE T_{ICE}	Number of values $n_{\mathrm{ICE,T}}$	50
	Maximum value $T_{\mathrm{ICE,max}}$ [Nm]	95
	Minimum value $T_{\mathrm{ICE,min}}$ [Nm]	0

6.3.4 Results

In the following subsections, the state of charge, energy balance and fuel consumption of the THS and EVT based drive train are compared.

State of Charge

The most important constraint for the DP algorithm is related to the SoC: SoC_0 must equal SoC_{end}. It is thus important to check whether the algorithm succeeded in this tasks. Fig. 6.23 shows the SoC as function of time for all considered simulations. The maximum deviation on the constraint is 0.3% (Fig. 6.23 (c), EVT based, $SoC_{\mathrm{end}} = 50.3\%$). This means that more energy has been stored in the battery than was strictly necessary. With ideal settings of the DP algorithm (higher n_{SoC}), SoC_{end} will be closer to 50% which will further decrease the fuel consumption.

Due to the small deviation between SoC_0 and SoC_{end}, it is concluded that all the simulations are valid and that the results in terms of losses and fuel consumption can be compared.

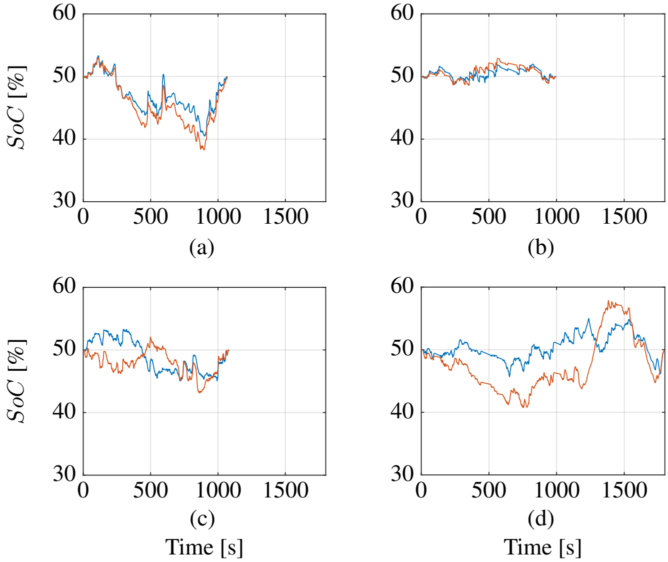

Figure 6.23: SoC of the battery used in the EVT (blue) and THS (red) based drive train for different driving cycles: (a) Artemis highway, (b) Artemis urban, (c) Artemis road and (d) WLTC.

DC-bus voltage

As mentioned before, the DC-bus voltage of the THS system is kept constant at 500V. The voltage of the EVT, in contrast, is varied to optimize the losses (see Fig. 6.24). However, due to the optimal choice of the gear ratio and the scaling of the EVT, the DC-bus is kept at a minimum for almost the entire driving cycle resulting in minimal losses in the EVT. Only when the required torque rises towards the maximum achievable torque, the DC-bus voltage is increased. The dynamics of the control of the DC-bus voltage are ignored in this analysis (theoretical maximum variation equals 300V/s, but this never occurs).

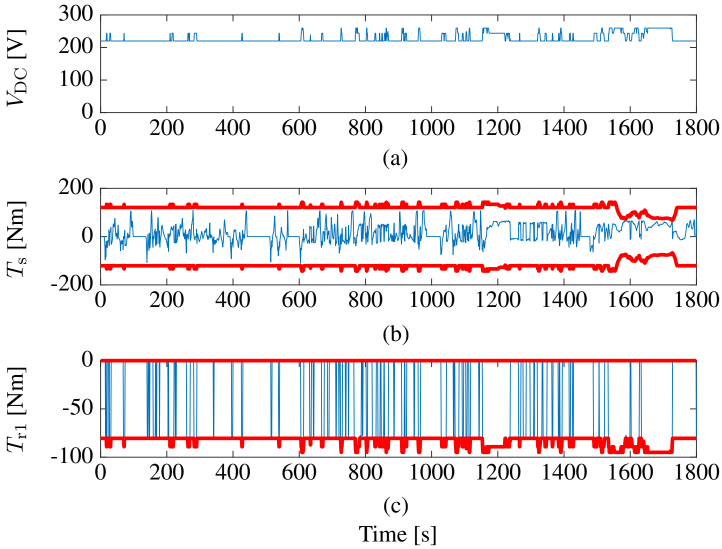

Figure 6.24: Variation of the DC-bus voltage (a) and the impact on the torque limits for the stator (b) and inner rotor (c).

Energy balance

The energy balance of the system gives an idea of the losses in the system (see Fig. 6.25). The figure includes the losses due to the auxiliary components, the losses in the electrical machines in which the stator losses are denoted by $M/G1$ and the inner rotor losses by $M/G2$ (both include inverter losses). Furthermore the battery losses E_{bat} and losses in the mechanical gears, are shown on the bar diagram as E_{GB}.

From Fig. 6.25, one thing is clear: the EVT consumes less energy than the THS. Explaining why is complex as it depends on the chosen power flows by the DP algorithm. The DP algorithm can for example decide to use the stator in a bad operating point as this could allow to use the ICE in a more optimal point. This makes it difficult to compare single loss components as it shows only a part of the story.

The battery losses are comparable. This makes perfect sense as the SoC of the THS and EVT based drive train follow similar trends (see Fig. 6.23). This means that the current through the battery is similar and thus also the losses. In contrast to the battery losses, higher DC/DC converter losses are found for the EVT based drive train. This is also fairly easy to explain based on Fig. 6.20 that presents the losses of the DC/DC converter. The THS is used at a constant DC-bus voltage of 500V which means that the DC/DC converter is used in a highly efficient operating area. The EVT on the other hand, works at very low voltage (see Fig. 6.24). This results in much higher losses and thus explains the higher E_{DCDC}. However, comparing the losses in DC/DC converter with the overall energy consumption shows that the impact of these losses is close to be negligible.

However, the most important difference is to be found in the energy consumption of the mechanical gear(s). The difference can be explained based on Fig. 6.15 and Fig. 6.21: the EVT based HEV uses only a single gearbox and that explains the lower energy consumption. This is of high importance, because it shows that there is a good alternative for the mechanical power split based on a planetary gear: the EVT. Where the difference in machine losses could be reduced over time through design optimizations, the THS will always suffer from the disadvantage of the extra planetary gear.

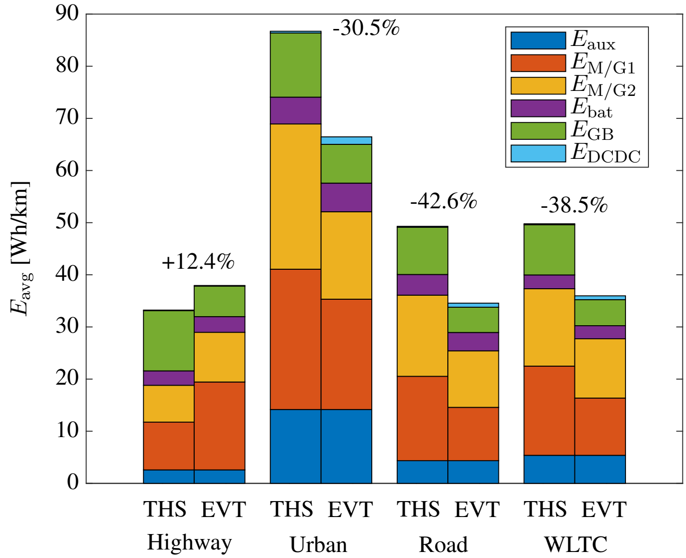

Figure 6.25: Energy balance of EVT and THS for different driving cycles. The numbers above the bar diagram indicate the difference $\frac{E_{\mathrm{EVT}}-E_{\mathrm{THS}}}{E_{\mathrm{EVT}}}$ [%] between EVT and THS.

Fuel consumption

The fuel consumption of the THS and EVT based drive train are presented in Table 6.7. As could be expected based on the comparison of the losses, the EVT performs better than the THS. The gains are a bit lower than reported in Fig. 6.25, but that is because the energy consumption of the ICE was not taken into account.

Fig. 6.26 shows the chosen operating points of the ICE (lefthand side) and

Table 6.7: Comparison of the fuel consumption of a THS and EVT based drive train for different driving cycles

Driving cycle	THS fuel consumption [l/100km]	EVT fuel consumption [l/100km]	Decrease in fuel consumption by using EVT [%]
Artemis highway	5.94	5.52	-7.6
Artemis urban	4.79	4.24	-13.0
Artemis road	4.15	3.71	-11.9
WLTC	4.59	4.17	-10.1

the consumed energy (righthand side), valid for the WLTC. Apart from the lower losses in the EVT, the EVT based drive train is also able to use the ICE in operating points with a higher efficiency. As the DP algorithm is responsible for the selected operating points, it is difficult to find any reasoning behind it. The only thing that is certain is that the DP algorithm strives to minimize the losses of the complete system as this optimizes the fuel consumption.

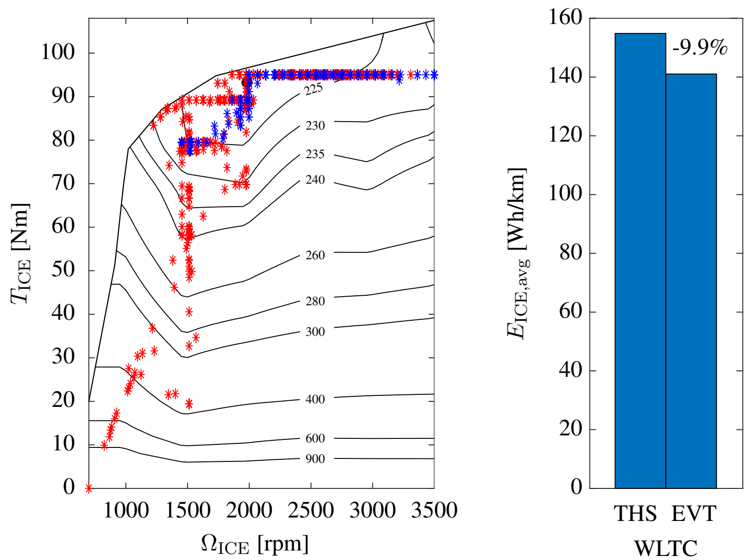

Figure 6.26: The chosen operating points of the ICE are presented on the lefthand side (blue: EVT, red: THS). The energy consumption [Wh/km] is shown on the righthand side. The number above the bar diagram indicates the difference $\frac{E_{\mathrm{EVT}}-E_{\mathrm{THS}}}{E_{\mathrm{EVT}}}$ [%] between EVT and THS.

6.3.5 Conclusion

The comparison between the THS and EVT have shown that the EVT is a promising technology. The losses in the EVT and its system are lower compared to the THS. The need for only one gearbox in the EVT structure is the main reason for the reduction in fuel consumption.

6.4 Overall conclusion

This chapter presents a comparison between 3 types of variable transmissions, the belt CVT, toroidal CVT and EVT, on the component level and system level. Consequently, the third and forth research goal, given in section 1.2, have been completed in this chapter.

The component level comparison has shown that the 3 considered technologies can be designed to have a similar maximum output torque. However, the speed ratio spread of the EVT is significantly larger compared to its mechanical variants. In terms of efficiency, the belt CVT generally performs best, although this conclusion depends on the chosen operating point. Moreover, the differences in efficiency between the considered variable transmissions remains limited to a maximum of 4%. Note that both the belt CVT and the toroidal CVT have been idealized in terms of clamping force control and synchronization of the rollers, respectively. As a consequence, differences between the variable transmissions will be even smaller in reality.

At system level, 2 applications have been considered: a CVT based vehicle and a hybrid electrical vehicle. The conclusion of both applications is that the EVT outperforms the classical topologies. For the CVT based vehicle, the difference in ratio spread is the main reason for the excellent results of the EVT based vehicle. Due to this wide speed ratio range, the clutch is seldom used and more efficient operating points of the ICE can be chosen.

The importance of the chosen operating points of the ICE are still important in the comparison between the Toyota Prius II and the EVT based HEV. However, the difference in mechanical losses in the gears is crucial. This is due to the fact that the EVT only needs a single gearbox (transfer power to the wheels), while the THS is equipped with 2 gears (one for the power split, one for the wheels). This means that the mechanical losses in the THS are significantly higher, which has a negative effect on the fuel consumption. The comparison shows that an EVT based drive train can reduce the fuel consumption up to 13% compared to a Toyota Prius II. Important to mention is that the models used to determine the losses of the EVT are validated on an actual prototype. With the THS, the overall efficiency estimations are realistic, but they are not validated. It is thus to be expected that the differences in reality can be even bigger, in favor of the EVT.

The overall comparison thus proves the potential of the EVT and shows the importance of system level comparisons. Comparing just the component is clearly not enough to draw the correct conclusions.

Chapter 7

Concluding remarks

In this chapter, the conclusions of this dissertation are summarized. The research goals that were formulated in the introduction are used as guideline. Furthermore, at the end of the chapter, possibilities for future research are presented.

7.1 Conclusions

This thesis has 4 important research goals that were defined in section 1.2. The most important goals, the second and third, are related to comparing variable transmissions throughout their operating range, both at component level and system level. However, in order to pursue those objectives, component models and design rules to match the size of the variable transmissions are needed (first and second research goal).

Chapters 2, 3 and 4, focus on the modeling of the variable transmissions (first goal). For each transmission, a similar model structure (inputs and outputs) was made in order to facilitate the comparison. Moreover, the component control is derived and the simulated efficiency is validated based on available data from literature.

Besides the primary goal, other interesting conclusions are drawn based on the first 3 chapters. For the toroidal CVT, it is shown that the design of the loading cam, which is responsible for the clamping force, has a significant impact on the dynamic behavior and efficiency. Moreover, there is a trade-off between dynamics and efficiency. This is shown based on a stiffer design of the loading cam that resulted in faster dynamics but lower efficiency. Furthermore, the maximum torque of the toroidal CVT is described as function of geometrical variables in order to aid in the design of the CVT (second goal). Slip dynamics were derived for both the toroidal as the belt CVT to optimize the efficiency. In case of the belt CVT this means that the safety factor for the clamping forces (ratio of applied clamping force and minimum clamping force) equals 1, which results in high efficiency.

In contrast with the toroidal and belt CVT, multiple models for the EVT have been described: a static, hybrid and dynamic model. The static model ignores all dynamics and is used for the vehicle simulations. The hybrid model takes the rotational dynamics into account and the dynamic model also inherits the current dynamics. In order to be able to redesign the EVT to match the size of the reference variable transmission, i.e. the belt CVT, a magnetic equivalent circuit model is made. This model structure is solved much faster than the FE model and still provides results with acceptable accuracy. However, it still takes too much time to quickly analyze the effect of a general change of dimensions.

To solve this, scaling laws for the EVT have been developed in chapter 5. Although the concept of the scaling laws is not new, it has not been presented before for an EVT. Moreover, the combination between the scalable design and scalable control is entirely new. Based on the scaling laws and an accurate description of the influence of the 5 independent current components on the flux linkage with the stator and inner rotor of a reference machine, it is possible to calculate copper and iron losses of a scaled EVT in about 0.02 s. This is more than 2000 times faster compared to the FE based method. The method can thus be used as part of a general optimization routine, which selects the optimal components of a drive train with an EVT. As an EVT is developed for HEV applications, the primary use of the presented method is in the optimization of such drive trains, which matches the second research goal.

Finally, all models are used to compare the 3 types of variable transmissions, both on the component and system level. The comparison of the operating range reveals that the EVT has a significantly larger speed ratio spread compared to its mechanical variants. In terms of efficiency, the belt CVT as a component generally performs best, although this conclusion depends on the chosen operating point (third research goal).

On the system level, 2 different system level analysis have been performed: based on a CVT driven vehicle (third research goals and a HEV (forth research goal). The results of the CVT driven vehicle show that the wide ratio range of the EVT is much more important than the difference in efficiency between the variable transmissions. Due to that wider ratio spread, the ICE can be operated in an operating area that is more efficient, which reduces the overall fuel consumption.

The importance of the chosen operating points of the ICE are still important in the comparison between the Toyota Prius II and the EVT based HEV. However, the difference in mechanical losses in the gears is crucial. The EVT only needs a single gearbox to transfer power to the wheels, while the THS is equipped with 2 gears, one for the power split and one for the wheels. Furthermore, the losses in the THS are bigger compared to the EVT. Consequently, the fuel consumption of the THS are higher. The comparison shows that an EVT based drive train can reduce the fuel consumption up to 13% compared to a THS (Toyota Prius II). It is important to mention that the models used to determine the losses of the EVT are validated on an actual prototype. With the THS, the overall efficiency estimations are realistic, but they are not validated. It is thus to be expected that the differences in reality can be even bigger, in favor of the EVT.

7.2 Recommendations for future work

For both the toroidal CVT as the EVT, the maximum torque has been quantified in equations. However, for the belt CVT this has not been done yet. Although the variator model (CMM) is used to calculate that maximum torque, the computational effort is very high. Finding a way to express the maximum torque in a formula with easy to determine parameters would certainly be an asset.

In terms of slip control, the impact of the dynamics of the hydraulic circuit needs to be modeled and investigated. Furthermore, it would be interesting to apply the developed slip controller on an actual belt CVT. Although the slip controller remained stable during load variations, measurements could prove if the safety factor can actually drop to 1.

Scaling laws have shown how the EVT can be redesigned. However, the boundaries of optimality, i.e. maximum or minimum scaling factor for which the design is still optimal, are unknown. To investigate this, one could use the magnetic equivalent circuit model to do a fast assessment of the impact of certain design changes (for example adjusting the diameter of the inner and outer rotor), given fixed outer dimensions equal to the scaled design. Later, when a new design is found, a detailed FE model can be constructed. For scaling factors close to 1, it is likely that the differences between the scaled design and the completely new optimal design will be small. The interesting part is of course, finding the pair of scaling factors for which this is not anymore the case: the boundaries of optimality. Defining these boundaries of optimality would be entirely new and of great importance if the EVT would be, for example, used in a truck.

The electromagnetic aspects are covered with the scaling laws. However, while down scaling the EVT, thermal issues might occur. At this moment there is no scalable thermal model to investigate the impact. Deriving such a model would be an important step in the overall design methodology.

In terms of the system level comparison, it would be interesting to investigate the losses in the planetary gear as function of the power flows. The basic framework for this analysis has already been presented in appendix A. However, measurements on the planetary gear of the THS are required to accurately predict the efficiency.

The presented work provides a comparison between 3 different variable transmissions. This decision was made based on their applicability in automotive applications and the efficiency. As a result, the hydraulic variants of a variable transmission are not discussed. However, new types of variable transmissions will be launched in the future. It is thus important to follow up these new contributions to the state of the art and extend the comparison if necessary. Furthermore, the EVT can be used for much more applications than just a passenger car. Hence, the added value of an EVT in off-road vehicles where the torque converter could be removed (also the case in some passenger cars and trucks) or in towing boats that now suffer from sudden load variations, could have a far greater impact on the environment due to the increased power scale.

Appendix A

Planetary gear model

In this appendix, a method to calculate the efficiency of a planetary gearbox with 2 degrees of freedom is proposed. Standard measurement procedures in which the efficiency is measured as function of the load torque and input speed become infeasible due to the many possible input output configurations. To solve this, a method is proposed that combines the theory of virtual power and a limited set of measurements. The theory of virtual power is used to link the power flow in the device with an expression to calculate the efficiency of the planetary gear in terms of the efficiency of the power path between sun & carrier and carrier & ring. The efficiency of the aforementioned power paths is shown to depend only on the torque applied to these paths which means that speed dependent losses such as churning losses are negligible. Measurements of the efficiency as function of the torque applied to the sun for a varying speed ratio between ring and carrier are added to validate the approach.

A.1 Theoretical model

The considered planetary gear consists of a sun, carrier with planets and a ring, organized as in Fig. A.1. The main parameters of the planetary gear can be found in Table A.1.

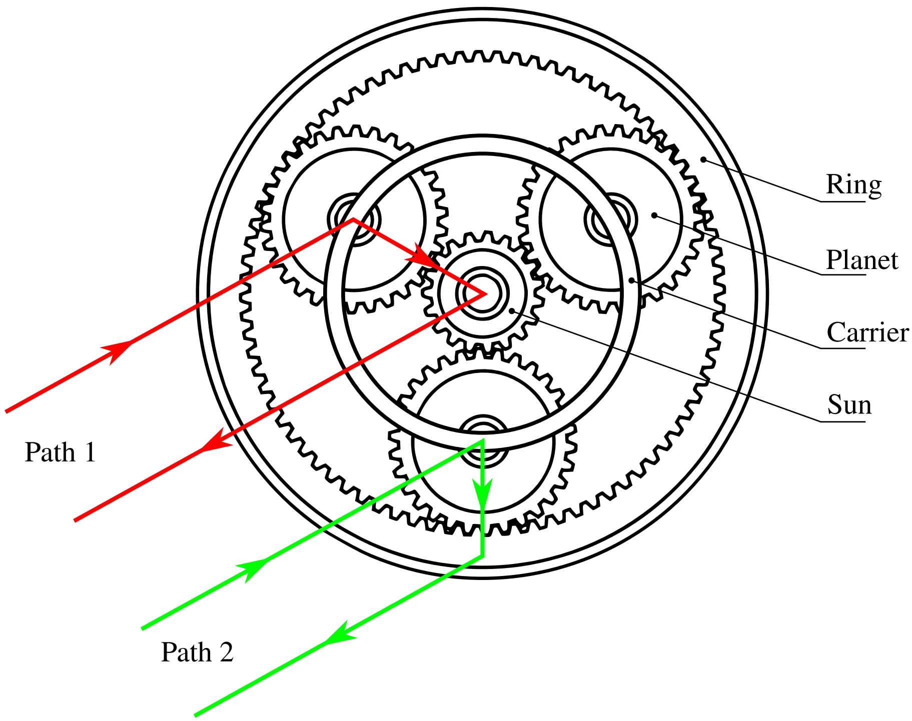

Figure A.1: Principle scheme of the planetary gear.

Table A.1: Characteristics of the planetary gear train

Number of teeth ring Z_{r} [-]	108
Number of teeth planets Z_{p} [-]	26
Number of teeth sun Z_{s} [-]	54
Maximum torque ring $T_{\mathrm{r,max}}$ [Nm]	90
Maximum torque carrier $T_{\mathrm{c,max}}$ [Nm]	137
Maximum torque sun $T_{\mathrm{s,max}}$ [Nm]	45

As described in [135], it is possible to derive the efficiency of the 2-DOF planetary gearbox as function of the power flow (P_{s},P_{c},P_{r}), speed ratio between carrier and sun $\left(\frac{\Omega_{\mathrm{c}}}{\Omega_{\mathrm{s}}}\right)$ and 2 efficiency values that describe the efficiency of power path 1 and 2 (η_1,η_2). Deriving the equations for the considered planetary gear is straightforward based on the content of [135] as all the equations of a similar planetary gear are derived in that paper. Hence, only the definition of parameter C_2 (see (A.6)) is different compared to the original paper which is due to the slightly different configuration of the planetary gear.

Table A.2, gives an overview of all the possible equations to calculate the efficiency. The first step in selecting the correct equation is to determine the power flow. Based on the power flow, it is possible to select a row in Table A.2. If, for example, the power flows from the sun ($P_\mathrm{s} < 0$) to the carrier ($P_\mathrm{c} > 0$) and ring ($P_\mathrm{r} > 0$), row 3 is selected. The second step is to select the correct subcase (A or B). The conditions for these subcases are given in Table A.3 and depend on the speed ratio between carrier and sun. For more information concerning the derivation of the subcases and separate efficiency equations, the reader is referred to [135].

Table A.2: Equations to calculate the efficiency as function of the power flow and a given subcase.

	Subcase A	Subcase B
$P_\mathrm{s} > 0$, $P_\mathrm{c} > 0$ and $P_\mathrm{r} < 0$	$\eta = \frac{1-A}{1-A+AC_2}$	$\eta = \frac{1}{1-A+AC_2}$
$P_\mathrm{s} > 0$, $P_\mathrm{c} < 0$ and $P_\mathrm{r} > 0$	$\eta = \frac{-C_1+AC_1+C_2-AC_1C_2}{-C_1+AC_1+C_2}$	$\eta = \frac{C_1-C_2+AC_2-AC_1C_2}{C_1-C_2+AC_2}$
$P_\mathrm{s} < 0$, $P_\mathrm{c} > 0$ and $P_\mathrm{r} > 0$	$\eta = \frac{1}{1-A+AC_1}$	$\eta = \frac{1-A}{1-A+AC_1}$
$P_\mathrm{s} > 0$, $P_\mathrm{c} < 0$ and $P_\mathrm{r} < 0$	$\eta = 1 - AC_1$	$\eta = \frac{-1+A-AC_1}{-1+A}$
$P_\mathrm{s} < 0$, $P_\mathrm{c} > 0$ and $P_\mathrm{r} < 0$	$\eta = \frac{C_1-AC_1-C_2}{C_1-C_2-AC_1+AC_1C_2}$	$\eta = \frac{-C_1-AC_1+C_2}{-C_1+C_2-AC_2+AC_1C_2}$
$P_\mathrm{s} < 0$, $P_\mathrm{c} < 0$ and $P_\mathrm{r} > 0$	$\eta = \frac{-1+A-AC_2}{-1+A}$	$\eta = 1 - AC_2$

The variables in Table A.2 are calculated as:

$$A = \lambda_1 + \lambda_2 - \lambda_1\lambda_2 \tag{A.1}$$

$$\lambda_1 = 1 - \eta_1\left(T_\mathrm{s}, \Omega_\mathrm{p}\right) \tag{A.2}$$

$$\lambda_2 = 1 - \eta_2\left(T_\mathrm{r}, \Omega_\mathrm{p}\right) \tag{A.3}$$

$$k = \frac{\Omega_\mathrm{c}}{\Omega_\mathrm{s}} \tag{A.4}$$

Table A.3: Conditions of the subcases.

	Subcase A	Subcase B
$P_\mathrm{s} > 0$, $P_\mathrm{c} > 0$ and $P_\mathrm{r} < 0$	$k < 0$	else
$P_\mathrm{s} > 0$, $P_\mathrm{c} < 0$ and $P_\mathrm{r} > 0$	$\frac{Z_\mathrm{s}}{Z_\mathrm{r+Zq}} < k < 1$	else
$P_\mathrm{s} < 0$, $P_\mathrm{c} > 0$ and $P_\mathrm{r} > 0$	else	$0 < k < \frac{Z_\mathrm{s}}{Z_\mathrm{r}+Z_\mathrm{s}}$
$P_\mathrm{s} > 0$, $P_\mathrm{c} < 0$ and $P_\mathrm{r} < 0$	$0 < k < \frac{Z_\mathrm{s}}{Z_\mathrm{r}+Z_\mathrm{s}}$	else
$P_\mathrm{s} < 0$, $P_\mathrm{c} > 0$ and $P_\mathrm{r} < 0$	$k > 1$	else
$P_\mathrm{s} < 0$, $P_\mathrm{c} < 0$ and $P_\mathrm{r} > 0$	else	$k < 0$

$$C_1 = 1 - k \tag{A.5}$$

$$C_2 = \frac{(k-1)\,Z_\mathrm{s}}{(k-1)\,Z_\mathrm{s} + kZ_\mathrm{r}} \tag{A.6}$$

A.2 Measurement setup

The measurement setup consists of a planetary gear, a belt, 3 torque sensors and 3 electrical machines to load the shafts of the planetary gear (see Fig. A.2). The purpose of the belt is to transmit torque from the ring to the load machine (and vise-versa). The torque sensors are used to measure the mechanical power going through each shaft. Each shaft can be mechanically locked to go from a 2-DOF system to a 1-DOF system. These fixing mechanisms are used to block the sun and ring in 2 separate measurements in order to set up the 1-DOF efficiency maps of power path 1 and 2. Note that the efficiency map for the power path from carrier to ring includes the efficiency of the belt. The planetary gear system as such is thus the combination of the planetary gear component and the belt. During all measurements, the temperature has been controlled at 32±1°C. This is of high importance due to the impact of temperature on the viscosity of the oil and thus the efficiency of the gearbox [136].

A.2.1 Measurement accuracy

The accuracy of the measured efficiency depends on the accuracy of the torque sensors and the AD conversion of the signals. The torque sensors are equipped with strain gauges and have a contactless signal transmission from rotor to stator. The details in terms of range and accuracy of the 3 torque sensors can be found in Table A.4.

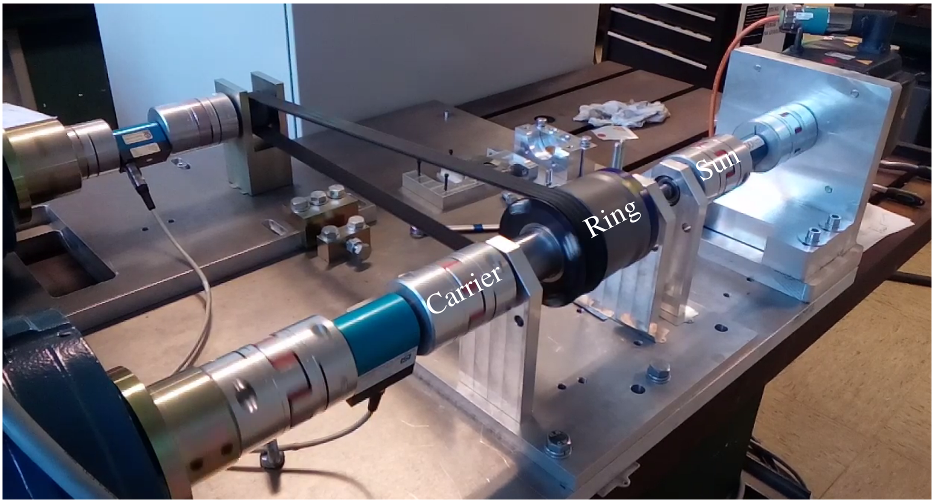

Figure A.2: Measurement setup.

Table A.4: Accuracy of the torque sensors.

Range	Accuracy	Absolute fault	Location
50 Nm	0.2% full scale	±0.1 Nm	Sun
100 Nm	0.1% full scale	±0.1 Nm	Ring
200 Nm	0.1% full scale	±0.2 Nm	Carrier

The accuracy of the AD conversion is 0.11% full scale. The range goes from 0 to 5 V for the torque sensors with a range of 50 and 100 Nm. For the torque sensor with a range of 200 Nm, the output range is 0 to 10 V.

To demonstrate how the Absolute Fault (AF) on an efficiency measurement can be calculated, an example is presented for a blocked ring gear. In this case, power flows from carrier to sun. The torque at the sun T_s equals 26 Nm, at the carrier T_c a torque of 80 Nm is applied, the speed of the sun Ω_s equals 792 rpm and the speed of the carrier Ω_c is equal to 264 rpm. The efficiency of this path can be calculated as:

$$\eta = \frac{P_{\text{out}}}{P_{\text{in}}} = \frac{T_s\Omega_s}{T_c\Omega_c} = \frac{T_s\Omega_c\frac{Z_s+Z_r}{Z_s}}{T_c\Omega_c} = \frac{T_s\left(Z_s+Z_r\right)}{T_cZ_s} = 97.5\% \tag{A.7}$$

The total uncertainty of this measurement depends on the uncertainty of the torque sensor and the uncertainty of the AD conversion (output of the torque sensor is an analogue signal). The accuracy of the speed measurement has no impact on the measured efficiency as can be seen in (A.7). The total Relative Fault (RF) and AF are calculated using the following equations:

$$RF(tot) = \sqrt{RF(T_\mathrm{s})^2 + RF(T_\mathrm{c})^2} = \sqrt{\left(\frac{AF(T_\mathrm{s})}{|T_\mathrm{s}|}\right)^2 + \left(\frac{AF(T_\mathrm{c})}{|T_\mathrm{c}|}\right)^2} \quad \text{(A.8)}$$

$$AF(tot) = RF(tot)\eta \quad \text{(A.9)}$$

According to Table A.4, the AF on the torque sensor of the sun is ± 0.1 Nm and of the carrier ± 0.2 Nm. The AF due to the AD converter of the torque sensor of the sun is 10 V$\times$11%=$\pm$11 mV which translates to ± 0.055 Nm. The same can be done for the torque sensor mounted at the carrier which results in an AF of ± 0.22 mNm. Based on (A.8) it is now possible to calculate the total relative fault $RF(tot)$:

$$RF(tot) = \sqrt{\left(\frac{0.1 + 0.055}{26}\right)^2 + \left(\frac{0.2 + 0.22}{80}\right)^2} = 0.79\% \quad \text{(A.10)}$$

which yields an AF of:

$$AF(tot) = \frac{0.79}{100} \times \frac{97.5}{100} = 0.77\% \quad \text{(A.11)}$$

A.3 Measurement of 1-DOF efficiency map

In the following sections the results of the 1-DOF measurements of the 2 power paths are discussed. Note that only a limited dataset is presented here. Hence, the variation of the efficiency with the speed of the planets is discussed based on 4 measurements. However, the real measured dataset covers the efficiency for 18 different speed values, each for 31 torque values.

A.3.1 Path 1 (sun to carrier)

As mentioned in (A.2), the efficiency η_1 is a function of torque and speed. The efficiency η_1 is related to the power path between the sun and carrier (see Fig. A.1) and is written as function of the torque applied to the sun T_s and the speed of the planets Ω_p. As, in normal operation, the power could split towards the ring, the ring is blocked which reduces the 2-DOF planetary gear to a 1-DOF system. Hence, the only power path which remains goes from the sun to the carrier (and vise-versa). Under the assumption that the direction of the power of the 1-DOF contacts has no impact on the efficiency, it does not matter which element (sun or planets) is chosen as input or output to measure the efficiency map. As the torque on the planets cannot be measured, the measurable quantity for the planets is speed. Therefore, the efficiency η_1 can be measured as function of the torque on the sun T_s (output property) and the speed of the planets Ω_p (input property).

Fig. A.3 shows the efficiency as function of the torque applied to the sun for varying speed of the planets. As can be seen in the graph, the efficiency is fairly constant in a wide range of torque values. This can support the assumption of taking a constant value for η_1. However, at low torque, as expected, the efficiency drops. Furthermore, the dependency with the speed is very low and only noticeable at low torque.

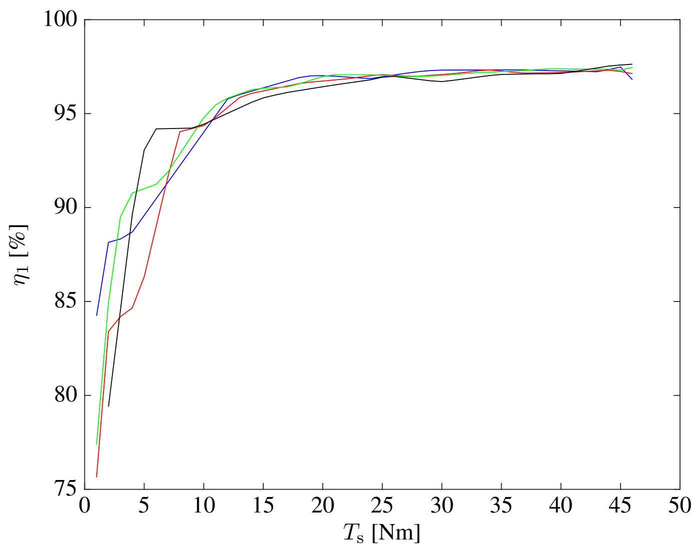

Figure A.3: Efficiency of the path going from sun to carrier η_1 as function of the torque applied to the sun T_s for varying speed of the planets Ω_p. Blue: Ω_p=500 rpm, red: Ω_p=1000 rpm, green: Ω_p=1500 rpm, black: Ω_p=2000 rpm.

Based on the complete dataset, it is possible to fit a surface (see Fig. A.4). This theoretical expression is equal to:

$$\eta_1 = (a_1 + b_1\Omega_\mathrm{p})\, T_\mathrm{s}^{(c_1\Omega_\mathrm{p}+d_1)} + e_1 \tag{A.12}$$

with $a_1 = -7.558 \times 10^{-5}$, $b_1 = -0.134$, $c_1 = -5.326 \times 10^{-5}$, $d_1 = -0.7706$ and $e_1 = 0.9836$. Note that this is an empirical formula which tends to be a good fit for most of the operating range. For extremely low torque values, (A.12) becomes useless as the efficiency goes to infinity. The advantage, however, is that, based on (A.12), it is easy to investigate the impact of reducing $\eta_1(T_s, \Omega_p)$ to $\eta_1(T_s)$.

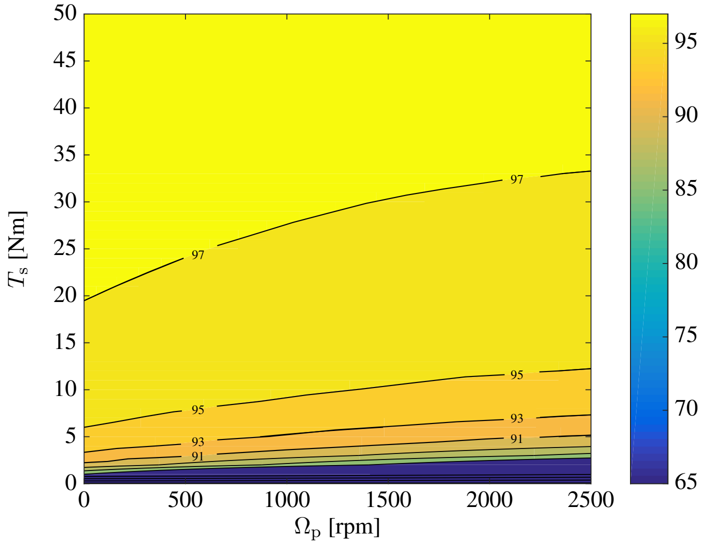

Figure A.4: Fitted efficiency of power path 1 as function of the speed of the planets and torque applied to the sun.

A.3.2 Path 2 (carrier to sun)

A similar methodology has been applied to measure the efficiency map of the second power path. Now the sun is fixed, allowing a unique power flow from carrier to ring. Fig. A.5 shows the results as function of torque applied to the ring for varying speed of the planets. Again, the efficiency is rather constant and almost independent of the speed of the planets. Note that the efficiency is 1 to 2% lower compared to the power path from sun to carrier. One of the reasons for this lower efficiency is that the efficiency of power path 2 is the combination of the efficiency of the planetary gear and the belt.

Based on the measured data it is again possible to fit a surface (see Fig. A.6). This theoretical expression is equal to:

$$\eta_2 = (a_2 + b_2\Omega_p)\, T_s^{(c_2\Omega_p + d_2)} + e_2 \tag{A.13}$$

with $a_2 = -14.2 \times 10^{-5}$, $b_2 = -0.5826$, $c_2 = -2.337 \times 10^{-14}$, $d_2 = -0.901$ and $e_2 = 0.9791$.

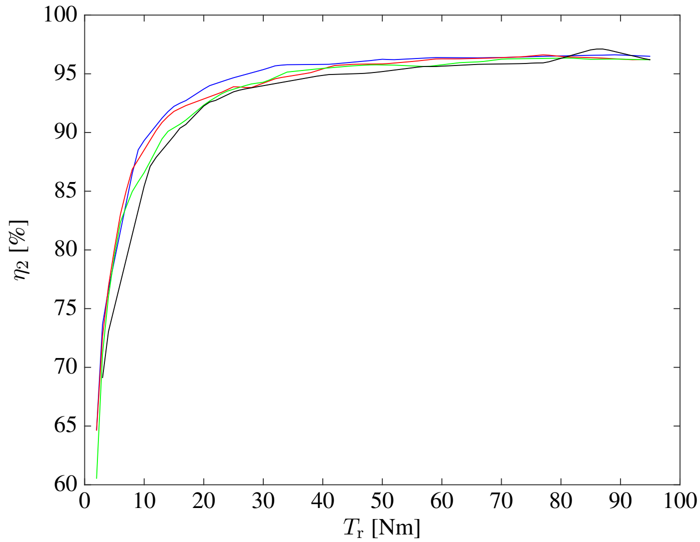

Figure A.5: Efficiency of the path going from carrier to ring η_2 as function of the torque applied to the ring T_r for varying speed of the planets Ω_p. Blue: Ω_p=500 rpm, red: Ω_p=1000 rpm, green: Ω_p=1500 rpm, black: Ω_p=2000 rpm.

Based on the equations written down in Table A.2, (A.12) and (A.13), it is possible to calculate the efficiency for all possible operating points. Fig. A.7 shows the measured efficiency values of the planetary gear as function of varying speed ratio (ratio of carrier speed and ring speed) and torque applied to the sun. The ring speed was chosen constant at 200 rpm. Note that as all 3 shafts are rotating, speed cannot be excluded anymore from the equation to calculate the efficiency. Therefore, in contrast with the earlier explanation on the measurement accuracy, accuracy of the speed measurement does have an effect.

The results presented in Fig. A.7 will be used as reference to benchmark the 3 cases: efficiency depending on both the load torque and input speed (case 1), efficiency as function of the load torque (case 2) and fixed efficiency (case 3). For case 1, (A.12) and (A.13) are used to calculate the efficiency of power path 1 and 2, denoted by η_1 and η_2, respectively. For case 2, (A.12) and (A.13) are again used but at a fixed speed of the planets. This speed is arbitrarily chosen at 500 rpm. For case 3, a fixed efficiency is chosen equal to 97% and 96% for η_1 and η_2, respectively. This decision is taken purely on the average efficiency in the operating range starting from 20 Nm until the maximum torque.

Fig. A.8 provides a comparison between the cases and the actual measured efficiency. The results show that the model is clearly capable of estimating the

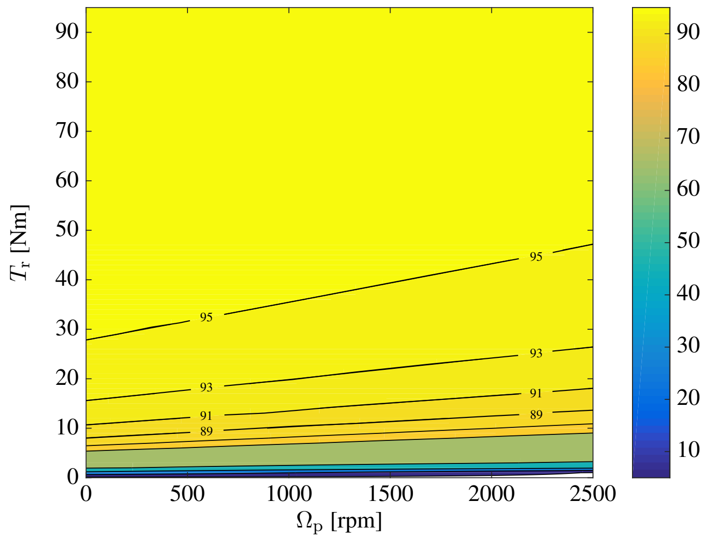

Figure A.6: Fitted efficiency of power path 2 as function of the speed of the planets and torque applied to the ring.

efficiency of the planetary gear, certainly for higher torque values.

Comparing the outcome based on case 1 and 2 shows that the results are almost identical. This means that there is no added value in measuring a complete efficiency map to resemble power path 1 and 2 as the variation of the efficiency with the speed is just too insignificant. However, there is a significant added value at low torque between case 2 ($\eta_{1,2}$ vary as function of $T_{\mathrm{s,r}}$) and case 3 ($\eta_{1,2}$= constant). At higher torque, η_1 and η_2 become fairly constant (see Fig. A.4 and A.6), which explains why the differences between case 2 and 3 diminish for higher torque.

Based on this analysis it is possible to conclude that the efficiency of a planetary gearbox can be estimate based on 2 measurements which take into account the efficiency of power path 1 and 2 as function of the load torque. For case 2, a complete efficiency map has been set up and is presented as Fig. A.9. It's clear by comparing Fig. A.7 and A.9 that there is a close match between measurement and model results. The average mismatch (complete operating range) between estimation and measurement is 1.7%. If torque values below 10 Nm are excluded, the average difference is below 1% which is close to the error bands of the measurements.

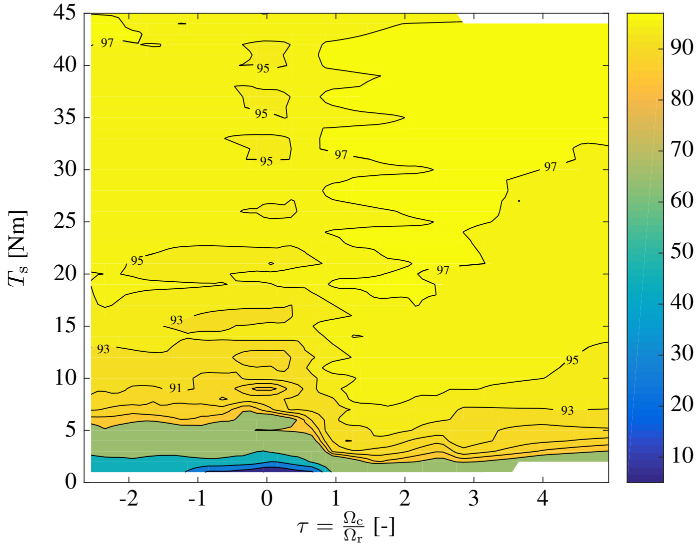

Figure A.7: Measured efficiency of the planetary gearset as function of varying speed ratio $\tau = \frac{\Omega_c}{\Omega_r}$ and torque applied to the sun T_s.

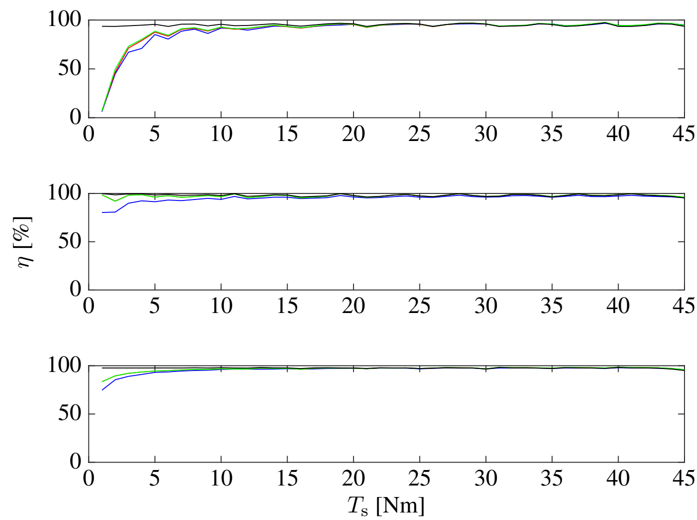

Figure A.8: Efficiency of the planetary gear for varying torque applied to the sun. (a) For a speed ratio of 0. (b) For a speed ratio of 1. (c) For a speed ratio of 2. Blue: measurement, red: case 1, green: case 2, black: case 3.

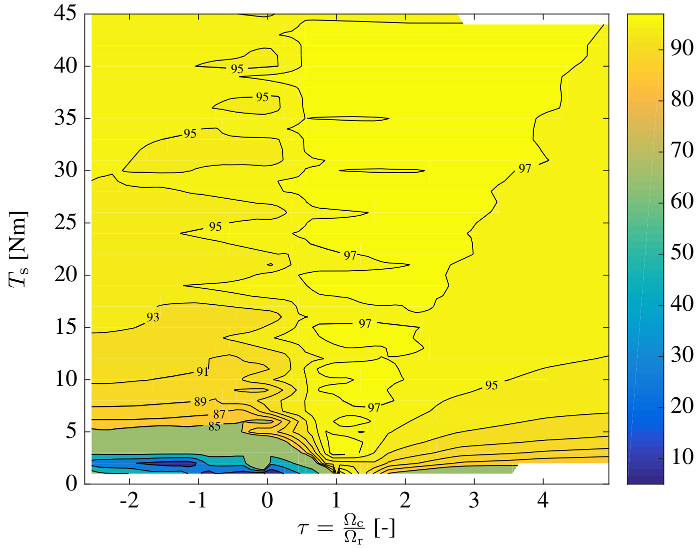

Figure A.9: Simulated efficiency of the planetary gearset for varying speed ratio $\tau = \frac{\Omega_c}{\Omega_r}$ and torque applied to the sun T_s.

A.4 Conclusion

In this chapter, a method is described to estimate the efficiency of a 2-DOF planetary gearbox over a wide range of operating points. The model combines the theory of virtual power with a limited set of measurements. These measurements are conducted to calculate the efficiency of 2 power paths: between sun & carrier and carrier & ring. It is shown that these efficiency terms merely depend on the load torque. The required measurement time is thus limited as the variation with speed does not have to be taken into account. The results show the good match between measured efficiency of the planetary gearbox and the estimated value. Average difference between both is 1.7% if the complete operating range is considered. This drops to less than 1% is torque values below 10 Nm are excluded.

Bibliography

[1] E. Hesla, “Electric propulsion [history],” *IEEE Industry Applications Magazine*, vol. 15, no. 4, pp. 10–13, 2009.

[2] F. Ju, J. Wang, J. Li, G. Xiao, and S. Biller, “Virtual battery: A battery simulation framework for electric vehicles,” *IEEE Transactions on Automation Science and Engineering*, vol. 10, no. 1, pp. 5–15, 2013.

[3] K. Sarrafan, K. M. Muttaqi, D. Sutanto, and G. E. Town, “A real-time range indicator for EVs using web-based environmental data and sensorless estimation of regenerative braking power,” *IEEE Transactions on Vehicular Technology*, vol. 67, no. 6, pp. 4743–4756, 2018.

[4] V. Monteiro, J. C. Ferreira, A. A. Nogueiras Melendez, C. Couto, and J. L. Afonso, “Experimental Validation of a Novel Architecture Based on a Dual-Stage Converter for Off-Board Fast Battery Chargers of Electric Vehicles,” *IEEE Transactions on Vehicular Technology*, vol. 67, no. 2, pp. 1000–1011, 2018.

[5] R. Atallah, C. Assi, W. Fawaz, M. H. K. Tushar, and M. J. Khabbaz, “Optimal Supercharge Scheduling of Electric Vehicles: Centralized vs. Decentralized Methods,” *IEEE Transactions on Vehicular Technology*, vol. 67, no. 9, pp. 7896–7909, 2018.

[6] Y. Wang, W. Ding, L. Huang, Z. Wei, H. Liu, and J. A. Stankovic, “Toward Urban Electric Taxi Systems in Smart Cities: The Battery Swapping Challenge,” *IEEE Transactions on Vehicular Technology*, vol. 67, no. 3, pp. 1946–1960, 2018.

[7] H. Wu, G. K. H. Pang, K. L. Choy, and H. Y. Lam, “An Optimization Model for Electric Vehicle Battery Charging at a Battery Swapping Station,” *IEEE Transactions on Vehicular Technology*, vol. 67, no. 2, pp. 881–895, 2017.

[8] S. Mercati, F. Panizzolo, and G. Profumo, “Power split Hydro-mechanical Variable Transmission (HVT) for off-highway application,” in *10th International Fluid Power Conference (IFK2016)*, 2016, pp. 69–80.

[9] K. T. Renius and R. Resch, "Continuously Variable Tractor Transmissions," in *American Society of Agricultrual Engineers*, 2005, pp. 1–37.

[10] R. H. Staunton, C. W. Ayers, L. D. Marlino, J. N. Chiasson, and T. a. Burress, "Evaluation of 2004 Toyota Prius Hybrid Electric Drive System," Tech. Rep., 2006.

[11] P. O. Rasmussen, T. V. Frandsen, K. K. Jensen, and K. Jessen, "Experimental evaluation of a motor-integrated permanent-magnet gear," *IEEE Transactions on Industry Applications*, vol. 49, no. 2, pp. 850–859, 2013.

[12] P. O. Rasmussen, H. H. Mortensen, T. N. Matzen, T. M. Jahns, and H. A. Toliyat, "Motor integrated permanent magnet gear with a wide torque-speed range," in *IEEE Energy Conversion Congress and Exposition*, 2009, pp. 1510–1518.

[13] Y. Cheng, R. Trigui, C. Espanet, and A. Bouscayrol, "Specifications and Design of a PM Electric Variable Transmission for Toyota Prius II," *IEEE Transactions on vehicular technology*, vol. 60, no. 9, pp. 4106–4114, 2011.

[14] E. Vinot, R. Trigui, Y. Cheng, C. Espanet, A. Bouscayrol, and V. Reinbold, "Improvement of an EVT-based HEV using dynamic programming," *IEEE Transactions on Vehicular Technology*, vol. 63, no. 1, pp. 40–50, 2014.

[15] M. J. Hoeijmakers and M. Rondel, "The electrical variable transmission in a city bus," *PESC Record - IEEE Annual Power Electronics Specialists Conference*, vol. 4, no. 1, pp. 2773–2778, 2004.

[16] M. Comellas, J. Pijuan, X. Potau, M. Nogués, and J. Roca, "Efficiency sensitivity analysis of a hydrostatic transmission for an off-road multiple axle vehicle," *International Journal of Automotive Technology*, vol. 14, no. 1, pp. 151–161, 2013.

[17] G. Carbone, L. Mangialardi, and G. Mantriota, "Fuel Consumption of a Mid Class Vehicle with Infinitely Variable Transmission," in *SAE Technical Papers*, 2001, pp. 2474–2484.

[18] F. Van der Sluis, T. Van Dongen, G. J. Van Spijk, A. Van der Velde, and A. Van Heeswijk, "Fuel consumption potential of the pushbelt CVT," in *Proceedings of FISITA 2006 World Automotive Congress*, 2006, pp. 1–12.

[19] L. Mangialardi and G. Mantriota, "Dynamic behavior of wind power systems equipped with automatically regulated continuously variable transmission," *Renewable Energy*, vol. 7, no. 2, pp. 185–203, 1996.

[20] M. L. Shaltout, J. F. Hall, and D. Chen, "Optimal Control of a Wind Turbine With a Variable Ratio Gearbox for Maximum Energy Capture and Prolonged Gear Life," *Journal of Solar Energy Engineering*, vol. 136, no. 3, 2014.

[21] G. C. Tyreas and P. G. Nikolakopoulos, "Development and friction estimation of the Half-Toroidal Continuously Variable Transmission: A wind generator application," *Simulation Modelling Practice and Theory*, vol. 66, pp. 63–80, 2016.

[22] G. Carbone, L. Mangialardi, B. Bonsen, C. Tursi, and P. A. Veenhuizen, "CVT dynamics: Theory and experiments," *Mechanism and Machine Theory*, vol. 42, no. 4, pp. 409–428, 2007.

[23] N. Srivastava and I. Haque, "A review on belt and chain continuously variable transmissions (CVT): Dynamics and control," *Mechanism and Machine Theory*, vol. 44, no. 1, pp. 19–41, 2009.

[24] L. Bertini, L. Carmignani, and F. Frendo, "Analytical model for the power losses in rubber V-belt continuously variable transmission (CVT)," *Mechanism and Machine Theory*, vol. 78, pp. 289–306, 2014.

[25] B. Bonsen, M. Steinbuch, and P. a. Veenhuizen, "CVT ratio control strategy optimization," in *EEE Vehicle Power and Propulsion Conference*, 2005, pp. 227–231.

[26] M. a. Kluger and D. M. Long, "An Overview of Current Automatic , Manual and Continuously Variable Transmission Efficiencies and Their Projected Future Improvements," in *SAE Technical Papers*, 1999, pp. 1–6.

[27] T. Imanishi and S. Miyata, "Development of the Next-Generation Half-Toroidal CVT," *Motion & Control*, vol. 14, no. 5, pp. 20–24, 2003.

[28] S. Simons, T. Klaassen, P. Veenhuizen, and G. Carbone, "Shift dynamics modelling for optimisation of variator slip control in a pushbelt CVT," *International Journal of Vehicle Design*, vol. 48, no. 1/2, p. 45, 2008.

[29] T. Shinojima, T. Toyoda, S. Miyata, T. Imanishi, E. Inoue, and H. Machida, "Development of the Next-Generation Half-Toroidal CVT with Geared Neutral and Power-Split Systems for 450 Nm Engines," *2004 International Continuously Variable Transmission Congress*, pp. 46–54, 2004.

[30] A. Brown, J. van Rooij, and A. Frank, "The design of an inline GCI chain CVT for large vehicles," in *International Continuously Variable and Hybrid Transmission Congress*, 2004, pp. 1–15.

[31] E. Solik, A. Frank, and P. Erickson, "Design improvements on a vee belt CVT and application to a new in-line CVT concept," in *SAE Technical Paper*, 2005, pp. 1–9.

[32] L. Xu, Y. Zhang, and X. Wen, "Multioperational modes and control strategeis of dual-mechanical-port-machine for hybrid electrical vehicles,"

IEEE transactions on Industrial Applications, vol. 45, no. 2, pp. 747–755, 2009.

[33] M. Hoeijmakers and J. Ferreira, "The electric variable transmission," *IEEE Transactions on Industrial Applications*, vol. 42, no. 4, pp. 1092–1100, 2006.

[34] M. Hoeijmakers, "Electromechanical converter, Patent US 7 164 219," 2007.

[35] H. Cai and L. Xu, "Modeling and control for cage rotor dual mechanical port electric machine part II: Independent control of two rotors," *IEEE Transactions on Energy Conversion*, vol. 30, no. 3, pp. 966–973, 2015.

[36] J. Druant, F. De Belie, P. Sergeant, and J. Melkebeek, "Field-oriented control for an induction-machine-based electrical variable transmission," *IEEE Transactions on Vehicular Technology*, vol. 65, no. 6, pp. 4230–4240, 2016.

[37] K. Atallah and D. Howe, "A novel high-performance magnetic gear," *IEEE Transactions on Magnetics*, vol. 37, no. 4, pp. 2844–2846, 2001.

[38] L. Jian and K. Chau, "Design and analysis of a magnetic-geared electronic-continuously variable transmission system using finite element method," *Progress In Electromagnetics Research*, vol. 107, no. July, pp. 47–61, 2010. [Online]. Available: http://www.jpier.org/PIER/pier.php?paper=10062806

[39] J. Bai, P. Zheng, C. Tong, Z. Song, and Q. Zhao, "Characteristic Analysis and Verification of the Magnetic-Field-Modulated Brushless Double-Rotor Machine," *IEEE Transactions on Industrial Electronics*, vol. 62, no. 7, pp. 4023–4033, 2015.

[40] M. Hoeijmakers, "Rotating electromechnical converter," *Patent US 9 018 863*, 2015.

[41] J. Druant, H. Vansompel, F. De Belie, J. Melkebeek, and P. Sergeant, "Torque Analysis on a Double Rotor Electrical Variable Transmission With Hybrid Excitation," *IEEE Transactions on Industrial Electronics*, vol. 64, no. 1, pp. 60–68, 2017.

[42] F. Verbelen, S. Derammelaere, P. Sergeant, and K. Stockman, "Visualizing the Efficiency of a Continuously Variable Transmission," in *EEMODS*, 2017.

[43] ——, "A comparison of the full and half toroidal continuously variable transmissions in terms of dynamics of ratio variation and efficiency," *Mechanism and Machine Theory*, vol. 121, pp. 299–316, 2018. [Online]. Available: https://doi.org/10.1016/j.mechmachtheory.2017.10.026

[44] ——, “Half toroidal continuously variable transmission: trade-off between dynamics of ratio variation and efficiency,” *Mechanism and Machine Theory*, vol. 107, pp. 183–196, 2017.

[45] N. A. Attia, “An overview on research developments of toroidal,” vol. 2, no. 1, 2003.

[46] T. Imanishi and H. Machida, “Development of POWERTOROS Unit Half-Toroidal CVT (2) Comparison between Half-Toroidal and Full-Toroidal CVTs,” *Motion & Control*, vol. 10, no. 1, pp. 1–8, 2001.

[47] H. Mori, T. Yamazaki, K. Kobayashi, and T. Hibi, “A study on the layout and ratio change characteristics of a dual-cavity half-toroidal CVT,” *JSAE Review*, vol. 22, no. 3, pp. 299–303, 2001.

[48] T. Yamamoto, T. Osidari, and M. Nakano, “Improvement of loading cam performance in a toroidal CVT,” *JSAE Review*, vol. 23, no. 4, pp. 481–487, 2002.

[49] S. Miyata and D. Liu, “Study of the Control Mechanism of a Half-Toroidal CVT during Load Transmission,” *Journal of Advanced Mechanical Design, Systems, and Manufacturing*, vol. 1, no. 3, pp. 346–357, 2007.

[50] G. Carbone, L. Mangialardi, and G. Mantriota, “A comparison of the performances of full and half toroidal traction drives,” *Mechanism and Machine Theory*, vol. 39, no. 9, pp. 921–942, 2004.

[51] M. Delkhosh and M. S. Foumani, “Multi-object geometrical optimization of full toroidal CVT,” *International Journal of Automotive Technology*, vol. 14, no. 5, pp. 707–715, 2013.

[52] F. Bottiglione, G. Carbone, L. De Novellis, L. Mangialardi, and G. Mantriota, “Mechanical hybrid KERS based on toroidal traction drives: An example of smart tribological design to improve terrestrial vehicle performance,” *Advances in Tribology*, vol. 2013, 2013.

[53] H. Tanaka, N. Toyoda, H. Machida, and T. Imanishi, “Development of a 6 Power-Roller Half-Toroidal CVT,” *NSK Technical Journal Motion and Control*, vol. 9, pp. 15–26, 2000.

[54] H. Tanaka, “Speed ratio control of a parallel layout double cavity half-toroidal CVT for four-wheel drive,” *JSAE Review*, vol. 23, no. 2, pp. 213–217, 2002.

[55] L. De Novellis, G. Carbone, and L. Mangialardi, “Traction and Efficiency Performance of the Double Roller Full-Toroidal Variator: A Comparison With Half- and Full-Toroidal Drives,” *Journal of Mechanical Design*, vol. 134, no. 7, pp. 1–14, 2012.

[56] A. Yildiz, O. Kopmaz, and S. T. Cetin, "Dynamic modeling and analysis of a four-bar mechanism coupled with a CVT for obtaining variable input speeds," *Journal of Mechanical Science and Technology*, vol. 29, no. 3, pp. 1001–1006, 2015. [Online]. Available: http://link.springer.com/10.1007/s12206-015-0214-y

[57] Q. Li, H. Li, D. Yu, and J. Yao, "A novel continuously variable transmission with logarithmic disc generatrix," *Mechanism and Machine Theory*, vol. 93, no. 24, pp. 147–162, 2015.

[58] G. K. Nikas, "Fatigue Life and Traction Modeling of Continuously Variable Transmissions," *Journal of Tribology*, vol. 124, no. 4, p. 689, 2002.

[59] J. P. Newall, S. Cowperthwaite, M. Hough, and A. P. Lee, "Efficiency modelling in the full toroidal variator: investigation into optimisation of EHL contact conditions to maximize contact efficiency," in *Tribology Series, Proceedings of the 31st Leeds-Lyon Symposium on Tribology*, 2004, pp. 245–255.

[60] T. Yamamoto, "Analysis of the efficiency of a half-toroidal CVT," *JSAE Review*, vol. 22, no. 4, pp. 565–570, 2001.

[61] Y. Zhang, X. Zhang, and W. Tobler, "A Systematic Model for the Analysis of Contact, Side Slip and Traction of Toroidal Drives," *Journal of Mechanical Design*, vol. 122, no. 4, p. 523, 2000.

[62] T. Osumi, K. Ueda, H. Nobumoto, M. Sakaki, and T. Fukuma, "Transient analysis of geared neutral type half-toroidal CVT," *JSAE Review*, vol. 23, no. 1, pp. 49–53, 2002.

[63] M. Delkhosh, M. Saadat Foumani, M. Boroushaki, M. Ekhtiari, and M. Deghani, "Geometrical optimization of half toroidal continuously variable transmission using particle swarm optimization," *Scientia Iranica*, vol. 18, no. 5, pp. 1126–1132, 2011.

[64] S. Akehurst, D. A. Parker, and S. Schaaf, "Dynamic modeling of the Milner continuously variable transmission - The basic kinematics," *Journal of Mechanical Design*, vol. 129, no. 11, pp. 1170–1178, 2007.

[65] K. Sharif, H. P. Evans, R. W. Snidle, and J. P. Newall, "Modelling of film thickness and traction in a variable ratio traction drive rig," *Journal of Tribology*, vol. 126, pp. 92–104, 2004.

[66] J. Hamrock, S. R. Schmid, and B. O. Jackobson, *Fundamentals of Fluid Film Lubrication*. CRC Press, 2004.

[67] D. Dowson, “Modelling of Elastohydrodynamic Lubrication of Real Solids by Real Lubricants,” *Meccanica*, vol. 33, pp. 47–58, 1998.

[68] SKF, “Rolling bearing catalogue,” Tech. Rep., 2013.

[69] B. Bonsen, T. Klaassen, R. Pulles, S. Simons, M. Steinbuch, and P. Veenhuizen, “Performance optimisation of the push-belt CVT by variator slip control,” *International Journal of Vehicle Design*, vol. 39, no. 3, p. 232, 2005.

[70] M. Pesgens, B. Vroemen, B. Stouten, F. Veldpaus, and M. Steinbuch, “Control of a hydraulically actuated continuously variable transmission,” *Vehicle System Dynamics*, vol. 44, no. 5, pp. 387–406, 2006.

[71] J. Chauvin, G. Corde, P. Moulin, M. Castagne, N. Petit, and P. Rouchon, “Real-time combustion torque estimation on a diesel engine test bench using time-varying Kalman filtering,” in *43rd IEEE Conference on Decision and Control (CDC)*, vol. 2, 2004, pp. 1688–1694.

[72] Y. H. Zweiri, J. F. Whidborne, and L. D. Seneviratne, “Diesel Engine Indicated and Load Torque Estimation Using Sliding Mode Observer,” *Journal of Automobile Engineering*, vol. 220, no. 6, pp. 95–103, 2006.

[73] Y. Hasuda and R. Fuchs, “Development of IVT variator dynamic model,” *Koyo Engineering Journal English Edition*, vol. 24, no. 106E, pp. 24–28, 2002.

[74] R. Fuchs, N. Mccullough, and K. Matsumoto, “The Making of the Full Toroidal Variator,” *JTEKT Engineering Journal*, no. 1006E, pp. 31–36, 2009.

[75] Z. Zou, Y. Zhang, X. Zhang, and W. Tobler, “Modeling and Simulation of Traction Drive Dynamics and Control,” *Journal of Mechanical Design*, vol. 123, no. 4, p. 556, 2001.

[76] J. S. Park, “Motion profile planning of repetitive point-to-point control for maximum energy conversion efficiency under acceleration conditions,” *Mechatronics*, vol. 6, no. 6, pp. 649–663, 1996.

[77] F. Verbelen, M. Haemers, J. D. Viaene, S. Derammelaere, K. Stockman, and P. Sergeant, “Adaptive PI Controller for Slip controlled Belt Continuously Variable Transmission,” in *PID-IFAC*, vol. 51, no. 4, 2018, pp. 101–106.

[78] B. Bonsen, T. Klaassen, K. van de Meerakker, M. Steinbuch, and P. Veenhuizen, “Analysis of slip in a continuously variable transmission,” in *Prodeedings of IMECE*, 2003, pp. 1–6.

[79] B. Bonsen, “Efficiency optimization of the push-belt CVT by variator slip control,” Ph.D. dissertation, 2006. [Online]. Available: http://www.em.tue.nl/pdfs/BonsenBram.pdf

[80] E. Shafai, M. Simons, U. Neff, and H. P. Geering, “Model of a continuously variable transmission,” in *Advances in Automotive Control*, 1995, pp. 105–113.

[81] T. Ide, A. Udagawa, and K. Ryuji, “A dynamic response analysis of a vehicle with a metal V-belt CVT,” *JSAE Review*, vol. 2, no. 16, 1995.

[82] T. Ide, “Experimental investigation on shift speed characteristics of a metal V-belt CVT,” in *Proceedings of CVT*, 1996, pp. 59–64.

[83] G. Carbone, L. Mangialardi, and G. Mantriota, “The Influence of Pulley Deformations on the Shifting Mechanism of Metal Belt CVT,” *Journal of Mechanical Design*, vol. 127, no. 1, p. 103, 2005.

[84] ——, “Theoretical Model of Metal V-Belt Drives During Rapid Ratio Changing,” *Journal of Mechanical Design*, vol. 123, no. 1, p. 111, 2001.

[85] A. Yildiz, A. Piccininni, F. Bottiglione, and G. Carbone, “Modeling chain continuously variable transmission for direct implementation in transmission control,” *Mechanism and Machine Theory*, vol. 105, pp. 428–440, 2016. [Online]. Available: http://dx.doi.org/10.1016/j.mechmachtheory.2016.07.015

[86] A. Yildiz, F. Bottiglione, A. Piccininni, O. Kopmaz, and G. Carbone, “Experimental validation of the Carbone-Mangialardi-Mantriota model of continuously variable transmissions,” *Journal of Automobile Engineering*, pp. 1–10, 2017. [Online]. Available: http://journals.sagepub.com/doi/10.1177/0954407017711320

[87] S. Prakash and T. Hofman, “Clamping Strategies for Belt-Type Continuously Variable Transmissions : An Overview,” in *IEEE Vehicle Power and Propulsion Conference (VPPC)*, 2017, pp. 1–6.

[88] B. Bonsen, R. J. Pulles, S. W. H. Simons, M. Steinbuch, and P. A. Veenhuizen, “Implementation of a slip controlled CVT in a production vehicle,” in *Control Applications, 2005. CCA 2005. Proceedings of 2005 IEEE Conference on*, 2005, pp. 1212–1217.

[89] T. Hofman, M. Steinbuch, R. van Druten, and A. F. a. Serrarens, “Design of CVT-based hybrid passenger cars,” *IEEE Transactions on Vehicular Technology*, vol. 58, no. 2, pp. 572–587, 2009.

[90] J. Druant, "Modeling and Control of an Electrical Variable Transmission with Hybrid Excitation," Ph.D. dissertation, 2018.

[91] F. Verbelen, J. Druant, A. De Kock, K. Stockman, and P. Sergeant, "Magnetic Equivalent Circuit Model of a Permanent Magnet Electrical Variable Transmission," in *Proceedings - 2018 23rd International Conference on Electrical Machines, ICEM 2018*, 2018, pp. 819–825.

[92] J. Druant, H. Vansompel, F. De Belie, and P. Sergeant, "Optimal Control for a Hybrid Excited Dual Mechanical Port Electric Machine," *IEEE Transactions on Energy Conversion*, vol. 32, no. 2, pp. 599–607, 2017.

[93] S. D. Sudhoff, B. T. Kuhn, K. a. Corzine, and B. T. Branecky, "Magnetic Equivalent Circuit Modeling of Induction Motors," *IEEE Transactions on Energy Conversion*, vol. 22, no. 2, pp. 259–270, 2006.

[94] Y. Mollet, G. Barbierato, and J. Gyselinck, "Finite-element and magnetic-equivalent-circuit modelling of brushed wound-field DC machines with cross-saturation," *Proceedings - 2016 22nd International Conference on Electrical Machines, ICEM 2016*, vol. 50, no. 0, pp. 350–356, 2016.

[95] D. Faustner, W. Kemmetmüller, and A. Kugi, "Magnetic equivalent circuit modeling of a saturated surface-mounted permanent magnet synchronous machine," 2016.

[96] J. Perho, "Reluctance network for analysing induction machines," *Ph.D. dissertation, Dept. Electr. Commun. Eng., Aalto Univ., Esbo, Finland*, pp. 1–147, 2002.

[97] L. Dang, N. Bernard, N. Bracikowski, and G. Berthiau, "Analytical model and reluctance network for high-speed PMSM design optimization application to electric vehicles," *Proceedings - 2016 22nd International Conference on Electrical Machines, ICEM 2016*, pp. 1359–1365, 2016.

[98] M. F. Hsieh and Y. C. Hsu, "A generalized magnetic circuit modeling approach for design of surface permanent-magnet machines," *IEEE Transactions on Industrial Electronics*, vol. 59, no. 2, pp. 779–792, 2012.

[99] D. Sato and J.-i. Itoh, "Loss Minimization Design Using Magnetic Equivalent Circuit for a Permanent Magnet Synchronous Motor," in *International Power Electronics Conference*, 2014, pp. 3815–3822.

[100] H. W. Derbas, J. M. Williams, A. C. Koenig, and S. D. Pekarek, "A comparison of nodal- and mesh-based magnetic equivalent circuit models," *IEEE Transactions on Energy Conversion*, vol. 24, no. 2, pp. 388–396, 2009.

[101] S. Sudhoff, "Magnetic equivalent circuit toolbox." [Online]. Available: https://engineering.purdue.edu/ECE/Research/Areas/PEDS/MEC{_}toolbox

[102] A. Abdallh, G. Crevecoeur, P. Sergeant, and L. Dupré, "Magnetic matieral identification of a switched reluctance motor," *International journal of applied electromagnetics and mechanics*, vol. 37, no. 1, pp. 35–49, 2011.

[103] J. Melkebeek, *Electrical machines and drives - fundamentals and advanced modelling*.

[104] G. Bertotti, *Hysteresis in magnetism: for physicists, materials scientists, and engineers*. Academic Press, 1998.

[105] A. Wintrich, U. Nicolai, W. Tursky, and T. Reimann, *Application Manual Power Semiconductors*. SEMIKRON International GmbH, 2011.

[106] J. Druant, H. Vansompel, F. De Belie, and P. Sergeant, "Loss Identification in a Double Rotor Electrical Variable Transmission," *IEEE Transactions on Industrial Electronics*, vol. 64, no. 10, pp. 7731–7740, 2017.

[107] ——, "Loss Identification in a Double Rotor Electrical Variable Transmission," *IEEE Transactions on industrial electronics*, vol. 64, no. 10, pp. 7731–7740, 2017.

[108] P. Pisek, B. Stumberger, T. Marcic, and P. Virtic, "Design analysis and experimental validation of a double rotor synchronous PM machine used for HEV," *IEEE Transactions on Magnetics*, vol. 49, no. 1, pp. 152–155, 2013.

[109] Y. Cheng, C. Espanet, R. Trigui, A. Bouscayrol, and S. Cui, "Design of a permanent magnet electric variable transmission for HEV applications," *2010 IEEE Vehicle Power and Propulsion Conference*, 2010.

[110] G. R. Slemon, "On the design of high-performance surface-mounted PM motors," *IEEE Transactions on Industry Applications*, vol. 30, no. 1, pp. 134–140, 1993.

[111] S. Stipetic, D. Zarko, and M. Popescu, "Ultra-fast axial and radial scaling of synchronous permanent magnet machines," *IET Electric Power Applications*, vol. 10, no. 7, pp. 658–666, 2016.

[112] E. A. Grunditz and T. Thiringer, "Electric Vehicle Acceleration Performance and Motor Drive Cycle Energy Efficiency Trade-Off," in *2018 XIII International Conference on Electrical Machines (ICEM)*, 2018, pp. 717–723.

[113] K. Ramakrishnan, S. Stipetic, M. Gobbi, and G. Mastinu, "Optimal Sizing of Traction Motors Using Scalable Electric Machine Model," *IEEE Transactions on Transportation Electrification*, vol. 4, no. 1, pp. 314–321, 2018.

[114] Q. S. Gu and M. Stiebler, "Scaling and Dimensioning of Switched Reluctance Machines," *International Transactions on Electrical Energy Systems*, vol. 7, no. 5, pp. 301–310, 1997.

[115] J. Bone, "Influence of rotor diameter and length on the rating of induction motors," *IEE Journal on Electric Power Applications*, vol. 1, no. 1, pp. 1–5, 1978.

[116] H. Li, Z. Chen, and H. Polinder, "Optimization of multibrid permanent-magnet wind generator systems," *IEEE Transactions on Energy Conversion*, vol. 24, no. 1, pp. 82–92, 2009.

[117] A. McDonald, M. Mueller, and H. Polinder, "Structural mass in direct-drive permanent magnet electrical generators," *Renewable Power Generation, IET*, vol. 1, no. 1, pp. 10–16, 2007.

[118] S. Stipetic, J. Goss, and D. Zarko, "Calculation of Efficiency Maps Using Scalable Saturated Model of Synchronous Permanent Magnet Machines," *IEEE Transactions on Industry Applications*, vol. 54, no. 5, pp. 4257 – 4267, 2018.

[119] H. Polinder, S. de Haan, and M. Dubois, "Basic Operation Principles and Electrical Conversion Systems of Wind Turbines," *EPE Journal*, vol. 15, no. 4, pp. 43–50, 2005.

[120] J. Pyrhönen, T. Jokinen, and V. Hrabovcová, *Design of Rotating Electrical Machines*. John Wiley & Sons, Ltd, 2009.

[121] A. Grauers and P. Kasinathan, "Force Density Limits in Low-Speed PM Machines Due to Temperature and Reactance," *IEEE Transaction on Energy Conversion*, vol. 19, no. 3, pp. 518–525, 2004.

[122] P. Kasinathan, A. Grauers, and E. S. Hamdi, "Force Density Limits in Low-Speed Permanent-Magnet Machines Due to Saturation," *IEEE Transaction on Energy Conversion*, vol. 20, no. 1, pp. 37–44, 2005.

[123] R. Pelders, S. Van Vuuren, and L. Van Seeters, "High Torque CVT P930 , design and test results," in *Mech. E*, 1997, pp. 1–17.

[124] S. Van Der Meulen, "High-Performance Control of Continuously Variable Transmissions," Ph.D. dissertation, 2010.

[125] T. J. Barlow, S. Latham, I. S. McCrae, and P. G. Boulter, "A reference book of driving cycles for use in the measurement of road vehicle emissions," TRL Published Project Report, Tech. Rep., 2009.

[126] European Commission, "Commission Regulation (EU) 2018/1832, Emission type approval tests and procedures for light passenger and commercial vehicles," *Official Journal of the European Union*, vol. 1832, p. 301, 2018.

[127] E. Vinot, "Comparison of different power-split hybrid architectures using a global optimisation design method," *International Journal of Electric and Hybrid Vehicles*, vol. 8, no. 3, pp. 225–241, 2016.

[128] E. Vinot, R. Trigui, Y. Cheng, C. Espanet, A. Bouscayrol, and V. Reinbold, "Improvement of an EVT-Based HEV Using Dynamic Programming," *IEEE Transactions on Vehicular Technology*, vol. 63, no. 1, pp. 40–50, 2014.

[129] J. Druant, H. Vansompel, F. De Belie, and P. Sergeant, "Efficiency of a CVT Operated EVT Experimentally Evaluated against Half-Toroidal and Push-belt CVTs," *IEEE Transactions on Industrial Electronics*, vol. 65, no. 4, pp. 3095–3103, 2018.

[130] T. Watanabe, E. Tsuchiya, M. Ebina, Y. Osada, T. Toyama, and A. Murakami, "High Efficiency Electromagnetic Torque Converter for Hybrid Electric Vehicles," *SAE International Journal of Alternative Powertrains*, vol. 5, no. 2, pp. 228–236, 2016.

[131] M. Koot, J. Kessels, B. de Jager, M. Heemels, P. van den Bosch, and M. Steinbuch, "Electric Power Systems Textbooks," *IEEE Transactions on Power Apparatus and Systems*, vol. 54, no. 9, pp. 771–782, 2007.

[132] O. Sundström and L. Guzzella, "A Generic Dynamic Programming Matlab Function," in *IEEE Multi-conference on Systems and Control*, 2009, pp. 1625–1630.

[133] D. P. Bertsekas, *Dynamic programming and optimal control. Vol.* Belmont, MA: Athena Scientific, 1995.

[134] T. Cormen, C. Leiserson, R. Rivest, and C. Stein, *Introduction to algorithms*, 3rd ed. The MIT PRess, 2009, no. 2. [Online]. Available: http://www.pubmedcentral.nih.gov/articlerender.fcgi?artid=2560149{&}tool=pmcentrez{&}rendertype=abstract

[135] K. Davies, C. Chen, and B. K. Chen, "Complete Efficiency Analysis of Epicyclic Gear Train With Two Degrees of Freedom," *Journal of Mechanical Design*, vol. 134, no. 7, p. 071006, 2012. [Online]. Available: http://mechanicaldesign.asmedigitalcollection.asme.org/article.aspx?articleid=1450844

[136] S. Dereyne, E. Algoet, P. Defreyne, and K. Stockman, "An energy efficiency measurement test bench for gearboxes," in *Energy efficieny of Motor Driven Systems*, 2013.